Single-Molecule Chemistry

Studied Using the Protein Pore – α-Hemolysin

A dissertation by

Lai-Sheung Choi

Submitted to the University of Oxford in partial satisfaction of the requirements for

the Degree of Doctor of Philosophy

Major Subject: Chemical Biology

Trinity College

May 2012

Declaration

The work described in this thesis was completed in the Department of Chemistry, University of Oxford, UK under the supervision of Professor Hagan Bayley F. R. S. from October 2008 to May 2012. I declare that the work in this thesis is solely my work, unless acknowledged and stated otherwise in the text. No work described in this thesis has been submitted for any degree or other qualifications within the University of Oxford or elsewhere.

Lai-Sheung Choi

May, 2012

Acknowledgements

I would like to give my sincere thanks to Professor Hagan Bayley F. R. S. who gave me the opportunity to work in his laboratory. In his lab, I have improved in critical thinking and independence.

I am very grateful to the Croucher Foundation (Hong Kong) for awarding the three-year University of Oxford Croucher Scholarship (UOCS) (October 2008 – September 2011). Without the financial support, I won't be able to study abroad which has broadened my horizon both in research and in my life.

I would like to thank the Bayley lab members. Their ideas, discussion and technical supports helped me to solve many research problems. Special thanks are given to Dr. Arnold Boersma, Dr. Lajos Hofler, Dr. Gokce Su Pulcu and Dr. Sarah Rogers for reading my thesis. I would also like to say thanks to my great friends who were in the Bayley lab – Qiu Hong, Ruhma, Marsi, Sarah, Leon and DJ. In addition to working together in late hours or holidays, we also had good leisure times.

Special thanks are dedicated to my MPhil supervisor Dr. Hak-Fun Chow and my mentor Dr. Sze-Lock Chan in the Chinese University of Hong Kong. Their encouragements give me the confidence in research. Moreover, my parents, sister, brother, Ivan, Jasmine, Shan, Mina, Mackins and Ngus have provided endless mental (and food!) supports that made me strong to go through all the challenges.

Thanks are also given to the examiners, Professor Veronique Gouverneur and Professor Willem Koppenol, for reading my thesis and gave valuable feedbacks.

Abstract

Single-molecule detection has provided insights into how molecules behave. Without the averaging effect of ensemble measurements, the stochastic behaviour of single molecules can be observed and intermediate steps in multistep transformations can be clearly detected. The single-molecule reactants range from small molecules (e.g. propene) to proteins of several tens of kDa (e.g. myosin). One single-molecule detection technique is single-channel electrical recording. This approach is based on the measurement of the transmembrane ionic current flowing through a nanoscale transmembrane pore under an applied potential. In this thesis, the protein α-hemolysin was employed as a nanoreactor. α-Hemolysin is a toxin secreted by *Staphylococcus aureus*. Its transmembrane pore (~100 Å in length and ≥14 Å in diameter) allows ions, water and small molecules to pass through its lumen. Under an applied potential, chemical changes in reactants attached to the internal wall of the pore modulate the flow of ions, leading to changes in the transmembrane ionic current. Analysis of this current provides information about the reaction kinetics and mechanisms.

Chapter 1 – Single-Molecule Chemistry and α-Hemolysin is an introductory chapter that is divided into two parts. Section 1.1 provides an overview of the different techniques for the detection of chemical reactions at the single-molecule level. Section 1.2 gives a brief review of the protein pore α-hemolysin, including its structure, properties and various applications.

Chapter 2 – *S*-Nitrosothiol Chemistry applies cysteine-containing α-hemolysins to study the biologically relevant chemistry of *S*-nitrosothiols (RSNO). RSNO are important molecules involved in cell signalling, which control physiological processes such as vasodilation and bronchodilation. Three reactions, namely transnitrosation (the transfer of the 'NO' group from RSNO to a thiol), *S*-thiolation (the formation of a disulfide from RSNO and thiol) and *S*-sulfonation (the generation of an *S*-sulfonate ($RSSO_3^-$) from RSNO and sulfite ion), were investigated at the single-molecule level. The pH-dependency of the two competing reactions (transnitrosation and *S*-thiolation), the lifetime of the proposed transnitrosation intermediate, and nature of the chemical reaction between RSNO and sulfite (a bronchoconstrictor) were determined.

Chapter 3 – Silver(I)-thiolate and cadmium(II)-thiolate complexes describes the kinetics of the formation and breakdown of these two metal-thiolate complexes. Ag^+ and Cd^{2+} are commonly used in probing the membrane topology and gating properties of ion channels using the scanning cysteine accessibility method (SCAM). The binding of two Ag^+ ions per thiol group and the stepwise build-up and dissociation of Cd^{2+}-glutathione complexes were unambiguously characterized.

Chapter 4 – Copper(II)-Catalyzed Diels-Alder Reactions reports the attempt to carry out copper(II)-catalyzed Diels-Alder reactions inside an engineered α-hemolysin. An iminodiacetate ligand was covalently attached within the lumen of the α-hemolysin pore. This ligand chelates Cu^{2+} ion, which can bind bidentate dienophiles and activate them towards Diels-Alder reaction with dienes. However, due to the ‘slow’ reaction rate of the Diels-Alder reaction (rate constant ~10^{-1} $M^{-1}s^{-1}$) relative to the time-scale of the single-molecule experiment, we failed to observed chemical conversion at the single-molecule level. Nevertheless, the engineered metal-binding α-hemolysin may be useful for sensing molecules bearing metal-coordinating groups.

Table of Contents

Declaration i
Acknowledgements ii
Abstract iii
Table of Contents v
Abbreviations ix

Chapter 1 Single-Molecule Chemistry and α-Hemolysin

1.1 Single-molecule detection techniques 1
    1.1.1 Single-molecule fluorescence microscopy (SMFM) 1
    1.1.2 Force microscopy 4
    1.1.3 Scanning tunneling microscopy (STM) 7
    1.1.4 Single-channel ionic current detection 8
1.2 α-Hemolysin 11
    1.2.1 Structure of α-Hemolysin 11
    1.2.2 Properties of α-Hemolysin 13
    1.2.3 Single-channel recording technique 15
    1.2.4 Analysis of stochastic single-molecule data 17
    1.2.5 Incorporation of reaction sites 18
    1.2.6 Examples of single-molecule chemistry in αHL 19
    1.2.7 Strategies for the investigation of chemical reactions 21
    1.2.8 Criteria of a detectable chemical transformation 23
    1.2.9 Factors affecting the reaction rate constants measured with a nanoreactor compared to ensemble experiment. 25
    1.2.10 Other applications of αHL 26
1.3 Conclusions 27
1.4 References 28

Chapter 2 *S*-Nitrosothiol chemistry

2.1 Introduction 33
    2.1.1 Intracellular generation and interconversion of NO, RSNO and HNO 34
    2.1.2 Propagation of nitrergic signal 37
    2.1.3 Termination of nitrergic signal 38
    2.1.4 Medical conditions associated with NO, RSNO, HNO *etc*. 39
    2.1.5 Chemistry of NO, RSNO and HNO 40
    2.1.6 Detection of NO, RSNO, HNO 45

2.2 Objectives 46
2.3 Results 48
2.3.1 Single-channel recording conditions 48
2.3.2 Transnitrosation versus *S*-thiolation 50
2.3.3 Reversible transnitrosation 56
2.3.4 *S*-Sulfonation 60
2.4 Discussion 66
2.4.1 Lifetime of nitroxyl disulfide intermediate 66
2.4.2 Proposed mechanism of *S*-sulfonation 66
2.4.3 Acidic environment favours *S*-thiolation over transnitrosation 69
2.5 Conclusions 70
2.6 Materials and Methods 71
2.6.1 General Information 71
2.6.2 Synthetic procedures 72
2.6.3 Details of NMR experiments 75
2.6.4 Saville assay for quantifying *S*-nitrosothiols 76
2.6.5 Griess assay for quantification of nitrite ion 77
2.6.6 Griess assay for the quantification of nitrate ion 78
2.6.7 Hydroxylamine assay 78
2.6.8 Kinetic measurements in ensemble solution 79
2.6.9 Protein preparation 80
2.6.10 Planar lipid bilayer recording 82
2.6.11 Data analysis 83
2.6.12 Calculation of single-molecule reaction rate constant (k_t) 84
2.6.13 Reaction rate constant (k'_t) with respect to thiolate 86
2.6.14 Calculation of $k_{thiolation}$ 87
2.6.15 Amount of reactive protein cysteine thiol 88
2.6.16 PS-DTT intermediate 89
2.6.17 Quantification of the products in *S*-sulfonation 91
2.7 References 93

Chapter 3 Silver(I)-thiolate and cadmium(II)-thiolate complexes

3.1 Introduction 101
3.1.1 Heavy metal-thiolate interactions in vivo 101
3.1.2 Heavy metal ions as probes for studying ion channels 103
3.1.3 Coordination chemistry of silver(I)-thiolate and cadmium(II)-thiolate 105
3.1.4 Metal ion binding studies using αHL 107
3.2 Objectives 110

3.3 Results 110
  3.3.1 Design of new mutant 110
  3.3.2 Characterization of the new mutant $(AG)_7$ 113
  3.3.3 Denaturing effect of nitrate ion on αHL 116
  3.3.4 Reversible binding of two silver(I) ions 118
  3.3.5 Silver(I)-thiolate oligomer formation 123
  3.3.6 Reversible cadmium(II) ion binding 130
  3.3.7 Reversible cadmium(II)-thiolate complex formation 135
3.4 Discussion 142
  3.4.1 Two silver(I) ions are bound per cysteine thiol group 142
3.5 Conclusions 144
3.6 Materials and Methods 145
  3.6.1 Hemolytic assay 145
  3.6.2 Multiple site-directed mutagenesis 147
  3.6.3 Further site-directed mutagenesis 148
  3.6.4 Protein preparation 150
  3.6.5 Planar lipid bilayer recordings 151
  3.6.6 Data analysis of single-channel recordings 151
  3.6.7 Ion selectivity 152
  3.6.8 Single channel conductance in KNO_3 buffer 153
  3.6.9 Analysis of stochastic single-molecule data using QuB 154
  3.6.10 Proof of the presence of a single cysteine residue in PSH 157
  3.6.11 Complete blockade of αHL induced by Ag^+ ion 159
  3.6.12 Kinetics of the individual binding steps in HC and CC mutants 162
  3.6.13 Oxidation of both cysteine residues in the CC mutant 169
  3.6.14 Attempt to determine the cysteine thiol pK_a values 170
3.7 References 177

Chapter 4 Copper(II)-Catalyzed Diels-Alder Reactions

4.1 Introduction 184
  4.1.1 Artificial metalloenzymes 184
  4.1.2 Metal-catalyzed Diels-Alder reaction 186
  4.1.3 Artificial Diels-Alderases 188
4.2 Objectives 191
4.3 Results 192
  4.3.1 Preparation of chelator-containing protein (P_{PIDA}) 192
  4.3.2 Binding of Cu^{2+} ion to P_{PIDA} 194
  4.3.3 Interactions of Diels-Alder reactants and products with the pore-bound copper(II) complex 197

4.3.4 Copper(II)-catalyzed Diels-Alder reaction 199
4.4 Discussion 202
4.4.1 Mean waiting time for the catalytic reaction to occur – mathematical derivation 202
4.4.2 Mean waiting time for the catalytic reaction to occur – theoretical calculation 204
4.4.3 Other problems of the catalytic system 206
4.5 Conclusions 207
4.6 Materials and Methods 208
4.6.1 General Information 208
4.6.2 Synthetic procedures 209
4.6.3 Targeted chemical modification 214
4.6.4 Protein preparation 215
4.6.5 Planar lipid bilayer recordings 216
4.6.6 Data analysis 216
4.6.7 Literature value of K_d between *N*-methyliminodiacetate and Cu^{2+} at pH 7.0 217
4.7 References 218

Appendix

A.1 Vector Map of pT7-WT-αHL A-1
A.2 DNA sequences of αHL gene in pT7 vector A-2
A.3 NMR spectra A-4

Abbreviations

AFM	Atomic force microscopy
Bis-Tris	2-Bis(2-hydroxyethyl)amino-2-(hydroxymethyl)-1,3-propanediol
Bis-Tris propane	1,3-Bis(tris(hydroxymethyl)methylamino)propane
bPP	Bovine pancreatic polypeptides
BST	Biotin-switch technique
CAPS	3-(Cyclohexylamino)-1-propanesulfonic acid
CD	Circular dichroism spectroscopy
βCD	β-Cyclodextrin
dcbpy	2,2'-Bipyridine-4,4'-dicarboxylic acid
DPhPC	1,2-Diphytanoyl-*sn*-glycero-3-phosphocholine
DNA	Deoxyribonucleic acid
DMSO	Dimethyl sulfoxide
DNA-PK	DNA-Activated protein kinase
DTNB	5,5'-Dithiobis-(2-nitrobenzoic acid)
DTPA	Diethylenetriaminepentaacetate
DTT	Dithiothreitol
EDRF	Endothelium-derived relaxing factor
EDTA	Ethylenediaminetetraacetate
EPR	Electron paramagnetic resonance spectroscopy
ESI	Electrospray ionization
GADPH	Glyceraldehyde 3-phosphate dehydrogenase
GC	Guanylate cyclase
GCMS	Gas chromatography-mass spectrometry
cGMP	Cyclic guanosine monophosphate
GSH	Glutathione
GSNO	*S*-Nitrosoglutathione
GSNOR	*S*-Nitrosoglutathione reductase
GTP	Guanosine triphosphate
HDAC2	Histone deacetylase-2
αHL	α-Hemolysin
HNO	Nitroxyl
HPLC	High performance liquid chromatography
HSQC NMR	Heteronuclear Single Quantum Coherence NMR
I27	Immunoglobulin module 27
IVTT	*In vitro* transcription and translation

MES	2-(4-Morpholinyl)ethanesulfonic acid
MIDA	*N*-Methyliminodiacetate
MOPS	3-(4-Morpholinyl)-1-propanesulfonic acid
MT	Metallothionein
MTS	Methanethiosulfonate
$MTS\text{-}EA^+$	2-Aminoethyl methanethiosulfonate
$MTS\text{-}ES^-$	2-Sulfonatoethyl methanethiosulfonate
$MTS\text{-}ET^+$	2-(Trimethylammonium)ethyl methanethiosulfonate
NADH	Nicotinamide adenine dinucleotide – reduced form
NADPH	Nicotinamide adenine dinucleotide phosphate – reduced form
NED	*N*-Naphthalen-1-ylethane-1,2-diamine dihydrochloride
NEM	*N*-Ethylmaleimide
NMR	Nuclear magnetic resonance
NOS	Nitric oxide synthase
PCR	Polymerase chain reaction
PEG	Polyethylene glycol
PFT	Pore-forming toxin
PIDA	2,2'-(3-(2-Iodoacetamido)propylazanediyl)diacetic acid
rRBCM	Rabbit red blood cell membrane
RNA	Ribonucleic acid
RNS	Reactive nitrogen species
ROS	Reactive oxygen species
RSNO	*S*-Nitrosothiol
RSOH	Sulfenic acid
RSO_2H	Sulfinic acid
SCAM	Substituted cysteine accessibility method
SDS-PAGE	Sodium dodecyl sulfate polyacrylamide gel electrophoresis
SIRT1	Sirtuin-1
SMFM	Single-molecule fluorescence microscopy
SNAP	*S*-Nitroso-*N*-acetyl-D-penicillamine
SNOSID	*S*-Nitrosothiol site identification
SPEN	*S*-Nitroso-D-penicillamine
STM	Scanning tunnelling microscopy
TCEP	Tris(2-carboxylethyl)phosphine
TMR	Tetramethylrhodamine
Trx	Thioredoxin
TrxR	Thioredoxin reductase
XIAP	X-Linked inhibitor of apoptosis

Chapter 1. Single-Molecule Chemistry and α-Hemolysin

1.1 Single-molecule detection techniques

The first experiment on functional single molecules was reported in the 1970s by Neher and Sakmann[1] in their patch clamp studies of single ion channels on cell membranes. Single-molecule detection reveals the stochastic behaviour of individual molecules, which is inaccessible by ensemble measurements due to ensemble averaging. Single-molecule techniques can also provide direct and detailed information about the reaction mechanisms that the molecules undergo. Although bond formation and cleavage are too fast (< 1 ps)[2] to be resolved in a single-molecule experiment today, the waiting time for the reaction is much longer and its stochastic occurrence can be analyzed. Both enzymatic and non-enzymatic reactions have been investigated. Examples of enzymatic reactions include the movement of myosin on actin filaments[3] and the gene expression in living cells,[2] while non-enzymatic chemical reactions include catalytic conversions on metal surface[4,5] and the thiol-disulfide exchange reactions.[6] The discussion below will focus on the study of non-enzymatic chemical reactions by the following four single-molecule techniques, namely single-molecule fluorescence microscopy (SMFM),[7] force microscopy[8] (e.g. atomic force microscopy (AFM)), scanning tunneling microscopy (STM)[5] and single-channel ionic current detection.[9]

1.1.1 Single-molecule fluorescence microscopy (SMFM)

Single-molecule fluorescence microscopy (SMFM) detects the fluorescence change of a fluorophore that is either directly involved in a chemical reaction[4] or acts as a reporter that is sensitive to the reaction site identity.[10] Laser beams excite single molecules in the smallest possible volume. The fluorescence emissions from single molecules are detected by a sensitive detector that has high spatial and time resolution. One of the reactants is usually attached to a solid surface so that diffusion is avoided and the behaviour of a single molecule can be tracked for an extended period of time

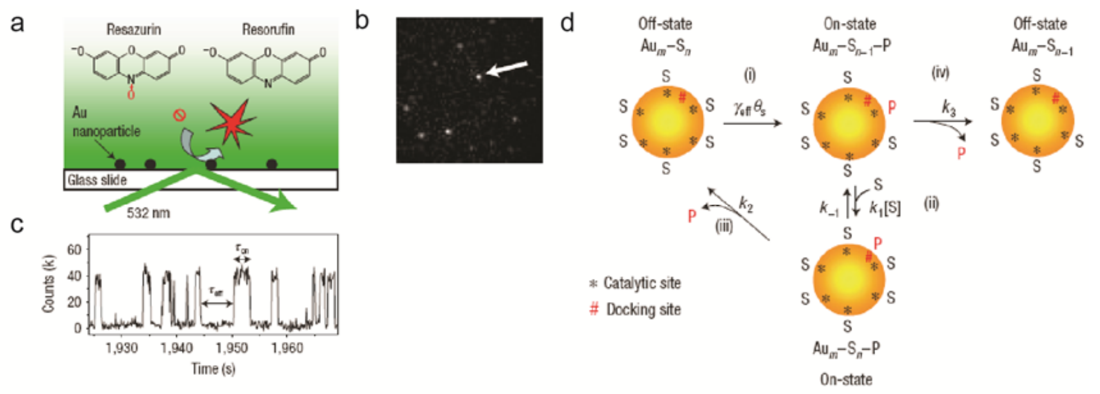

Figure 1.1. *Single-molecule fluorescence microscopy (SMFM) for the detection of single-molecule catalysis on a metal surface. (a) Au-nanoparticle-catalyzed reduction of non-fluorescent resazurin to strongly fluorescent resorufin by hydroxylamine. (b) An image (~18 × 18 μm^2) showing the fluorescent product during catalysis. (c) A segment of fluorescence trajectory for a particular Au-nanoparticle (marked by the arrow in (b)) showing the turnover of catalytic activity. The reduction of resazurin to resorufin on Au surface is irreversible. The 'on' and 'off' states correspond to the states depicted in (d), i.e. 'on' is with resorufin(s) adsorbed, 'off' is without any adsorbed resorufin. Only one molecule of resorufin was bound during the 'on' period in this trace. (d) Schematic diagram of the catalytic cycle. The filled yellow circle represents a Au-nanopaticle. Six catalytic sites (represented by '*') are shown. Each site can be vacant, occupied by resazurin (S) or resorufin (P). A docking site (#) for resorufin is shown. Reprinted by permission from Macmillan Publishers Ltd: Nature Material (ref. 4), copyright (2008).*

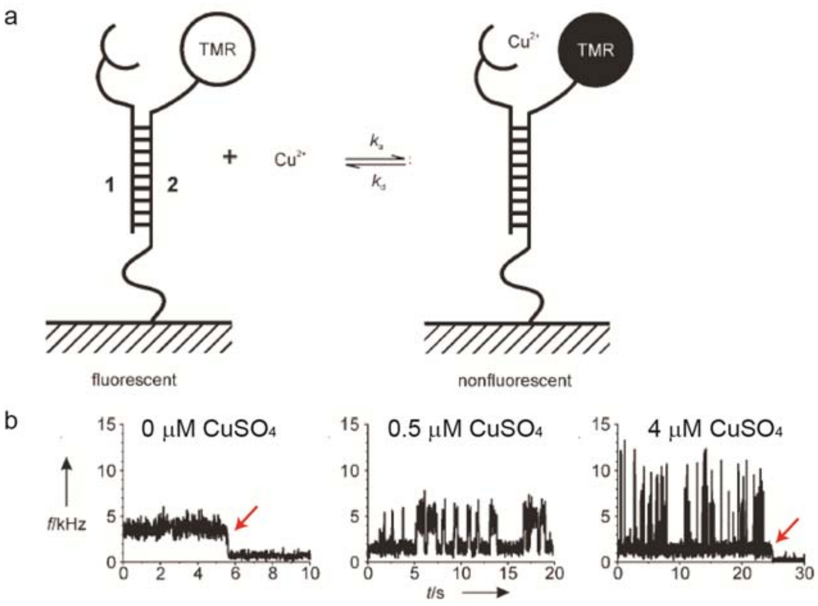

Figure 1.2. *Single-molecule fluorescence-based metal complex formation study. (a) Diagram illustrating the structure of the double-stranded DNA (dsDNA) scaffold and mechanism for detecting* Cu^{2+}*-2,2′-bipyridine complex formation, i.e. binding of* Cu^{2+} *ions to 2,2′-bipyridine-4,4′-dicarboxylic acid (dcbpy) quenches the fluorescence from the nearby tetramethylrhodamine (TMR).*[10] *(b) Fluorescence-time traces of the TMR-dcbpy conjugate in (a) at 0, 0.5 and 4 μM* $CuSO_4$*. Photobleaching was seen in the traces at 0 and 4 μM* $CuSO_4$ *(marked by red arrows). Variations in the intensity levels are due to the imperfect positioning of the molecules in the laser focus. The reported* k_a*,* k_d *and* K_a *values are* $3.3 \pm 0.3 \times 10^6\ M^{-1}s^{-1}$*,* $1.2 \pm 0.4\ s^{-1}$ *and* $2.7 \pm 0.9 \times 10^6\ M^{-1}$*, respectively. Adapted with permission from ref. 10. Copyright (2007) by Wiley.*

before photobleaching. Thus, SMFM is particularly suited for studying catalytic processes on solid surface, such as the catalytic reduction of the non-fluorescent resazurin to the highly fluoroscent resorufin with hydroxylamine on a Au-nanoparticle[4] (Figure 1.1a). The fluorescence signal from a Au-nanoparticle (Figure 1.1c) represents the catalytic formation of resorufin. Detailed kinetics (the adsorption of resazurin, the conversion to resorufin and the desorption of resorufin) were calculated from the fluorescence-time recordings (Figure 1.1d).

Reversible Cu^{2+}-2,2'-bipyridine complex formation was studied by the incorporation of a fluorophore as the reporter.[10] A double-stranded DNA (dsDNA) was used as the scaffold to bring the ligand (2,2'-bipyridine-4,4'-dicarboxylic acid (dcbpy)) and the reporter (tetramethylrhodamine (TMR)) into close proximity. Fluorescence from TMR is quenched by the formation of intramolecular Cu^{2+}-dcbpy complex (Figure 1.2a). Thus the flashings of TMR over time manifest the reversible bindings of Cu^{2+} ions onto dcbpy (Figure 1.2b). The association rate constant (k_a), dissociation rate constant (k_d) and the binding constant (K_a) were determined from the fluorescence-time recordings.

1.1.2 Force microscopy

Atomic force microscopy (AFM) has been applied to acquire a wealth of information about biomolecules.[8] For instance, high resolution imaging and unfolding studies of membrane proteins have provided valuable information about their structure and membrane topology.

Force microscope can manipulate single molecules with the tip and supply mechanical energy to the reaction system. An example is the acceleration of bimolecular ligand substitution reaction on palladium(II) centre by an applied force. Using AFM, Kersey *et al.*[11] found that the displacement of monodentate pyridine ligand **2** by dimethylsulfoxide (DMSO) shows a ten-fold acceleration when a ~50 pN mechanical pulling force is applied to the leaving group **2** (Figure 1.3).

Recently, competing intra- and intermolecular thiol-disulfide exchange reactions were studied using immunoglobulin module 27 (I27) by AFM (Figure 1.4).[6] The I27 module was engineered by site-directed mutagenesis to contain two disulfide bonds (between Cys-24 and Cys-55, and between Cys-32 and Cys-75). Cys-32 is first released by the reduction of the disulfide bond 32-75 with free L-cysteine (Figure 1.4b). Thiol-disulfide exchange on disulfide 24-55, either intramolecularly by the deprotected Cys-32 or intermolecularly by free L-cysteine, are monitored as the different step sizes in chain straightening associated with reaction (Figures 1.4c,d). Reaction kinetics for each route are calculated from the inter-event dwell times and the concentration of L-cysteine added (Figure 1.4e).

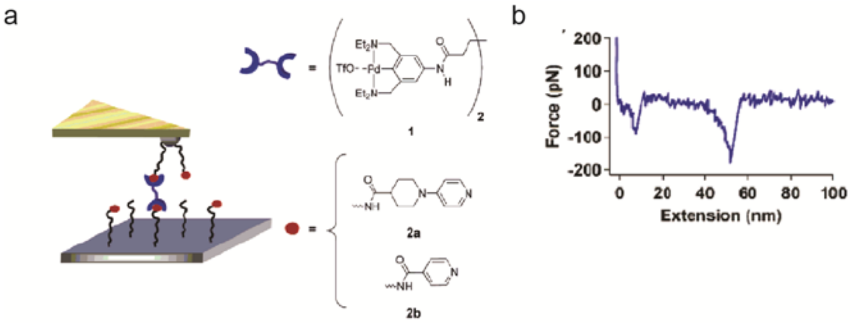

Figure 1.3. *Atomic force microscopy (AFM) for studying bimolecular nucleophilic ligand substitution at a palladium(II) centre.*[11] *(a) Schematic representation of the AFM experiment. Both of the AFM tip and the surface were modified with polyethylene glycols (PEG, black wavy lines), which were subsequently functionalized with monodentate pyridine ligands (**2a** or **2b**, shown as red circles). The bifunctional pincer palladium(II) complex **1** bridges the tip and the surface by the formation of square-planar complexes with **2**. Ligand displacement of **2** by dimethylsulfoxide (DMSO), which is used as solvent, is accelerated by the mechanical pulling force applied through the tip. (b) A representative force-separation curve showing bond rupture at ~43 nm during the retraction of the AFM tip. This length corresponds to the sum of lengths of the two PEG tethers. Reprinted with permission from ref. 11. Copyright (2006) American Chemical Society.*

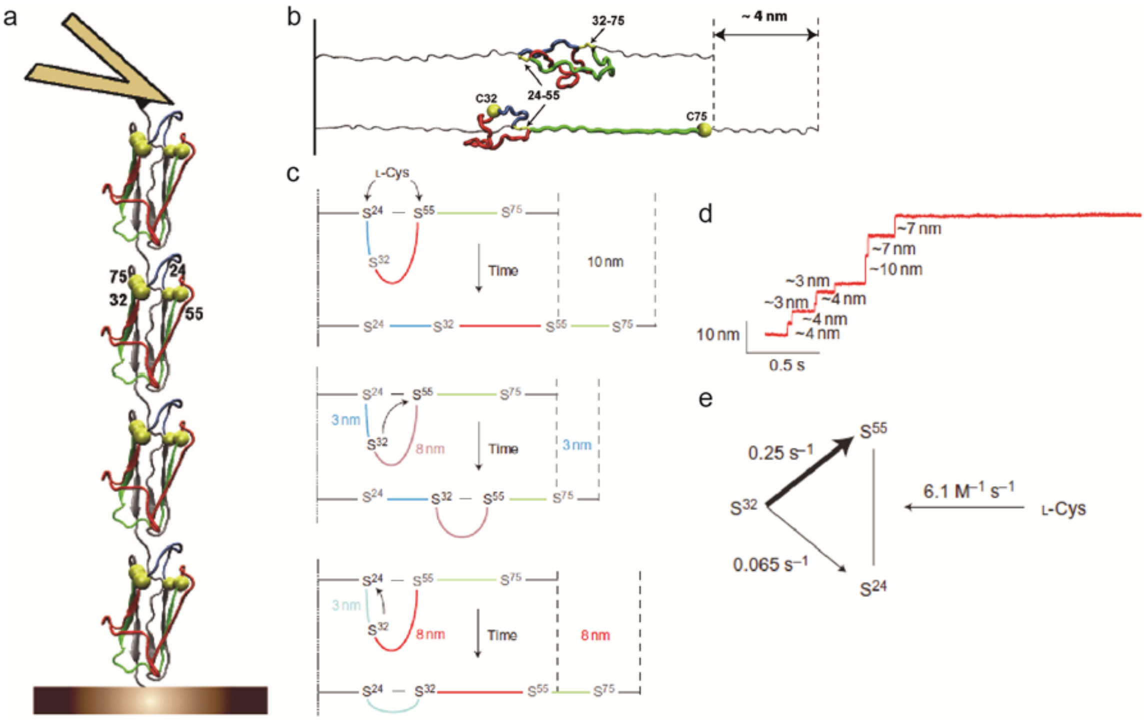

Figure 1.4. *Intra- and intermolecular thiol-disulfide exchange reactions followed by force microscopy.*[6] *(a) Four tandem immunoglobulin modules 27* $(I27)_4$ *were pulled with an AFM working in the force-clamp mode. Each I27 was designed to contain two disulfide bonds: between Cys-24 and Cys-55, and between Cys-32 and Cys-75. (b) Uncaging of Cys-32. The first step in the thiol-disulfide exchange reaction sequence is the release of Cys-32 by the cleavage of disulfide 32-75 by free* L*-cysteine. This led to a step size of ~4 nm. Only one I27 module is depicted for clarity. (c) Thiol-disulfide exchange on disulfide 24-55. The second step in the reaction sequence is the intermolecular thiol-disulfide exchange on disulfide 24-55 by free* L*-cysteine (step size ~10 nm), or the intramolecular attack by freed Cys-32 (*S^{32}*) at positions 24 (*S^{24}*, step size 7–8 nm) or 55 (*S^{55}*, step size 2–3 nm). (d) Experimental trace on* $(I27)_4$ *showing various reduction events in the presence of* L*-cysteine at 250 pN. The steps correspond to the aforementioned thiol-disulfide exchange reactions. (e) Reaction rate constants determined for the three competing thiol-disulfide exchange reactions illustrated in (c). Reprinted by permission from Macmillan Publishers Ltd: Nature Chemistry (ref. 6), copyright (2011).*

1.1.3 Scanning tunneling microscopy (STM)

Single-molecule oxidation catalysis on a liquid-solid surface has been studied with STM.[5] Self-assembled monolayers of manganese porphyrins on Au(111) surface react with molecular oxygen (O_2) to form the Mn(IV)-oxo species. With the good resolution of STM, the oxidation of two adjacent manganese porphyrins by an O_2 molecule was observed (Figure 1.5b). The attached oxygen atom is subsequently

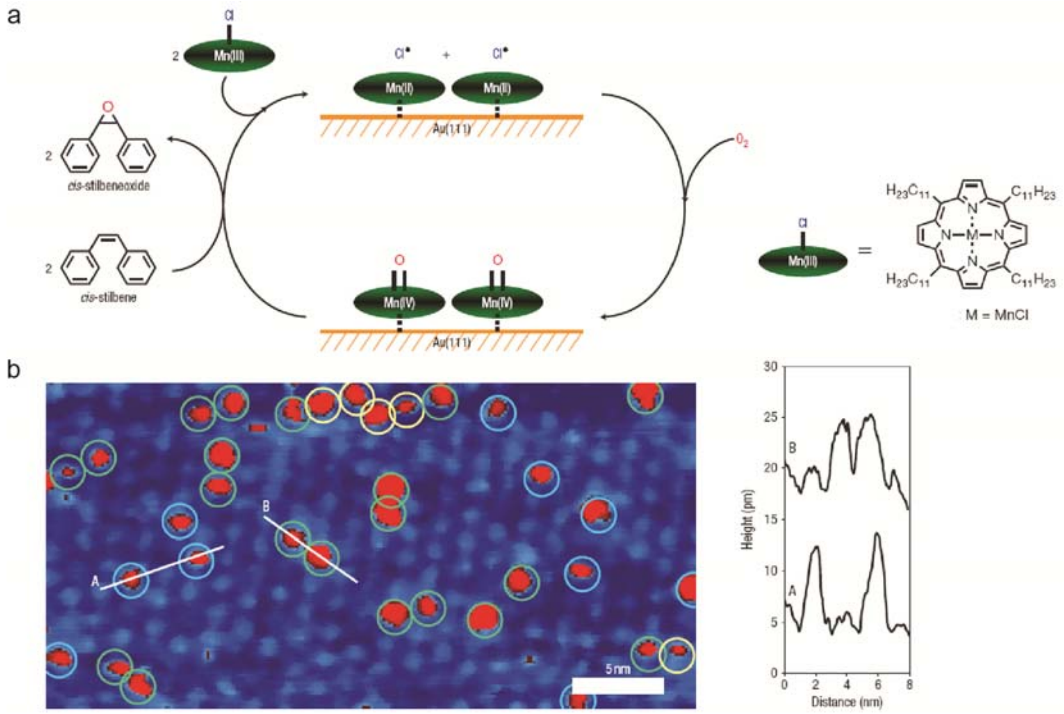

Figure 1.5. *Catalytic olefin epoxidation on a liquid-solid surface.*[5] *(a) Schematic representation of the proposed catalytic mechanism. Self-assembled monolayer of manganese porphyrins (illustrated by the green ovals) on Au(111) surface reacts with molecular oxygen to yield the activated Mn(IV)-oxo complex. This complex converts cis-stilbene into cis-stilbeneoxide by inserting the attached oxygen into the alkene double bond. (b) STM image showing the preferential oxidation of two adjacent manganese centres by molecular oxygen. Cross-section analyses of the corresponding lines A and B are shown on the right. Reprinted by permission from Macmillan Publishers Ltd: Nature Nanotechnology (ref. 5), copyright (2007).*

transferred to an alkene double bond to convert it into an epoxide (Figure 1.5a).

Apart from being a detection tool, STM can also supply electrical and vibrational energies to the reaction system through inelastically tunneling electrons from the tip. The reactant molecules are deposited on a metal surface and a beam of tunneling electrons is targeted to a single molecule. Examples include single-molecule dehydrogenation of propene ($CH_3CH=CH_2$) to allene ($CH_2=C=CH_2$) on Cu(111) surface,[12] and N–H bond cleavage of methylaminocarbyne ($C=NHCH_3$) to methylisocyanide ($C\equiv NCH_3$) adsorbed on Pt(111) surface.[13] In the latter example, the reverse reaction (N–H bond formation) can take place in the presence of molecular hydrogen using the catalytic hydrogenation ability of platinum. Besides bond cleavages, STM can induce conformational changes in molecules, such as the *cis-trans* isomerization of azobenzene.[14] The directional movement of a molecular car adsorbed on Cu(111) surface was made possible by the electrical and vibrational excitations mediated by the applied tip potential.[15]

1.1.4 Single-channel ionic current detection

The modulation of the ionic current flowing through protein nanopores by single molecules has been used to follow chemical reactions and to detect analytes in solution. This is based on the comparable size of nanopores and single molecules so that a chemical change occurring near the entrance or inside the pore causes detectable alteration in the ionic current. An advantage of ionic current detection is that no fluorophore is required.

The first example of single-molecule chemistry observed with a protein nanopore was the thiol-disulfide exchange reaction with methanethiosulfonate (MTS) reagents in diphtheria toxin channel (Figure 1.6).[16] A cysteine residue was introduced by site-directed mutagenesis at the interhelical loop located at the *trans* entrance of the protein pore. MTS reagent added to the *trans* side modified the cysteine via irreversible thiol-disulfide bond exchange. The time required for the occurrence of reaction was used to calculate the second-order reaction rate constant (~10^3 $\text{M}^{-1}\text{s}^{-1}$). Note that the structure of this diphtheria toxin channel is still unknown.

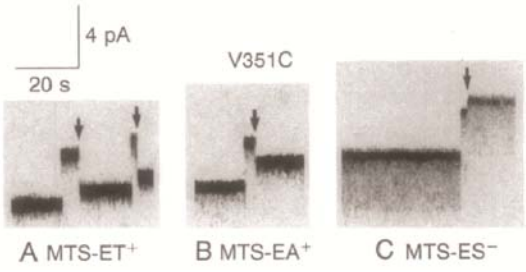

Figure 1.6. *Thiol-disulfide exchange reaction observed with diphtheria toxin channel.[16] Multiple channels bearing the V351C mutation sequentially inserted into the planar lipid bilayer at +60 mV. Each channel insertion was seen as an increase in conductance. Methanethiosulfonate (MTS) reagent in the trans side reacted with the newly inserted channels (indicated by the arrows). The cysteine residue in V351C is located near the trans entrance of the pore. MTS-ET$^+$: 2-(trimethylammonium)ethyl methanethiosulfonate; MTS-EA$^+$: 2-aminoethyl methanethiosulfonate; MTS-ES$^-$: 2-sulfonatoethyl methanethiosulfonate. Reprinted from ref. 16. Copyright (1994) by the National Academy of Sciences.*

Reversible thermal *cis-trans* isomerization of the C–N bond in carbamate (Figure 1.7) was studied with gramicidin, a dimeric pore-forming peptide.[17] The carbamate group was formed at the pore entrance by linking the C-terminus of the peptide to ethylenediamine. *Cis-trans* isomerizations of the carbamate C–N bond leads to differences in the location of the protonated amino group of the attached ethylenediamine relative to the pore entrance, resulting in different conductance levels. Isomerization rate constants and thermodynamic parameters were determined by variable temperature experiments.

Gramicidin was also applied to follow the deprotection of *tert*-butyloxycarbonyl (Boc) protected amine to the free amine and the subsequent diazotization/hydrodediazotization of the amine to a hydroxyl group.[18] However, due to the short life-time of gramicidin dimer compared to the half-lifes of both reactions, the reaction steps could not be observed (Figure 1.8).

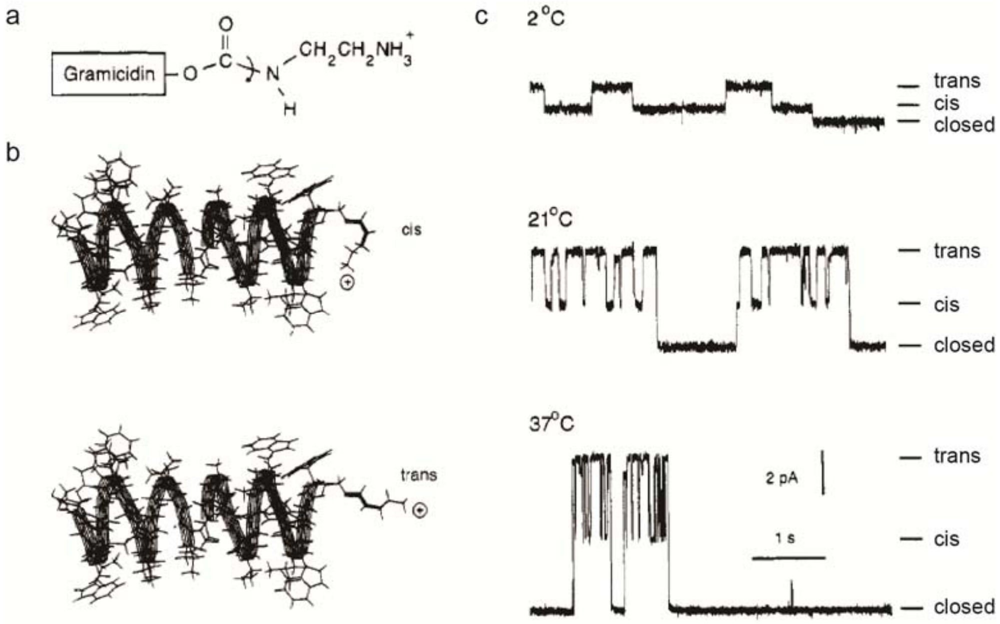

Figure 1.7. *Thermal cis-trans isomerization of carbamate observed at the single-molecule level.*[17] *(a) Ethylenediamine was linked to the C-terminus of gramicidin via carbamate group. (b) Structural diagrams showing the position of the ethylenediamine chain relative to the pore entrance of gramicidin dimer. The protonated amino group in ethylenediamine locates near the entrance in the cis conformation and acts as an electrostatic barrier to the flow of cations through gramicidin. Thus the cis state is proposed to have lower conductance than the trans state. (c) Thermal isomerization at various temperatures at +150 mV. At this applied voltage, the isomerization at the entrance of the channel dominates the current change, while the isomerization at the exit causes insignificant current changes. Adapted with permission from ref. 17. Copyright (1995) American Chemical Society.*

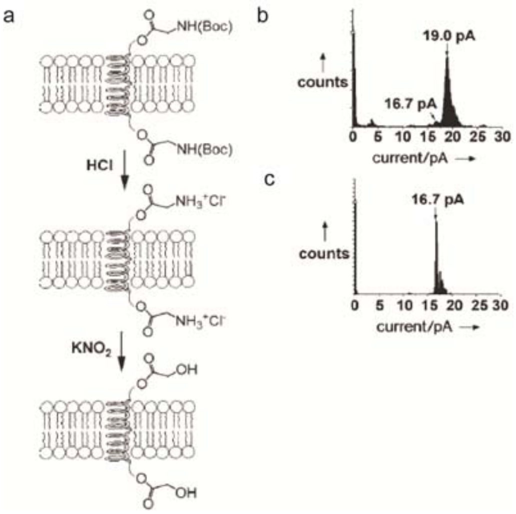

Figure 1.8. *Boc-deprotection and diazotization/hydrodediazotization on gramicidin inserted in planar lipid bilayer.*[18] *(a) Pictorial representation of the two reactions. tert-Butyloxycarbonyl (Boc) protected amino group was introduced to the C-terminus of gramicidin. (b, c) Histograms showing the change in transmembrane current upon Boc-deprotection by HCl after (b) 10 min and (c) 60 min. The transmembrane currents of Boc-protected and deprotected gramicidin are 19.0 pA and 16.7 pA, respectively. Similar changes in transmembrane current over time were observed for diazotization/hydrodediazotization with* KNO_2 *at pH 3.8. Images adapted with permission from ref. 18.*

Much more works for investigating single-molecule chemistry have been carried out with α-hemolysin (αHL). These are discussed in detail in the following sections.

1.2 α-Hemolysin

1.2.1 Structure of α-Hemolysin

The transmembrane toxin α-hemolysin (αHL)[19] from *Staphylococcus aureus* is a mushroom-shaped homoheptameric porin (Figures 1.9a,b). It is secreted as a 33.2 kDa

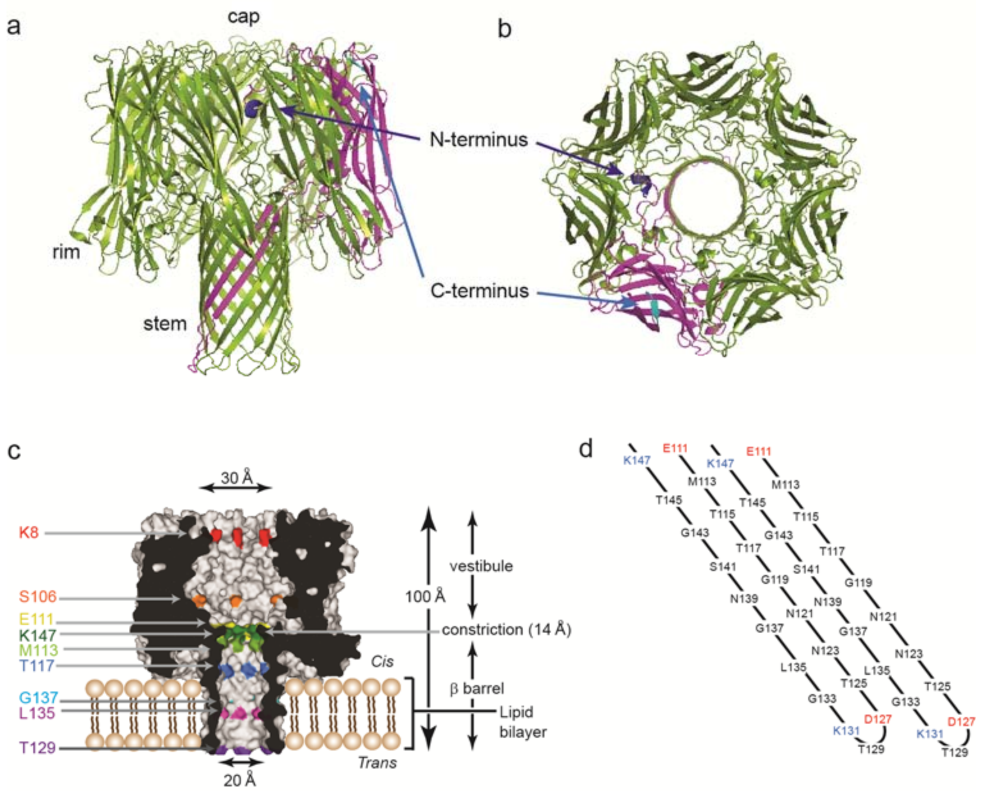

Figure 1.9. *Structure of αHL heptamer. (a) X-ray crystal structure (PDB code 7AHL) of αHL heptamer showing the mushroom-shaped protein. One of the seven identical subunits is coloured in pink. The cap, rim and stem domains are indicated.*[19] *(b) View above the cap into the pore. The N and C-termini of the pink subunit are labeled and coloured in blue and cyan respectively. (c) Cross section of αHL showing the internal cavity inside the transmembrane ion channel. Various key residues are highlighted and labeled on the left hand side. In single-channel recording experiments, the side where the cap domain resides is defined as the cis side (ground), while the opposite side across the lipid bilayer is called the trans side. (d) Schematic representation of the amino acid residues that define the inner surface of the β barrel, i.e. their side chains point into the lumen of the pore. The view is from inside the pore. Lysines (basic residues), aspartate and glutamate (acidic residues) are labeled in blue and red, respectively. β strands from two subunits are shown.*

water-soluble monomer consisting of 293 amino acids without any cysteine residues. The αHL heptamer is ~10 nm both in length and in outer diameter, and is largely made up of β structure. A water-filled channel is aligned with the seven-fold axis of the protein and crosses the lipid bilayer. The αHL heptamer can be divided into three domains: the cap, the rim and the stem. The cap domain resides above the lipid bilayer (Figure 1.9c) and has polar amino acid residues on its surface. It forms the *cis* entrance (diameter ~ 3 nm) and the vestibule part of the pore. Both N- and C-termini lie in this domain (Figures 1.9a,b). The rim domain is in contact with the lipid bilayer. The stem domain is formed by residues E111–K147, which is a glycine-rich region that constitutes the transmembrane β barrel of the pore (Figure 1.9d). This barrel is composed of 14 β strands, formed by the seven αHL monomers each contributing two antiparallel β strands with a hairpin loop around T129. The barrel is 5.2 nm long and about 2 nm in inner diameter, with the narrowest part of the whole channel located at the *cis* end of the barrel, i.e. the inner constriction (~1.4 nm in diameter, formed by residues E111, M113 and K147).

1.2.2 Properties of α-Hemolysin

Pore formation mechanism

Different methods (scanning cysteine mutagenesis,[20] fluorescence studies,[21] trypsinolysis,[22] hemolytic assay and truncation studies[23] etc.) have been applied for investigating the transmembrane pore formation mechanism of αHL. This β pore-forming toxin (β-PFT) is secreted as water-soluble monomers (α_1, state 1 in Figure 1.10). They first bind onto the lipid membrane to form the membrane-associated αHL monomers (α_1^*, state 2), which assemble to form the nonlytic membrane-bound heptameric prepores (α_7^*, state 3). Finally, the stem domain inserts into the membrane to yield the functional pores (α_7, state 4). This prepore mechanism is now generally accepted.[24] The whole process can happen spontaneously, for example, on a planar lipid bilayer formed by 1,2-diphytanoyl-*sn*-glycero-3-phosphocholine (DPhPC). On sensitive cells, such as rabbit red blood cells, pore formation is rapid and believed to be receptor-mediated (e.g. the disintegrin and metalloprotease 10 (ADAM10)[25]), which increases the affinity of αHL to the cell membrane. Membrane-embedment of the water-filled heptameric channels lead to the disruption of the chemiosmotic balance and eventually cell lysis.

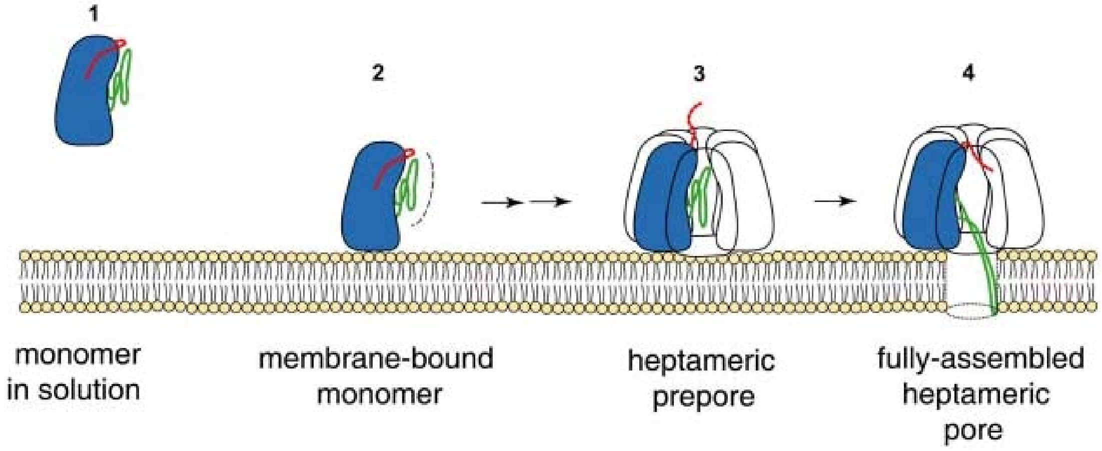

Figure 1.10. *Pore formation mechanism of αHL. The N-terminus is represented by the red line. The prestem or stem domain is shown by the green line. Other parts of αHL are depicted by the blue kidney-shaped figure. αHL is secreted as a water-soluble monomer (α_1, state 1). The monomer binds to membranes (α_1^*, state 2) spontaneously or via a receptor-mediated pathway. Oligomerization of α_1^* yields the nonlytic membrane-bound heptameric prepore (α_7^*, state 3). In the last step, the stem domain inserts into the membrane to form the water-filled channel and functional pores (α_7, state 4). Adapted from ref. 26. Copyright (2006) by the American Society for Biochemistry and Molecular Biology.*

Outstanding stability of αHL

The αHL heptameric pore is stable to sodium dodecyl sulfate (SDS), a detergent commonly used to denature proteins.[27] Thus the αHL heptamer can be purified by sodium dodecyl sulfate-polyacrylamide gel electrophoresis (SDS-PAGE). Once inserted into a lipid bilayer, the αHL heptamer is stable at high temperatures (up to at least 93 °C),[28] extreme pH (pH 3–12),[29,30] high urea concentration (7 M)[31] and high ionic strength (4 M KCl or NaCl, see Chapter 2, Section 2.3.1). The αHL heptamer has a uniform conductance (~1 nS in 1 M KCl) at voltages below ±100 mV. At higher applied voltages, it shows occasional reversible closures. The robustness of the αHL pore is also reflected in its stability towards mutations and/or chemical modifications in the β barrel region (see below).

1.2.3 Single-channel recording technique

Pore-forming membrane proteins can be studied in a planar lipid bilayer by single-channel recording technique. An artificial planar lipid bilayer is formed across an orifice (100–150 μm in diameter) in a thin Telfon film (25-μm thick) by the "folding technique" of Montal and Mueller.[32,33] In more detail, a hexadecane-treated orifice is first generated by applying 1–10% (v/v) hexadecane in pentane or hexane onto both side of the Telfon film. Buffer solution is added to both sides of the film and one to two drops of lipid solution (e.g. 1% (w/v) 1,2-diphytanoyl-*sn*-glycero-3-phosphocholine (DPhPC) in pentane) are added to the buffer surface. A planar lipid bilayer is formed by lowering the liquid level in each compartment below the orifice. Bilayer formation is monitored by applying a triangular waveform. The amplitude of the generated square wave current pulse corresponds to the capacitance of the bilayer, which is proportional to the area of the bilayer. Voltage is applied across the planar lipid bilayer with a pair of agarose-coated Ag/AgCl electrodes (Figure 1.11a). In the

Bayley lab, the compartment to which the membrane proteins are added is called the *cis* side (connected to ground), while the other compartment is called the *trans* side. Preformed heptameric αHL pore inserts spontaneously into planar lipid bilayer, while monomeric αHL also self-assembles on the planar lipid bilayer to form the heptameric αHL pore. The transmembrane ionic current passing through the inserted membrane protein under a constant applied potential (or a programmed voltage protocol) is recorded over time.[34]

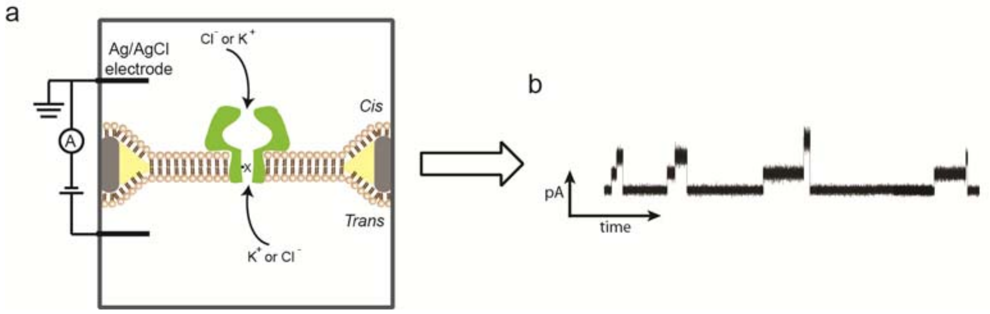

Figure 1.11. *Single-channel recording technique. (a) Pictorial representation (not to scale) of the single-channel ionic current recording set-up. The transmembrane protein is represented by the green mushroom-shaped pore. A reaction site inside the pore is denoted by X. The cis compartment is connected to ground, while constant or programmed potentials are applied to the trans compartment. Agarose-coated Ag/AgCl electrodes are used. A transmembrane ionic current is carried by the electrolyte (KCl in this case) in the buffer. (b) Under a constant applied potential, reactions between the added reactant(s) and the protein reaction site X cause stepwise changes in the transmembrane current, which are recorded in real-time by connecting the setup in (a) to a PC computer through a patch-clamp amplifier (Axopatch 200B, Axon Instruments) and an analog-to-digital (A/D) converter (DigiData 1320, Axon Instruments).*

1.2.4 Analysis of stochastic single-molecule data

The αHL heptamer has a uniform ionic conductance under a fixed applied voltage (e.g. ~1 nS in 1 M KCl at +100 mV). Analyte binding or chemical reaction taking place inside the pore modulates the transmembrane current (Figures 1.11b, 1.12a). The current-time recording in Figure 1.12a shows the reversible binding of analyte A within the pore P (see equation in Figure 1.12a). The mean dwell time ($\bar{\tau}_{P\text{-}A}$,

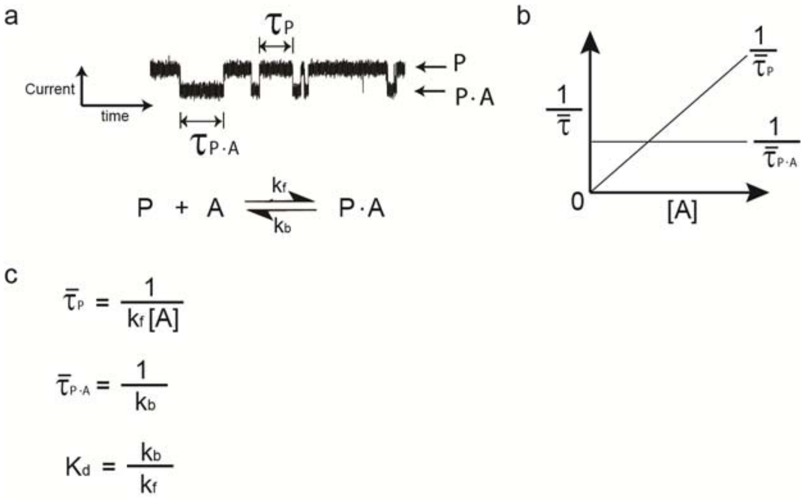

Figure 1.12. *Analysis of single-channel recording data. (a) An example of current-time trace illustrating the reversible binding of analyte A to the pore P to form P·A (see the equation).* $\tau_{P\cdot A}$ *and* τ_P *are the inter-event intervals at levels P·A and P, respectively. (b) Plot of the reciprocal of mean dwell time (*$1/\bar{\tau}$*, where* $\bar{\tau}$ *represents mean* τ*) against the analyte concentration [A].* $1/\bar{\tau}_P$ *shows a linear dependence on [A] and passes through the origin, suggesting that the pathway leading away from level P (i.e. formation of P·A) has first-order dependence on A.* $1/\bar{\tau}_{P\cdot A}$ *is independent of [A], reflecting that the breakdown of P·A has zeroth-order dependence on A. (c) Equations for calculating the association (*k_f*), dissociation (*k_b*) rate constants and the dissociation equilibrium constant (*K_d*) for the binding of A to P.* k_f *is obtained from the slope of* $1/\bar{\tau}_P$ *against [A] in (b).*

which is the mean value of $\tau_{P\text{-}A}$) and the current amplitude of the events are characteristic of the species, while the mean inter-event interval ($\bar{\tau}_P$, the mean value of τ_P) is inversely proportional to the concentration of the species. At the single-molecule level, the mean lifetime ($\bar{\tau}$) at each level is equal to the reciprocal of the sum of unimolecular rate constants of reactions leading away from it, e.g. $\bar{\tau}_{P\cdot A} = 1/k_b$ and $\bar{\tau}_P = 1/k_f[A]$ (in the example in Figure 1.12, k_f is a bimolecular rate constant. Thus $k_f[A]$ represents a unimolecular rate constant) (Figures 1.12a,c).[35] Molecularities with respect to A in the binding of A to P and the breakdown of P·A are determined by plotting the reciprocal of mean dwell times ($1/\bar{\tau}$) against [A] (Figure 1.12b).[35,36] Values of $1/\bar{\tau}$ shows linear-dependence on [A] in reaction that has first-order dependence on [A] (i.e. the binding of A to P), while it is independent of [A] in reaction that has zeroth-order dependence on [A] (i.e. the breakdown of P·A to P). Therefore, the formation of P·A is overall a bimolecular reaction (it involves the collision between two reactants – A and P), while the breakdown of P·A is unimolecular (the reaction involves only one species – P·A). Forward and backward rate constants (k_f and k_b, respectively), and the dissociation equilibrium constant (K_d) are determined from the equations stated above and in Figure 1.12c. Examples of more complicated reaction systems that involve more states are discussed in Chapter 3.

1.2.5 Incorporation of reaction sites

In the nanoreactor approach, the reaction sites are usually constructed on the pore-lining residues or near the pore entrance, so that a chemical transformation at the reaction sites would cause a current change. These solvent-exposed reaction sites also allow for the access of small chemical compounds.

The introduction of specific reaction sites can be done by site-directed mutagenesis[37] and/or site-specific chemical modification of amino acid side chains.[38,39,40] In αHL, the mutation site is usually located inside the β barrel with the amino acid side chain pointing into the lumen, i.e. the odd number residues in 113–147 (Fig. 1.9d).[19] The thiol group (-SH), which undergoes a wide range of biological important reactions, has been introduced as cysteine residue by site-directed mutagenesis. Removal of native cysteine residues is unnecessary as WT-αHL does not contain any cysteine residues. The introduced cysteine thiol group is also a useful handle for the covalent attachment of molecules carrying a desired functional group. This targeted chemical modification of a thiol can be done by thioether formation (alkylation with iodoacetyl group,[38,39,40] Michael addition with maleimide,[41] acrylate or vinyl sulfone) or via disulfide bond formation (with 2-pyridyldisulfide[42,43] or methanethiosulfonate (MTS) reagents[41]) (Figure 1.13).

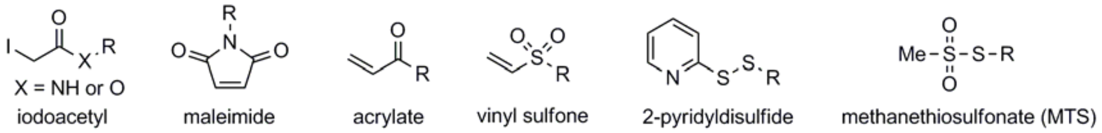

Figure 1.13. *Chemical reagents for the covalent attachment of molecules to the thiol group.*

1.2.6 Examples of single-molecule chemistry in αHL

The defined structure and nano-scale lumen inside the αHL pore provides an excellent reactor for studying single-molecule reactions. Different irreversible and reversible reactions have been investigated with αHL using the single-channel recording technique. Examples of irreversible covalent reactions include the thiol-disulfide bond exchange,[42,44] the reductive 1,4-Michael addition of thiol group to quinone[45] (Figure 1.14c), the redox reaction between quinone and hydroquinone[45] and the stepwise photochemical cleavage of a 2-nitrobenzyl protecting group[38] (Figure

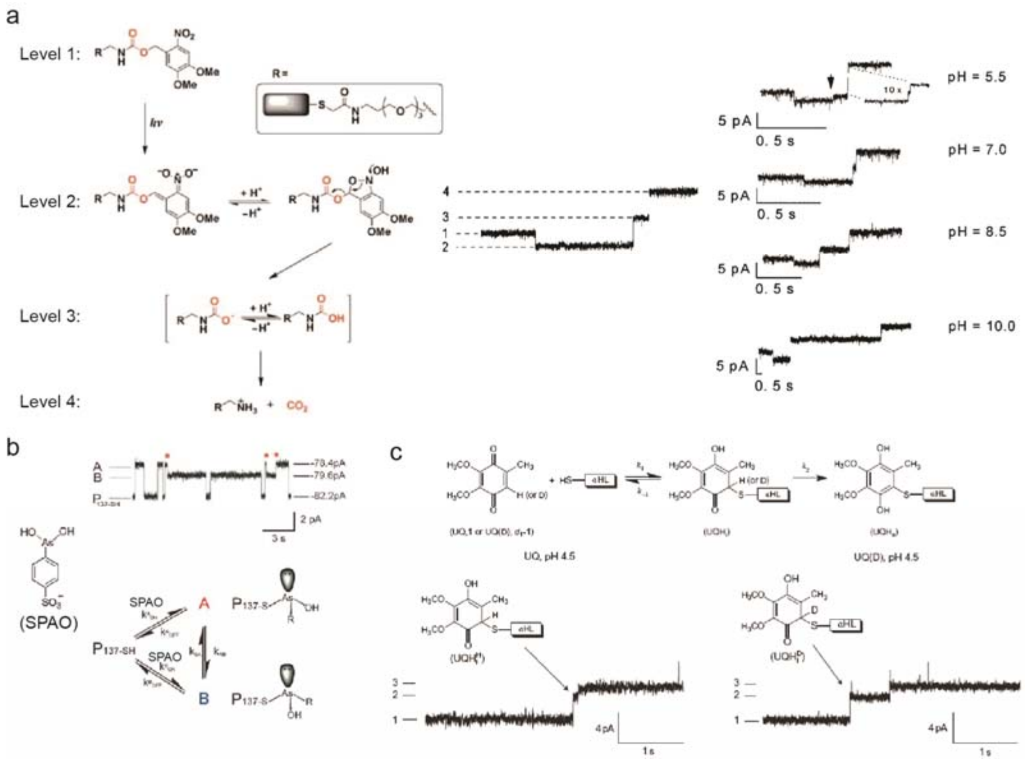

Figure 1.14. *Examples of single-molecule chemistry investigated using the nanoreactor αHL. (a) Light-activated deprotection of the 4,5-dimethoxy-2-nitro-benzylcarbamate group*[38] *(left). This group was attached to a cysteine residue on αHL through an oligo(ethylglycol) linker terminated with an iodoacetamide group. Three sequential steps (middle) were observed at the single-molecule level. Each level was proposed to correspond to different structure in the reaction pathway shown on the left (the levels are labeled on the far left-hand side). The pH-dependence of the third step (decarboxylation) (right) were also studied. Adapted with permission from ref. 38. Copyright (2003) by Wiley. (b) Reversible formation of a S-As bond with 4-sulfophenylarsane oxide (SPAO) and the pyramidal inversion at the As(III) centre in P-S-As(OH)R, where P represents αHL.*[46] *Adapted with permission from ref. 46. Copyright (2007) by Wiley. (c) Reductive 1,4-Michael addition of thiol group to 2,3-dimethoxy-5-methyl-1,4-benzoquinone studied by the hydrogen-deuterium kinetic isotope effect.*[45] *Reprinted by permission from Macmillan Publishers Ltd: Nature Chemistry (ref. 45), copyright (2010).*

1.14a). In the last example, the breakdown of a 2-nitrobenzyl carbamate group appeared as a characteristic three-step change in transmembrane current. Each current change corresponds to a reaction step. By studying the pH-dependence, each level could be assigned to a different proposed structure(s) in the reaction mechanism. Short-lived intermediates, such as the nitronate and the carbamic acid, were observed. The reaction rate constant for each step was determined unambiguously from the mean dwell time of the level leading to that step. Moreover, a fast reaction step (the decarboxylation of the carbamic acid ($k = 313\ s^{-1}$ at pH 5.5)) that follow a slower step (the breakdown of nitronate ($k = 1.6\ s^{-1}$)) was observed with this technique. This clearly shows the advantage of single-molecule detection over ensemble measurement – fast reaction step occurring after the rate-determining step can be measured unambiguously.

Reversible reactions that have been studied include the photoisomerization of azobenzene,[39] Zn^{2+} ion binding to two iminodiacetate chelators[40] (Figure 3.4) and S-As bond formation[37] (Figure 1.14b). Pyramidal inversion at the diastereomeric As(III) centre[46] was also observed in the latter reaction when a different αHL mutant was used, revealing the high sensitivity of the nanopore detection technique to subtle structural changes.

1.2.7 Strategies for the investigation of chemical reactions

Different ensemble solution strategies can be applied in conjunction with the nanoreactor approach in order to unravel the reaction mechanisms.[9] These include the hydrogen-deuterium kinetic isotope effect[45] (Figure 1.14c), the pH-dependence of reaction steps[38,47] (Figures 1.14a, 1.15a) and the substituent effects (e.g. Hammett analysis).[48] Moreover, the time-consuming data collection for irreversible reactions (only one data point can be obtained per experiment) can be remedied where possible

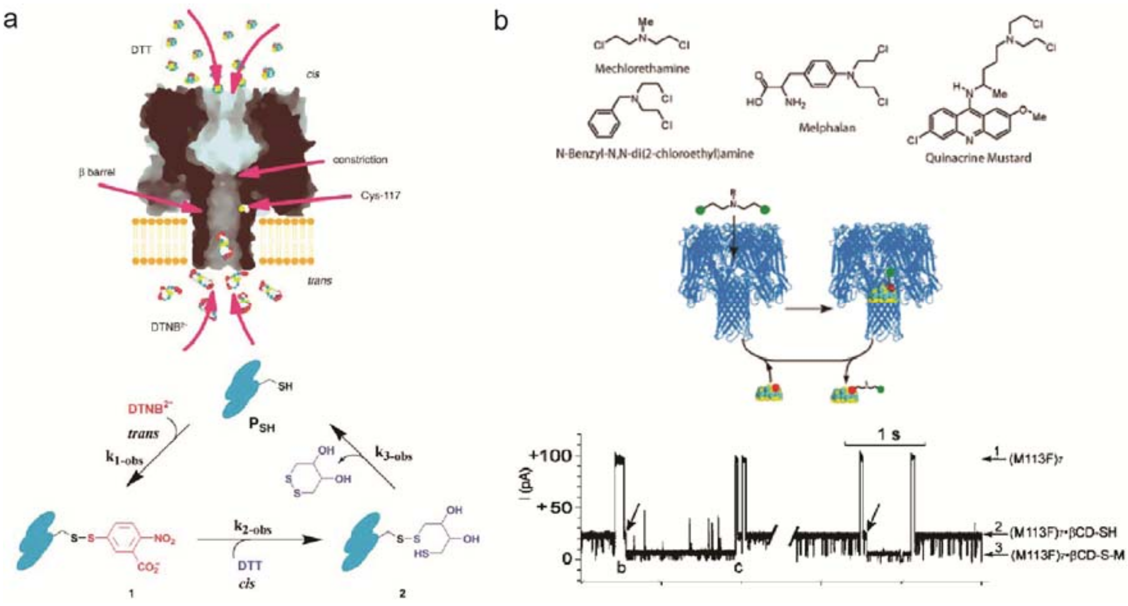

Figure 1.15. *Efficient ways to study irreversible chemical reactions. Multiple turnovers of reactants can be achieved by using (a) spatially separated reactants:*[47] *5,5'-dithiobis(2-nitrobenzoic acid) (DTNB) and D,L-dithiothreitol (DTT) were added to the trans and the cis sides, respectively (or the opposite way around). A cysteine thiol group on αHL that underwent a thiol-disulfide bond exchange reaction with DTNB was regenerated by DTT. The structure of the proposed intermediate 2 is supported by the pH-dependence of its lifetime. Adapted with permission from ref. 47. Copyright (2003) by Wiley. (b) Replacement with a new reactant. Nitrogen mustard (cis) was detected by the bimolecular nucleophilic substitution (S_N2) reaction with a thiol-containing β-cyclodextrin adaptor (6-monodeoxy-6-monothio-β-cyclodextrin) (trans).*[49] *β-Cyclodextrin is non-covalently bound in the lumen of the αHL pore. After reaction with nitrogen mustard, the reacted adaptor diffuses away and new, unreacted adaptor goes into the pore. This enables irreversible reactions to be observed repeatedly with one αHL pore. In the current-time trace, alkylation reactions are indicated by the black arrows. Adapted with permission from ref. 49. Copyright (2008) American Chemical Society.*

by using spatially separated reactants[47] or non-covalently bound reactant.[49] The first approach makes use of the lipid bilayer which separates the two compartments. A cysteine-containing αHL is shown to undergo clces of thiol-disulfide exchange reactions with separated 5,5'-dithiobis(2-nitrobenzoic acid) (DTNB) (present in one compartment) and D,L-dithiothreitol (DTT) (present in the opposite compartment)[47] (Figure 1.15a). An example of the second approach is using the thiol-containing β-cyclodextrin as the reactant. β-Cyclodextrin binds non-covalently and reversibly inside the αHL pore. When it is bound, nucelophilic substitution reaction of the thiol group with nitrogen mustard can be detected (Figure 1.15b).[49] The reacted β-cyclodextrin then diffuses away and a new, unreacted β-cyclodextrin can enter the pore and allow the chemical conversion to be observed many times. Both of these two methods ensure multiple turnovers of the reactants so that many reaction cycles can be observed with a single protein pore. Moreover, titration experiments using different concentrations of reactant can be performed.

1.2.8 Criteria of a detectable chemical transformation

The examples above demonstrated the versatility of protein nanopores in investigating chemical reactions, for instance, the observation of short-lived intermediates[38,45,47] and the ability to distinguish small structural differences (*cis-trans* isomers,[39] diastereoisomers[46]). However, several criteria must be fulfilled so that a chemical reaction can be studied with a protein nanopore using the planar lipid bilayer system depicted in Figure 1.11. These criteria[9] are (1) reaction in aqueous media. The reactants and reagents need to be water-soluble (preferably >10–100 μM) and moderately stable in the high-salt buffer (typically ≥1 M); (2) reactions take place in the temperature range of ~0–100 °C. Note that the lipid DPhPC shows no phase transition over this temperature range; (3) pH 3–12, due to the instability of αHL outside this range; (4) reactants react specifically with the desired chemical moiety on αHL, i.e. no detectable reaction with other amino acid side chains (e.g. amino groups on lysine, carboxyl groups on glutamate and aspartate) inside the lumen at the concentrations of reactants used. Nonspecific reactions outside the lumen, e.g. with amino acid residues on the outer surface of αHL or with lipid molecules, is tolerable as long as these reactions are undetectable in the transmembrane current and do not cause significant depletion of reactants; (5) the amounts of reactants and reagents added do not destabilize the lipid bilayer. Some thiol compounds (thiophenol) are prone to cause rupture of lipid bilayer; (6) reaction rate constants lie in a suitable range. For first-order reactions, $k_1 \sim 10^{-1}$ to 10^3 s^{-1} ($\tau = 1/k_1 = 1$ ms – 10 s); for second-order reaction, $k_2 \sim 10^0$ to 10^4 $M^{-1}s^{-1}$ (τ value depends on the concentration of reactant). The lower limit of k is due to the limited lifetime of the planar lipid bilayer, and also the rare reaction steps may be confused by the adventitious spikes in current. The upper limit of k is restricted by the time-resolution of the single-channel recording technique (in the μs time domain); (7) reaction causes current change (ideally ≥0.5 pA) or noise fluctuations. Current changes in αHL can arise from changes in size, shape and charge of the reacting group; (8) at least one of the reactants needs to be bound (either covalently or non-covalently) to the nanopore. Small molecules free in solution translocate through the pore in the ns time scale (mean residence time ($x^2/2D$) is only 100 ns, where $x = 10$ nm for the length of the pore, $D = 0.5 \times 10^{-9}$ m^2s^{-1} for the diffusion coefficient of a small molecule such as sucrose in water). This is too fast to be detected by the single-channel recording technique (detection limit is in the μs time domain due to instrument noise). Even though reactions may take place on unattached reactants inside the lumen of the pore, the small molecule reactants would have passed through the pore before they could undergo the whole transformation (as we are looking at reactions with ≥ μs time scale).

Thus the reactions are undetectable. Therefore, if the reacting moiety comes off from the pore in the middle of a sequence of reaction steps, the subsequent steps will be unobservable.

Several strategies can be applied to tackle some of these constraints. Mixed solvent systems (e.g. 10% (v/v) acetonitrile (MeCN) or dimethyl sulfoxide (DMSO) in the aqueous buffer) can be used in single-channel recording in order to aid the dissolution of organic compounds (criterion 1). In this case, the organic solvent should be added after pore-insertion to avoid the slow down of pore-insertion due to the denaturation of protein in solution.[50] Current changes associated with a chemical reaction (criterion 7) can be maximized by using a higher electrolyte concentration and a higher applied potential (see Section 2.3.1). The latter factor needs to be optimized because of the increasing current noise with higher applied potential, and also the possible difficulties for the electrodiffusion of charged reactants through the pore. The stability of the planar lipid bilayer (criteria 5 and 6) can be prolonged by using an encapsulated bilayer chip.[51] A lipid bilayer-free system based on the embedment of αHL into a solid-state nanopore[52] can be used as well. Attachment of reactant to the pore for reaction observation (criterion 8) can be avoided by trapping the reactant (e.g. adamantane-based molecule) inside the lumen of the αHL pore by two β-cyclodextrin adaptors.[53] This can lengthen the residence time of the reactant.

1.2.9 Factors affecting the reaction rate constants measured with a nanoreactor compared to ensemble experiment

The reaction rate constants measured with αHL by the single-molecule ionic current detection technique might show differences from their ensemble solution counterparts.[47] This might due to the bulkier nature of the protein αHL compared to its small molecular analogue (e.g. glutathione (GSH) as an analogue to the cysteine mutant of αHL) used in ensemble measurements. In addition, several factors may affect the measured bimolecular reaction rate constants.[9] (1) Electrophoretic and electroosmotic transport of reactants through the pore. Due to the necessity of applying a potential across the planar lipid bilayer so that a transmembrane current is detected, the passage of a charged compound through the pore depends on the sign of its charge, the side of addition (*cis* or *trans*), and the sign and magnitude of the applied potential. Transport of neutral compounds is also affected by the applied potential as a result of the electroosmotic flow of solvent molecules driven by the electrophoretic movement of ions. (2) Retarded access of added reactants to the reaction site. The narrowest part of the pore, i.e. the inner constriction in αHL (~14 Å in diameter, Figure 1.9) and electrostatic interaction with residues lining the pore inhibit the translocation of reactants. Again, this will depend on the side of addition. (3) The unknown pK_a values of functional group(s) at the reaction site. The pK_a values of functional groups in proteins are sensitive to the local environment, as seen with cysteine residues in enzyme active sites.[54] Factor (2) would reduce the effective concentration of the added reactants inside the nanopore compared to the bulk concentration (i.e. the value used in calculation), leading to an underestimation of the reaction rate constant. With the reaction site usually located inside the β barrel (on the *trans* side of the inner constriction), the kinetics of a reaction step is preferably reported with the reactant added to the *trans* compartment.[47] Electrophoretic diffusion and electrostatic interaction with the wall can be alleviated by using low applied voltage (e.g. ≤ 50 mV) and a high electrolyte concentration (e.g. ≥ 1 M), respectively. The applied voltage can also be minimized with the alternating current (AC) measurement.[55]

1.2.10 Other applications of αHL

In addition to studying the mechanisms and kinetics of chemical reactions, αHL is also a versatile detector. A wide range of analytes, ranging from divalent metal ions[56,57] (see Chapter 3 for more discussion), nitrogen mustards,[49] single-stranded DNA (ssDNA)[31,34,58] and peptides[59] have been sampled. Adaptor(s), such as β-cyclodextrin (βCD)[29] and cucurbit[6]uril,[60] have been incorporated into the pore lumen to facilitate the discrimination of mononucleotides (DNA[61] and RNA[62] bases) and enantiomeric drugs.[63] The detection of enzyme-substrate binding is also possible by the covalent attachments of substrates onto either the *cis* or *trans* side of αHL. For instance, biotin, disaccharides, protein kinase inhibitor peptides and a thrombin-binding DNA aptamer have been attached for sensing streptavidin,[64] carbohydrate-binding protein lectins,[65] protein kinases[43,66] and thrombin,[67] respectively.

1.3 Conclusions

Single-channel ionic current recording has been applied to study a variety of single-molecule chemistry and to detect different analytes (drugs, enzymes, DNA and RNA). In comparison to other single-molecule techniques for investigating chemical kinetics, this technique does not require a fluorescence tag and can work with molecules of a few hundred Daltons. However, as current-time recording is the sole output from single-channel recording and the current alteration (both magnitude and sign) associated with a chemical species is unpredictable, spectroscopic methods are sometimes used in parallel to provide additional information about the identity of the chemical species involved in a reaction.

With the nanoreactor approach based on αHL, the next three chapters will discuss the biological-relevant covalent chemistry of *S*-nitrosothiols (Chapter 2), the reversible binding of soft metal cations to thiolates (Chapter 3) and the attempt to engineer a copper(II)-metalloprotein for monitoring catalytic Diels-Alder reactions (Chapter 4).

1.4 References

1. Neher, E.; Sakmann, B. *Nature* **1976**, *260*, 799–803.
2. Li, G.-W.; Xie, S. *Nature* **2011**, *475*, 308–315.
3. Veigel, C.; Schmidt, C. F. *Nat. Rev. Mol. Cell Biol.* **2011**, *12*, 163–176.
4. Xu, W.; Kong, J. S.; Yeh, Y.-T. E.; Chen, P. *Nat. Mater.* **2008**, *7*, 992–996.
5. Hulsken, B.; Van Hameren, R.; Gerritsen, J. W.; Khoury, T.; Thordarson, P.; Crossley, M. J.; Rowan, A. E.; Nolte, R. J. M.; Elemans, J. A. A. W.; Speller, S. *Nat. Nanotechnol.* **2007**, *2*, 285–289.
6. Alegre-Cebollada, J.; Kosuri, P.; Rivas-Pardo, J. A.; Fernández, J. M. *Nat. Chem.* **2011**, *3*, 882–887.
7. de Cremer, G.; Sels, B. F.; De Vos, D. E.; Hofkens, J.; Roeffaers, M. B. J. *Chem. Soc. Rev.* **2010**, *39*, 4703–4717.
8. Scheuring, S.; Sapra, K. T.; Müller, D. J. in *Handbook of single-molecule biophysics*; Hinterdorfer, P.; Oijen, A., Eds.; Dordrecht; London: Springer, 2009; pp 449–485.
9. Bayley, H.; Luchian, T.; Shin, S.-H.; Steffensen, M. B. in *Single molecules and Nanotechnology*; Rigler, R.; Vogel, H., Eds.; Springer: Heidelberg, 2008, pp 251–277.
10. Kiel, A.; Kovacs, J.; Mokhir, A.; Krämer, R.; Herten, D.-P. *Angew. Chem. Int. Ed.* **2007**, *46*, 3363–3366.

11. Kersey, F. R.; Yount, W. C.; Craig, S. L. *J. Am. Chem. Soc.* **2006**, *128*, 3886–3887.
12. Parschau, M.; Rieder, K.-H.; Hug, H. J.; Ernst, K.-H. *J. Am. Chem. Soc.* **2011**, *133*, 5689–5691.
13. Katano, S.; Kim, Y.; Hori, M.; Trenary, M.; Kawai, M. *Science*, **2007**, *316*, 1883–1886.
14. Henzl, J.; Mehlhorn, M.; Gawronski, H.; Rieder, K.-H.; Morgenstern, K. *Angew. Chem. Int. Ed.* **2006**, *45*, 603–606.
15. Kudernac, T.; Ruangsupapichat, N.; Parschau, M.; Maciá, B.; Katsonis, N.; Harutyunyan, S. R.; Ernst, K.-H.; Feringa, B. L. *Science* **2011**, *479*, 208–211.
16. Mindell, J. A.; Zhan, H.; Huynh, P. D.; Collier, R. J.; Finkelstein, A. *Proc. Natl. Acad. Sci. U. S. A.* **1994**, *91*, 5272–5276.
17. Jaikaran, D. C.; Woolley, G. A. *J. Phys. Chem.* **1995**, *99*, 13352–13355.
18. Blake, S.; Mayer, T.; Mayer, M.; Yang, J. *ChemBioChem* **2006**, *7*, 433–435.
19. Song, L.; Hobaugh, M. R.; Shustak, C.; Cheley, S.; Bayley, H.; Gouaux, J. E. *Science* **1996**, *274*, 1859–1866.
20. Walker, B.; Bayley, H. *J. Biol. Chem.* **1995**, *270*, 23065–23071.
21. Valeva, A.; Weisser, A.; Walker, B.; Kehoe, M.; Bayley, H.; Bhakdi, S.; Palmer, M. *EMBO J.* **1996**, *15*, 1857–1864.
22. Walker, B.; Krishnasastry, M.; Zorn, L.; Bayley, H. *J. Biol. Chem.* **1992**, *267*, 21782–21786.
23. Cheley, S.; Malghani, M. S.; Song, L.; Hobaugh, M.; Gouaux, J. E.; Yang, J.; Bayley, H. *Protein Eng.* **1997**, *10*, 1433–1443.
24. Mueller, M.; Grauschopf, U.; Maier, T.; Glockshuber, R.; Ban, N. *Nature*, **2009**, *459*, 726–731. Also News and Views: Bayley, H. *Nature* **2009**, *459*, 651–652.
25. Wilke, G. A.; Wardenburg, J. B. *Proc. Natl. Acad. Sci. U.S.A.* **2010**, *107*, 13473–13478.

26. Jayasinghe, L.; Miles, G.; Bayley, H. *J. Biol. Chem.* **2006**, *281*, 2195–2204.
27. Bhakdi, S.; Füssle, R.; Tranum-Jensen, J. *Proc. Natl. Acad. Sci. U. S. A.* **1981**, *78*, 5475–5479.
28. Kang, X.-F.; Gu, L.-Q.; Cheley, S.; Bayley, H. *Angew. Chem. Int. Ed.* **2005**, *44*, 1495–1499.
29. Gu, L.-Q.; Braha, O.; Conlan, S.; Cheley, S.; Bayley, H. *Nature* **1999**, *398*, 686–690.
30. Maglia, G.; Henricus, M.; Wyss, R.; Li, Q.; Cheley, S.; Bayley, H. *Nano. Lett.* **2009**, *9*, 3831–3836.
31. Japrung, D.; Henricus, M.; Li, Q.; Maglia, G.; Bayley, H. *Biophys. J.* **2010**, *98*, 1856–1863.
32. Montal, M.; Mueller, P. *Proc. Natl. Acad. Sci. U.S.A.* **1972**, *69*, 3561–3566.
33. White, S. H. in *Ion channel reconstitution*; Miller, C. Eds.; Plenum Press: New York, 1986; pp 3–36.
34. Maglia, G.; Heron, A. J.; Stoddart, D.; Japrung, D.; Bayley, H. *Methods Enzymol.* **2010**, *475*, 591–623.
35. Colquhoun, D.; Hawkes, A. G. in *Single-channel recording*; Sakmann, B.; Neher, E., Eds.; Plenum: New York, 1995; pp 397–482.
36. Colquhoun, D. *Lectures on biostatistics: an introduction to statistics with applications in biology and medicine*; Clarendon Press: Oxford, 1971.
37. Shin, S.-H.; Luchian, T.; Cheley, S.; Braha, O.; Bayley, H. *Angew. Chem. Int. Ed.* **2002**, *41*, 3707–3709.
38. Luchian, T.; Shin, S.-H.; Bayley, H. *Angew. Chem. Int. Ed.* **2003**, *42*, 1926–1929.
39. Loudwig, S.; Bayley, H. *J. Am. Chem. Soc.* **2006**, *128*, 12404–12405.
40. Hammerstein, A. F.; Shin, S.-H.; Bayley, H. *Angew. Chem. Int. Ed.* **2010**, *49*, 5085–5090.

41. Lundblad, R. L. The modification of cysteine. in *Chemical reagents for protein modification*, 3rd ed.; 139–192; CRC Press, **2005**.
42. Wu, H.-C.; astier, Y.; Maglia, G.; Mikhailova, E.; Bayley, H. *J. Am. Chem. Soc.* **2007**, *129*, 16142–16148.
43. Xie, H.; Braha, O.; Gu, L.-Q.; Cheley, S.; Bayley, H. *Chem. Biol.* **2005**, *12*, 109–120.
44. Movileanu, L.; Bayley, H. *Proc. Natl. Acad. Sci. U. S. A.* **2001**, *98*, 10137–10141.
45. Lu, S.; Li, W.-W.; Rotem, D.; Mikhailova, E.; Bayley, H. *Nat. Chem.* **2010**, *2*, 921–928.
46. Shin, S.-H.; Steffenson, M. B.; Claridge, T. D. W.; Bayley, H. *Angew. Chem. Int. Ed.* **2007**, *46*, 7412–7416.
47. Luchian, T.; Shin, S.-H.; Bayley, H. *Angew. Chem. Int. Ed.* **2003**, *42*, 3766–3771.
48. Shin, S.-H. Kinetics of covalent chemistry at the single-molecule level. DPhil Dissertation, University of Oxford, Nov 2005.
49. Wu, H.-C.; Bayley, H. *J. Am. Chem. Soc.* **2008**, *130*, 6813–6819.
50. Choi, L.-S. Unpublished results.
51. Kang, X.-F.; Cheley, S.; Rice-Ficht, A. C.; Bayley, H. *J. Am. Chem. Soc.* **2007**, *129*, 4701–4705.
52. Hall, A. R.; Scott, A.; Rotem, D.; Mehta, K. K.; Bayley, H.; Dekker, C. *Nat. Nanotechnol.* **2010**, *5*, 874–877.
53. Gu, L.-Q.; Cheley, S.; Bayley, H. *Science* **2001**, *291*, 636–640.
54. Harris, T. K.; Turner, G. J. *IUBMB Life* **2002**, *53*, 85–98.
55. Ervin, E. N.; White, R. J.; Owens, T. G.; Tang, J. M.; White, H. S. *J. Phys. Chem. B* **2007**, *111*, 9165–9171.
56. Braha, O.; Gu, L.-Q.; Zhou, L.; Lu, X.; Cheley, S.; Bayley, H. *Nat. Biotechnol.* **2000**, *18*, 1005–1007.

57. Wen, S.; Zeng, T.; Liu, L.; Zhao, K.; Zhao, Y.; Liu, X.; Wu, H.-C. *J. Am. Chem. Soc.* **2011**, *132*, 18312–18317.
58. Stoddart, D.; Heron, A. J.; Mikhailova, E.; Maglia, G.; Bayley, H. *Proc. Natl. Acad. Sci. U. S. A.* **2009**, *106*, 7702–7707.
59. Zhao, Q.; Jayawardhana, D. A.; Wang, D.; Guan, X. *J. Phys. Chem. B.* **2009**, *113*, 3572–3578.
60. Braha, O.; Webb, J.; Gu, L.-Q.; Kim, K.; Bayley, H. *ChemPhysChem* **2005**, *6*, 889–892.
61. Clarke, J.; Wu, H.-C.; Jayasinghe, L.; Patel, A.; Reid, S.; Bayley, H. *Nat. Nanotechnol.* **2009**, *4*, 265–270.
62. Ayub, M. unpublished results.
63. Kang, X.-F.; Cheley, S.; Guan, X.; Bayley, H. *J. Am. Chem. Soc.* **2006**, *128*, 10684–10695.
64. Movileanu, L.; Howorka, S.; Braha, O.; Bayley, H. *Nat. Biotechnol.* **2000**, *18*, 1091–1095.
65. Howorka, S.; Nam, J.; Bayley, H.; Kahne, D. *Angew. Chem. Int. Ed.* **2004**, *43*, 842–846.
66. Cheley, S.; Xie, H.; Bayley, H. *ChemBioChem* **2006**, *7*, 1923–1927.
67. Rotem, D.; Jayasinghe, L.; Salichou, M.; Bayley, H. *J. Am. Chem. Soc.* **2012**, *134*, 2781–2787.

Chapter 2 *S*-Nitrosothiol chemistry

Parts of this chapter are published:
Choi, L.-S.; Bayley, H. *S*-Nitrosothiol Chemistry at the Single-Molecule Level. *Angew. Chem. Int. Ed.* **2012**, *51*, 7972–7976.
Author contributions: L.-S.C carried out the experimental work and analyzed the data. L.-S.C. and H.B. designed the experiments and wrote the paper.

2.1 Introduction

Nitric oxide (NO) and its relatives (notably *S*-nitrosothiol (RSNO) and nitroxyl (HNO)) are involved in many biological processes, such as the inhibition of platelet aggregation, memory storage, bronchodilation and inflammation.[1-6] The identification in the 1980s that NO is the primary endothelium-derived relaxing factor (EDRF) responsible for smooth muscle relaxation initiated diverse research into its biological functions.[7] NO[8] is one of the smallest signaling molecules found *in vivo*. It usually interacts with proteins either by binding to an iron centre, e.g. activation of guanylate cyclase (GC) by binding to its ferrous heme,[7] or by converting a cysteine residue into RSNO, e.g. cyclooxygenase-2 is activated by *S*-nitrosation on Cys-526.[10] With improved detection techniques, more than 1000 protein-SNO have been identified today.[11] Due to its short lifetime and the difficulty in detecting HNO, the crucial physiological roles of HNO emerged only in the last decade.[12,13] HNO often has biological effects that differ from or oppose those of NO.[12-14] NO, RSNO, HNO and other nitrogen oxides (dinitrosyl iron complexes, peroxynitrite ($ONOO^-$), nitrosonium ion (NO^+), nitrite (NO_2^-), nitrate (NO_3^-), nitrogen dioxide (NO_2) and dinitrogen trioxide (N_2O_3), etc.) are collectively called reactive nitrogen species (RNS).[13] When present at elevated concentrations, RNS cause cell death by inducing nitrosative stress.[15] In the following sections, I will focus on the three main "NO" species, namely NO, RSNO and HNO.

2.1.1 Intracellular generation and interconversion of NO, RSNO and HNO

NO is generated endogenously by nitric oxide synthases (NOS). NOS convert one of the terminal nitrogen atoms in the guanidine group in L-arginine into NO in the presence of molecular oxygen and NADPH, via *N*$^{\omega}$-hydroxy-L-arginine with L-citrulline as the side product (Figures 2.1 and 2.2).[16] A pivotal pathway in NO signaling is the activation of guanylate cyclase (GC),[7] which catalyzes the conversion of guanosine triphosphate (GTP) to the second messenger cyclic guanosine monophosphate (cGMP). Additional targets include cytochrome *c* oxidase, which is inhibited by NO.[17]

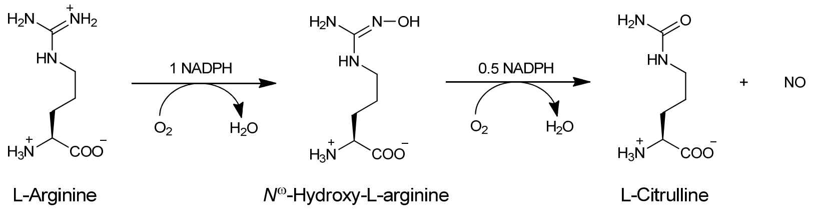

Figure 2.1. *Conversion of L-arginine into nitric oxide (NO) by nitric oxide synthase (NOS).*

Through poorly understood mechanisms,[18,22,23] NO is converted to RSNO. There are three potential pathways, namely (1) transfer of the nitroso group from a metal nitrosyl complex onto a thiol group;[7] (2) radical-radical reactions between thiyl radicals and NO;[24–26] and (3) nitrosation of thiol groups by HNO_2.[27]

1) Metal-NO transfer (M^{n+} = Fe(III) metal complex):

$$NO + M^{n+} \rightarrow [M\text{-}NO]^{n+}$$

$$[M\text{-}NO]^{n+} + RSH \rightarrow M^{(n-1)+} + RSNO + H^+$$

2) Free radical mechanism:

$$RSH \rightarrow RS\cdot + H\cdot$$

$$RS\cdot + NO \rightarrow RSNO$$

3) *S*-Nitrosation by HNO_2:[27]

$$RSH + NO_2^- + H^+ \rightarrow RSNO + H_2O$$

Biological examples of pathway (1) have been discovered. An example is the direct *S*-nitrosation by the heme iron nitrosyl complex in NOS; cyclooxygenase-2 binds inducible NOS and is thereby activated by *S*-nitrosation on Cys-526.[10] The "NO" group in the formed RSNO can be transferred to other thiol groups by transnitrosation (see reaction 12 in Section 2.1.5), forming new RSNO. Examples of natural protein and peptide RSNO include the SNO-derivatives of albumin, haemoglobin, glutathione (GSH) and L-cysteine.[29] Apart from *S*-nitrosation, RSNO can also convert protein cysteine residues into disulfide derivatives (*S*-thiolation, Figure 2.2, see also reaction 13 in Section 2.1.5), such as *S*-glutathionylated proteins by the reaction with GSNO,[30] generating a complex signaling web. NO has been suggested to be regenerated from RSNO by the action of a copper(I)-containing protein on the platelet surface.[19]

HNO often has biological effects that differ from or oppose those of NO.[12-14] This is not surprising as NO and HNO differ considerably in their mechanisms of formation and in their chemistry (see below).[12,13] HNO has been reported to be an intermediate in the turnover of NOS and therefore it may be released by this enzyme,[31] especially in the absence of one of the cofactors, tetrahydrobiopterin. In addition, oxidation of N^{ω}-hydroxy-L-arginine,[32] an intermediate in the generation of

NO from L-arginine, might produce HNO. *S*-Thiolation also yields HNO from RSNO.[21,33]

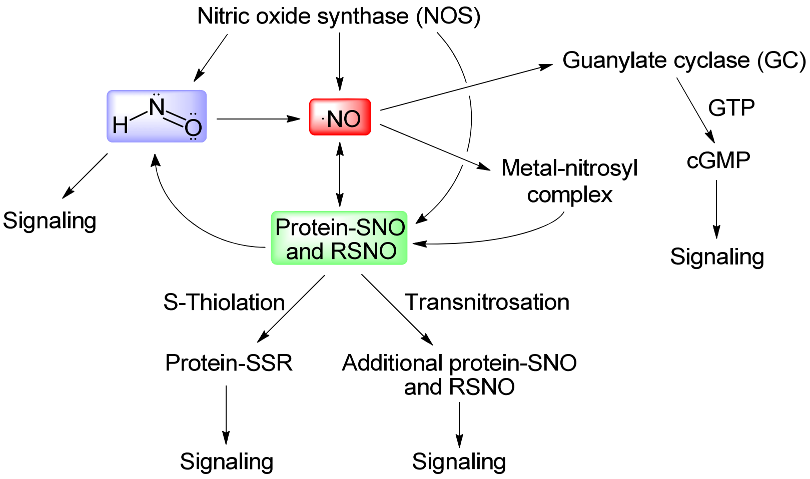

Figure 2.2. *Interconversions between NO, HNO and RSNO and associated signaling pathways. Nitric oxide synthases (NOS) generate nitric oxide (NO) intracellularly.*[16] *One important NO signaling pathways is the activation of guanylate cyclase (GC), which catalyzes the transformation of guanosine triphosphate (GTP) into cyclic guanosine monophosphate (cGMP).*[7] *The second messenger cGMP activates other enzymes and elicits physiological responses, such as smooth muscle relaxation. Precise mechanism(s) for the in vivo formation of RSNO from NO are still unclear.*[18] *One possible pathway is via the reaction between a metal-nitrosyl complex with protein cysteine residue. NOS has been found to directly S-nitrosate protein cysteine residues to form S-nitrosothiol (RSNO).*[10] *NO has been suggested to be regenerated from RSNO by the action of a copper(I)-containing protein on the platelet surface.*[19] *RSNO reacts with protein cysteine either by transferring the NO group (transnitrosation), or by forming a disulfide bridge (S-thiolation).*[20] *HNO has been reported to be an intermediate in the turnover of NOS and therefore may be released by this enzyme.*[16] *Conversion of NO to HNO is physiologically unfavourable due to the highly negative reduction potential ($NO/^3NO^-$ = –0.8 ± 0.2 V*[76]*). HNO is released from RSNO by attack nucleophiles, such as the thiolate ion in S-thiolation.*[21] *Due to the different chemistry of HNO compared with NO, HNO elicits dissimilar physiological effects.*[13]

2.1.2 Propagation of nitrergic signal

To begin the NO signaling cascade, NO produced by NOS can directly diffuse to and bind onto a metal centre in a target protein (called nitrosylation). The formed metal-nitrosyl complex can convert protein cysteine thiol into RSNO (called *S*-nitrosation). Due to its short lifetime (<1 s) (see Section 2.1.5), NO is unlikely to diffuse more than a few cells from the generating cell, and hence NO acts locally.[18] To effect signaling at distant site, RSNO has been regarded as a carrier. For example, RSNO derivatives of albumin and haemoglobin are sufficiently long-lived to be transported in the circulation.[29] Transfer of "NO" group from RSNO to R′SH (transnitrosation) helps the propagation of the nitrergic signal. Protein functions are modulated by this reversible *S*-nitrosation (e.g. X-linked inhibitor of apoptosis (XIAP) is inactivated by *S*-nitrosation on Cys-450),[2] which is analogous to protein phosphorylation. However, unlike phosphorylation, in which specific classes of enzymes (kinases and phosphatases) exist for the addition and removal of phosphate group to and from target proteins, no new classes of enzymes (nitrosylases and denitrosylases) have been found for nitros(yl)ation or denitros(yl)ation. The propagation of the nitrergic signal is controlled by protein-protein interactions:[11,22,23] nitros(yl)ated proteins bind to the next proteins in a signalling cascade, and then transfer the "NO" group to a particular cysteine residue on the target protein. Thus the nitros(yl)ated proteins serve as both enzyme catalysts (nitrosylases) and co-substrates ("NO" donors). Examples include the transnitrosation from *S*-nitrosated glyceraldehyde 3-phosphate dehydrogenase (GADPH, at Cys-150) to target proteins in the nucleus, including the deacetylation enzyme sirtuin-1 (SIRT1), histone deacetylase-2 (HDAC2) and DNA-activated protein kinase (DNA-PK),[22,23] and the aforementioned transfer of "NO" from the heme iron-nitrosyl centre in inducible NOS to Cys-526 in cyclooxygenase-2.[10]

Studies to discover consensus sequences have also shown that *S*-nitrosation of a particular cysteine residue on protein is favoured by the presence of nearby hydrophobic residues ("hydrophobic motif") and/or both acidic and basic amino acid residues ("acid-base motif") either in a linear sequence or clustered spatially in the three-dimensional structure.[11,28] These two motifs work by enhancing the nucleophilicity of thiolate and stabilizing the transition state during transnitrosation, respectively.

In addition to forming metal nitrosyl complexes and RSNO, the nitrergic signal is networked with other thiol modifications, including *S*-thiolation and *S*-oxidation. The control of *S*-thiolation has not been well investigated in detail.[20,34] Hydrolysis of RSNO to the sulfenic acid (RSOH)[35] and the subsequent oxidation to a sulfinic acid (RSO_2H) also regulate signal transduction.

2.1.3 Termination of nitrergic signal

Termination of NO signal is performed by denitrosylases. There are two already known protein systems, (GSNO/GSNO reductase (GSNOR) and thioredoxin (Trx)/thioredoxin reductase (TrxR)), that are capable of denitrosation under physiological conditions (Figure 2.3).[11,36] GSNO is an important small molecule RSNO as it carries and transfers the "NO" group to the proteome. Protein-SNO levels are regulated indirectly by GSNOR through the breakdown of GSNO. The Trx/TrxR system works through its disulfide reduction mechanism. The dithiol moiety in Trx reacts with protein-SNO by transnitrosation or *S*-thiolation (Figure 2.3b), followed by an intramolecular *S*-thiolation or disulfide exchange reaction to form oxidized Trx and the protein-SH. Reduced Trx is regenerated by TrxR.[36]

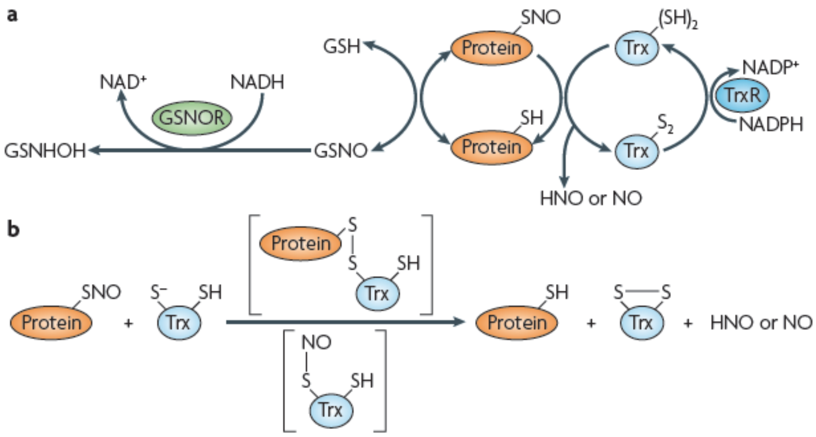

Figure 2.3. *Mechanisms of protein denitrosylation. (a) GSNO/GSNO reductase (GSNOR) system and (b) thioredoxin (Trx)/thioredoxin reductase (TrxR) system.*[36] *N-Hydroxysulfenamide (GSNHOH) generated in (a) will either rearrange irreversibly to S-sulfinamide (GS(=O)NH2) or react with another thiol to form disulfide, which can be reduced by reductase to give back both thiols.*[37] *Reprinted by permission from Macmillan Publishers Ltd: Nature Reviews Molecular Cell Biology (ref. 36), copyright (2009).*

2.1.4 Medical conditions associated with NO, RSNO, HNO etc.

The ubiquitous roles of NO and its relatives in many physiological processes are reflected in their involvements in numerous pathological conditions.[38] Although the actual effectors (NO, RSNO, HNO etc.) are not always clearly distinguished, "NO" has been implicated in numerous medical disorders beyond its well-known role in erectile function. Examples include conditions involving the cardiovascular system,[1] neuronal cell death in trauma and disease,[2,3] the immune system[6] and cancer.[1] Not surprisingly then, numerous agents that generate "NO" (such as organonitrates)[39] are under development as therapeutic agents.[1,12,39]

An example of NO in the airway inflammatory disease, asthma, is the detection of an increased level of NO in exhaled air, and higher expression and activity of GSNO reductase (GSNOR) in asthma patients.[4,5] GSNO is a bronchodilator presents in the human airway. Depletion of GSNO due to its breakdown by excess GSNOR (Section 2.1.3) therefore causes bronchoconstriction and other symptoms of asthma.

2.1.5 Chemistry of NO, RSNO and HNO

Nitric oxide (NO)

NO is a free radical with one unpaired electron. It has limited lifetime *in vivo* (<1 s) because of the fast reactions with ferrous proteins and radicals such as superoxide O_2^- and dioxygen O_2. Facile coordination of NO onto iron(II) in a heme produces ferrous-nitrosyl complexes (10^6–10^8 $\mathrm{M^{-1}s^{-1}}$) (reaction 1).[13] This nitrosylation reaction is involved in many mechanisms involving NO, such as its intracellular generation by nitric oxide synthase (NOS)[16] and signaling by the activation of guanylate cyclase (GC).[7] Besides, NO reacts with superoxide O_2^- in a near diffusion-limited manner (1.6×10^{10} $\mathrm{M^{-1}s^{-1}}$) to form peroxynitrite ($OONO^-$) (reaction 2)[40] and with dioxygen O_2 (2×10^6 $\mathrm{M^{-2}s^{-1}}$) to yield nitrite NO_2^- (reaction 3).[8,37] On the other hand, NO does not dimerize, presumably because of the delocalization of the unpaired electron in the anti-bonding π* molecular orbital between nitrogen and oxygen atoms. Although direct reaction between NO and thiol is possible in the presence of an electron acceptor, such as O_2 (reaction 4),[41,42] this reaction is too slow to be of biological importance (rate law is $-d[NO]/dt = 4k[NO]^2[O_2]$, where $4k = (1.17 \pm 0.12) \times 10^7$ $\mathrm{M^{-2}s^{-1}}$, under physiological conditions, $[NO] < 1$ μM and $[O_2] < 200$ μM).[42]

(1) $NO + \text{heme-Fe}^{II} \rightarrow \text{heme-Fe}^{II}\text{-NO}$ $(10^6–10^8\ \mathrm{M^{-1}s^{-1}})$[13]

(2) $NO + O_2^- \rightarrow OONO^-$ $(1.6 \times 10^{10}\ \mathrm{M^{-1}s^{-1}})$[40]

(3) $4\ NO + O_2 + 2\ H_2O \rightarrow 4\ NO_2^- + 4H^+$ $(2 \times 10^6\ \mathrm{M}^{-2}\mathrm{s}^{-1})$[8,37]

(4) $2\ NO + RSH + O_2 \rightarrow RSNO + OONO^- + H^+$ $((1.17 \pm 0.12) \times 10^7\ \mathrm{M}^{-2}\mathrm{s}^{-1})$[42]

NO has small dipole moment, thus has low water-solubility (1.57 mM at 35 °C) and high lipophilicity.[8] It can diffuse rapidly through cells (diffusion coefficient = 3300 $\mu m^2 s^{-1}$),[43] but the diffusion distance is limited by its fast quenching by O_2^- and the heme group as mentioned above. Therefore free NO acts locally *in vivo* and is unlikely to travel more than 100 µm from the site at which it is generated, a range of a few cells.[18]

S-Nitrosothiol (RSNO)

RSNO (Figure 2.4a) exists in *syn* and *anti* conformations[44,45] around the S–N bond and show electron resonance on the sulfur, nitrogen and oxygen atoms (Figure 2.4b). Primary and secondary thiols form red or pink RSNO compounds, while tertiary ones are green. They have absorption maxima around 330–350 nm ($\pi \rightarrow \pi^*$, $\varepsilon \sim 10^3\ M^{-1}cm^{-1}$) and 550–600nm ($n \rightarrow \pi^*$, $\varepsilon \sim 10^1\ M^{-1}cm^{-1}$) (Figure 2.5).[46] Therefore, reactions involving RSNO can be conveniently followed by UV-visible spectrophotometry.

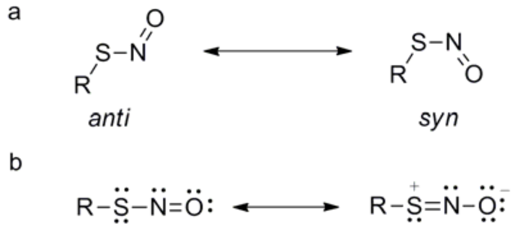

Figure 2.4. *Structure and resonance of RSNO.*[45] *(a) anti and syn conformations around the S–N bond. These two conformations arise from the partial double bond character in S–N bond due to the resonance structure illustrated in (b). (b) Resonance structures of RSNO. The conventional structure without charge separation is shown on left, a zwitterionic structure is shown on the right.*

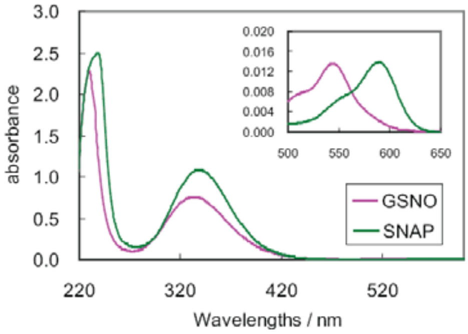

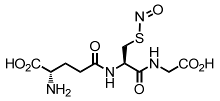
S-Nitrosoglutathione
(GSNO)

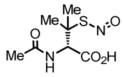
S-Nitroso-*N*-acetyl-D-penicillamine
(SNAP)

Figure 2.5. *UV-visble absorption spectra (220–600 nm) of GSNO (1 mM) and SNAP (1 mM). Inset: enlarged region showing the weak absorption maxima at 500–650 nm.*

RSNO can be synthesized chemically by nitrosation (addition of NO) of thiols with nitrous acid (HNO_2) (reaction 5) or an alkyl nitrite (R'ONO) (reaction 6). Reaction 5 is also a potential physiological RSNO generation pathway (Section 2.1.1).

(5) $RSH + HNO_2 \rightarrow RSNO + H_2O$

(6) $RSH + R'ONO \rightarrow RSNO + R'OH$

RSNO degrades by thermal and photochemical homolysis (reactions 7–8). Decomposition is accelerated by the presence of metal ions, especially Cu^+, Fe^{2+}, Hg^{2+} and Ag^+.[46] The first two metal ions lead to the formation of a disulfide and NO (reactions 9–10), while the latter two result in thiol and nitrite (reaction 11). Reaction with Hg^{2+} forms the basis for quantitation of RSNO by the Saville spectrophotometric assay (see Chapter 5). It is proposed that the complexation of RSNO to a metal centre is necessary for decomposition. Therefore, chelating agents, such as diethylenetriaminepentaacetate (DTPA) and neocuprione, are often added to solutions containing RSNO.

(7) $RSNO \rightarrow RS\cdot + NO$

(8) $RS\cdot + RSNO \rightarrow RSSR + NO$

(9) For Cu^+ and Fe^{2+}: $RSNO + M^{n+} \rightarrow RS^- + NO + M^{(n+1)+}$

(10) $2\ RS^- + 2\ M^{(n+1)+} \rightarrow RSSR + 2\ M^{n+}$

(11) For Hg^{2+} and Ag^+: $RSNO + M^{n+} + OH^- \rightarrow RS\text{-}M^{(n-1)+} + NO_2^- + H^+$

RSNO also reacts with nucleophiles, such as thiols, ascorbate, amines and sulfites,[46] resulting in heterolytic cleavage. The nucleophiles can attack either at the sulfur atom or nitrogen atom, depending on the degree of steric hindrance of both reactants. Two important reactions of RSNO in signal transduction are transnitrosation (reaction 12) and *S*-thiolation (reaction 13).[21] Transnitrosation involves the reversible attack of thiolate ($R'S^-$) on the nitrogen atom of RSNO, leading to the formation of new *S*-nitrosothiol, R'SNO.[46] On the other hand, *S*-thiolation results from the attack of thiolate at the sulfur atom of RSNO, yielding disulfide and HNO.[21,33] *S*-Thiolation is an alternative mechanism of protein mixed disulfide formation, in addition to thiol-disulfide exchange.

(12) Transnitrosation: $RSNO + R'S^- \leftrightarrow RS^- + R'SNO$

(13) *S*-Thiolation: $RSNO + R'S^- + H_2O \rightarrow RSSR' + HNO + OH^-$

Due to the more stable nature of RSNO, it has been regarded as an *in vivo* NO reservoir and used as experimental surrogate of NO. However, RSNO has been shown to affect cells in ways that differ from the direct action of NO and do not involve the release of free NO.[47] Furthermore, RSNO generates HNO instead of NO under certain circumstances (e.g. by *S*-thiolation).[21]

Nitroxyl (HNO)

Another NO-derivative that is gaining increasing attention is HNO.[12] It is the protonated form of the one-electron reduction product of NO and has singlet ground state. It has a high pKa value of 11.4[48] and hence HNO predominates in the HNO/NO^-

equilibrium at physiological pH. Because of the spin-forbidden deprotonation to form NO^-, which has triplet ground state (NO^- is isoelectronic to O_2), the rate constant for deprotonation by OH^- is slow (5×10^4 $\mathrm{M}^{-1}\mathrm{s}^{-1}$). $NO/{}^3NO^-$ couple has highly negative redox potential (–0.8 ± 0.2 V[76]), thus conversion of NO to NO^- (or HNO) is unfavourable under physiological conditions.

HNO is more reactive than NO.[49] It is unstable and dimerizes quickly to form nitrous oxide N_2O (8×10^6 $\mathrm{M}^{-1}\mathrm{s}^{-1}$) (reaction 14).[50,51] Therefore, HNO is usually generated *in situ* using donors such as Angeli's salt ($Na_2N_2O_3$) or Piloty's acid (*N*-hydroxybenzenesulfonamide).[49]

(14) $2\ HNO \rightarrow [HO\text{-}N{=}N\text{-}OH] \rightarrow N_2O + H_2O$ (8×10^6 $\mathrm{M}^{-1}\mathrm{s}^{-1}$)[50,51]

In contrast to NO, HNO is thiophilic and reacts readily with thiols, forming *N*-hydroxysulfenamide (RSNHOH) (10^5–10^9 $\mathrm{M}^{-1}\mathrm{s}^{-1}$) (reaction 15).[13] In this reaction, HNO behaves as an electrophile similar to formaldehyde.[13] Moreover, ferric proteins (e.g. metmyoglobin) capture HNO quickly, giving the ferrous-nitrosyl complex (10^5 $\mathrm{M}^{-1}\mathrm{s}^{-1}$) (reaction 16).[49–51]

(15) $HNO + RSH \rightarrow RSNHOH$ (10^5–10^9 $\mathrm{M}^{-1}\mathrm{s}^{-1}$)[13]

(16) $HNO + \text{heme-Fe}^{III} \rightarrow \text{heme-Fe}^{II}\text{-NO} + H^+$ (10^5 $\mathrm{M}^{-1}\mathrm{s}^{-1}$)[49–51]

(17) $HNO + O_2 \rightarrow HNO/O_2$ complex (10^3 $\mathrm{M}^{-1}\mathrm{s}^{-1}$)[49]

Besides, HNO reacts relatively slow with O_2 due to different spin states to form an unknown HNO/O_2 complex (10^3 $\mathrm{M}^{-1}\mathrm{s}^{-1}$) (reaction 17).[49] Given the above reactions, HNO is short-lived and its *in vivo* action is local.[12,13]

The different chemistry of NO versus HNO towards O_2, metals and thiols, in addition to their low propensity to interconvert, explains the orthogonality of their biological functions.[12]

2.1.6 Detection of NO, RSNO, HNO

Many techniques have been developed for the detection of NO and its derivatives. Their principals and the detection limits have been reviewed.[52] Hence only a brief summary will be given here for the detection of NO, HNO and protein-SNO.

NO can be quantified electrochemically by NO-selective electrodes,[52] or spectroscopically by trapping with hemoglobin (detection by UV-visible absorption spectroscopy), carboxy-2-phenyl-4,4,5,5-tetramethylimidazoline-1-oxyl-3-oxide (Carboxy-PTIO) or Fe-dithiocarbamate complex (detection by electron paramagnetic resonance spectroscopy (EPR)). In addition, ozone-based chemiluminescence detection,[52] nitrite-based colorimetric method (Griess diazotization assay) [52] and nitrite-based ion chromatorgraphy can be used for NO measurement.

Because of the instability and short half life of HNO, its measurement relies on indirect methods for the detection of decomposition reaction products.[12] These include the measurement of N_2O (by GCMS), trapping with metmyoglobin (detection by UV-visible absorption spectroscopy or EPR) and reaction with thiols (detection by HPLC).

Protein and small molecule RSNOs can be quantified by measuring NO or other degradation products, which can be detected by ozone-based Hg-coupled photolysis-chemiluminescence, nitrite-based spectroscopic method (Saville diazotization method) or ion chromatography. In contrast to these NO-based techniques, a sulfur-based method called the biotin-switch technique (BST) has been developed for protein-SNO (Figure 2.6).[53,54] This technique is based on a three-step chemical modification: (1) capping of all free cysteine thiols by *S*-methylthiolation with *S*-methyl methanethiosulfonate (MMTS); (2) selective reduction of protein-SNO to thiol, usually with ascorbate; and (3) labelling of the generated thiols with a thiol-specific biotinylating reagent, *N*-[6-(biotinamido)hexyl]-3'-(2'-pyridyldithio)propionamide (biotin-HPDP). The samples are subsequently analyzed by SDS-PAGE/immunoblotting. The location of post-translational *S*-nitrosylation can be determined by a modified version of BST called SNOSID (SNO site identification).[55] In this technique, the protein samples undergo the same three-step modification in Figure 2.6, then the biotinylated proteins are subjected to trypsin digestion, purified with streptavidin agarose and sequenced by liquid chromatography/tandem MS.

Due to the lack of specificity in some of the detection methods, there are controversies about the identity and quantity of NO species *in vivo*. But with improving techniques, the understanding of NO signalling and its biological effects is getting clearer.

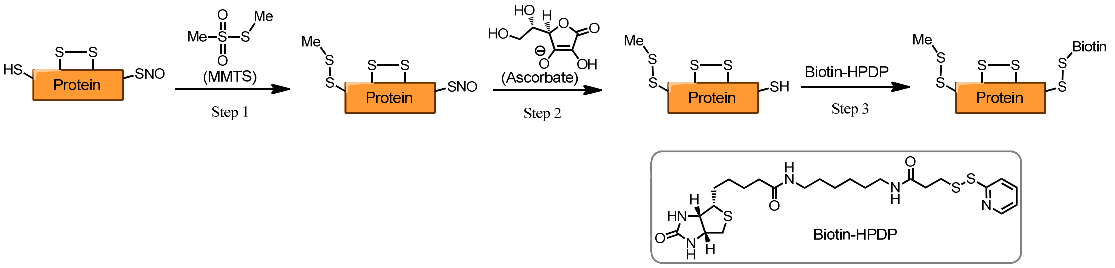

***Figure 2.6.** Three-step modification of proteins in the biotin-switch technique (BST).*

2.2 Objectives

In the following sections, RSNO chemistry was examined at the single-molecule level by using two α-hemolysin mutants, the heteroheptamer $(WT)_6(G137C)_1$ and the homoheptamer $(G137C)_7$ (abbreviated as PSH and P7SH respectively). The former carries six copies of wild-type (WT) subunits and one copy of a mutated monomer that has the Gly at position 137 mutated to Cys, so there is only one cysteine residue in the lumen. P7SH bears seven copies of the mutated subunit, thus there are a total of seven cysteine residues. *S*-Nitrosoglutathione (GSNO) and *S*-nitroso-*N*-acetyl-D-penicillamine (SNAP) were used as NO donors (Figure 2.7). In addition to transnitrosation from these donors, *S*-glutathionylation by GSNO, *S*-sulfonation of PSNO (the *S*-nitrosothiol derivative of PSH) by sulfite ion (conversion of PSNO into $PSSO_3^-$) and hydrolysis of PSNO are also observed. The pH-dependency of *S*-glutathionylation versus transnitrosation and the depletion of RSNO by sulfite ion suggest possible mechanisms for the regulation of NO signaling and the asthmatic effect of sulfite, respectively.

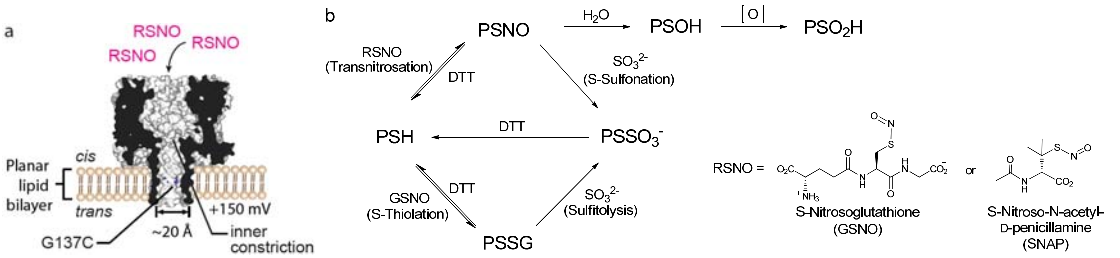

Figure 2.7. *Summary of S-nitrosothiol chemistry observed at the single-molecule level. (a) Cross section of an α-hemolysin (αHL) pore, (G137C-D8)$_7$ (abbreviated as P7SH), located in a planar lipid bilayer (see Chapter 1). Cysteine residues at position 137, near the middle of the transmembrane β barrel, are highlighted in blue. The position of the inner constriction (diameter ~15 Å) is indicated. The internal diameter of the transmembrane barrel is ~20 Å. S-nitrosothiols (RSNO) were added to the cis compartment, which is the side where the cap domain of the αHL pore resides and is connected to ground. The potential difference of the trans compartment relative to the cis compartment was +150 mV. (b) Summary of S-nitrosothiol chemistry observed using the nanopore approach. PSH: (WT)$_6$(G137C-D8)$_1$, an αHL pore with a single cysteine thiol; PSNO: the S-nitrosothiol derivative of PSH; $PSSO_3^-$: the S-sulfonate derivative; PSSG: the glutathione mixed disulfide derivative; PSOH: the sulfenic acid derivative; PSO_2H: the sulfinic acid derivative; DTT: DL-dithiothreitol. The structures of the two RSNO used here are shown: S-nitrosoglutathione (GSNO) and S-nitroso-N-acetyl-D-penicillamine (SNAP).*

2.3 Results

2.3.1 Single-channel recording conditions

Initial investigation on the transnitrosation of PSH with *S*-nitroso-D-penicillamine (SPEN) showed no detectable current change (Figure 2.8a). SPEN is a reactive synthetic *S*-nitrosothiol.[56] It was added to both compartments at +50 or –50 mV and pH 8.4 (2 M KCl, 80 mM 3-(4-morpholinyl)-1-propanesulfonic acid (MOPS), 100 μM ethylene-diaminetetraacetate (EDTA) at 22 ± 1 °C) in this experiment. To confirm the reactivity of thiol group on protein, Ag^+ ion (as $AgNO_3$) was added to PSH prior to the addition of SPEN (see Chapter 3 for the interaction of Ag^+ with cysteine residue thiol group). This showed that the thiol did react soon after the addition of SPEN (Figure 2.8b). However, no change in transmembrane current from the open pore level could be observed. This is not surprising considering that NO is a small group and thus the steric change from a thiol group to an *S*-nitroso group is small. To maximize the current change associated with transnitrosation, different conditions, such as higher voltages, higher electrolyte concentrations and/or other

Table 2.1. *Comparison of transmembrane current changes associated with transnitrosation inside PSH.*

Entry	Buffer	Applied voltage (mV)	Current change (pA)
1	2 M KCl, 80 mM MOPS, 100 μM EDTA, pH 8.4	+50 and –50	0
2		+150	–1.0
3		–150	0
4	2 M KCl, 80 mM Bis-Tris, 100 μM EDTA, pH 8.4	+150	–1.0
5	4 M KCl, 80 mM MOPS, 100 μM EDTA, pH 8.4	+150	–0.9
6		–150	0
7	4 M NaCl, 80 mM MOPS, 100 μM EDTA, pH 8.4	+150	–0.3
8	150 mM NaCl, 80 mM MOPS, 100 μM EDTA, pH 7.4	+150	–0.2

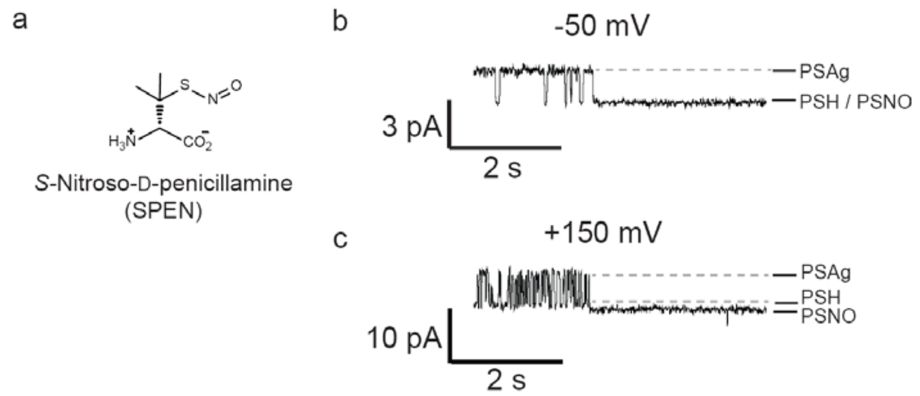

Figure 2.8. *Screening the conditions for studying transnitrosation. (a) Structure of S-nitroso-D-penicillamine (SPEN). (b) and (c): two example traces with PSH. (b) –50 mV, and (c) +150 mV. Silver nitrate (200 μM) was added to the cis compartment to aid the observation of transnitrosation. Reduced thiol group binds silver ion reversibly, while RSNO does not. SPEN (133 μM) was then added to the opposite compartment. The cessation of reversible silver ion binding in the current-time recordings indicates the occurrence of transnitrosation. No difference in ionic current between PSH and PSNO levels is observed at –50 mV, while a change of –1.0 pA is seen at +150 mV. Each level is labelled with the proposed chemical functionality on Cys-137 (PSH: pore with free thiol; PSAg: pore with silver ion(s) bound; PSNO: the S-nitrosothiol derivative of PSH). Conditions: 2 M KCl, 80 mM 3-morpholinopropane-1-sulfonic acid (MOPS), 100 μM ethylenediaminetetraacetate (EDTA), pH 8.4, at 22 ± 1 ℃. Note that Ag^+ and SPEN were added to opposite compartments of the chamber to avoid the decomposition of SPEN by Ag^+.[57] Solubility of AgCl in water is very low (solubility product = 1.77×10^{-10} M^2). So in our buffer containing 2 M KCl, only ~90 pM free Ag^+ is present in solution. Another water-soluble species, $AgCl_2^-$, may be present under such high concentration of Cl^-. $AgCl_2^-$ in solution may also participate in the formation of PSAg.*

electrolytes, were screened using Ag^+ as indicator (Figure 2.8). The data are summarized in Table 2.1.

Positive applied voltage gave a larger current change compared to negative voltages (entries 2 vs 3; 5 vs 6), while increasing the electrolyte concentration from 2 M to 4 M KCl did not increase the current jump (entries 2 vs 5). Changing the electrolyte to NaCl reduced the current change (entries 5 vs 7). Therefore +150 mV and 2 M KCl were chosen for all the following measurements. 100 µM EDTA was present because multivalent metal ions, especially Cu^{2+} and Fe^{2+}, catalyze the decomposition of RSNO (see Section 2.1.5).[58]

2.3.2 Transnitrosation versus *S*-thiolation

GSNO is a naturally occurring RSNO. It can mediate cell signaling through transnitrosation,[38,59] the transfer of the NO group to protein cysteine residues, or by *S*-glutathionylation, the formation of a mixed disulfide, again with protein cysteine residues.[20] Thus the single-molecule chemistry of RSNO was first examined by reacting GSNO with the seven cysteine residues in P7SH. To aid the electrodiffusion of the negatively charged GSNO through the αHL pore (at +150 mV and pH ≥ 7.4), GSNO was added to the *cis* compartment (Figure 2.7a). The addition of GSNO (2 mM) at +150 mV and pH 7.4 (2 M KCl, 80 mM MOPS, 100 µM EDTA, 22 ± 1 °C) produced a series of small step changes in the transmembrane ionic current (ΔI = –1.2 ± 0.3 pA, 107 steps out of a total 121 steps in 34 experiments). A maximum of seven steps was observed in a single experiment, corresponding to the total number of cysteine residues in each P7SH pore (Figure 2.9a). The heteroheptamer PSH, which contains only one cysteine residue, showed a single step change (success rate 83%, n = 60 experiments, see Section 2.6.15 and Table 2.5), suggesting that each step observed with P7SH is due to a separate reaction with a cysteine residue. Because a different RSNO, SNAP (Figure 2.7b), produced a similar current step with P7SH (ΔI = –1.1 ± 0.3 pA, 41 steps from 14 experiments), the steps were attributed to transnitrosation reactions.

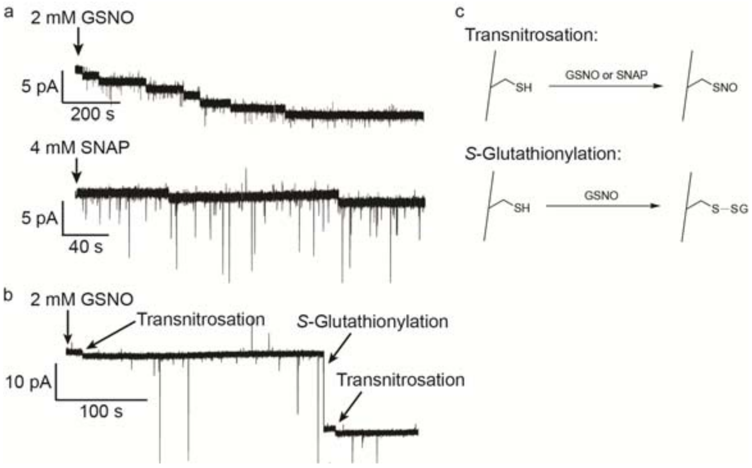

Figure 2.9. *Transnitrosations and S-thiolation by GSNO and SNAP****.*** *(a) Seven successive transnitrosations by GSNO observed with P7SH. Similar changes in transmembrane current were observed when SNAP was used instead of GSNO. Conditions: 2 M KCl, 80 mM MOPS, 100 μM EDTA, pH 7.4, at +150 mV and 22 ± 1 °C. GSNO or SNAP was added to the cis compartment. (b) S-Glutathionylation by GSNO under the same conditions as in (a). Two transnitrosation steps (indicated) can also been seen. (c) Transnitrosation and S-glutathionylation reactions.*

Table 2.2. *Transnitrosation reaction rate constants k_t ($M^{-1}s^{-1}$).*

		Single-channel recording with P7SH				**Bulk solution reaction with L-cysteine**
	pH	Number of experiments	Observed number of reaction steps[a]	Number of *S*-thiolation	k_t	k_t^b
GSNO	7.4	34	121	14	1.0 ± 0.2	120 ± 60
	8.4	14	51	1	2.5 ± 0.7	280 ± 60
SNAP	7.4	14	41	0	1.4 ± 0.2	7.0 ± 0.1
	8.4	12	45	0	4.5 ± 1.1	57 ± 6

[a] *Sum of transnitrosation and S-thiolation.*

[b] *Ensemble transnitrosation rate constants, k_t, for GSNO and SNAP ($M^{-1}s^{-1}$). k_t is the apparent second-order rate constant (rate = k_t[RSH][R'SNO], where [RSH] and [R'SNO] represent the concentration of thiol and S-nitrosothiol, respectively). HPLC was used to determine the reaction rates between GSNO and L-cysteine in bulk solution, while stopped-flow or conventional UV-visible spectrophotometry was used for the reactions between SNAP and L-cysteine. The value represents mean ± s.d. for three experiments. Conditions: 2 M KCl, 80 mM MOPS, 100 μM EDTA, pH 7.4 or 8.4, 22 ± 1 °C.*

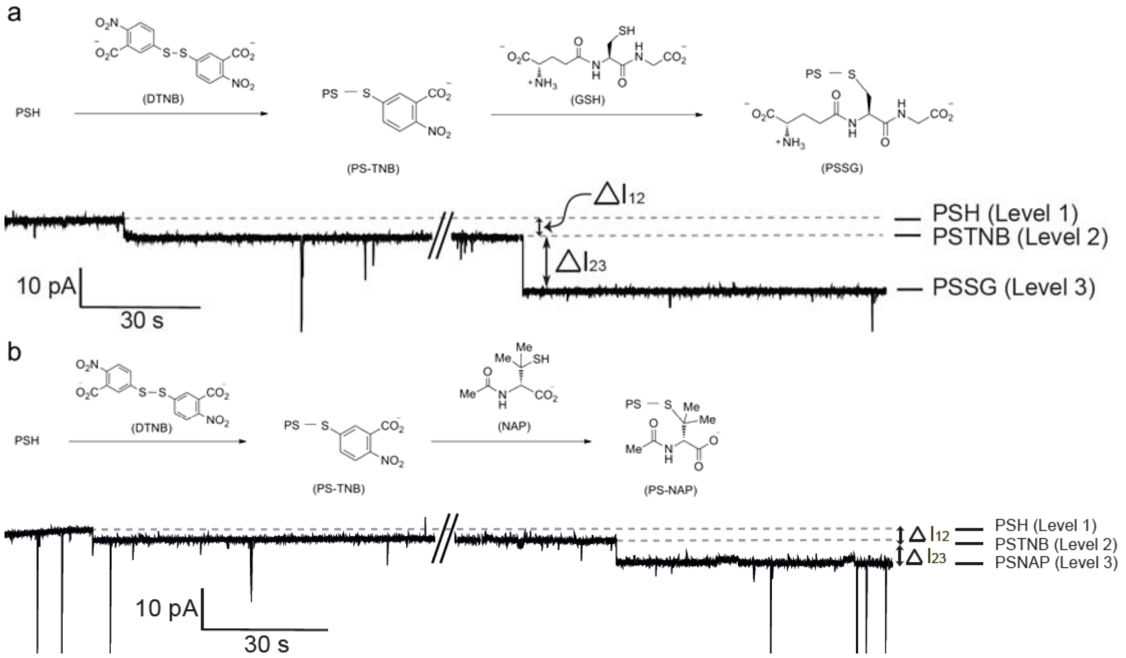

Figure 2.10. *An alternative route to PSSR. (a) PSSG formation. The thiol group in PSH was first activated by 5,5'-dithiobis-(2-nitrobenzoic acid) (DTNB, 200 μM, cis) to form PS-TNB. Then excess glutathione (GSH, 2.6 mM, cis) was added to form the mixed disulfide PSSG.* ΔI_{12} *and* ΔI_{23} *are –4.1 ± 0.4 pA (n = 3) and –16 ± 3 pA (n = 3), respectively. (*ΔI_{12} *denotes the change in current in going from level 1 to level 2, etc.) (b) PS-NAP formation. PS-TNB was first formed as in (a), followed by the addition of N-acetyl-D-penicillamine (NAP, 3 mM, cis).* ΔI_{12} *and* ΔI_{23} *are –4.2 ± 0.7 pA (n = 3) and –6.7 ± 1.4 pA (n = 3) respectively. Conditions: 2 M KCl, 80 mM MOPS, 100 μM EDTA, pH 7.4, at +150 mV and 22 ± 1 °C.*

In addition to the transnitrosation steps, much bigger current jumps (ΔI = –20 ± 5 pA, 14 steps out of 121 steps from 34 experiments, i.e. 12%) were observed less often with GSNO (Figure 2.9b, Table 2.2). The current change associated with these steps and the ability to reverse them with DL-dithiothreitol (DTT, 10 mM, *trans*) suggested that they might arise by *S*-glutathionylation. To confirm this possibility, the *S*-glutathionyl derivative of PSH was generated separately by first activating the thiol group of the pore with 5,5'-dithiobis-(2-nitrobenzoic acid) (DTNB, 200 μM, *cis*),[60] followed by disulfide exchange with reduced glutathione (GSH, 2.6 mM, *cis*) (Figure 2.10a). This reaction gave a ΔI value of –20 ± 3 pA (n = 3), which within experimental error is the same as that observed with GSNO and P7SH. *S*-Thiolation was not observed with SNAP, which should have given a ΔI value of –11 ± 2 pA (n = 3, Figure 2.10b). The absence of S-thiolation with SNAP has been reported in bulk solution[61] and was attributed to the greater steric hindrance around the tertiary sulfur atom in SNAP (Figure 2.7b). An alternative route to the *S*-glutathionyl derivative of P7SH by reaction with oxidized glutathione (GSSG) proved to be very slow at pH 7.4,[62] ruling out contamination of the freshly prepared GSNO with GSSG as the source of *S*-glutathionylation.

The reactions of GSNO and SNAP with P7SH were further investigated at pH 8.4 (Table 2.2). Only one *S*-glutathionylation by GSNO was observed (among 51 reaction steps), while SNAP again did not produce *S*-thiolation.[61]

Lifetime of nitroxyl disulfide intermediate in transnitrosation

Transnitrosation is proposed to proceed through an associative nitroxyl disulfide intermediate[63] (Figure 2.11a). This intermediate ($[PSN(O)SG]^-$) could not be observed even in experiments (n = 3) performed with GSNO at both lower pH and reduced temperature (pH 6.0 and 5°C) at the maximum data acquisition rate (corner frequency 30 kHz, sampling at 150 kHz). It has been suggested that the intermediate is short-lived;[63] and according to our measurements, if it does exist, the lifetime must be well under 200 μs (Figure 2.11c,d). This limit was estimated by assuming that the nitroxyl disulfide ($[PSN(O)SG]^-$) intermediate has a similar current amplitude (~ –20 pA) to the glutathione mixed disulfide (PSSG, Figures 2.9b, 2.10a and 2.11b).

Comparison of single-molecule kinetic data with bulk solution data

The second-order rate constants, k_t, for transnitrosation by GSNO and SNAP at pH 8.4 were increased by 2 to 3-fold compared to k_t at pH 7.4 (Table 2.2), consistent

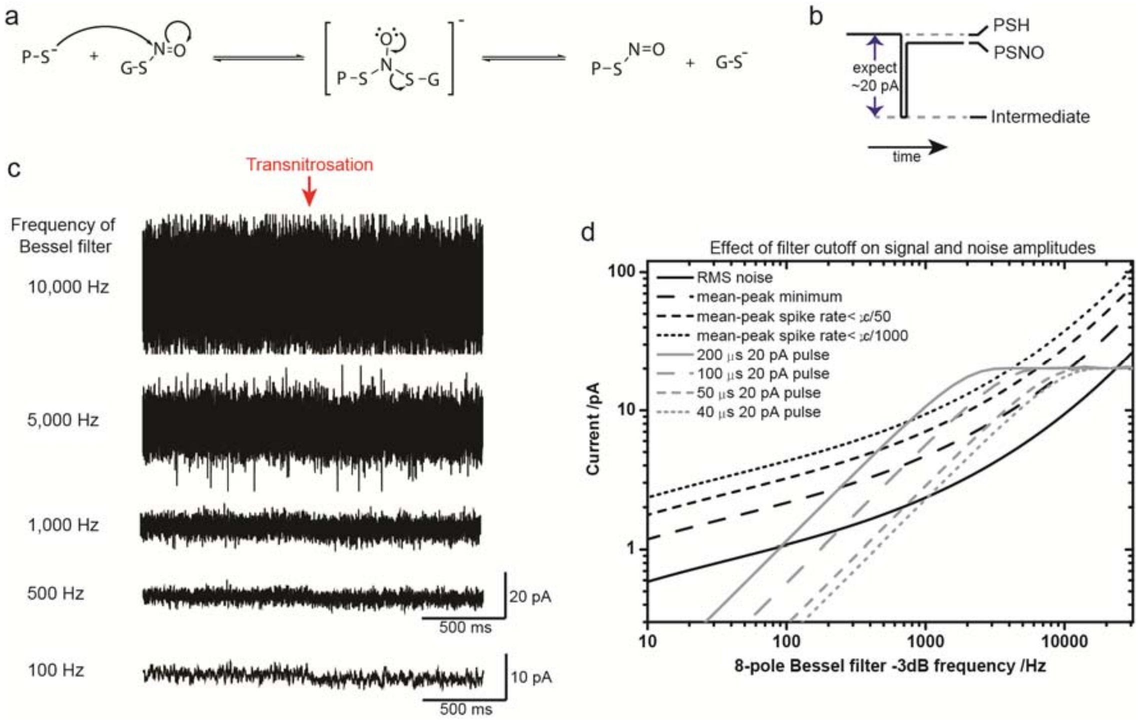

Figure 2.11. *Estimation of the lifetime of the associative intermediate in the transnitrosation reaction by single-channel recording. (a) Proposed mechanism of transnitrosation. The structure of the nitroxyl disulfide intermediate is shown. (b) Idealized current-time trace showing the expected current signal in the absence of noise. We assumed that the nitroxyl disulfide ($[PSN(O)SG]^-$) intermediate has a similar current peak height (~ –20 pA) to the glutathione mixed disulfide (PSSG, Figures 2.9b and 2.10a). (c) An experimental electrical recording trace filtered at different post-recording frequencies (as stated on the left) with a low-pass Bessel filter. The trace was obtained from an experiment performed with PSH in 2 M KCl, 80 mM MES (2-(4-morpholinyl)ethanesulfonic acid), 100 μM EDTA, pH 6.0, at 5 ± 1 °C. GSNO (2 mM) was added to the cis chamber. During the measurement, the signal was filtered with an external low-pass 4-pole Bessel filter (80 dB/decade) (model 900C9L8L, Frequency Devices, inserted between the unfiltered amplifier output and the digitizer) with a corner frequency of 30 kHz, and sampled at 150 kHz. In data analysis with Clampfit, the recorded trace was further filtered with a low-pass 8-pole Bessel filter at various frequencies (as stated on the left). The traces are all shown on the same scale, except the last one, in which the y-axis has been expanded. (d) The effect of filter cut-off on signal and noise amplitudes. The compromise between the reduction of noise and the truncation of signal by filtering is emphasized. The first four lines (in black) show the root mean square (rms – continuous line), and the*

mean-to-peak current noise at various threshold values (long dash curve: calculated with a crest factor of 2, bounding 90% of transient noise peaks; short dash and dot curves: mean-to-peak values of noise not crossed more often than once in 50- and 1000-times in the characteristic inverse filter time, respectively), of the experimental trace shown in 'c' as a function of 8-pole Bessel filter frequency. The other four lines (in grey) represent the theoretical amplitude of the filter response of a rectangular signal (20 pA, see 'b') of different lifetimes as a function 8-pole Bessel filter frequency. A signal with ≥200 μs lifetime can clearly be distinguished from the noise in the filter frequency range 800 to 4000 Hz. The inability to observe the proposed signal for the nitroxyl disulfide intermediate in our experiment within this filter frequency range suggests that the intermediate's lifetime must be shorter than 200 μs. This is a conservative estimate as the amplitude of a 50 μs signal would still be above the bulk of the noise peaks (long dashed black line) under optimal filtering.

with the participation of thiolate anions as the reactive species.[64]

Ensemble reaction rate constants of GSNO and SNAP with L-cysteine were determined under the same solution conditions by either UV-visible spectroscopy or HPLC (Table 2.2). Our ensemble k_t values are comparable to those reported in the literature,[56,65] and are larger than those obtained from the single-molecule experiments. The differences persist after correction for the extent of ionization of the thiol groups in P7SH and free L-cysteine, particularly for the reactions with GSNO (Table 2.3). These are attributed to the greater steric hindrance around the cysteine residue in P7SH compared to free L-cysteine. Much larger differences in rate constants with GSNO (52- and 67-fold at pH 7.4 and 8.4, respectively) between the ensemble reaction and the nanoreactor approach can be explained by the bigger size of GSNO relative to SNAP. Thus the narrow central constriction (~15 Å, Figure 2.7a) retards the passage of GSNO (added to the *cis* compartment), thereby reducing its effective concentration at the reaction site. As a result, although GSNO (carries a net charge of -1 at the pH tested) is electrophoretically driven into the pore by the applied potential

(+150 mV), its effective concentration in the pore is lower than that of SNAP, which has zero net charge and is not electrostatically attracted into the pore.

Table 2.3. *Second-order rate constants, k'_t, for transnitrosation by the thiolate anion (RS^-).*

	pH	Single-channel recording with P7SH ($M^{-1}s^{-1}$) [a]	Bulk solution reaction with L-cysteine ($M^{-1}s^{-1}$) [a]
GSNO	7.4	23	1200
	8.4	8.1	540
SNAP	7.4	33	71
	8.4	15	110

[a] *These values were calculated from the second-order rate constants of transnitrosation, k_t, in Table 2.2 by using equation (4) in Section 2.6.13.*

2.3.3 Reversible transnitrosation

Transnitrosation is a reversible reaction. The regeneration of PSH by the removal of "NO" from pre-formed PSNO can be effected by adding a thiol compound into the opposite reaction chamber. Using spatially separated reagents,[66] multiple turnovers of transnitrosation of the thiol group in PSH were observed at pH 8.4. GSNO and DL-dithiothreitol (DTT) were added to the *cis* and *trans* compartments, respectively (Figure 2.12a). The dithiol compound DTT was chosen because it can reduce disulfide into the free thiols. This was advantageous to our experiment, as PSH could be regenerated from the occasional *S*-thiolation taking place between PSH and GSNO, or between PSNO and DTT.

Two conductance levels that differ by –0.7 ± 0.1 pA (n = 6) were observed (Figure 2.12d). The dependence of the forward and backward reaction rates on the concentrations of GSNO and DTT was determined by titration experiments, in which the concentration of one reagent was varied, while that of the other was kept constant (Figures 2.12b-d) These titration experiments showed linear dependences for the

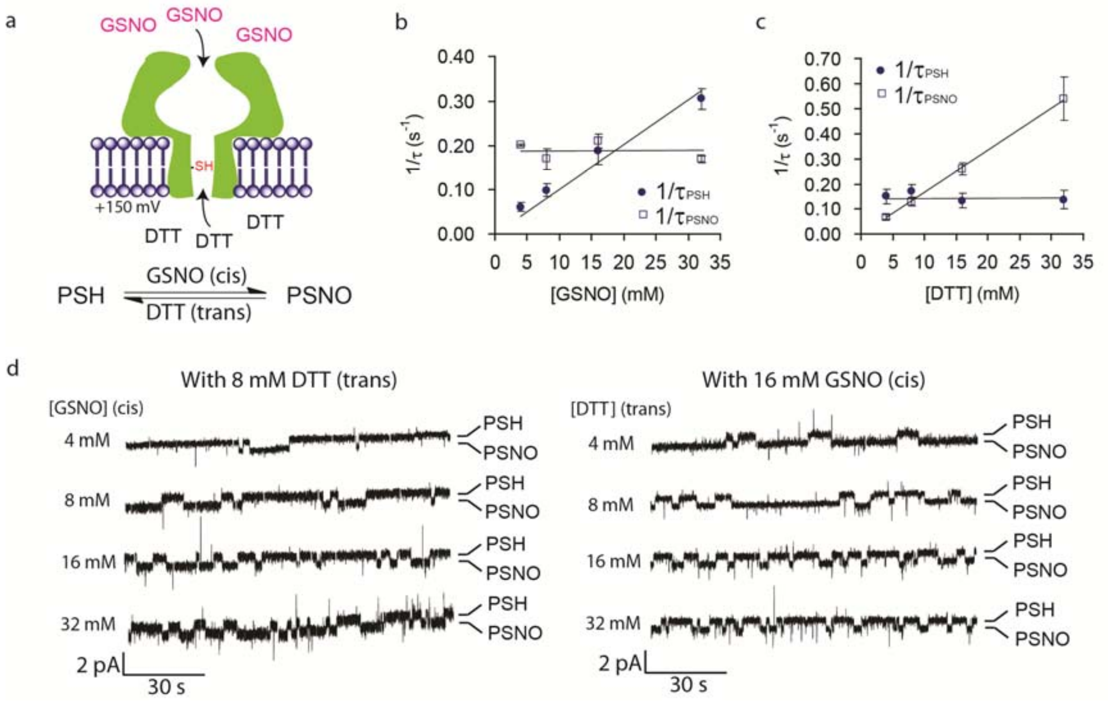

Figure 2.12. *Reversible transnitrosation. (a) Reversible transnitrosations in the PSH nanoreactor in the presence of GSNO (cis) and DTT (trans). Conditions: 2 M KCl, 80 mM MOPS, 100 μM EDTA, pH 8.4, at +150 mV and 22 ± 1 ℃. (b) Reciprocals of the mean dwell times for both the PSH ($1/\bar{\tau}_{PSH}$) and PSNO ($1/\bar{\tau}_{PSNO}$) levels versus the concentration of GSNO. The same concentration of DTT (8 mM) was used throughout this set of experiments. (c) As in (b), but the concentration of DTT was varied and a fixed concentration of GSNO (16 mM) used. Each point represents the mean ± s.d. for three experiments. (d) Single-channel recordings under the above conditions at various concentrations of GSNO and DTT. The levels corresponding to PSH and PSNO are marked.*

reciprocals of the mean dwell times at the PSH level ($\bar{\tau}_{PSH}$) and at the PSNO level ($\bar{\tau}_{PSNO}$) on the concentration of GSNO and DTT respectively (Figures 2.12b,c). Thus the forward and backward reactions have first-order dependence on [GSNO] and on [DTT], and the second-order rate constants k_t are given by $1/(\bar{\tau}_{PSH}[GSNO])$ and $1/(\bar{\tau}_{PSNO}[DTT])$, respectively. The k_t calculated for the forward transnitrosation reaction between PSH and GSNO is 10 ± 1 $M^{-1}s^{-1}$, while k_t for the reverse transnitrosation between PSNO and DTT is 17 ± 1 $M^{-1}s^{-1}$. Infrequent *S*-

glutathionylations between PSH and GSNO were excluded in these calculations. Occasionally, *S*-thiolation between PSNO and DTT, instead of transnitrosation, occurred and formed a short-lived PS-DTT mixed disulfide intermediate (lifetime = 7 ± 1 ms, ΔI = –10 ± 0.3 pA, n = 2, Figure 2.24 in Section 2.6.16). The rate constant for the reaction of PSH with GSNO is about four times larger than that measured with P7SH (2.5 ± 0.3 $\text{M}^{-1}\text{s}^{-1}$, Table 2.2). The backward rate constant for PSNO and DTT is about double that of the forward one, most likely because DTT contains two thiol groups compared to only one thiol group in PSH.

In addition to transnitrosation and *S*-thiolation, an additional two-step reaction from the PSNO level was observed, after which no more transnitrosations took place (Figure 2.13). The first step showed a drop in transmembrane current, ΔI = –0.7 ± 0.1

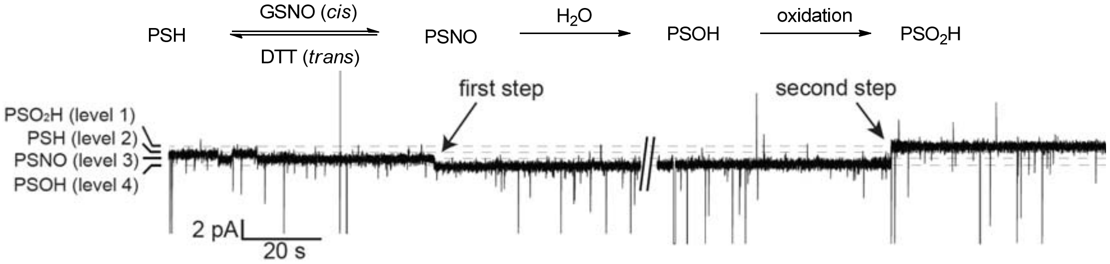

Figure 2.13. *Hydrolysis and oxidation of PSNO. Occasionally, a two-step reaction starting from the PSNO level was observed during reversible transnitrosation with GSNO (4 to 32 mM, cis) and DTT (4 to 32 mM, trans). Protein: PSH. Conditions: 2 M KCl, 80 mM MOPS, 100 μM EDTA, pH 8.4, at +150 mV and 22 ± 1 °C. Each level is labelled with the proposed chemical functionality on Cys-137.* ΔI_{23} *= –0.7 ± 0.1 pA (n = 9),* ΔI_{34} *('first step') = –0.7 ± 0.1 pA (n = 9),* ΔI_{41} *('second step') = +1.8 ± 0.1 pA (n = 5). (*ΔI_{12} *denotes the change in current in going from level 1 to level 2, etc.). Based on a separate experiment with* H_2O_2 *(Figure 2.14), we propose that the 'first step' is the hydrolysis of PSNO to the sulfenic acid (PSOH), while the second step is the oxidation of PSOH to the sulfinic acid (*PSO_2H*). The mean of the total time spent at the PSNO level in each experiment before hydrolysis was 830 ± 360 s (n = 9); the mean lifetime of PSOH before oxidation to* PSO_2H *was 230 ± 140 s (n = 5).*

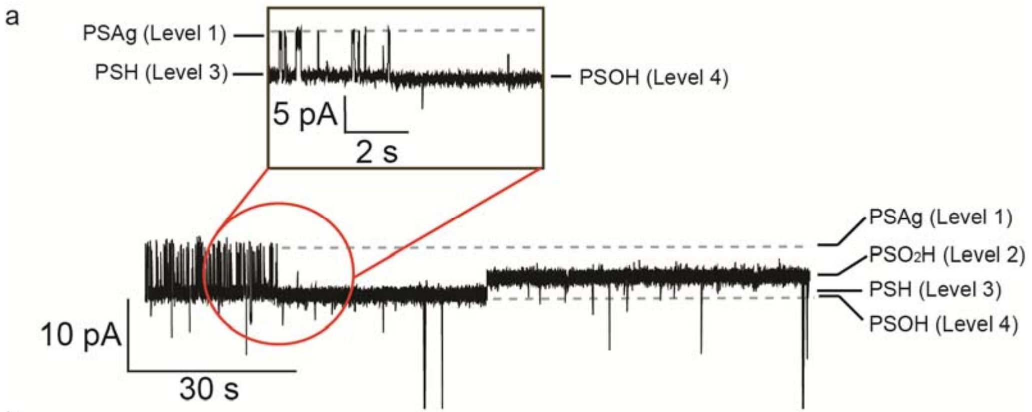

b

	PSH + GSNO/DTT	PSH + Ag^+/H_2O_2
	Amplitude (pA)	Amplitude (pA)
PSH → PSNO	–0.7 ± 0.1 (n = 9)	PSH → PSOH –0.6 ± 0.2 (n = 3)
PSNO → PSOH	–0.7 ± 0.1 (n = 9)	
PSOH → PSO_2H	+1.8 ± 0.6 (n = 5)	+2.5 ± 0.1 (n = 3)
PSO_2H → PSH	–0.4 (n = 1)	Not applicable

Figure 2.14. *Oxidation of PSH by H_2O_2. (a) A current recording trace showing the oxidation of the thiol in PSH by H_2O_2 (9.8 mM, trans). Each level is labelled with the proposed chemical functionality on Cys-137. Because thiol oxidation causes a very small current change, silver nitrate (200 μM) was first added to the cis compartment to aid the observation. Reduced thiol groups bind silver ion reversibly, while oxidized thiols do not. Protein: PSH. Conditions: 2 M KCl, 80 mM MOPS, 100 μM EDTA, pH 8.4, at +150 mV and 22 ± 1 ℃. ΔI_{13} = +7.3 ± 1.2 pA, ΔI_{34} = –0.6 ± 0.2 pA and ΔI_{42} = +2.5 ± 0.1 pA (n = 3). (ΔI_{12} denotes the change in current in going from level 1 to level 2, etc.). The mean dwell time at level 3 before the current jump to level 4 after the addition of H_2O_2 was 160 ± 90 s (9.8 mM H_2O_2, n =3), while the mean dwell time at level 4 before the current jump to level 2 was 42 ± 35 s (9.8 mM H_2O_2, n = 3). The expanded inset shows the recording when the reversible Ag^+ binding events ceased. Note the small current change from Level 3 (PSH) to Level 4. We surmised that the cessation of the Ag^+ ion binding events is due to the oxidation of PSH (level 3) to the sulfenic acid (PSOH, level 4), while the following current jump to level 2 corresponds to the further oxidation to the sulfinic acid (PSO_2H). (b) Table summarizing the current changes associated with each chemical transformation observed in Figure 2.13 and in (a). The difference in the change of current in the proposed PSH to PSOH step observed in (a) (ΔI_{34}, –0.6 ± 0.2 pA) compared to that in the hydrolysis of PSNO*

(–1.4 ± 0.2 pA, Figure 2.13) may due to the presence of Ag^+ *ion, which apart from binding to cysteines, can also interact with other amino acid residues, such as methionine, lysine and arginine (see Chapter 3, Section 3.3.1). By contrast, the changes in the current in the step from PSOH to* PSO_2H *in the two experiments are within experimental error.*

pA (measured from the PSNO level, n = 9), while the second step showed an increase of +1.8 ± 0.1 pA (measured from the PSOH level (see below), n = 9). In two out of nine experiments, this change could be reversed by the addition of a high concentration of DTT (10 mM, *trans*), upon which transnitrosations reappeared. The two-step transition might be due to hydrolysis of PSNO to the sulfenic acid (PSOH) (first step), which could undergo further oxidation to generate the sulfinic acid (PSO_2H) (second step) (Figures 2.7b and 2.13).[35] The mean lifetimes of PSNO before hydrolysis and PSOH before further oxidation are 830 ± 360 s (n = 9) and 230 ± 140 s (n = 5) respectively. Control experiments using hydrogen peroxide (H_2O_2) to oxidize the thiol group in PSH gave similar two-step changes under the same conditions (Figure 2.14), supporting the assignments proposed above.

2.3.4 *S*-Sulfonation

The reaction between *S*-nitrosothiols and sulfite ion has been reported previously,[67–69] with RSH proposed as the end product. However, the product was not spectroscopically characterized. Further, 5,5'-dithiobis-(2-nitrobenzoic acid) (DTNB) was used to detect thiol formation, but the disulfide bond of this reagent can also be cleaved by sulfite (sulfitolysis). To clarify the chemistry between sulfite, a notorious bronchoconstrictor, and low-molecular weight and protein *S*-nitrosothiols, which are present in human airways and responsible for bronchodilation,[4,5] a detailed spectroscopic and kinetic study with GSNO as a representative RSNO was performed.

^{1}H NMR spectroscopy and mass spectrometry (Figure 2.15b,c) revealed that *S*-sulfoglutathione ($GSSO_3^-$) was formed from GSNO and sulfite at pH 7.4 and 22°C. Authentic $GSSO_3^-$ was generated *in situ* by sulfitolysis of oxidized glutathione (GSSG) with 25 equivalents of sulfite ion to yield a one-to-one mixture of GSH and $GSSO_3^-$.[70] The $GSSO_3^-$ in this crude product mixture showed the same signals for the CH_2S protons (two doublets of doublets at δ 3.65 and 3.47, red framed in Figure 2.15b) as did the products from GSNO and sulfite ion. High-resolution electrospray ionization-mass spectrometry (ESI-MS) confirmed the formation of $GSSO_3^-$ (found *m/z* 386.0328, calculated $[M–H]^-$: *m/z* 386.0333) from GSNO and sulfite. Note that in ^{1}H NMR spectra, the CH_2S protons in GSNO appear as broad peaks (blue-framed in Figure 2.15b). This phenomenon has been observed previously[44,71] and might due to the presence of *syn* and *anti* geometries (Figure 2.4a) around the S–N bond. These two conformers have a high interconversion barrier (~11 kcal/mol)[41] and have been reported to give two separate peaks on ^{15}N NMR spectra at low temperature (–50 °C). In addition, restricted C–C bond rotation in $CHCH_2SNO$ due to intramolecular hydrogen bonding between the oxygen atom in SNO and the nearby N–H hydrogen atom, forming a seven-membered ring structure, might also lead to peak broadening.

^{15}N NMR and mass spectroscopy showed hydroxylamine-*N*-sulfonate ($HONHSO_3^-$) as the other reaction product, which inherits the nitrogen atom in the *S*-nitrosothiol group. ^{15}N NMR of the crude reaction products formed by mixing $GS^{15}NO$ and sulfite in 1:2 mole ratio gave a peak at 160.4 ppm (referenced to liquid ammonia, Figure 2.15d). This peak was assigned to [^{15}N]hydroxylamine-*N*-sulfonate, as confirmed by ^{15}N NMR of the authentic compound (Figure 2.16b). ESI-MS showed a peak at *m/z* 111.97 in negative mode, supporting the formation of hydroxylamine-*N*-sulfonate (calculated $[HONHSO_3]^-$: *m/z* 111.97) (Figure 2.15c). The

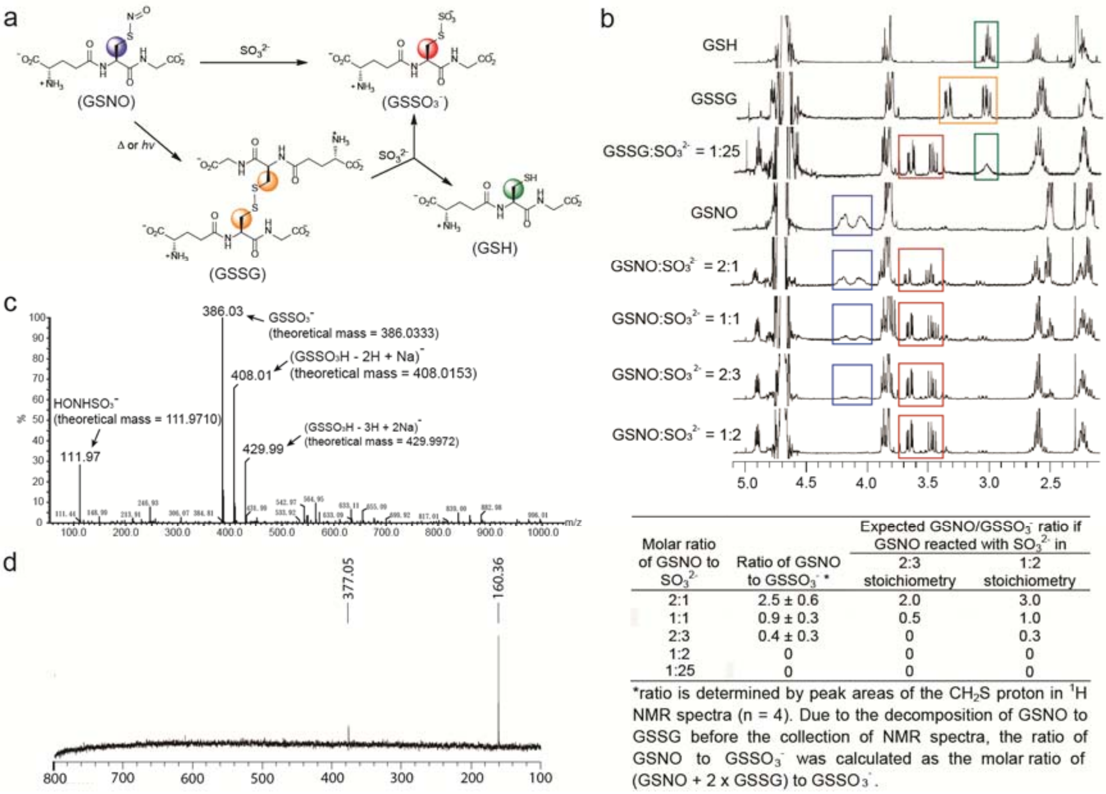

Molar ratio of GSNO to SO_3^{2-}	Ratio of GSNO to $GSSO_3^-$ *	Expected GSNO/$GSSO_3^-$ ratio if GSNO reacted with SO_3^{2-} in 2:3 stoichiometry	1:2 stoichiometry
2:1	2.5 ± 0.6	2.0	3.0
1:1	0.9 ± 0.3	0.5	1.0
2:3	0.4 ± 0.3	0	0.3
1:2	0	0	0
1:25	0	0	0

*ratio is determined by peak areas of the CH_2S proton in ^1H NMR spectra (n = 4). Due to the decomposition of GSNO to GSSG before the collection of NMR spectra, the ratio of GSNO to $GSSO_3^-$ was calculated as the molar ratio of (GSNO + 2 x GSSG) to $GSSO_3^-$.

Figure 2.15. *Product characterization for the reaction between GSNO and sulfite ion in bulk solution. (a) Reaction between GSNO and sulfite ion. (b) Stacked 400 MHz ^1H NMR spectra (5.1–2.1 ppm) in D_2O containing 2 M KCl, 80 mM sodium phosphate, 100 μM EDTA, pD 7.4, at 22 ± 1 °C. Glutathione derivatives at 10 mM were used in each experiment. S-Sulfonation or sulfitolysis was carried out for 10 min before spectra were recorded. All spectra were collected within 1 h after sample preparation to avoid the slow light and heat-induced decomposition of GSNO to GSSG. Peaks from the CH_2S protons are framed with colors corresponding to various glutathione derivatives highlighted in (a). The table shows the ratios of the integrations of the CH_2S protons from GSNO and $GSSO_3^-$ from ^1H NMR spectra recorded after GSNO (10 mM) was mixed with various concentrations of sulfite ion. (c) Electrospray ionization mass spectroscopy (ESI-MS, negative ion mode) showing the peak corresponding to $GSSO_3^-$. The sample was prepared by mixing GSNO and sodium sulfite in 1:2 ratio in water and the products were analyzed without purification. (d) ^{15}N NMR spectrum (50 MHz, 800–100 ppm) after the reaction between $GS^{15}NO$ (83 mM) and sodium sulfite mixed in a 1:2 ratio in the same buffer as in (b).*

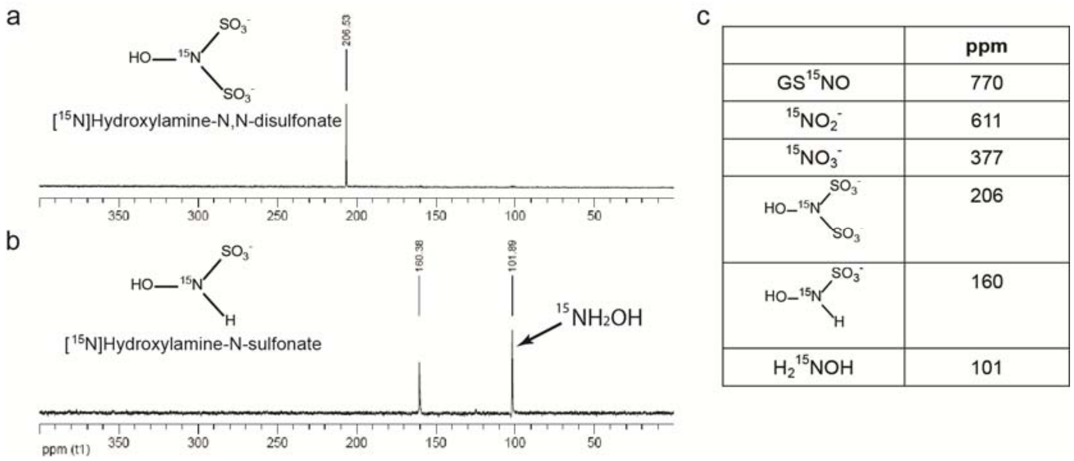

	ppm
GS^{15}NO	770
$^{15}NO_2^-$	611
$^{15}NO_3^-$	377
	206
	160
$H_2{}^{15}NOH$	101

Figure 2.16. *Stacked ^{15}N NMR (50 MHz) spectra (400–0 ppm) of authentic [^{15}N]hydroxylamine-N,N-disulfonate and [^{15}N]hydroxylamine-N-sulfonate. (a) [^{15}N]Hydroxylamine-N,N-disulfonate and (b) [^{15}N]hydroxylamine-N-sulfonate were synthesized to confirm the identity of nitrogen-containing products in the S-sulfonation of GS^{15}NO by sulfite ion. Conditions: pD 7.4, 2 M KCl, 80 mM sodium phosphate, 100 μM EDTA, 22 ± 1 °C, externally referenced to liquid ammonia. [^{15}N]Hydroxylamine formed by hydrolysis of [^{15}N]hydroxylamine-N-sulfonate in 'b' is labelled. (c) ^{15}N NMR chemical shifts[72] of various ^{15}N-containing reagents in 2 M KCl, 80 mM sodium phosphate, 100 μM EDTA, pD 7.4.*

equivalent of hydroxylamine-*N*-sulfonate formed was measured by the quantification of the small nitrogen-containing compounds (e.g. nitrite, hydroxylamine) formed from the hydrolysis of the hydroxylamine-*N*-sulfonate (see Section 2.6.17). One equivalent of hydroxylamine-*N*-sulfonate was produced from each GSNO. These assays also supported the formation of hydroxylamine-*N*-sulfonate, instead of the isomer hydroxylamine-*O*-sulfonate ($H_2N–OSO_3^-$).

The reaction stoichiometry was determined by ^{1}H NMR titration experiments. The ratio of peak areas of the CH_2S protons in GSNO and $GSSO_3^-$ reveals that GSNO reacts with sulfite ions in a 1:2 ratio (Figure 2.15b). Nitric oxide (NO) or nitroxyl (HNO), which might be formed as a short-lived intermediate, could not be detected with electron paramagnetic resonance (EPR) by trapping with oxymyoglobin and metmyoglobin.[12] The kinetics of the reaction between GSNO and sulfite were followed by monitoring the disappearance of GSNO at 334 nm with a stopped-flow UV-visible spectrophotometer. The rate equation found is: rate = $k_{SO3}{}^{2-}$ [GSNO][sulfite], which shows first-order dependencies on the concentrations of both GSNO and sulfite ion. The second-order rate constant, $k_{SO3}{}^{2-}$, at pH 7.4 is 124 ± 3 $M^{-1}s^{-1}$ at 22°C and 264 ± 5 $M^{-1}s^{-1}$ at 37°C. The latter agrees with a previously reported value.[64]

S-Sulfonation of protein-SNO at the single-molecule level was examined by current recording. P7SNO was first formed by treating P7SH with GSNO. The subsequent addition of sodium sulfite to the *cis* compartment (in excess over GSNO, which also had been added to the *cis* side) elicited several steps in the transmembrane current ($\Delta I \sim +1.4$ to $+3.7$ pA) (Figure 2.17). No intermediate steps were observed and the calculated second-order rate constant $k_{SO3}{}^{2-}$ is 82 ± 40 $M^{-1}s^{-1}$ (11 steps from 6 experiments) at pH 7.4 and 22°C.

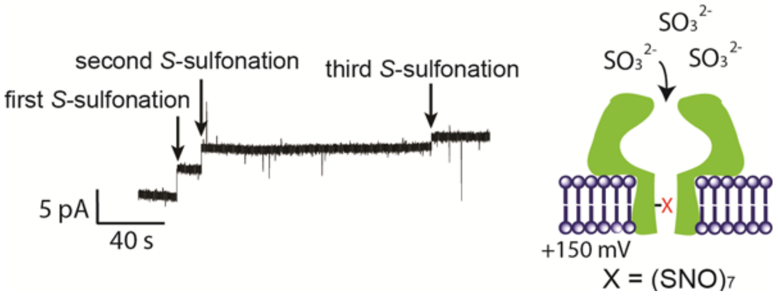

Figure 2.17. *S-Sulfonation of RSNO. Three successive S-sulfonations by sulfite ion on S-nitrosothiols observed at the single-molecule level. Sodium sulfite (12 mM) was added to the cis side of pre-formed P7SNO obtained from the reaction of GSNO (2 mM, cis) with P7SH. Conditions: 2 M KCl, 80 mM MOPS, 100 μM EDTA, pH 7.4, at +150 mV and 22 ± 1°C. The three S-sulfonation steps are of different amplitudes because the environment within the pore is altered after each reaction.*

S-Sulfonation was also tested with other RSNO in solution. Both SNAP and *S*-nitroso-L-cysteine were transformed to the corresponding *S*-sulfonates by sulfite ion (confirmed by ^{1}H NMR spectroscopy and mass spectrometry), showing the generality of sulfite ion's action on RSNO.

The chemistry of RSNO with nucleophiles was further examined with another sulfur nucleophile, thiosulfate ($S_2O_3^{2-}$). The reaction rate was reported in the literature (~2 $\text{M}^{-1}\text{s}^{-1}$ with SPEN or *S*-nitrosocysteine at 25 °C), but no product characterization

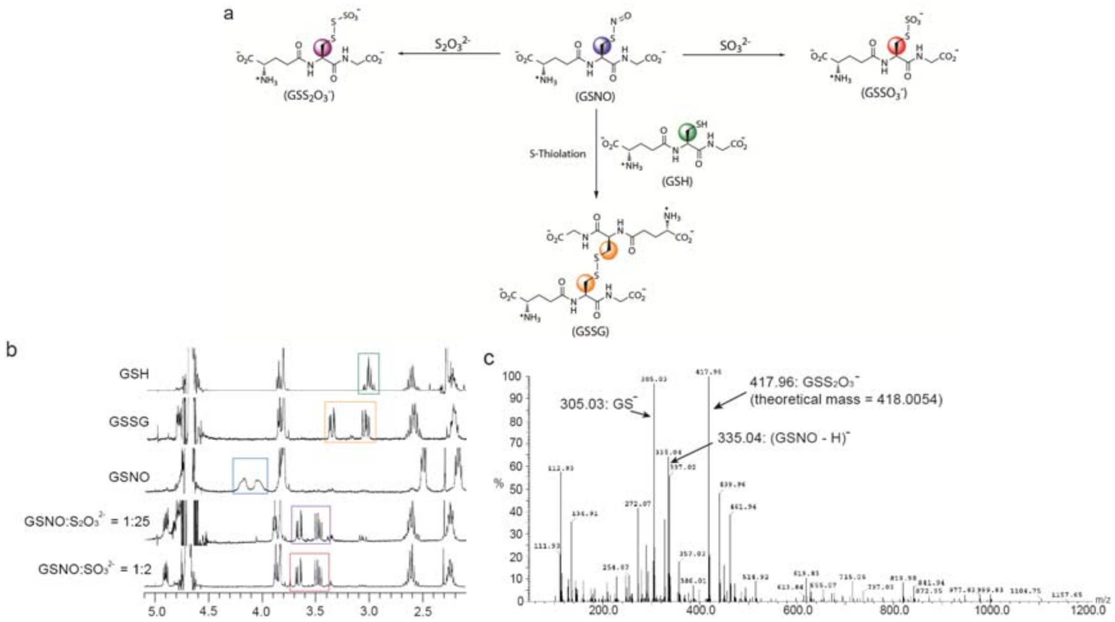

Figure 2.18. *Product characterization for the reaction between GSNO and thiosulfate ion ($S_2O_3^{2-}$). (a) Schematic representation of the reaction between GSNO and various sulfur nucleophiles: thiosulfate, sulfite and thiolate. For thiolate, only S-thiolation is depicted, transnitrosation is not shown. (b) Stacked ^{1}H NMR (400 MHz) spectra (δ 5.1–2.1) in D_2O containing 2 M KCl, 80 mM sodium phosphate, 100 µM EDTA, pD 7.4 at 22 ± 1 ℃. 10 mM of glutathione derivatives were used in each experiment and all spectra were collected within one hour after mixing. Peaks from the CH_2S protons were framed with colours corresponding to various glutathione derivatives as highlighted in (a). Spectrum of $GSSO_3^-$ (generated by S-sulfonation of GSNO by sulfite) is shown for comparison. (c) Electrospray ionization mass spectroscopy (ESI-MS, negative mode) showing the peak corresponding to $GSS_2O_3^-$. The sample was prepared by mixing GSNO and sodium thiosulfate in 1:2 ratio in water and analyzed without purification.*

was carried out.[72] Using GSNO and SNAP as the model compounds, we found that $RSS_2O_3^{2-}$ was formed with both compounds (Figure 2.18). As thiols do not react with thiosulfate, it is likely that $RSS_2O_3^{2-}$ is produced by similar reaction mechanism as in the case for sulfite ion (see Section 2.4.2).

2.4 Discussion

2.4.1 Lifetime of nitroxyl disulfide intermediate

It was proposed that transnitrosation occurs through an associative mechanism, with the transient formation of a nitroxyl disulfide intermediate ($[RSN(O)SR]^-$) (Figure 2.11a).[63,73] Evidence for such a structure in the gas phase has been obtained by mass spectrometry.[63] In our work, we failed to observe an intermediate in aqueous solution and made a conservative estimate of 200 μs at pH 6.0 and 5°C as the maximum lifetime (Figures 2.11c–d). It has been claimed that high concentration of the intermediate formed from ethyl L-cysteine can be observed in methanol by ^1H, ^{13}C and ^{15}N NMR.[73] However, the ^1H NMR obtained by these authors is consistent with disulfide formation, which can occur slowly by *S*-thiolation in aqueous solution (see Sections 2.3.2 and 2.6.14).

2.4.2 Proposed mechanism of *S*-sulfonation

In Section 2.3.4, the reaction stoichiometry, products and rate equation of *S*-sulfonation between RSNO and sulfite ion were determined. RSNO and sulfite react in 1:2 ratio, the final products are one equivalent each of the *S*-sulfonate ($RSSO_3^-$) and hydroxylamine-*N*-sulfonate ($HONHSO_3^-$), and the rate equation is rate = $k_{SO3}{}^{2-}$ [GSNO][sulfite]. The overall reaction is depicted by reaction 18 in Figure 2.19.

The above observations can be described by two possible mechanisms (Figure 2.19). In the first one, we propose that the sulfite ion attacks the nitrogen atom of RSNO in a rate-determining step to form RS-N(OH)-SO_3^- (reaction 19). Substitution by a second sulfite ion at the sulfenamide sulfur atom in this intermediate yields the *S*-sulfonate product, $RSSO_3^-$, together with hydroxylamine-*N*-sulfonate as the leaving group (reaction 20). Similar associative intermediate (GS-N(OH)-SG) has been reported in the reaction between GSNO and GSH.[74] Another possible mechanism involves the direct attack of sulfite anion at the sulfur atom of RSNO in the rate-determining step, with concerted protonation at the nitrogen atom (reaction 21). *S*-sulfonate and nitroxyl (HNO) are formed. HNO is consumed by the second sulfite ion in the next step to generate hydroxylamine-*N*-sulfonate (reaction 22). Indeed, it has been reported that sulfite reacts with HNO to form hydroxylamine-*N*-sulfonate.[75] The inability to detect HNO intermediate using electron paramagnetic resonance (EPR) spectroscopy by trapping with metmyoglobin[12] may due to the fast reaction of HNO with sulfite. *In vivo*, the released HNO in reaction 21 would react rapidly with thiols, which are present at high physiological concentrations compared to sulfite, converting them to sulfinamides ($RS(=O)NH_2$) and sulfinates (RSO_2^-).[13] Nucleophilic attack with concerted protonation in reaction 21 circumvents the difficulty posed by the fact that the nitroxyl anion (NO^-) is a triplet in the ground state, and is spin-forbidden to act as leaving group.[48,76] Singlet excited-state nitroxyl anion is too energetic to be formed under our reaction conditions. Because only one step was observed in the single-molecule experiment (Figure 2.17), P7S-N(OH)-SO_3^- and $P7SSO_3^-$ would have to have similar conductance values for our observations to be consistent with this pathway. Further in the similar *S*-thiolation reaction, the immediate products are the disulfide and HNO.[21] Therefore, all things considered, we favour the second mechanism for *S*-sulfonation.

The depletion of RSNO and the proposed formation of HNO manifest possible pathways for the asthmatic effect of sulfite. GSNO and other protein *S*-nitrosothiols are present in the human airway. GSNO (0.2–0.5 μM in normal lungs)[5] exerts bronchodilatory effects by transnitrosating a range of ion channels and receptor systems, leading to airway smooth muscle relaxation.[4] While the mechanisms for

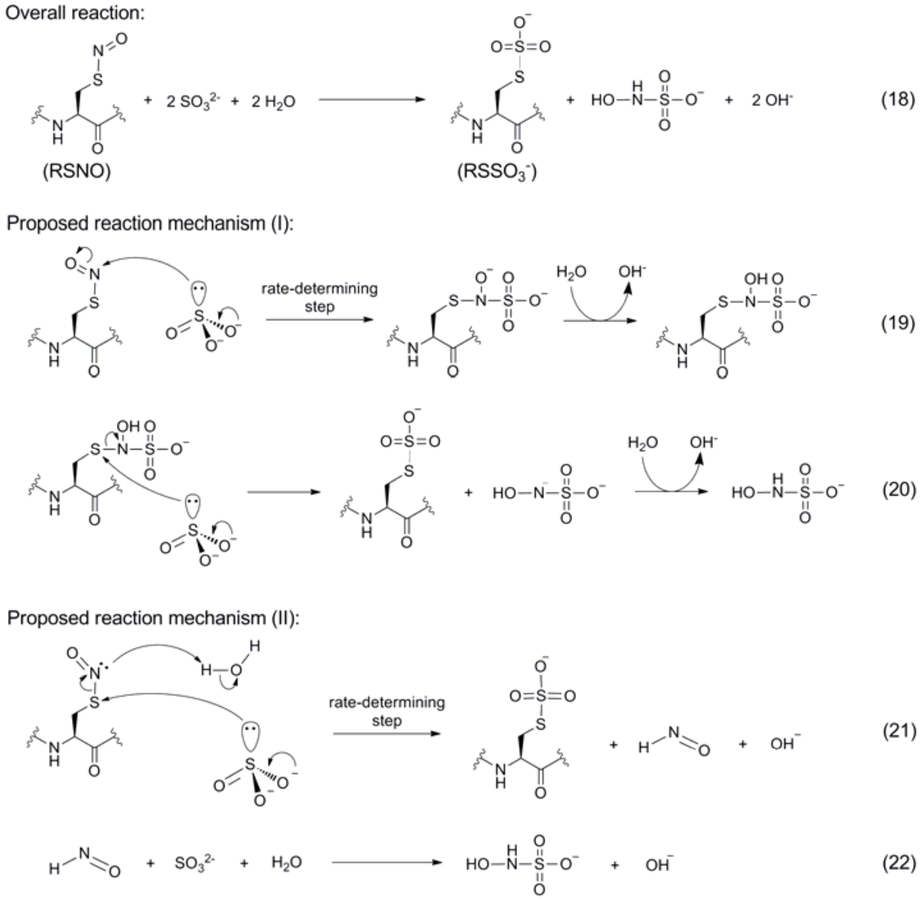

Figure 2.19. *Proposed reaction mechanisms for S-sulfonation of RSNO by sulfite ion. The overall reaction observed at pH 7.4, 22 °C is shown in reaction 18. The first proposed mechanism involves the nucleophilic attack at the N atom of RSNO by sulfite ion in the rate-determining step (reaction 19). The second proposed mechanism involves nucleophilic attack at the S atom of RSNO by sulfite ion with concerted protonation at the RSNO nitrogen atom (reaction 21) to form an S-sulfonate ($RSSO_3^-$) and HNO in a rate-determining step.*

sulfite allergy remain unclear,[77] we propose that the consumption of GSNO (k_2 = 264 ± 5 $\mathrm{M^{-1}s^{-1}}$ at pH 7.4, 37°C) and protein-SNO in the human airway might terminate the signaling cascade for airway dilation. The proposed generation of HNO, which has different physiological effects to free NO,[13] may alter the normal nitrergic signaling cascade by irreversibly modifying cysteine thiol group on key enzymes to sulfinamides ($RS(=O)NH_2$) or sulfinates (RSO_2^-), leading to breathing difficulties. The importance of this pathway deserves further investigations.

2.4.3 Acidic environment favours *S*-thiolation over transnitrosation

Nitric oxide signaling cascade is believed to propagate specifically through controlled protein-protein interactions[22,23] (see Section 2.1.2). Protein post-translational modifications by "NO" species include transnitrosation and *S*-thiolation. Factors controlling transnitrosation have been widely investigated, but the regulation of *S*-thiolation is still unclear. We found that *S*-thiolation by GSNO was enhanced at pH 7.4 compared to pH 8.4 with respect to the competing transnitrosation (Table 2.2). This can be explained by the different mechanisms of *S*-thiolation versus transnitrosation. *S*-Thiolation requires the concomitant protonation of RSNO during the attack of thiolate (similar to reaction 21 in Figure 2.19), so that HNO can act as the leaving group. In contrast, transnitrosation does not involve protonation during the attack of thiolate (Figure 2.11a). Therefore, we propose that the acidity of the protein microenvironment around the reacting thiolate and RSNO might dictate whether transnitrosation or *S*-thiolation takes place, with *S*-thiolation favored by lower pH. The ability of the nanoreactor to monitor directly two competing reactions (transnitrosation and *S*-thiolation) was critical for this analysis.

2.5 Conclusions

In this chapter, RSNO chemistry was investigated at the single-molecule level for the first time. Synthetic fluorogenic RSNO[78] is not required with the nanoreactor approach. Moreover, we have overcome the difficulties of observing the small current change associated with the formation of RSNO by applying a higher transmembrane potential (+150 mV). By this means, transnitrosation, *S*-glutathionylation, *S*-sulfonation and hydrolysis of RSNO to the short-lived sulfenic acid (RSOH) and the subsequent oxidation to sulfinic acid (RSO_2H) were studied. We have set a limit on the lifetime of the proposed nitroxyl disulfide intermediate in transnitrosation (<200 μs), investigated the pH-dependence of two competing NO signalling pathways (*S*-glutathionylation and transnitrosation) and pinned down the importance of HNO release by the nucleophilic attack on *S*-nitrosothiols. The depletion of RSNO by sulfite ion and the concomitant generation of HNO might be responsible for sulfite's bronchoconstrictive effect.

A new area of exploration might be the selenium analogs of RSNO, i.e. *Se*-nitrososelenol (RSeNO).[79] RSeNO is proposed as an intermediate in the inactivation of glutathione peroxidase (GPx) by nitric oxide donors in cells.[80] RSeNO are more unstable than RSNO. This has inhibited a detailed study of its chemistry. With our single-channel recording technique and the isolated reaction site in the α-hemolysin pore, the chemistry of RSeNO might be investigated either by reacting a small molecule RSeNO with PSH, or by using an engineered α-hemolysin pore that carries a selenocysteine residue.

Apart from NO, other gases, e.g. carbon monoxide (CO) and hydrogen sulfide (H_2S), have been shown to be synthesized naturally in cells and act as signaling molecules (gasotransmitters).[81] The chemical biology of these gases might be explored with the nanoreactor technique, such as by attaching a heme group inside the α-hemolysin pore.

2.6 Materials and Methods

2.6.1 General Information

Aqueous solutions were prepared with Milli-Q quality water (Millipore Corporation). The pH values of aqueous solutions were measured with an Orion 8172BNWP ROSS Sure-Flow pH electrode (Thermo Scientific) calibrated at 22 ± 1°C with standard buffers. pD values were measured with pH electrode using the equation pD = pH meter reading + 0.4.[82]

^{1}H NMR, ^{13}C NMR and ^{15}N NMR spectra were recorded on Bruker DPX400 (^{1}H: 400 MHz), Bruker AV400 (^{1}H: 400 MHz; ^{13}C: 100 MHz) or Bruker DRX500 (^{15}N: 50 MHz) spectrometers. All NMR experiments were performed in D_2O or CD_3OD at 22 ± 1°C unless otherwise stated. Chemical shifts are reported as parts per million (ppm) on the δ scale by using solvent residual peaks as internal standards for ^{1}H and ^{13}C NMR, or with liquid ammonia (referenced as 0 ppm) as the external standard for ^{15}N NMR. ^{15}N NMR was measured with an at least 5-s relaxation delay. Coupling constants (J) are reported in Hz.

Low resolution mass spectra were recorded on a Waters LCT Premier mass spectrometer using electrospray ionization (ESI). High resolution mass spectra were recorded using negative ionization mode ESI on a Bruker FT0ICR-MS Apex Qe (9.4 T) mass spectrometer. m/z values are reported in Daltons.

Conventional UV-visible absorption spectra were collected with a 1 cm-path-length cuvette by using a Varian Cary 400 spectrophotometer at 22 ± 1 °C. Stopped-flow UV-visible measurements were carried out with an SX20 stopped-flow spectrometer (Applied Photophysics) with the monochromator set at 334 nm for monitoring GSNO or with a photodiode array at 180–720 nm, at 22 ± 1°C or 37 ± 1°C, as stated. The data were processed by Pro-Data viewer 4.0 (Applied Photophysics) and OriginPro 8.1 SR3 (OriginLab Corporation).

Unless otherwise stated, all reagents were purchased from commercial suppliers and used without further purification.

2.6.2 Synthetic procedures

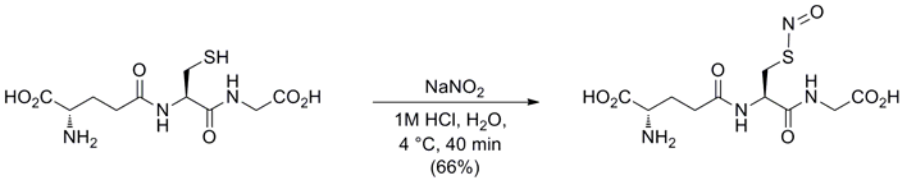

***S*-Nitrosoglutathione (GSNO).**[83,84] Sodium nitrite (0.69 g, 10 mmol) was added in one portion to a stirred solution of reduced glutathione (3.1 g, 10 mmol) in ice-cold degassed water (20 mL) and 1 M HCl (10 mL). After stirring on ice for 40 min, acetone (20 mL) was added to the reaction mixture and the suspension that formed was stirred for another 10 min at 0°C. The pink solid was collected by filtration and washed once with ice-cold water (10 mL) and then three times with diethyl ether (20 mL). The solid was dried *in vacuo* to afford the desired compound (2.2 g, 66%). This GSNO·HCl salt was stored at –20°C in the dark. ^{1}H NMR (400 MHz, D_2O, pD 7.4, 2 M KCl, 80 mM sodium phosphate, 100 μM EDTA): δ 4.88 (dd, *J* = 7.2 and 5.6 Hz, C*H*CH_2S, 1H), 4.38–4.21 (m, CH_2S, 1H), 4.20–4.02 (m, CH_2S, 1H), 3.92 (t, *J* = 6.4 Hz, C*H*NH_2, 1H), 3.89 (d, *J* = 1.6 Hz, CH_2CO_2, 2H), 2.66–2.51 (m, $CH_2C\mathit{H}_2CO$, 2H), 2.35–2.18 (m, $C\mathit{H}_2CH_2CO$, 2H); ^{13}C NMR (100 MHz, D_2O, pD 7.4, 2 M KCl, 80 mM sodium phosphate, 100 μM EDTA): δ 176.9, 175.3, 174.6, 171.8, 54.8, 53.1, 44.1, 32.0, 26.8, 26.7; ESI-MS (*m/z*): $[M{-}H]^-$ calcd. for $C_{10}H_{16}N_4O_7S$, 335.07; found, 335.08 (84%); (Although this batch of GSNO had >95% purity by ^{1}H NMR, a prominent peak corresponding to GS^- at 305.07 (100%) was observed by MS. This is attributed to the decomposition of GSNO under MS conditions.); ε_{334} (2 M KCl, 80 mM MOPS, 100 μM EDTA, pH 7.4, 22°C) = 714 ± 2 $M^{-1}cm^{-1}$. ^{15}N-Labelled GSNO was synthesized similarly using sodium [^{15}N]nitrite.

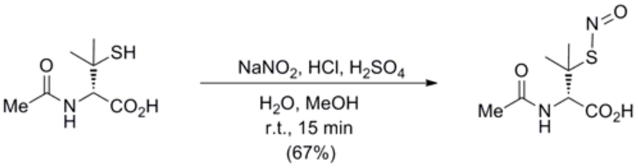

***N*-Acetyl-*S*-nitroso-D-penicillamine (SNAP).** The procedure was similar to that reported.[85] Sodium nitrite (0.71 g, 10 mmol) in water (10 mL) was added over 20 min to a vigorously stirred solution of *N*-acetyl-D-penicillamine (1 g, 5.2 mmol) in methanol:1 M HCl (1:1) (total 20 mL) containing concentrated H_2SO_4 (1 mL) at room temperature. After 15 min, the green product was separated by filtration, washed with ice-cold water and dried *in vacuo*, to give a deep green solid with red reflections (0.77 g, 67%). SNAP was stored at –20°C in the dark and is stable for several months. ^1H NMR (400 MHz, CD_3OD): δ 5.32 (s, CH, 1H), 2.04 (s, CH_3, 3H), 2.01 (s, CH_3, 3H), 1.97 (s, CH_3, 3H); ^{13}C NMR (100 MHz, CD_3OD, with small amount of *N*-acetyl-D-penicillamine): δ 173.2, 172.2, 61.1, 58.7, 27.2, 25.8, 22.3; ESI-MS (*m/z*): $[M–H]^-$ calcd. for $C_7H_{12}N_2O_4S$, 219.04; found, 219.03 (32%); (Although this batch of SNAP had >96% purity by ^1H NMR, a prominent peak corresponding to the disulfide of *N*-acetyl-D-penicillamine at 379.08 (100%) was observed by MS. This is attributed to the instability of SNAP and rapid oxidation of *N*-acetyl-D-penicillamine under MS conditions.); ε_{334} (2 M KCl, 80 mM MOPS, 100 μM EDTA, pH 7.4, 22 °C) = 1140 ± 20 $M^{-1}cm^{-1}$.

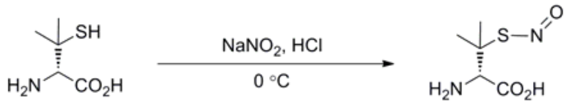

***S*-Nitroso-D-penicillamine (SPEN).**[68] The reactive SPEN for testing the activity of the cysteine thiol group in the initial experiment was generated *in situ* just before use. In an Eppendorf tube, D-penicillamine (14.9 mg, 0.1 mmol) was dissolved in water:1 M HCl (1:2) (total 0.3 mL) at 0 °C. Sodium nitrite (6.9 mg, 0.1 mmol) was added and the mixture changed from colourless to green immediately, indicative of tertiary *S*-nitrosothiol formation. The crude product mixture was diluted to 100 mM with the buffer for single-channel recording experiment and used without purification.

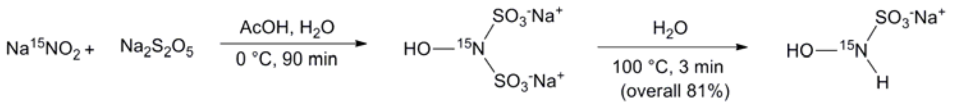

^{15}N-Labelled sodium hydroxylamine-*N*-sulfonate. Disodium [^{15}N]hydroxylamine-*N*,*N*-disulfonate[86] was first prepared by mixing sodium [^{15}N]nitrite (0.20 g, 2.9 mmol) and sodium metabisulfite (0.54 g, 2.9 mmol) in water (3.3 mL) at 0°C. Acetic acid (0.3 mL) was added in one portion and the mixture was stirred for 90 min at 0°C. The solvent was removed from the straw-coloured solution by freeze-drying. This crude disodium [^{15}N]hydroxylamine-*N*,*N*-disulfonate was hydrolyzed to the monosulfonate by treatment with boiling water (3 mL) for 3 min.[87] After cooling to room temperature, the solution was neutralized to pH 7 with 2 M NaOH. The crude product mixture was freeze dried and used for ^{15}N NMR without further purification. The content of sodium [^{15}N]hydroxylamine-*N*-sulfonate (81% (w/w)) was assessed by both the Griess assay and hydroxylamine assay (*vide infra*). ^{15}N NMR (50 MHz, D_2O, pD 7.4, 2 M KCl, 80 mM sodium phosphate, 100 μM EDTA): δ 160.4 (with $^{15}NH_2OH$ at δ 101.9).

2.6.3 Details of NMR experiments

Separate stock solutions of GSH, GSSG, GSNO, GS^{15}NO, Sodium [^{15}N]hydroxylamine-*N*-sulfonate, sodium [^{15}N]hydroxylamine-*N*,*N*-disulfonate (100 mM each) and Na_2SO_3 (1 M) were freshly prepared by dissolving the reagent in D_2O buffer (2 M KCl, 80 mM sodium phosphate, 100 uM EDTA), followed by pD-adjustment to 7.4.[82]

In ^{1}H NMR titration experiments, solutions containing different molar ratio of GSNO to sulfite were made by mixing the corresponding amounts of reagents in an Eppendorf tube. The volume was brought up with the above buffer at pD 7.4, so that after dilution the concentration of the glutathione derivative was 10 mM. This mixture was transferred to an NMR tube and ^{1}H NMR spectroscopy was performed within one hour.

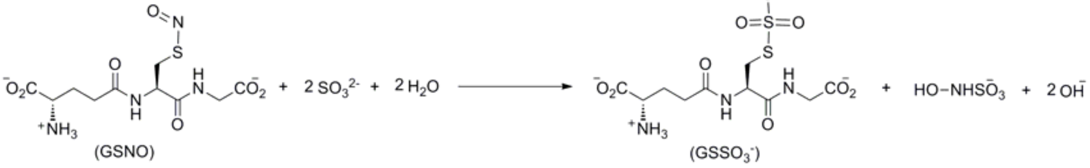

Crude *S*-sulfoglutathione ($GSSO_3H$) formed from GSNO and sulfite ion has the following spectral characteristics. ^{1}H NMR (400 MHz, D_2O, pD 7.4, 2 M KCl, 80 mM sodium phosphate, 100 μM EDTA): δ 4.90 (dd, *J* = 8.8 and 4.8 Hz, $C\mathit{H}CH_2S$, 1H), 3.87 (t, *J* = 6.4 Hz, $C\mathit{H}NH_2$, 1H), 3.83 (s, CH_2CO_2, 1H), 3.82 (s, CH_2CO_2, 1H), 3.65 (dd, *J* = 14.8 and 4.8 Hz, CH_2S, 1H), 3.47 (dd, *J* = 14.8 and 8.8 Hz, CH_2S, 1H), 2.69–2.51 (m, $CH_2C\mathit{H}_2CO$, 2H), 2.33–2.16 (m, $C\mathit{H}_2CH_2CO$, 2H); HRMS (*m/z*): [M–H]$^-$ calcd. for $C_{10}H_{17}N_3O_9S_2$, 386.0333; found, 386.0328.

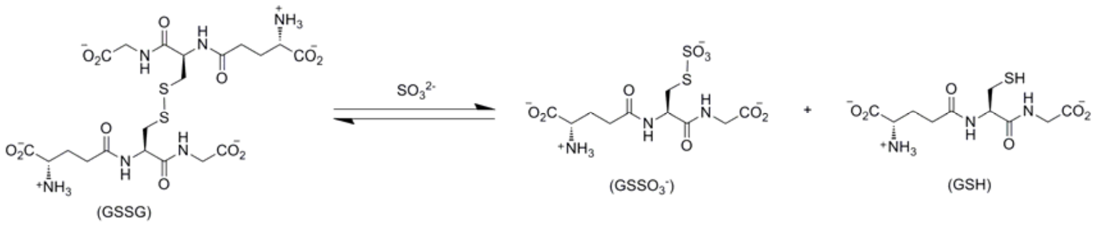

Generation of $GSSO_3^-$ from oxidized glutathione (GSSG) by sulfitolysis has been reported.[88] One mole of disulfide reacts with one mole of sulfite ion to give one mole each of *S*-sulfonate and reduced thiol. The reaction is reversible above pH 7. To obtain the reference spectrum for $GSSO_3^-$, excess sulfite ion (25 equivalents) was mixed with GSSG to give the spectrum shown in Figure 2.15b.

For ^{15}N NMR experiments, GS^{15}NO and Na_2SO_3 were mixed in 1:2 molar ratio to give a solution of 83 mM in glutathione derivative. ^{15}N-NMR measurement was performed without further dilution.

2.6.4 Saville assay for quantifying *S*-nitrosothiols

The Saville assay (Scheme 2.1) can detect *S*-nitrosothiols at concentrations as low as 10 μM.[89] Three reagent solutions are used: A: 0.5% (w/v) ammonium sulfamate in water; B: one portion of 1.0% (w/v) mercuric chloride in water mixed with four portions of 3.4% (w/v) sulfanilamide in 0.4 N HCl; C: 0.1% (w/v) *N*-naphthalen-1-ylethane-1,2-diamine dihydrochloride (NED) in 0.4 N HCl.

In a 96-well plate, solution A (5 μL) is added to the suspected *S*-nitrosothiol in water (30 μL), and mixed with a multichannel pipette. Ammonium sulfamate reacts with free nitrite ion. After 1 to 2 min at room temperature, solution B (50 μL) is added rapidly. Hg(II) ion converts *S*-nitrosothiols to nitrite, which subsequently reacts with sulfanilamide under acidic conditions to form the diazonium salt. After a further 1 to 2 min, solution C (40 μL) is added and the mixture is incubated for 5 to 10 min in the dark. Coupling of the diazonium salt with NED gives a magenta-colored azo compound. Its absorbance at 540 nm is measured with a plate reader. Calibration curves are generated using a dilution series of standard sodium nitrite solution (2 mM) in water with solution A added last.

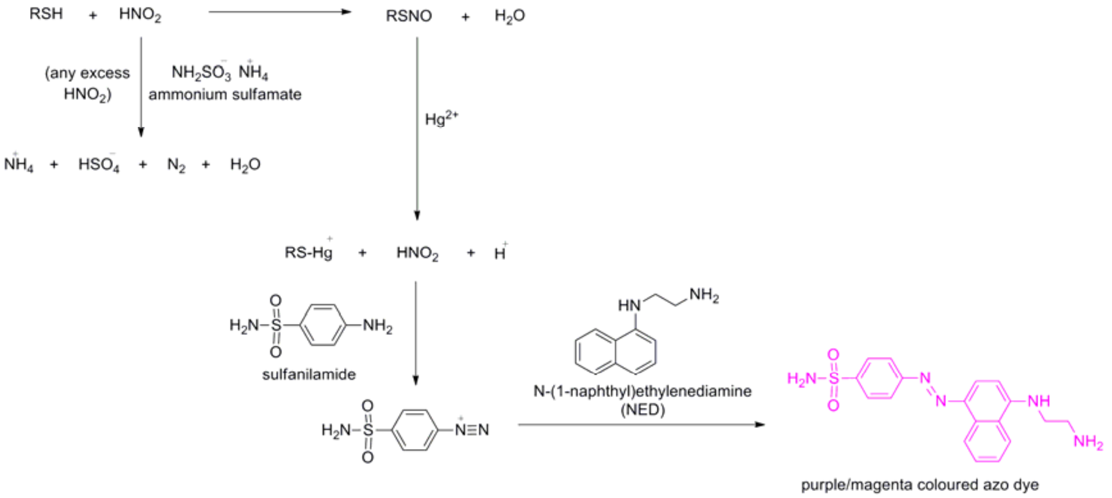

Scheme 2.1. *Principles of Saville assay.*[89]

2.6.5 Griess assay for quantification of nitrite ion

Detection and quantification of nitrite and nitrate ions are conveniently done by ion chromatography, which allows the simultaneous detection of different ions. Here, we used the colorimetric method instead to determine nitrite and nitrate (see next section) using the Griess assay.

The procedure is similar to that reported by Griess and can detect nitrite with lower limit of 2.5 μM.[90] Two reagent solutions are used: A: 1.0% (w/v) sulphanilamide and 5.0% (w/v) phosphoric acid in water; B: 0.1% (w/v) *N*-naphthalen-1-ylethane-1,2-diamine dihydrochloride (NED) in water. In a 96-well plate, solution A (50 μL) is added to the sample solution (20 μL) in water. The mixture is incubated for 5 min at room temperature in the dark. Then solution B (50 μL) is added and the mixture is allowed to stand at room temperature for 5 to 10 min in the dark. The absorbance is measured at 540 nm with a plate reader. Calibration curves are obtained using a dilution series of standard sodium nitrite solution (2 mM) in water.

2.6.6 Griess assay for the quantification of nitrate ion

The nitrate ion measurement used the same Griess assay, after conversion of the nitrate to nitrite by copper-coated cadmium.[91,92] Cadmium granules (4 g) are washed with 1 M H_2SO_4 (15 mL) for 2 min. The acid is decanted and the granules washed three times with water and then swirled in 5 mM $CuSO_4$ in 200 mM glycine (10 mL), pH 9.7, for 5 min. The $CuSO_4$ solution is removed by filtration and the granules are washed three times with the glycine buffer. The Cu-coated Cd granules are dried with filter paper and used within 10 min.

Cu-coated Cd (250–300 mg) is added to the sample (200 μL). The mixture is shaken several times and left for 90 min at room temperature. A portion of the sample (50 μL) is transferred into a 96-well plate and the procedure for nitrite ion quantification followed (Section 2.6.5). Calibration curves are generated by using standard potassium nitrate solutions in water.

2.6.7 Hydroxylamine assay

This colorimetric assay is based on the formation of green indooxine in the reaction between hydroxylamine and 8-hydroxyquinoline.[93] The lower limit of hydroxylamine that can be measured is 10 μM. Three reagent solutions are used: A: 10% (w/v) trichloroacetic acid in water; B: 1% (w/v) 8-hydroxyquinoline in ethanol; C: 1 M sodium carbonate in water.

Solution A (8 μL) and the sample (40 μL) in potassium phosphate buffer (72 μL, 100 mM), pH 6.8, are placed in a 1.5 mL Eppendorf tube. Solution B (40 μL) is added with rapid mixing and the solution is allowed to stand for 2 to 3 min at room temperature. Solution C (40 μL) is added with thorough mixing for 10 to 20 s. The mixture is heated at 95°C for 5 min, followed by cooling at room temperature for 15 min. A portion of the solution (150 μL) is transferred into a 96-well plate and the absorbance at 705 nm is measured. Calibration curves are generated by using a dilution series of a standard hydroxylamine hydrochloride solution in water.

2.6.8 Kinetic measurements in ensemble solution

Transnitrosation between GSNO (100 μM) and L-cysteine (50 to 200 μM) in buffer at pH 7.4 and 8.4 (2 M KCl, 80 mM MOPS, 100 μM EDTA), 22 ± 1°C, was followed by reverse-phase HPLC.[65] Aliquots (1 mL) were taken over a series of time points and quenched with *N*-ethylmaleimide (NEM, 400 μM). The solvent was removed by lyophilization and the residue was dissolved in water (200 μL), filtered, injected onto a Varian Polaris C8-A column and eluted isocratically with acetonitrile:water (1:99) containing 0.1% (v/v) trifluoroacetic acid (TFA) and 10 μM EDTA. The eluant was monitored at 220 and 334 nm. The area of the GSNO peak recorded at 334 nm was used for kinetic measurements.

Transnitrosation between SNAP (250 to 1000 μM) and L-cysteine (250 to 1000 μM) in buffer at pH 7.4 (2 M KCl, 80 mM MOPS, 100 μM EDTA), 22 ± 1°C, was followed with a UV-visible spectrophotometer by using the spectroscopic change at 500–600 nm.[57] At pH 8.4, the reaction was monitored with a stopped-flow UV-visible spectrophotometer (SNAP 5 to 10 mM, L-cysteine 5 to 50 mM). Rates were determined from the initial 5% of each reaction.

$$\underset{\lambda_{max} = 588\ \text{nm}}{\text{SNAP} + \text{L-cysteine}} \longrightarrow \underset{\lambda_{max} = 544\ \text{nm}}{\text{NAP} + \text{L-cysteine-SNO}}$$

S-Sulfonation of GSNO by sodium sulfite was measured by following the disappearance of GSNO at 334 nm with a stopped-flow UV-visible spectrophotometer.[68] Separate stock solutions of GSNO (1–2 mM) and sodium sulfite (200–1000 mM) were prepared by dissolving the reagents in buffer (2 M KCl, 80 mM MOPS, 100 uM EDTA), followed by pH adjustment to 7.4. 100 μL of each solution were mixed by the stopped-flow instrument. Measurements were carried out at a fixed concentration of GSNO with four different concentrations of sodium sulfite in large excess (>100-fold). Curve-fitting using Pro-Data Viewer 4.0 (Applied Photophysics) showed that the reaction is first-order in GSNO, and the pseudo first-order reaction rate constant, k_{obs} (rate = k_{obs}[GSNO]), obtained was plotted against [sulfite]. The linear-dependence of k_{obs} on [sulfite] showed that the reaction is also first-order in sulfite. The slope of the best-fit straight line gave the second-order reaction rate constant, $k_{SO3}{}^{2-}$ ($k_{obs} = k_{SO3}{}^{2-}$[sulfite]). Three repeats were done at both 22 ± 1 °C and 37 ± 1 °C.

2.6.9 Protein preparation

The heptameric *Staphylococcus aureus* α-hemolysin pores $(WT)_7$, $(WT)_6(G137C\text{-}D8)_1$ (abbreviated as PSH) and $(G137C\text{-}D8)_7$ (abbreviated as P7SH) were prepared as described earlier.[94–96] The plasmid DNA for G137C-D8 is in the RL3 background,[97] which contains six silent mutations that aid cassette mutagenesis in the region encoding the stem domain. The G137C-D8 polypeptide contains the mutation of glycine at position 137 to cysteine and an eight-aspartate tail at the C terminus to facilitate the separation of PSH from other heteroheptamers by SDS-polyacrylamide gel electrophoresis.[95,96,98]

In vitro transcription and translation (IVTT)

The proteins were expressed in the presence of [^{35}S]methionine by an *E. coli in vitro* transcription and translation (IVTT) system (*E. coli* T7 S30 Extract System for

Circular DNA, Cat. #L1130, Promega). To prepare PSH, the unpurified WT IVTT product (60 μL) was mixed with the G137C-D8 IVTT product (10 μL) and oligomerized on rabbit red blood cell membranes (rRBCM). To prepare $(WT)_7$ and P7SH, the corresponding unpurified IVTT products (50 μL) were used.

Protein oligomerization for cysteine-containing αHL

Before use, rabbit red blood cell membrane (rRBCm, 3 μL, 4.2 mg membrane protein mL^{-1}) was suspended in MBSA buffer (500 μL, 10 mM MOPS, 0.1% (w/v) bovine serum albumin, 150 mM NaCl, pH 7.4) containing 2 mM DTT. The membrane suspension was centrifuged for 10 min at 4°C and 25,000 × g and the supernatant was removed. The washed membrane was then resuspended with the IVTT protein mixture and incubated for 1.5 h at 37°C. Afterwards, the membrane was centrifuged, resuspended in MBSA containing 2 mM DTT (400 μL) and pelleted by centrifugation for 10 min at 4 °C and 25,000 × g. After removal of the supernatant, the pellet containing the assembled heptamers was solubilized in Laemmli sample buffer[99] (35 μL) containing 710 mM β-mercaptoethanol. Before loading the samples, the 5% SDS-polyacrylamide gel (SDS-PAGE) was pre-run with 1X Tris-Glycine-SDS (TGS) running buffer containing 1 mM sodium thioglycolate for 30 min at 200 V. The gel and buffer were allowed to cool to room temperature prior to sample loading. The samples were then loaded and the gel was run with the above sodium thioglycolate-containing TGS buffer for 15 h at 50 V and room temperature. After electrophoresis, the gel was dried under vacuum without heating onto Whatman 3M filter paper. The dried gel was exposed to photographic film for 5 h and the developed film was used to locate the target protein bands on the gel (Figure 2.20). The protein bands were

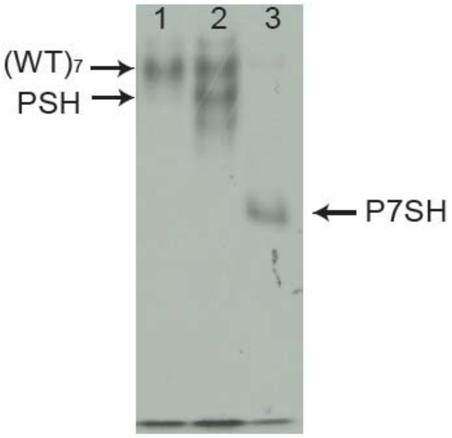

Figure 2.20. *5% SDS-PAGE gel showing the bands of various αHL oligomers. Lane 1: Heptamer made from wild-type monomer (WT) only. Lane 2: Heptamers formed from wild-type monomer and G137C-D8 monomer mixed in 6:1 ratio. Lane 3: Heptamer comprising G137C-D8 monomer only.*

excised and rehydrated in TE buffer (300 μL, 10 mM Tris.HCl, 1 mM EDTA, pH 8.0) containing 5 mM DTT for 40 min at room temperature. The paper was removed and the gel was crushed and filtered through a cellulose micro spin column (Microfilterfuge tubes, Cat. #7016-024, Rainin) for 60 min at 4°C and 25,000 × g. Aliquots of purified protein were stored at -80°C.

2.6.10 Planar lipid bilayer recordings

Electrical recordings was carried out with planar bilayers of 1,2-diphytanoyl-*sn*-glycero-3-phosphocholine (DPhPC, Avanti Polar Lipids) formed across an orifice (100–150 μm in diameter) in a 25-μm thick Teflon film (Goodfellow, Cambridge, Cat. #FP301200/10) by the method of Montal and Mueller.[100] The Teflon film separates the planar lipid bilayer apparatus into two 1 mL compartments. To form the planar bilayer, the film around the orifice was first pre-treated with 10% (v/v) hexadecane in hexane (for experiments below 18 °C, 5% (v/v) squalene in pentane was used instead). Buffer solution (1 mL) was added to each compartment, followed by 1 to 2 drops of

1% (w/v) DPhPC in *n*-pentane onto the solution surface. The pentane was allowed to evaporate and a bilayer was formed by lowering and raising the buffer level in both compartments across the orifice. A potential was applied across the bilayer with Ag/AgCl electrodes in bridges formed from 3 M KCl in 3% low-melting agarose. The capacitance of the bilayer was checked and its stability was monitored for 1 min at +40 mV. Heptameric α-hemolysin was then added to the *cis* compartment (ground) near the orifice and the applied voltage was increased to +140 mV. The *cis* solution was stirred until a single channel appeared, and then the solution was replaced (0.4 mL × 3) to avoid the insertion of additional pores. Current recordings were performed at 22 ± 1°C with a patch clamp amplifier (Axopatch 200B, Molecular Devices). Unless otherwise stated, the signal was filtered with a low-pass Bessel filter (80 dB/decade) with a corner frequency of 2 kHz, and sampled at 20 kHz with a DigiData 1320 A/D converter (Molecular Devices).

For proteins containing cysteine residues, the buffer was deoxygenated by purging with N_2 for 15 to 20 min every day before use. The agarose bridges were necessary because silver ions leach from bare Ag/AgCl electrodes into high chloride buffer solutions and react with thiol groups of the αHL pore. Freshly thawed aliquots of protein were used each day. Stock GSNO (100 mM), SNAP (100 mM), DTT (1 M) and DTNB (100 mM) solutions were freshly prepared every three hours in the buffer solution used for the single-channel recording, followed by pH titration to pH 7.4 or 8.4. These first three solutions were kept on ice.

2.6.11 Data analysis

The current traces were filtered digitally with a 50 Hz low-pass Gaussian filter in Clampfit 9.2 (Molecular Devices). Events were detected by using the single channel search feature. The mean dwell times ($\bar{\tau}$) of the current states were determined by fitting dwell-time histograms to single exponential functions. At least 40 events were used to determine the mean dwell time under each condition. The processed data were plotted by using OriginPro 8.1 SR3 (OriginLab Corporation).

2.6.12 Calculation of single-molecule reaction rate constant (k_t)

To take into account the existence of more than one reactive thiol groups in P7SH in the calculation of the second-order rate constants for transnitrosation (k_t), the following treatment of the observed inter-event intervals was carried out.

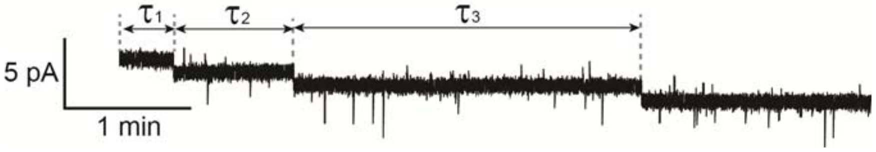

Figure 2.21. *An example trace showing the reaction of GSNO (cis, 2 mM) with P7SH in 2 M KCl, 80 mM MOPS, 100 μM EDTA, pH 7.4, +150 mV at 22 °C. Three transnitrosations are observed and the inter-event lifetimes are labelled as* τ_1, τ_2 *and* τ_3.

In Figure 2.21,

Number of transnitrosations + *S*-thiolations observed = 3 + 0.

The number of transnitrosations and *S*-thiolations observed in an experiment was taken to be the total number of reactive thiol groups present initially within the lumen of the pore. This is because some of the seven thiol groups were unreactive, presumably due to oxidation (see below, Figure 2.23 and Table 2.5). In the example above, four thiols were assumed to be oxidized and unreactive. Complete reaction of all the available thiols in each experiment was ensured by allowing at least 30 min for reaction after the first addition of RSNO (1–4 mM, *cis*). Then, more RSNO (10 mM, *cis*) was added and additional reactions were sought over 20 min. Only the dwell times of reactions observed before the second addition were used, while the total number of reactions observed after first and second additions were taken as the total number of reactive thiol groups present initially.

For a reaction such as transnitrosation, which in ensemble measurements has a first-order dependence on the concentration of thiol, the probability of reaction within the nanoreactor (per unit time) is directly proportional to the number of reactive thiol groups within the lumen. Therefore to derive rate constants from mean inter-event intervals (τ_{mean}), the observed intervals were multiplied by the number of remaining reactive thiols groups. In the example shown above, the τ values are: $3\tau_1$, $2\tau_2$ and τ_3.

The mean dwell times (τ_{mean}) were obtained by fitting the dwell-time histograms (obtained from all of the statistically adjusted τ values from different repeats) to single-exponential functions with Clampfit (Figure 2.22). The second-order rate constant, k_t, for transnitrosation (rate = k_t[RSNO][R'SH]) was calculated by using the equation $k_t = 1/(\tau_{mean}[RSNO])$ (Table 2.2).

In the above calculation, we have assumed that each thiol group in P7SH reacts independently. Sulfur atoms on Cys-137 on adjacent subunits in P7SH are on average separated by 8.8 Å (Pymol). As *S*-nitrosothiol is a small neutral functional group (the S–N and N–O bond lengths are ~1.8 Å and ~1.2 Å, respectively),[101,102] each transnitrosation on P7SH was assumed to be independent, i.e. previous reaction(s) do not affect subsequent reactions. On the other hand, transnitrosations observed after *S*-glutathionylation were excluded from the calculation above, because the change in the electrostatic and steric environment inside the pore after the covalent attachment of glutathione was expected to alter subsequent reaction rates.

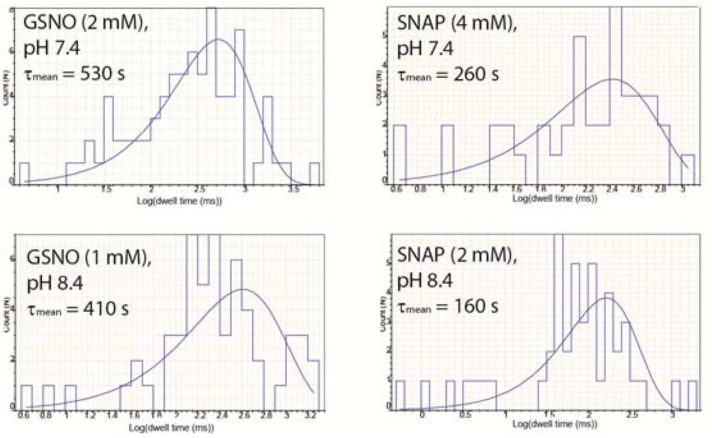

Figure 2.22. *Curve-fitting of the dwell-time histograms (obtained from all of the statistically adjusted* τ *values from different repeats) to single-exponential functions with Clampfit. The* τ_{mean} *value obtained is shown on each histogram and used for calculating the reaction rate constants summarized in Table 2.2.*

Table 2.4. *Mean dwell times (*τ_{mean}*) of transnitrosations on P7SH.*

	τ_{mean} (s)	**GSNO**	**SNAP**
pH 7.4	Clampfit [a]	530 [b]	260 [d]
	Arithmetic Mean	530 [b]	270 [d]
pH 8.4	Clampfit [a]	410 [c]	160 [e]
	Arithmetic Mean	400 [c]	140 [e]

[a] *By fitting to a single-exponential curve using Clampfit (see Figure 2.22).*

[b] *With 2 mM GSNO;* [c] *with 1 mM GSNO;* [d] *with 4 mM SNAP;* [e] *with 2 mM SNAP.*

2.6.13 Reaction rate constant (k'_t) with respect to thiolate

Thiolate anion is the active species in transnitrosation (Figure 2.11a).[64] To convert the total thiol concentration ($[RSH]_0$)-dependent k_t values in Table 2.2 into the thiolate concentration ($[RS^-]$)-dependent k'_t values (Table 2.3), the following calculations were employed:

$K_a = [H^+][RS^-] / [RSH]$

Therefore, $[RSH] / [RS^-] = [H^+] / K_a = 10^{pKa-pH}$ … (eq. 1)

The overall concentration $[RSH]_0$, is the sum of the concentrations of thiol and thiolate present at equilibrium, i.e.

$[RSH]_0 = [RSH] + [RS^-]$ … (eq. 2)

$\text{Rate} = k_t\,[RSH]_0[R'SNO] = k'_t\,[RS^-][R'SNO]$

Therefore, $k'_t = k_t\,[RSH]_0 / [RS^-]$ …(eq. 3)

Substituting equations (1) and (2) into (3):

$$k'_t = k_t\,(10^{pKa-pH} + 1) \text{ …(eq. 4)}$$

Three assumptions were made in calculating the values in Table 2.3, (1) each thiol group in P7SH reacts independently; (2) the pK_a values of all cysteines are identical; and (3) their pK_a values are assumed to be the same as the tripeptide glutathione. The first assumption is explained in Section 2.6.12. The second assumption itself, assumes that the side chains of the seven Cys-137 residues in P7SH are pointing towards the solvent-filled lumen. The distance between sulfur atoms on Cys-137 on adjacent subunits (~8.8 Å, Pymol) is too great for dipole-dipole (SH…SH) or dipole-charge ($SH…S^-$) interactions. Under our conditions with high salt (2 M KCl), the Debye length is 2.9 Å, the charge generated by deprotonation of one thiol is shielded and assumed not to affect the next deprotonation. By putting the pK_a values for P7SH ($pK_a = 8.75$ for GSH)[103] or L-cysteine ($pK_a = 8.36$)[103] and the pH value into equation (4), k'_t values were calculated and are summarized in Table 2.3.

2.6.14 Calculation of $k_{thiolation}$

The direct calculation of the second-order rate constants of *S*-glutathionylation, $k_{thiolation}$, from single-channel recording experiments with P7SH and GSNO would be inaccurate, because of the limited number of *S*-glutathionylations observed (Table 2.2). However, an approximate value at pH 7.4 can be obtained from the second-order rate constants of transnitrosation, k_t, and the observed ratio of *S*-glutathionylation to transnitrosation:

$k_{thiolation} = k_t\,(n_{thiolation}/\,n_t)$ …(eq. 5)

Substituting the values in Table 2.2 into equation (eq. 5), we obtain

$k_{thiolation} = 1.0 \times (14/107) = 0.13\ \mathrm{M}^{-1}\mathrm{s}^{-1}$ at pH 7.4

The value at pH 8.4 is not calculated because of the scarcity of *S*-glutathionylation events at this pH (only 1 event among a total of 51 reactions, Table 2.2).

2.6.15 Amount of reactive protein cysteine thiol

Most P7SH pores underwent only three to four reactions (transnitrosation plus *S*-thiolation), with the remaining thiol groups being unreactive (Figure 2.23). This is because thiol groups are easily oxidized to form disulfides, sulfenic acid and sulfinic acid, even though considerable efforts were made to keep cysteine residues in the reduced state (reducing agents at mM concentrations were present throughout the protein preparation and the SDS-PAGE purified protein was stored in buffer containing 5 mM DTT). In a separate set of experiments with PSH, 13% of the pores were unreactive (Table 2.5), while some of the pores showed fluctuating conductance (‘noisy’, 21%), which prevented the observation of chemical reactions. In 66% of the experiments (83% excluding the ‘noisy’ PSH), PSH showed the desired reactivity towards thiol-specific reagents.

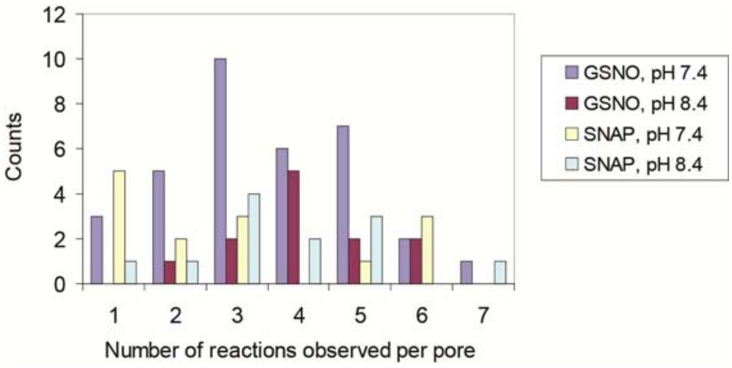

Figure 2.23. *Histogram showing the total number of reaction steps (sum of transnitrosations and S-thiolations), observed in single-channel recording experiments in which P7SH was reacted with either GSNO or SNAP at pH 7.4 or 8.4, 22 ± 1 ℃, in 2 M KCl, 80 mM MOPS, 100 μM EDTA, at +150 mV.*

Table 2.5. *Success rate of single-channel recording experiments.*[a]

Total number of experiments with PSH	76
Number of reactive PSH	50 (66%)
Number of unreactive PSH	10 (13%)
Number of 'noisy' PSH	16 (21%)

[a] *Conditions: 2 M KCl, 80 mM MOPS, 100 μM EDTA, pH 8.4, 22 ± 1 °C at +150 mV.*

2.6.16 PS-DTT intermediate

The proposed PS-DTT intermediate observed in the *S*-thiolation reaction between PSNO and DTT in Section 2.3.3 was proved by performing separate experiment which is known to generate PS-DTT. Under the same experimental conditions for transnitrosation, PS-DTT was formed by adding DTNB and DTT into opposite compartments as reported by Luchian *et al.*[66] (Figure 2.24). The PS-DTT intermediate observed in this experiment caused comparable current blockade and residence time as the proposed one formed between PSNO and DTT, proving the *S*-thiolation pathway in the breakdown of PSNO by DTT.

Notice that the lifetime of PS-DTT measured under the present conditions (7 ± 1 ms) is about 6-fold shorter than that reported previously (~40 ms) under similar buffer conditions: –50 mV and pH 8.5 in 2 M KCl, 30 mM MOPS, 100 uM EDTA, DTT (cis)/DTNB (trans) with (WT)$_6$(T117C)$_1$.[66] The breakdown of PS-DTT is a unimolecular reaction, i.e. its lifetime is independent of the concentrations of DTNB and DTT, which was shown to be the case in both the present and the earlier work. A possible reason for this dissimilarity is the very different applied potentials (+150 mV versus –50 mV). Different electrostatic forces exerted to the charged thiolate form of PS-DTT may stretch the attached DTT molecule to different extend and towards different directions. Faster cyclization of PS-DTT, for example, by the close proximity of the thiolate group to the disulfide bond in PS-DTT may be more favourable under the high applied voltage (+150 mV). Although both cysteine mutants employed in the present work and the earlier example has a cysteine residue

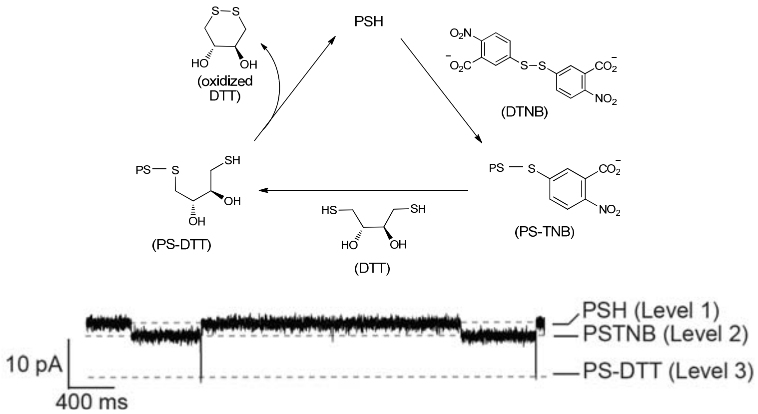

Figure 2.24. *Lifetime of PS-DTT mixed disulfide intermediate. In the study of reversible transnitrosation with spatially separated GSNO and DTT, DTT occasionally underwent S-thiolation with PSNO to form a mixed disulfide PS-DTT, which could regenerate PSH by the release of oxidized DTT. To measure the lifetime of PS-DTT, experiments with DTNB (400 μM, cis) and DTT (800 μM, trans) were performed on PSH as illustrated. Conditions: 2 M KCl, 80 mM MOPS, 100 μM EDTA, pH 8.4, at +150 mV and 22 ± 1 °C. ΔI_{12} and ΔI_{23} are –2.5 ± 0.1 pA and –7.8 ± 0.2 pA (n = 2), respectively. (ΔI_{12} denotes the change in current in going from level 1 to level 2, etc.). From this disulfide exchange experiment, the mean dwell time of the PS-DTT intermediate was found to be 7 ± 1 ms (n = 2).*

located in the β barrel, we cannot rule out the influence of the small difference in local protein environment on the reaction rate.

2.6.17 Quantification of the products in *S*-sulfonation

In *S*-sulfonation between RSNO and sulfite ion (Section 2.3.4), mass spectrometry and ^{15}N NMR analysis have confirmed the formation of hydroxylamine-*N*-sulfonate. To determine the equivalent of this product formed per mole of RSNO, hydroxylamine-*N*-sulfonate in the crude product mixture was converted into other small nitrogen-containing species, such as nitrite or hydroxylamine (NH_2OH), followed by the quantification using different assays (Sections 2.6.4–2.6.7). These assays also confirmed the formation of hydroxylamine-*N*-sulfonate, instead of the *O*-isomer (hydroxylamine-*O*-sulfonate).

Hydroxylamine-*N*-sulfonate and hydroxylamine-*O*-sulfonate undergo alkaline and acid hydrolysis as depicted in Figure 2.25. In acid hydrolysis (1 M HCl, 85°C, 2 h), both isomers form one equivalent each of hydroxylamine and hydrogen sulfate ion (reactions 2 and 4).[104] However, different products are produced upon alkaline hydrolysis (1 M KOH, 85°C, 5 h). Hydroxylamine-*N*-sulfonate produces one-third of an equivalent of nitrite ion after alkaline hydrolysis (reaction 1),[105] while hydroxylamine-*O*-sulfonate does not yield nitrite (reaction 3).[106] So the two isomers can be distinguished by alkaline hydrolysis, followed by the Griess assay for the quantification of nitrite.[90] Note that the other product formed in the *S*-sulfonation of GSNO, the *S*-sulfoglutathione ($GSSO_3^-$), is stable towards these two hydrolyses. So its presence in the crude product mixture does not interfere with the above characterization.

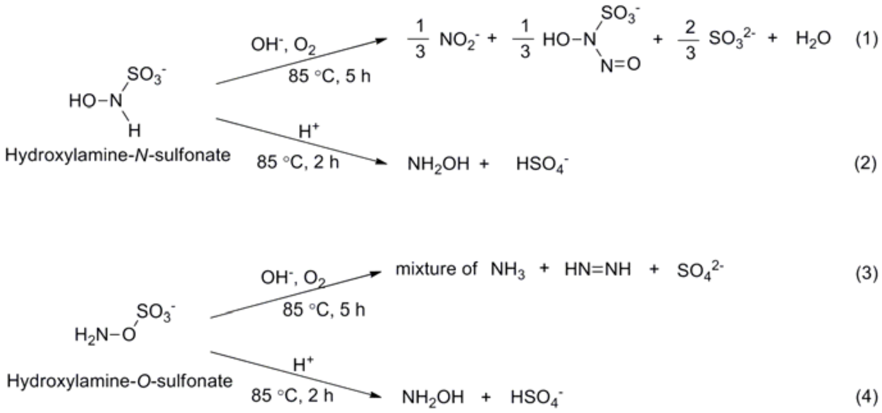

Figure 2.25. *Alkaline and acid hydrolysis of hydroxylamine sulfonate isomers. Different products are formed in the alkaline hydrolysis of the N-isomer and the O-isomer of hydroxylamine sulfonates. These helped to identify the final product in the S-sulfonation of RSNO by sulfite, which was found to be the N-isomer.*

Table 2.6. *Quantification of nitrogen-containing products produced after different treatments of the crude S-sulfonation products.*[a]

	Crude reaction mixture	**Acid-Hydrolyzed** [b]	**Alkaline-Hydrolyzed** [a]
NO_2^- [d]	0.5 ± 0.1%	0.4 ± 0.2%	36 ± 7%
NH_2OH [e]	0.9 ± 0.4%	97 ± 14%	0.8 ± 0.1%
N_2O or N_2 [f]	Undetectable	ND [g]	ND [g]

[a] *GSNO and Na_2SO_3 were mixed in a 1:2 ratio (50 mM to 100 mM) in 2 M KCl, 80 mM MOPS, 100 μM EDTA, pH 7.4, 22 ± 1 ℃. The mixture was allowed to stand at 22 °C for 10 min to ensure complete reaction. All percentages are relative to the initial amount of GSNO.*

[b] *The crude reaction mixture was treated with acid (1 M HCl, 85℃, 2 h) before assay.*

[c] *The crude reaction mixture was treated with base (1 M KOH, 85℃, 5 h) before assay.*

[d] *Griess assay by azo dye formation from sulfanilamide and N-naphthalen-1-ylethane-1,2-diamine (NED). Values were averaged from three repeats.*

[e] *Hydroxylamine assay by indooxine formation from 8-hydroxyquinoline. Values were averaged from three repeats.*

[f] *Determined by gas chromatography.*

[g] *ND = not determined.*

The results summarized in Table 2.6 support the formation of one equivalent of hydroxylamine-*N*-sulfonate in *S*-sulfonation: (1) negligible amounts (<1%, relative to the initial GSNO) of nitrite ion and hydroxylamine were detected in the nonhydrolyzed crude product mixture, (2) ~0.3 mole (36 ± 7%) of nitrite ion in the alkaline hydrolysis product and (3) ~1 mole (97 ± 14%) of hydroxylamine were detected in the acid hydrolysis product. The identity of the hydroxylamine-sulfonate isomer found here is in agreement with that determined by ^{15}N NMR experiment (Figures 2.15d and 2.16).

2.7 References

1. Switzer, C. H.; Flores-Santana, W.; Mancardi, D.; Donzelli, S.; Basudhar, D.; Ridnour, L. A.; Miranda, K. M.; Fukuto, J. M.; Paolocci, N.; Wink, D. A. *Biochim. Biophys. Acta* **2009**, *1787*, 835–840.
2. Nakamura, T.; Wang, L.; Wong, C. C.; Scott, F. L.; Eckelman, B. P.; Han, X.; Tzitzilonis, C.; Meng, F.; Gu, Z.; Holland, E. A.; Clemente, A. T.; Okamoto, S.; Salvesen, G. S.; Riek, R.; Yates, J. R. 3rd, Lipton, S. A. *Mol. Cell* **2010**, *39*, 184–195.
3. Brown, G. C. *Nitric Oxide* **2010**, *23*, 153–165.
4. Gaston, B.; Singel, D.; Doctor, A.; Stamler, J. S. *Am. J. Respir. Crit. Care Med.* **2006**, *173*, 1186–1193.
5. Que, L. G.; Yang, Z.; Stamler, J. S.; Lugogo, N. L.; Kraft, M. *Am. J. Respir. Crit. Care Med.* **2009**, *180*, 226–231.
6. Bogdan, C. *Nat. Immunol.* **2011**, *2*, 907–916.
7. Fleming, I.; Busse, R. *J. Mol. Cell. Cardiol.* **1999**, *31*, 5–14.
8. Hughes, M. N. *Methods Enzymol.* **2008**, *436*, 3–19.

9. Bellamy, T. C.; Wood, J.; Garthwaite, J. *Proc. Natl. Acad. Sci. U. S. A.* **2002**, *99*, 507–510.
10. Kim, S. F.; Huri, D. A.; Snyder, S. H. *Science* **2005**, *310*, 1966–1970.
11. Seth, D.; Stamler, J. S. *Curr. Opin. Chem. Biol.* **2011**, *15*, 129–136.
12. Irvine, J.C.; Ritchie, R. H.; Favaloro, J. L.; Andrews, K. L.; Widdop, R. E.; Kemp-Harper, B. K. *Trends Pharmacol. Sci.* **2008**, *29*, 601–608.
13. Flores-Santana, W.; Switzer, C.; Ridnour, L. A.; Basudhar, D.; Mancardi, D.; Donzelli, S.; Thomas, D. D.; Miranda, K. M.; Fukuto, J. M.; Wink, D. A. *Arch. Pharm. Res.* **2009**, *32*, 1139–1153.
14. Flores-Santana, W.; Salmon, D. J.; Donzelli, S.; Switzer, C. H.; Basudhar, D.; Ridnour, L.; Cheng, R.; Glynn, S. A.; Paolocci, N.; Fukuto, J. M.; Miranda, K. M.; Wink, D. A. *Antioxid. Redox Signal.* **2011**, *14*, 1659–1674.
15. Martínez, M. C.; Andriantsitohaina, R. *Antioxid. Redox Signal.* **2009**, *11*, 669–702.
16. Stuehr, D. J.; Santolini, J.; Wang, Z.-Q.; Wei, C.-C.; Adak, S. *J. Biol. Chem.* **2004**, *279*, 36167–36170.
17. Aguirre, E.; Rodriguez-Juarez, F.; Bellelli, A.; Gnaiger, E.; Cadenas, S. *Biochim. Biophys. Acta* **2010**, *1797*, 557–565.
18. Hill, B. G.; Dranka, B. P.; Bailey, S. M.; Lancaster, J. R. Jr.; Darley-Usmar, V. M. *J. Biol. Chem.* **2010**, *285*, 19699–19704.
19. Gordge, M. P.; Hothersall, J. S.; Neild, G. H.; Dutra, A. A. *Br. J. Pharmacol.* **1996**, *119*, 533–538.
20. Martínez-Ruiz, A.; Lamas, S. *Cardiovas. Res.* **2007**, *75*, 220–228.

21. Wong, P. S.-Y.; Hyun, J.; Fukuto, J. M.; Shirota, F. N.; DeMaster, E. G.; Shoeman, D. W.; Nagasawa, H. T. *Biochemistry* **1998**, *37*, 5362–5371. (correction p 18129)
22. Stamler, J. S.; Hess, D. T. *Nat Cell Biol* **2010**, *12*, 1024–1026.
23. Kornberg, M. D.; Sen, N.; Hara, M. R.; Juluri, K. R.; Nguyen, J. V.; Snowman, A. M.; Law, L.; Hester, L. D.; Snyder, S. H. *Nature Cell Biol.* **2010**, *12*, 1094–1100.
24. Carver, J.; Doctor, A.; Zaman, K.; Gaston, B. *Methods Enzymol.* **2005**, *396*, 95–105.
25. Zhang, Y.; Hogg, N. *Am. J. Physiol. Lung Cell Mol. Physiol.* **2004**, *287*, L467–474.
26. Keszler, A.; Zhang, Y.; Hogg, N. *Free Radical Biol. Med.* **2010**, *48*, 55–64.
27. Koppenol, W. H. *Inorg. Chem.* **2012**, *51*, 5637–5641.
28. Marino, S. M.; Gladyshev, V. N. *J. Mol. Biol.* **2010**, *395*, 844–859.
29. Stamler, J. S. *Circ. Res.* **2004**, *94*, 414–417.
30. Dalle-Donne, I.; Rossi, R.; Colombo, G.; Giustarini, D.; Milzani, A. *Trends Biochem. Sci.* **2009**, *34*, 85–96.
31. Adak, S.; Wang, Q.; Stuehr, D. J. *J. Biol. Chem.* **2000**, *275*, 33554–33561.
32. Fukuto, J. M.; Dutton, A. S.; Houk, K. N. *ChemBioChem* **2005**, *6*, 612–619.
33. Dicks, A. P.; Li, E.; Munro, A. P.; Swift, H. R.; Williams, D. L. H. *Can. J. Chem.* **1998**, *76*, 789–794.
34. Dalle-Donne, I.; Milzani, A.; Gagliano, N.; Colombo, R.; Giustarini, D.; Rossi, R. *Antioxid. Redox Signaling* **2008**, *10*, 446–473.
35. Reddie, K. G.; Carroll, K. S. *Curr. Opin. Chem. Biol.* **2008**, *12*, 746–754.
36. Benhar, M.; Forrester, M. T.; Stamler, J. S. *Nat. Rev. Mol. Cell Biol.* **2009**, *10*, 721–732.

37. Fukuto, J. M.; Cho, J. Y.; Switzer, C. H. in *Nitric oxide: biology and pathobiology*; Ignarro, L. J. eds; Academic Press, 2000; pp 23–41.
38. Foster, M. W.; Hess, D. T.; Stamler, J. S. *Trends Mol. Med.* **2009**, *15*, 391–404.
39. Miller, M. R.; Megson, I. L. *Br. J. Pharmacol.* **2007**, *151*, 305–321.
40. Nauser, T.; Koppenol, W. H. *J. Phys. Chem. A* **2002**, *106*, 4084–4086.
41. Gow, A. J.; Burek, D. G.; Ischiropoulos, H. *J. Biol. Chem.* **1997**, *272*, 2841–2845.
42. Goldstein, S.; Czapski, G. *J. Am. Chem. Soc.* **1996**, *118*, 3419–3420.
43. Malinski, T., Taha, Z., Grunfeld, S., Patton, S., Kapturczak, M., and Tomboulian, P. *Biochem. Biophys. Res. Commun.* **1993**, *193*, 1076–1082.
44. Bartberger, M. D.; Houk, K. N.; Powell, S. C.; Mannion, J. D.; Lo, K. Y.; Stamler, J. S.; Toone, E. J. *J. Am. Chem. Soc.* **2000**, *122*, 5889–5890.
45. Timerghazin, Q. K.; Peslherbe, G. H.; English, A. M. *Org. Lett.* **2007**, *9*, 3049–3052.
46. Williams, D. L. H. *Acc. Chem. Res.* **1999**, *32*, 869–876.
47. Zhang, Y. & Hogg, N. *Free Rad. Biol. Med.* **2005***, 38*, 831–838.
48. Shafirovich, V.; Lymar, S. V. *Proc. Natl. Acad. Sci. U.S.A.* **2002**, *99*, 7340–7345.
49. Miranda, K. M. *Coor. Chem. Rev.* **2005**, *249*, 433–455.
50. Miranda, K. M.; Paolocci, N.; Katori, T.; Thomas, D. D.; Ford, E.; Bartberger, M. D.; Espey, M. G.; Kass, D. A.; Feelisch, M.; Fukuto, J. M.; Wink, D. A. *Proc. Natl. Acad. Sci. U.S.A.* **2003**, *100*, 9196–9201.
51. Miranda, K. M.; Nims, R. W.; Thomas, D. D.; Espey, M. G.; Citrin, D.; Bartberger, M. D.; Paolocci, N.; Fukuto, J. M.; Feelisch, M.; Wink, D. A. *J. Inorg. Biochem.* **2003**, *93*, 52–60.
52. Hetrick, E. M.; Schoenfisch, M. H. *Annu. Rev. Anal. Chem.* **2009**, *2*, 409–433.

53. Jaffrey, S. R.; Erdjument-Bromage, H.; Ferris, C. D.; Tempst, P.; Snyder, S. H. *Nat. Cell. Biol.* **2001**, *3*, 193–197.
54. Forrester, M. T.; Foster, M. W.; Benhar, M.; Stamler, J. S. *Free Radical Biol. Med.* **2009**, *46*, 119–126.
55. Hao, G.; Derakhshan, B.; Shi, L.; Campagne, F.; Gross, S. S. *Proc. Natl. Acad. Sci. U.S.A.* **2006**, *103*, 1012–1017.
56. Meyer, D. J.; Kramer, H.; Özer, N.; Coles, B.; Ketterer, B. *FEBS Lett.* **1994**, *345*, 177–180.
57. Swift, H. R.; Williams, D. L. H. *J. Chem. Soc., Perkin Trans. 2* **1997**, 1933–1935.
58. McAninly, J.; Williams, D. L. H.; Askew, S. C.; Butler, A. R.; Russell, C. *J. Chem. Soc., Chem. Commun.* **1993**, 1758–1760.
59. Gaston, B.; Reilly, J.; Drazen, J. M.; Fackler, J.; Ramdev, P.; Arnelle, D.; Mullins, M. E.; Sugarbaker, D. J.; Chee, C.; Singel, D. J. *Proc. Natl. Acad. Sci. U. S. A.* **1993**, *90*, 10957–10961.
60. Ellman, G. L. *Arch. Biochem. Biophys.* **1959**, *82*, 70–77.
61. Konorev, E. A.; Kalyanaraman, B.; Hogg, N. *Free Radical Biol. Med.* **2000**, *28*, 1671–1678.
62. Singh, R.; Lamoureux, G. V.; Lees, W. J.; Whitesides, G. M. *Methods Enzymol.* **1995**, *251*, 167–173.
63. Houk, K. N.; Hietbrink, B. N.; Bartberger, M. D.; McCarren, P. R.; Choi, B. Y.; Voyksner, R. D.; Stamler, J. S.; Toone, E. J. *J. Am. Chem. Soc.* **2003**, *125*, 6972–6976.
64. Barnett, D. J.; McAninly, J.; Williams, D. L. H. *J. Chem. Soc., Perkin Trans. 2*, **1994**, 1131–1133.
65. Hogg, N. *Anal. Biochem.* **1999**, *272*, 257–262.

66. Luchian, T.; Shin, S.-H.; Bayley, H. *Angew. Chem. Int. Ed.* **2003**, *42*, 3766–3771.

67. Harvey, S. B.; Nelsestuen, G. L. *Biochim. Biophys. Acta* **1995**, *1267*, 41–44.

68. Munro, A. P.; Williams, D. L. H. *J. Chem. Soc., Perkin Trans. 2* **2000**, 1794–1797.

69. Holder, A. A.; Marshall, S. C.; Wang, P. G.; Kwak, C.-H. *Bull. Korean Chem. Soc.* **2003**, *24*, 350–356.

70. Chan, W. W. *Biochemistry* **1968**, *7*, 4247–4254.

71. Shaw, A. J.; Gescher, A.; Tooth, D.; Linhart, I.; Farmer, P. B. *Chem. Res. Toxicol.* **1990**, *3*, 27–32.

72. Witanowski, M., Stefaniak, L.; Webb, G. A. *Annu. Rep. NMR Spectrosc.* **1993**, *25*, 1–82.

73. Perissinotti, L. L.; Turjanski, A. G.; Estrin, D. A.; Doctorovich, F. *J. Am. Chem. Soc.* **2005**, *127*, 486–487.

74. Singh, S. P.; Wishnok, J. S.; Keshive, M.; Deen, W. M.; Tannenbaum, S. R. *Proc. Natl. Acad. Sci. U. S. A.* **1996**, *93*, 14428–14433.

75. Ackermann, M. N.; Powell, R. E. *Inorg. Chem.* **1966**, *5*, 1334–1337.

76. Bartberger, M. D.; Liu, W.; Ford, E.; Miranda, K. M.; Switzer, C.; Fukuto, J. M.; Farmer, P. J.; Wink, D. A.; Houk, K. N. *Proc. Natl. Acad. Sci. U. S. A.* **2002**, *99*, 10958–10963.

77. Vally, H.; Misso, N. L.; Madan, V. *Clin. Exp. Allergy* **2009**, *39*, 1643–1651.

78. Chen, X.; Wen, Z.; Xian, M.; Wang, K.; Ramachandran, N.; Tang, X.; Schlegel, H. B.; Mutus, B.; Wang, P. G. *J. Org. Chem.* **2001**, *66*, 6064–6073.

79. Shimada, K.; Goto, K.; Kawashima, T.; Takagi, N.; Choe, Y.-K.; Nagase, S. *J. Am. Chem. Soc.* **2004**, *126*, 13238–13239.

80. Asahi, M.; Fujii, J.; Suzuki, K.; Seo, H. G.; Kuzuya, T.; Hori, M.; Tada, M.; Fujii, S.; Taniguchi, N. *J. Biol. Chem.* **1995**, *270*, 21035–21039.

81. Li, L.; Moore, P. K. *Biochem. Soc. Trans.* **2007**, *35*, 1138–1141.
82. Glasoe, P. K.; Long, F. A. *J. Phys. Chem.* **1960**, *64*, 188–190.
83. Hart, T. W. *Tet. Lett.* **1985**, *26*, 2013–2016.
84. Liebeskind, S.; Korth, H.-G.; de Groot, H.; Kirsch, M. *Org. Biomol. Chem.* **2008**, *6*, 2560–2573.
85. Field, K.; Dilts, R. V.; Ravichandran, R.; Lenhert, P. G.; Carnahan, G. E. *J. Chem. Soc., Chem. Commun.*, **1978**, 249–250.
86. Wehrli, P. A.; Pigott, F. *Org. Synth.* **1972**, *52*, 83–87.
87. Degener, V. E.; Seel, F. *Anorg. Allg. Chem.* **1956**, *285*, 129–133.
88. Cecil, R.; McPhee, J. R. *Biochem. J.* **1955**, *60*, 496–506.
89. Saville, B. *Analyst* **1958**, *83*, 670–672.
90. Griess, P. *Chem. Ber.* **1879**, *12*, 426–428.
91. Morris, A. W.; Riley, J. P. *Anal. Chim. Acta* **1963**, *29*, 272–279.
92. Cortas, N. K.; Wakid, N. W. *Clin. Chem.* **1990**, *26*, 1440–1443.
93. Frear, D. S.; Burrell, R. C. *Anal. Chem.* **1955**, *27*, 1664–1665.
94. Cheley, S.; Braha, O.; Lu, X.; Conlan, S.; Bayley, H. *Protein Sci.* **1999**, *8*, 1257–1267.
95. Shin, S.-H.; Luchian, T.; Cheley, S.; Braha, O.; Bayley, H. *Angew. Chem. Int. Ed.* **2002**, *41*, 3707–3709.
96. Shin, S.-H.; Steffensen, M. B.; Claridge, T. D. W.; Bayley, H. *Angew. Chem. Int. Ed.* **2007**, *46*, 7412–7416.
97. Wolfe, A. J.; Mohammad, M. M.; Cheley, S.; Bayley, H.; Movileanu, L. *J. Am. Chem. Soc.* **2007**, *129*, 14034–14041.
98. Howorka, S.; Cheley, S.; Bayley, H. *Nat. Biotechnol.* **2001**, *19*, 636–639.
99. Laemmli, U. K. *Nature* **1970**, *227*, 680–685.

100. Montal, M.; Mueller, P. *Proc. Natl. Acad. Sci. U.S.A.* **1972**, *69*, 3561–3566.

101. Arulsamy, N.; Bohle, D. S.; Butt, J. A.; Irvine, G. J.; Jordan, P. A.; Sagan, E. *J. Am. Chem. Soc.* **1999**, *121*, 7115–7123.

102. Timerghazin, Q. K.; Peslherbe, G. H.; English, A. M. *Phys. Chem. Chem. Phys.* **2008**, *10*, 1532–1539.

103. Carballal, S.; Alvarez, B.; Turell, L.; Botti, H.; Freeman, B. A.; Radi, R. *Amino Acids* **2007**, *32*, 543–551.

104. Candlin, J. P.; Wilkins, R. G. *J. Am. Chem. Soc.* **1965**, *87*, 1490–1494.

105. Ackermann, M. N.; Powell, R. E. *Inorg. Chem.*, **1967**, 1718–1720.

106. Steinmetz, W. E.; Robison, D. H.; Ackermann, M. N. *Inorg. Chem.* **1975**, *14*, 421–425.

Chapter 3 Silver(I)-thiolate and cadmium(II)-thiolate complexes

3.1 Introduction

3.1.1 Heavy metal-thiolate interactions *in vivo*

Metal-thiolate complexes are biologically important. Cysteine residues are commonly found in the metal binding site of proteins, such as the zinc finger proteins and the cadmium carbonic anhydrase discovered in marine diatoms.[1] The high affinity of thiolates to soft metal ions, such as Hg^{2+}, Ag^{+}, Cd^{2+}, Zn^{2+} and Pb^{2+},[2] also represents the major mechanism for the toxic effect of heavy metal ions (Hg^{2+}, Cd^{2+} and Pb^{2+}) and the antimicrobial function of silver.[3] These heavy metal ions bind to the cysteine residues on vital proteins and glutathione (GSH), thus inhibiting their normal functions. For instance, one of the proposed mechanisms for the antimicrobial property of Ag^{+} ion is through its binding to GSH in bacteria. This decreases the GSH/GSSG ratio and impairs the intracellular antioxidant defense, leading to oxidative stress.[4a] Another possible pathway is the binding of Ag^{+} ion to NADH dehydrogenases (a cysteine-containing protein) in the respiratory chain. This leads to the uncoupling of ATP synthesis from respiratory control, eventually causing cell death.[4b,c]

Taking advantage of the thiophilicity of heavy metal ions, multiple cysteine-containing proteins that show even higher heavy metal affinity have evolved for the *in vivo* detoxification of heavy metal ions. For example, cytosolic heavy metal ions can be captured by the cysteine-rich protein called metallothionein (MT)[5] or pumped out by the P-type ATPase transporters.[6] These two types of proteins are discussed below.

Metallothionein

Metallothionein (MT) is a small cysteine-rich multiple metal ion-binding protein.[7] Cytosolic heavy metal ions, from the consumption of crops grown in contaminated areas or the inhalation of contaminated fumes, induce the gene expression of MT. About 30% of the amino acid residues in MT are cysteines.[5] For example, the 61 amino acid metallothionein-2 (MT-2) from rat contains 20 cysteines residues. *In vitro* study with Cd^{2+} ion showed that all of these cysteine residues participate in the binding of seven Cd^{2+} ions by forming two cadmium(II)-thiolate clusters (Figure 3.1).[8] One contains three Cd^{2+} ions held by nine cysteine residues, while the other has four Cd^{2+} ions bound by 11 cysteine residues. Each Cd^{2+} ion is tetrahedral coordinated by four sulfur atoms, which act as either μ_2-bridging ligand or terminal ligand. The metal complexes formed are then secreted into the bile by the liver or released into the blood circulation. Low amounts of heavy metals can be trapped as MT complexes and excreted via urination. Excess amounts are accumulated in kidneys and liver, leading to renal tubular dysfunction and liver damage.[9]

P-type ATPase transporters

Although Ag^+ ion and silver nanomaterials show microcidal activity[3,11] (see above), a number of Ag^+-resistant bacteria exist, including *Salmonella*, *E. coli* and *Pseudomonas*.[12,13] One common pathway for heavy metal-resistance is the active pumping of intracellular heavy metal ions into the extracellular environment by the P-type ATPases. Group IB-1 (for Cu^+ and Ag^+), group IB-2 (for Zn^{2+}, Cd^{2+} and Pb^{2+})

and group IB-3 (for Cu^{2+}, Cu^{+} and Ag^{+}) of the P-type ATPases have conserved amino acid sequences of CPC, CPC and CPH, respectively, on the sixth transmembrane fragment (H6) to allow for metal binding.[6] In addition, some of the group IB-1 and group IB-2 transporters possess the metal-binding CXXC motif (1–6 copies) at the cytoplasmic N-terminus.[6]

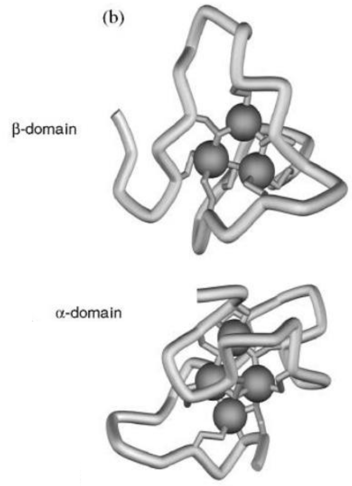

Figure 3.1. *Three-dimensional structure of the Cd^{2+} complex of rat metallothionein-2 (MT-2) ($[Cd_7]$-MT2) determined by ^{113}Cd NMR spectroscopy in aqueous solution.[8] Cd^{2+} ions are represented by dark grey spheres. The reconstituted complex contains two Cd^{2+} binding domains, one has three Cd^{2+} ions chelated by the sulfur atoms from nine cysteine residues (β domain), while the other has four Cd^{2+} ions bound by 11 cysteine residues (α domain). The discontinuity in the NMR structure is due to the lack of Nuclear Overhauser effect (NOE)-based information for the missing residues. Adapted with permission from ref. 10. Copyright (2005) by John Wiley & Sons, Ltd.*

3.1.2 Heavy metal ions as probes for studying ion channels

Ion channels are integral transmembrane proteins. They contain an ion-selective pore which allows permeant ions (e.g. K^{+} or Na^{+}) to flow through the cell membrane. By controlling the transmembrane potential this way, ion channels play vital roles in signal transduction, cognition, memory and muscle contraction. Malfunctioning ion channels are involved in many diseases, such as cystic fibrosis and heart diseases. Although membrane proteins make up a significant portion of the proteome (about

25% of all proteins) and they are the main drug targets (over 50% of small molecule drugs target at membrane proteins), far less is known about their structures compared to the soluble proteins. This is because of the challenges in their expression, purification and crystallization. This situation is improving with modern high-throughput techniques for protein preparation for X-ray crystallography.[14] But before the availability of crystal structures, much had been learned about the dynamic action of ion channels, such as the closed-open transitions (gating) and drug action.[15] This is achieved by using electrophysiologic techniques, which measure the transmembrane ionic current conducted by ion channels under applied potential.[15]

The membrane topology of ion channels has been studied using the substituted cysteine accessibility method (SCAM).[16] This method combines electrophysiologic techniques with genetic engineering, in which a series of single cysteine mutants of the target ion channel are constructed. The accessibility of the cysteine thiol group to hydrophilic thiol-specific reagents, such as methanethiosulfonate (MTS) reagents or soft metal ions (Ag^+,[17] Cd^{2+},[18,19] Zn^{2+} [18,20] and Hg^{2+} [21]) is tested. Only pore-lining cysteine residues with solvent-exposed thiol group would react and also produce blockade of the transmembrane current. The rate of the modification can be calculated from the rate of transmembrane current blockade. In general, the higher the modification rate constant, the more solvent-exposed the amino acid side chain. Comparisons of the rate constants from different mutants and different protein conformations reveal information such as the identity of pore-lining amino acid residues, the location of voltage gates and the conformational changes undergone by the pore-lining domains.

Metal ion probes have comparable size and similar water exchange rates to K^+ and Na^+ ions[22] (Table 3.1), therefore they can access sites deep in the lumen of ion channels, which may not be reachable by the larger MTS reagents.[17] Thus metal ion probes can provide more insight into ion channel structure.

The coordination chemistry of each metal ion probes is different. In addition to the thiol group on cysteine residues, the imidazole group on histidine residues can also act as a ligand at the metal binding site.[20,23,26,27] For example, strong binding of Cd^{2+} ion requires a cysteine-based coordination site (with 2–3 Cys[20,23] or 1 Cys/1 His[20,23,26]), while Zn^{2+} ion prefers a histidine-based chelation site (with 2 His[20,27] or 1 Cys/1 His[20]). These amino acid residues can come from different protein subunits, as long as they are located nearby in the quaternary structure of the ion channel. On the other hand, Ag^+ ion binds tightly to a single cysteine residue.[17] Different ion channels have been studied with these metal ion probes, including the Shaker K^+ channel,[17] the P2X receptor channel[23] and the cyclic nucleotide-gated (CNG) channel.[28]

Table 3.1. *Physical properties of ion channel permeant ions and the probe ions.*

	Shannon and Prewitt radii (Å)[29]	**Diffusion coefficient (cm^2/s)[24]**	**Water exchange rate (s^{-1})[25]**	**Protein cysteine residue modification rate constant ($M^{-1}s^{-1}$)**
Na^+	0.99	1.33×10^{-5}	10^8	Not applicable
K^+	1.37	1.96×10^{-5}	10^9	Not applicable
Cd^{2+}	0.95	0.72×10^{-5}	10^8	10^2–10^7 [a] [23]
Ag^+	1.15	1.65×10^{-5}	$>10^6$	Slow : 10^4–10^5 (limited solvent exposure)[23] Moderate: 10^6–10^7 Fast: 10^8–10^9 (solvent exposed)

3.1.3 Coordination chemistry of silver(I)-thiolate and cadmium(II)-thiolate

Thiolates are soft ligands with high polarizability and strong electron-releasing character. They have high affinity to soft metal ions such as Hg^{2+}, Ag^+, Cd^{2+}, Zn^{2+} and Pb^{2+}.[2] Apart from acting as terminal ligands, thiolates also have a high propensity to act as doubly bridging ligands (M–S(R)–M, as in metallothionein, see Section 3.1.1) and thereby they tend to form multinuclear metal complexes.[2] The sulfur atom in μ_2-bridging thiolates adopts a pyramidal geometry (the sulfur atom is bonded to one carbon and two metal ions). Inversion at this pyramidal sulfur centre is relatively rapid in solution (~10^2 s^{-1}).[2]

Ag^+ ion in silver(I)-thiolate complexes is two-coordinated. In the solid state, cyclohexanethiol acts as a μ_2-bridging ligand to Ag^+ and forms a cyclic $(AgSR)_{12}$ complex comprising alternating silver(I) and thiolate (Figure 3.2a).[30] Ag^+ ion and 3-methylpentane-3-thiol form a zig-zag polymer with –Ag–S(R)– repeat units. The bond angle is almost linear at Ag and is bent at S (Figure 3.2b).[30] Two polymer strands intertwine at every fourth silver atom to give a helical secondary structure. In aqueous solution, silver(I)-thiolates also form 1:1 coordination polymers, with the proposed primary structure consisting of the –Ag–S(R)– repeat unit as in the solid state.[31,32] For example, silver(I)-glutathione is proposed to produce a zig-zag polymer that shows reversible gelation.[33,34] Silver(I)-L-cysteine is proposed to form a helical polymer which exhibits high circular dichroism (CD) intensity (Figure 3.2c).[35] Argenophilic interactions (Ag···Ag) between adjacent Ag^+, and hydrogen bonding and electrostatic interactions between thiolates on adjacent polymer chains are suggested to mediate the stability of these polymers.[34,35] Depending on the molar ratio of Ag^+ to thiol, short oligomers or discrete silver(I)-thiolate complexes can exist in equilibrium with the polymer in solution. These led to the early observations that one to two Ag^+ ions were bound per thiol in solution.[31,36,37] Polymer formation is disfavoured with sterically hindered thiols, such as that on protein cysteines. Thus the binding of two Ag^+ ions to each cysteine residue thiol group on protein has been detected by amperometric and spectrophotometric titrations.[31]

In cadmium(II)-thiolate complexes, Cd^{2+} is in general coordinated by four thiolate ligands to form a tetrahedral complex.[2,38,39] Again, thiolates can act as either terminal ligands or μ_2-bridging ligands. With bridging ligands, cadmium(II)-thiolate clusters can form as seen in the structure of the cadmium(II) complex of rat metallothionein-2 (Figure 3.1). Sulfur atoms in a disulfide bond cannot coordinate to Ag^{+} [40] or to Cd^{2+}.[41]

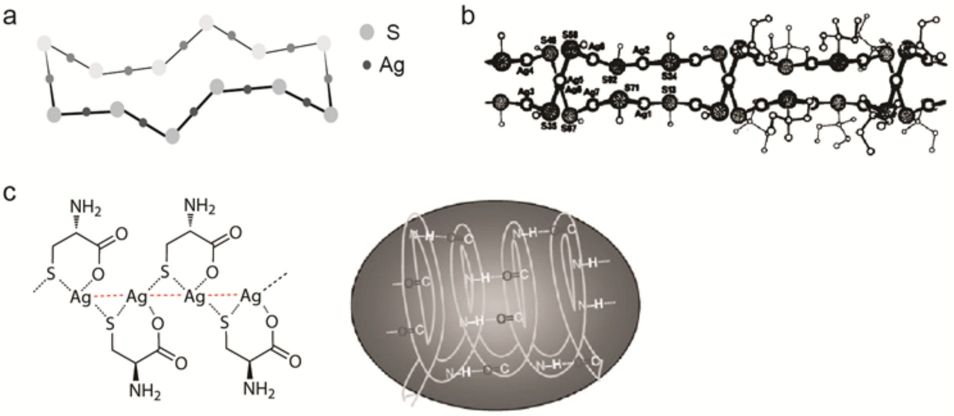

Figure 3.2. *Silver(I)-thiolate complexes. (a) The structure of the (cyclohexanethiolato)silver(I) complex. It has a cyclic structure with the formula* $(AgSR)_{12}$.[30] *(b) The crystal structure of (3-methylpentane-3-thiolato)silver(I) polymer. It has a repeat unit of –Ag–S(R)–. Two strands wind around each other to form a double helix, presumably to maximize crystal packing.*[30] *Reprinted from Polyhedron.*[2] *Copyright (1986), with permission from Elsevier. (c) The proposed primary structure of a silver(I)-cysteine polymer in aqueous solution.*[34,35] *Cysteine is suggested to chelate* Ag^{+} *ion via the thiolate and carboxylate groups. Argenophilic interactions, denoted by the red dashes, may stabilize the polymer. The silver(I)-cysteine polymer is proposed to form a helical secondary structure (shown on the right), possibly held by hydrogen bonds and electrostatic interactions, which gives rise to the high CD intensity of the polymer. Adapted with permission from ref. 35. Copyright (2010) by Wiley.*

3.1.4 Metal ion binding studies using αHL

Besides studying ion channels (Section 3.1.2), metal ions have been apllied to study the pore-forming mechanism of the αHL pore[42,43] and the structure its glycine-rich loop near the turn at T129.[44] With the known crystal structure of αHL published by Song *et al*.[45] in 1996, αHL has been engineered as a single-molecule divalent metal ion sensor.[46,47] Four closely spaced histidine residues were introduced into the stem domain by site-directed mutagenesis (Figure 3.3). An αHL heteroheptamer containing one copy of this engineered monomer can detect sunmicromolar levels of Cd^{2+}, Zn^{2+} and Co^{2+} ions simultaneously.

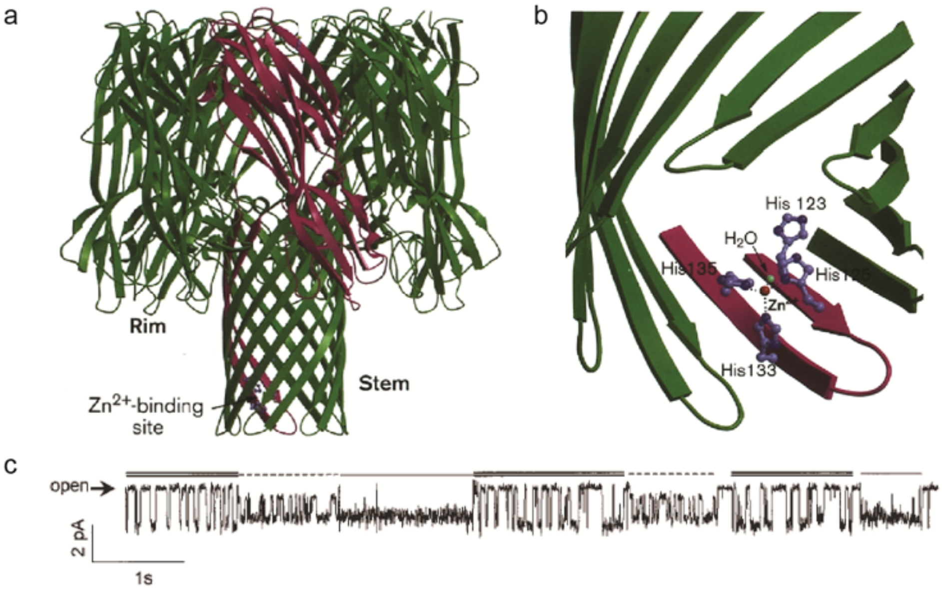

Figure 3.3. *Single-molecule detection of divalent metal ions with αHL.*[46,47] *(a) A heteroheptameric αHL consisting of six wild-type (WT) subunits (green) and one tetra-histidine-containing subunit (magenta) was used. The four histidine residues are located in the stem domain at positions 123, 125, 133 and 135. (b) Close-up view of the metal ion binding site. A Zn^{2+} ion (orange) binds to three of the four histidine residues, with its fourth binding site occupied by a water molecule (light green). Reprinted from ref. 46. Copyright (1997), with permission from Elsevier. (c) An example current recording showing the simultaneous sensing of Cd^{2+} (434 nM, marked by double line), Zn^{2+} (240 nM, dashed line) and Co^{2+} ions (4.06 μM, solid line) at pH 7.5. Reprinted by permission from Macmillan Publishers Ltd: Nature Nanotechnology (ref. 47), copyright (2000).*

The kinetics for the stepwise binding of two iminodiacetate ligands to a Zn^{2+} ion[48] was investigated. By the targeted chemical modification of two cysteine residues, two iminodiacetate chelators were covalently attached to αHL at positions 117 and 143 (they are located in the stem domain). Complex formation and the transfer of Zn^{2+} ion between the two chelators at pH 4.0 were observed (Figure 3.4). A similar protein construct carrying only one chelator showed distinctive binding characteristics to Cd^{2+}, Zn^{2+} and Mn^{2+} ions at pH 7.0.[49]

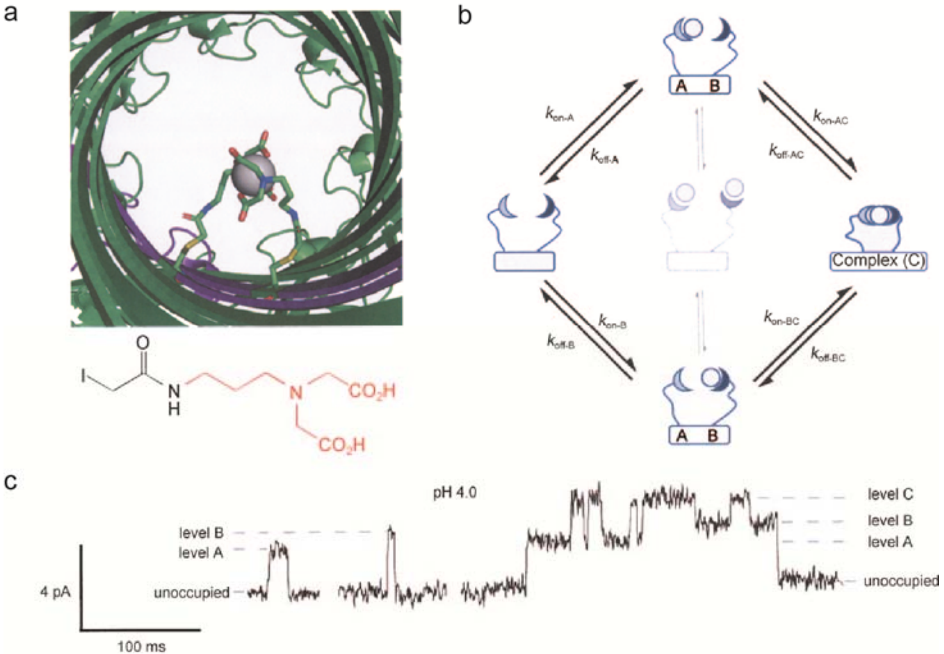

Figure 3.4. *Stepwise Zn^{2+} complex formation with two iminodiacetate chelators in αHL.*[48] *(a) (Top) Model showing the binding of a Zn^{2+} ion (grey) by two iminodiacetate chelators attached to the β barrel of αHL. This heteroheptameric αHL contains six WT subunits and one subunit carrying two covalently attached chelators. (Bottom) Structure of the iminodiacetate-containing molecule used for targeted chemical modification. The two cysteine residues at positions 117 and 143, introduced by site-directed mutagenesis, react with this molecule by thioether bond formation. (b) Kinetic scheme summarizing the binding of Zn^{2+} ion and its transfer between the two chelators. The simultaneous residence of two Zn^{2+} ions, one on each chelator, was not observed at pH 4.0. (c) Current recordings at pH 4.0 showing the binding of Zn^{2+} ion to either one of the two chelators (levels A and B) and to both chelators (level C). Adapted with permission from ref. 48. Copyright (2010) by Wiley.*

Examples of single-molecule metal complex formation detection with other techniques, such as single-molecule fluorescence (Figure 1.2) and single-molecule force microscopy (Figures 1.3), were discussed in Chapter 1 (Sections 1.1.1–1.1.2).

3.2 Objectives

Metal-thiolate interactions are involved in the normal function of metalloenzymes. Moreover, these interactions have been applied to study ion channel topology. In this chapter, the kinetics of the association and dissociation of two metal-thiolate complexes, namely silver(I)-thiolate and the cadmium(II)-thiolate complexes, were studied at pH 7.4 at the single-molecule level. This was done by carrying out the coordination reactions in cysteine-containing αHL pores, and monitoring them by ionic current recording. The study was performed in two stages: (1) the binding of metal ions to the cysteine residue(s) in αHL (Sections 3.3.4 and 3.3.6); and (2) the observation of the build-up of metal-thiolate complexes by the addition of small thiol compounds (Sections 3.3.5 and 3.3.7).

3.3 Results

3.3.1 Design of new mutant

The use of protein nanopores for studying chemical reactions necessitates that the added reactant(s) only reacts with specific functional group(s) inside the pore. In other words, the protein should provide a silent background.[50] It has been reported that the Ag^+ ion can interact with the side chain of amino acids apart from that of cysteine, for example, those carrying nitrogen or sulfur atom in the side chains, such as arginine, lysine, histidine, tryptophan and methionine.[51–54] In fact, silver staining of proteins in polyacrylamide gels is based on these silver(I)-amino acid residue interactions.[55,56] Although the binding of Ag^+ ion to these amino acid residues is weaker than to cysteine residue, cysteine-free $(WT)_7$ showed reversible interactions when ≥1 μM of $AgNO_3$ (*cis*) was added (2 M KNO_3, 10 mM MOPS, chelex, pH 7.4 at –50 mV and 22 °C) (Figure 3.5a). These interactions vanished when excess glutathione (GSH) was added to the *cis* compartment to quench free Ag^+ ion.

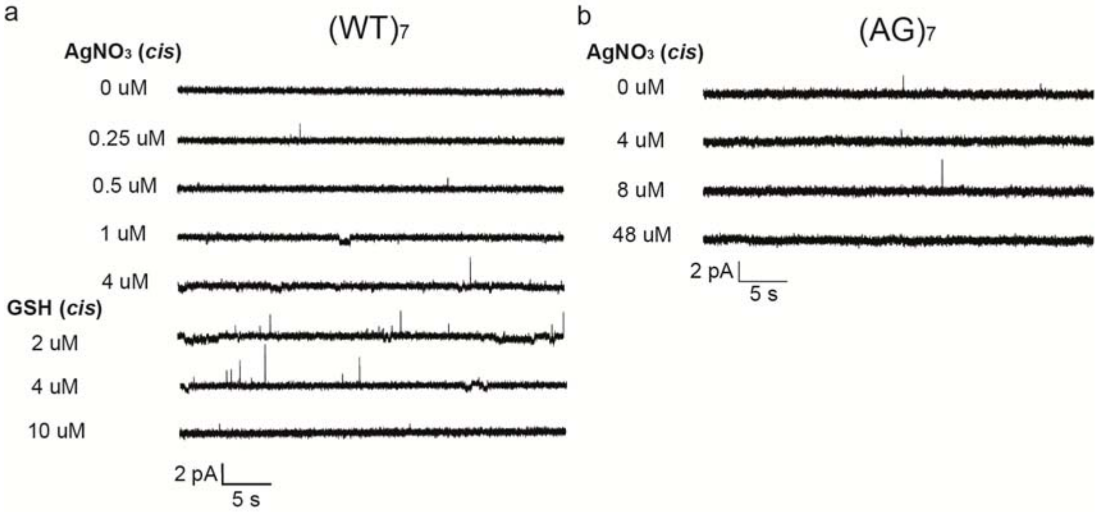

Figure 3.5. *Current traces showing the interactions of Ag^+ ion (as $AgNO_3$, cis) with (a) $(WT)_7$ and (b) $(AG)_7$ in 2 M KNO_3, 10 mM MOPS, 100 μM EDTA, pH 7.4, at –50 mV and 22 °C. Reversible interactions between $(WT)_7$ and Ag^+ ion appear at $[AgNO_3]$ ≥ 1 μM. These interactions are removed by the addition of excess GSH (cis, 10 μM) to quench Ag^+ ion (4 μM). No interaction between $(AG)_7$ and Ag^+ ion is observed even at 48 μM $AgNO_3$. The concentrations of $AgNO_3$ and GSH added are labelled on the left hand side of each trace.*

To create a silent protein background for studying metal-thiolate interactions, four point mutations (Lys8→Ala, Met113→Gly, Lys131→Gly and Lys147→Gly) were introduced by site-directed mutagenesis. This new mutant is termed AG. Mutations into alanine or glycine were chosen as their side chains cannot interact with Ag^+ ion. The K8A mutation has been previously incorporated into αHL and does not change the unitary conductance of the pore.[57] These four mutations encompass the amino acid residues located at the *cis* entrance (Lys8) and the β barrel (Met113, Lys131 and Lys147), which constitute the narrower regions of the lumen (Figure 3.6b and Figure 1.9c in Chapter 1). Other potentially interacting amino acid residues in the vestibule (Arg56, Lys58, Arg104, Lys110 and Lys154) were not mutated, because the vestibule is wider (maximum diameter ~46 Å[58]) and hence the binding of Ag^+ ion (diameter of dehydrated ion = 2.52 Å) at these positions is not expected to cause detectable current change. Other susceptible residues on the outer surface of the cap domain were not mutated for the same reason (Figure 3.6a).

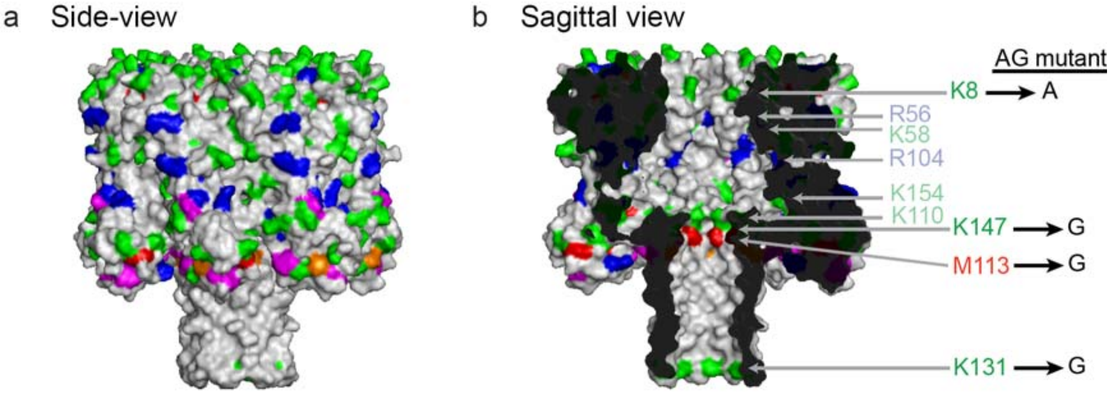

Figure 3.6. *Structure of αHL. Amino acid residues bearing nitrogen or sulfur-containing side chain are highlighted. These residues are colour-coded as follow: arginine (blue), histidine (orange), lysine (green), methionine (red) and tryptophan (magenta). (a) Side-view showing these residues on the surface of cap domain. (b) Cross section of αHL showing the cavity inside the transmembrane pore. The highlighted amino acid residues within the lumen are labeled on the right hand side. The four amino acid residues that were mutated by site-directed mutagenesis to make the AG mutant are indicated. WT αHL does not contain any cysteine residues.*

$(AG)_7$ showed no interactions even at 48 μM of $AgNO_3$ (*cis*) (Figure 3.5b), supporting the idea that the interactions observed with $(WT)_7$ were due to those lysine and methionine residues being mutated. With this silent mutant in hand, a heteroheptameric αHL, $(AG)_6(G137C\text{-}D8\text{-}AG)_1$ (abbreviated as PSH in this chapter), containing one subunit bearing a cysteine residue at position 137 was prepared and used for studying the metal-thiolate complexes (Sections 3.3.4–3.3.7).

3.3.2 Characterization of the new mutant $(AG)_7$

With three lumen-facing lysine residues (K8, K131 and K147) on each subunit mutated to the neutral residues (Gly or Ala), $(AG)_7$ presumably bears 21-less positive charges inside the lumen compared to $(WT)_7$ at pH 7.4. In addition, the long side chains of M113 and K147 at the narrow constriction are removed (Figures 1.9c and 3.6b). K131G and K147G mutations also remove their salt bridges with D127 and E111, respectively. Thus, it is interesting to study the influence of these mutations on the ionic current conductance, the conductance-voltage (G-V) relationship, the ion selectivity and the stability of the new mutant.[59]

Like $(WT)_7$, $(AG)_7$ forms pores with long open time at ±50 mV (2 M KCl, 80 mM MOPS, 100 μM EDTA, pH 7.4 at 22 ± 1 °C). The unitary conductance of $(AG)_7$ (2.73 ± 0.01 nS) is 1.5 times higher than that of $(WT)_7$ (1.78 ± 0.01 nS) at –50 mV (Figures 3.7a,b and Table 3.7 (in Section 3.6.8)). The G-V relationship of $(AG)_7$ in the 2.0 M KCl buffer is almost linear ($G_{+100\,mV}/G_{-100\,mV} = 1.0$), while that of $(WT)_7$ shows weak rectification ($G_{+100\,mV}/G_{-100\,mV} = 1.2$) (Figure 3.7e). $(AG)_7$ shows more frequent reversible voltage-dependent channel closures than $(WT)_7$ at high positive applied potential (>100 mV, *cis* side is ground, Figure 3.7c,d). Contrary to the weak anion selectivity of $(WT)_7$ ($P_{K^+}/P_{Cl^-} = 0.54$ in 100 mM KCl (*cis*)/1 M KCl (*trans*)), $(AG)_7$ is moderately cation selective ($P_{K^+}/P_{Cl^-} = 3.12$) (Figure 3.7f and Table 3.2). The charge selectivities of both $(AG)_7$ and $(WT)_7$ are independent of the direction of salt gradient (Table 3.2).

The higher conductance of $(AG)_7$ relative to $(WT)_7$ (1.5 times) is attributed to the widening of the narrow constriction by the M113G and K147G mutations. Asymmetry in the conductance of nanopores depends on the static charge distribution in the interior of the pore. The lost of current rectification in $(AG)_7$ might be due to the K147G mutation, as suggested by computer simulations.[60] On the other hand, ion selectivity is mainly governed by the charge at the narrowest part of the pore (i.e. the inner constriction of αHL).[60] The removal of the positively charged lysine by K147G makes $(AG)_7$ cation selective.

Light scattering hemolytic assays on rabbit red blood cells (rRBC) with AG monomer prepared by *in vitro* transcription and translation (IVTT) showed that AG has similar hemolytic activity as WT αHL (Figure 3.7g).

Table 3.2. *Charge selectivity of αHL pores.*

	V_r (mV)	P_{K^+}/P_{Cl^-} [c]
$(WT)_7$	+11.9 ± 2.3[a] (n = 5)	0.54 ± 0.10[a]
	–3.73 ± 0.55[b] (n = 5)	0.83 ± 0.12[b]
$(AG)_7$	–21.6 ± 0.7[a] (n = 6)	3.12 ± 0.10[a]
	+21.9 ± 0.3[b] (n = 4)	3.21 ± 0.05[b]

[a] *100 mM KCl (cis)/1 M KCl (trans); with 10 mM MOPS and 100 uM EDTA in each buffer at pH 7.4 and 22 °C.*

[b] *1 M KCl (cis)/100 mM KCl (trans);*

[c] *Ion selectivity is calculated using the Goldman–Hodgkin–Katz equation[15] (see Section 3.6.7).*

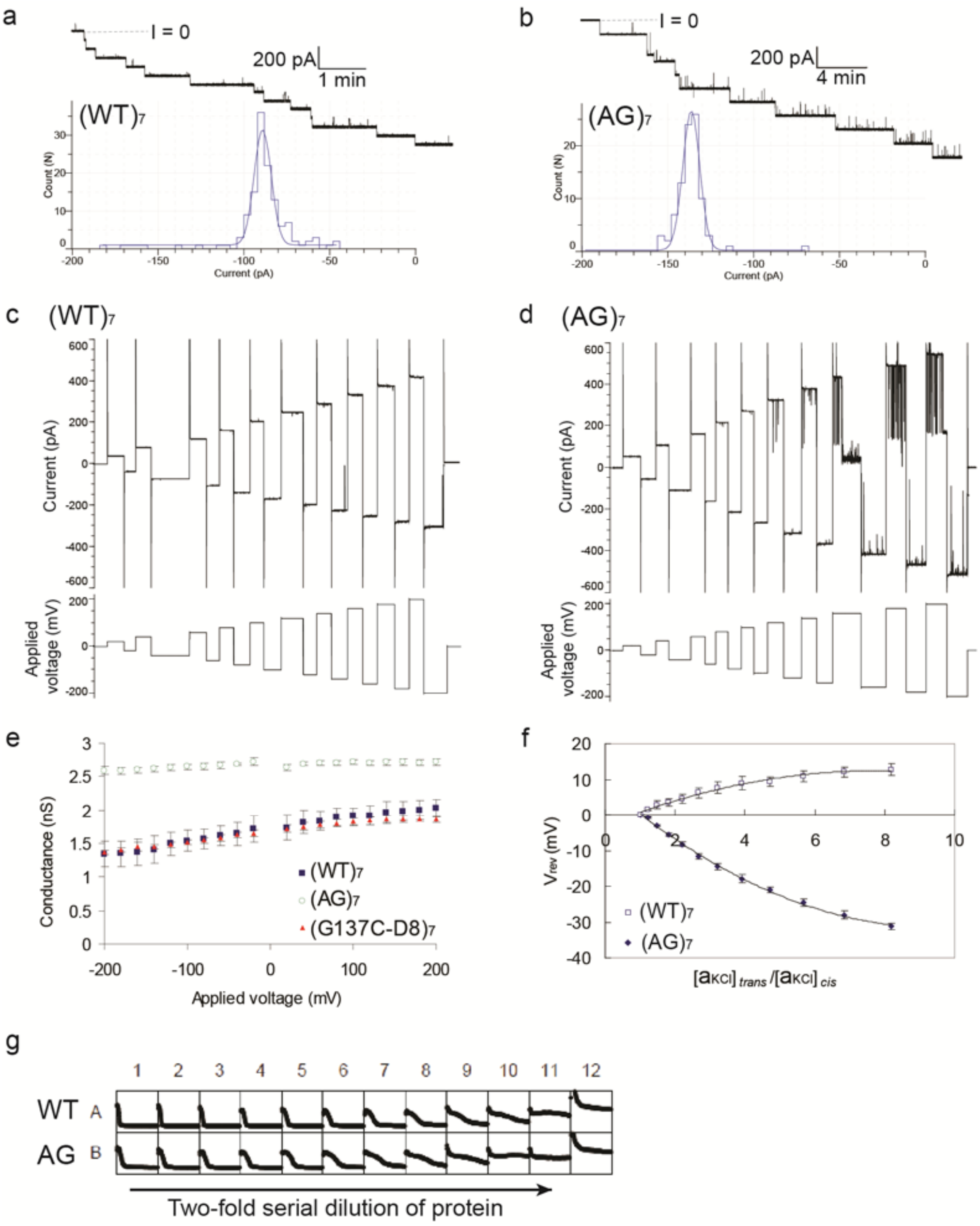

Figure 3.7. *Characterization of (AG)*$_7$*. (a,b) Current histograms of single channels formed by (WT)*$_7$ *and (AG)*$_7$ *at –50 mV. Buffer: 2 M KCl, 80 mM MOPS, 100 μM EDTA, pH 7.4 and 22 °C. Each histogram comprises the current values of over 100 channel formation events. The bin width is 4 pA. The solid lines indicate the best fit with a Gaussian distribution curve. Recording traces of multiple insertions of αHL are shown on top of each histogram. (c,d) Single-channel currents of (WT)*$_7$ *and (AG)*$_7$ *at alternating positive and negative potentials (20, 40, 60, 80, 100, 120, 140, 160, 180 and 200 mV). The voltage protocol is shown below the current trace. The results are representative of at least five experiments for each protein. (e) Conductance-voltage (G-V) relationship of (AG)*$_7$ *compared to (WT)*$_7$ *in the same buffer as in (a). G-V curve*

of (G137C-D8)$_7$ was shown for reference. Note that (WT)$_7$ and (G137C-D8)$_7$ have almost identical G-V curves. Each data point reprsents mean ± s.d. from at least three single-channel experiments. (f) Reversal potential (V_{rev}) plotted against $[a_{KCl}]_{trans}/[a_{KCl}]_{cis}$. $[a_{KCl}]_{trans}$ and $[a_{KCl}]_{cis}$ represents the activity of KCl in the trans and cis compartments, respectively. The concentration of KCl in the trans chamber was kept at 1.0 M. The buffer solutions in both cis and trans compartments contained 10 mM MOPS, 100 µM EDTA at pH 7.4 and 22 ± 1 °C. (g) Light scattering hemolytic assays on rabbit red blood cells (rRBC) with monomeric WT and AG αHL. In a microtitre plate, 175 µL MBSA (10 mM MOPS, 0.1% (w/v) bovine serum albumin, 150 mM NaCl, pH 7.4) was added to each initial well (column 1, rows A–B), while 90 µL MBSA was added to all other wells (columns 2–12, rows A–B). Then, monomeric αHL (5 µL, 5–25 ng, prepared by in vitro transcription and translation (IVTT)) was added to each well in column 1, rows A–B. Two-fold serial dilution of protein was carried out by transferring 90 µL of solution to each consecutive well from column 1 towards column 11. The last 90 µL taken out from column 11 was discarded, leaving column 12 with no protein. 10 µL of washed rRBC was added to each well and resulted in a total volume of 100 µL per well. Hemolytic activity was followed by measuring the absorbance change at 595 nm. The results shown are representative of three repeats.

3.3.3 Denaturing effect of nitrate ion on αHL

Nitrate ion is a chaotropic reagent which denatures proteins.[61,62] During the metal ion binding studies discussed in Sections 3.3.4–3.3.7, we found that it was difficult to get the insertion of heptameric αHL into the planar lipid bilayer in buffer containing 2 M KNO_3 (at pH 7.4). Once inserted, however, the αHL pore was as stable as that obtained in 2 M KCl buffer, and showed long open time. Ease of channel insertion improved at lower KNO_3 concentration, such as 0.5 M. When an asymmetric solution (2 M KCl (*cis* – the side where protein was added)/2 M KNO_3 (*trans*)) was used, protein insertion occurred as efficiently as in symmetric KCl buffer. The planar lipid bilayer formed by DPhPC in KNO_3 buffer was as stable as that formed in KCl buffer (in terms of ease of bilayer formation, capacitance and stability to applied potential), so the effect of nitrate ion on the lipid bilayer was excluded. The difficulty of pore insertion into the planar lipid bilayer is attributed to the denaturing effect of nitrate ion on non-membrane associated heptameric αHL.

The influence of nitrate ion on monomeric αHL was investigated by hemolytic assay. WT αHL monomer was added to rabbit red blood cells (rRBC) in buffer containing different concentrations of KNO_3 at pH 7.4 (Figure 3.8). Hemolytic assay in buffer containing KCl was performed for comparison. In the absence of αHL, rRBC were stable at all KNO_3 and KCl concentrations tested (0–2 M; 150 mM NaCl was present for osmotic balance, rows C-D in Figure 3.8). The addition of αHL caused cell lysis as shown by the drop of absorbance at 595 nm. αHL remained hemolytically active in buffer containing up to 1 M KNO_3, although a drop in activity with increasing KNO_3 concentration was observed (rows A in Figure 3.8). At 2 M KNO_3, αHL became inactive towards cell lysis. By contrast, αHL was active in all KCl concentrations tested (0–2 M), with a slight decrease in the rate of hemolysis in 2 M KCl only (rows B in Figure 3.8). In conclusion, nitrate ion at ≥1 M prevents αHL pore formation. Considering the pore formation mechanism of αHL (see Chapter 1, Section 1.2.2), this might arise from (1) the denaturation of the αHL monomer in solution; (2) the denaturation of receptor on membrane. Either (1) or (2) can prevent the binding of αHL monomer to membranes; (3) the inability of membrane-associated monomer to oligomerize to form the prepore; or (4) the failure of the prepore to form the fully-assembled pore.

To achieve efficient protein insertion in single-channel recording experiments performed in 2 M KNO_3 buffer, αHL was inserted under asymmetric salt conditions: 150 mM KNO_3 (*cis*)/2 M KNO_3 (*trans*) (both have the same concentrations of buffering agent and EDTA, and are at the same pH). After the insertion of a single pore, part of the buffer in the *cis* compartment was replaced with 2.5 M KNO_3 buffer until the final concentration of KNO_3 reached 2 M.

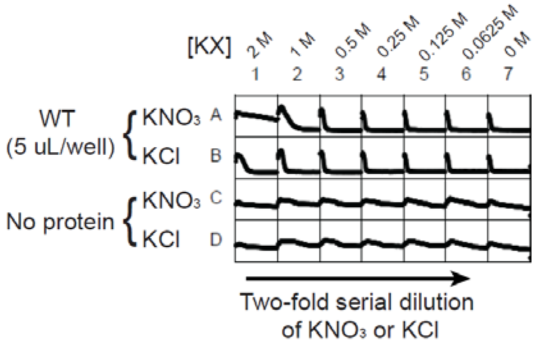

Figure 3.8. *Light scattering hemolytic assays in various concentrations of* KNO_3 *or KCl buffer. Monomeric WT αHL prepared by IVTT was used. In a 96-well microtitre plate, 170 μL of* KNO_3 *or KCl buffer (2.35 M)* KNO_3 *or KCl, 10 mM MOPS, 150 mM NaCl, pH 7.4) was added to each initial well (column 1, rows A,C for* KNO_3*; rows B,D for KCl), while 85 μL of 10 mM MOPS, 150 mM NaCl, pH 7.4 was added to all other wells (columns 2–7, rows A–D). Two-fold serial dilution of* KNO_3 *or KCl was carried out by transferring 85 μL of solution to each consecutive well from column 1 towards column 6. The last 85 μL taken out from column 6 was discarded, leaving column 7 with 0 M* KNO_3 *or KCl. Then monomeric WT αHL (5 μL) was added to each well in column 1–7, rows A–B. 5 uL of 10 mM MOPS, 150 mM NaCl, pH 7.4 was added to column 1–7, rows C–D as the control. 10 μL washed rRBC were added to each well, resulting in a total volume of 100 μL per well. Hemolytic activity was followed by measuring the absorbance change at 595 nm. The results shown are representative of three repeats. Rows C–D (without proteins) show the stability of rRBC under high salt conditions.*

3.3.4 Reversible binding of two silver(I) ions

The coordination of Ag^+ ion to the cysteine residue was studied in 2 M KNO_3, 10 mM MOPS, 10 mM EDTA, pH 7.4, at 22 °C. Nitrate buffer was used instead of chloride buffer because of the low solubility of AgCl in water. Amino groups are good ligands to Ag^+ ion,[63] thus a buffering agent with few amino groups was chosen (MOPS contains one tertiary amine). Phosphate buffer is not suitable as silver phosphate is water-insoluble. A relatively high concentration of EDTA (10 mM) was used to buffer Ag^+.[22] This improves the accuracy in the determination of the free Ag^+ ion concentration, as the presence of residual thiol reductants (DTT, β-mercaptoethanol and sodium thioglycolate) (tens to hundreds nM) from protein preparation would sequester the small amount of $AgNO_3$ (≤1 μM) needed in buffers without or with low EDTA (e.g. 100 μM). Free Ag^+ ion concentration was calculated with the program maxchelator.standford.edu[64] using the appropriate stability constants under our conditions (the $\log_{10}$ value of the association constant K_a of Ag^+ and EDTA is 7.32 ± 0.05[65a]).

$(AG)_6(G137C\text{-}D8\text{-}AG)_1$ (abbreviated as PSH in this chapter) has a single cysteine residue at position 137. It has a single-channel current of –96 ± 2 pA (n = 5) at –50 mV in the above nitrate buffer. Interestingly, the addition of $AgNO_3$ to the *cis* compartment (total $[AgNO_3]$ added = 4–32 μM) gave reversible blockades consisting of two distinct levels (ΔI = –1.6 ± 0.3 pA (level 1) and –3.6 ± 0.6 pA (level 2) relative to the PSH level, n = 3), with the latter level showing more current fluctuations, i.e. it was 'noisier' (Figure 3.9a). These blockades were not seen with $(AG)_7$, confirming the observation of a specific interaction between Ag^+ ion and the cysteine residue in PSH. The frequency of these blockades in PSH increased with the $AgNO_3$ concentration, with level 2 becoming more prominent than level 1. These observations suggest that the two levels arise from pore-Ag^+ ion-associated complexes. Using the software maxchelator,[64] the free Ag^+ ion concentrations at 4, 8, 16 and 32 μM total $AgNO_3$ in the presence of 10 mM EDTA were calculated to be 16, 33, 66 and 133 nM, respectively. It is assumed that the free Ag^+ ion concentration inside the pore is the same as that in bulk solution. Plots of the observed rate constants calculated by QuB (see Section 3.6.9) for each transition versus the free Ag^+ ion concentration revealed that both 0→1 (represents the transition from level 0 to level 1, Figure 3.9d) and 1→2 have a first-order dependence on the free Ag^+ ion concentration ($n_{0\text{-}1}/\sum\tau_0 = k_{0\text{-}1}[Ag^+]$ and $n_{1\text{-}2}/\sum\tau_1 = k_{1\text{-}2}[Ag^+]$; $n_{0\text{-}1}$ represents the total number of 0→1 transitions; $\sum\tau_0$ is the sum of residence times at level 0; $k_{0\text{-}1}$ is the rate constant for 0→1 and so on), while both 1→0 and 2→1 show zeroth-order dependence on the free Ag^+ ion concentration ($n_{1\text{-}0}/\sum\tau_1 = k_{1\text{-}0}$ and $n_{2\text{-}1}/\sum\tau_2 = k_{2\text{-}1}$) (Figure 3.9c,d). As level 0 represents the unoccupied pore bearing the free cysteine (PSH), level 1 is proposed to have one Ag^+ ion bound to the cysteine (P-S-Ag), while level 2 is proposed to have two Ag^+ ions bound (PS^+-Ag_2). It has been observed in crystal structures that the thiolate sulfur atom can act as a bridging ligand between two Ag^+ ions (see Section 3.1.3).[2,29] Hence the structure of level 2 (PS^+-Ag_2) is believed to have the structure Ag-S^+(P)-Ag (Figure 3.9d) rather than PS-Ag^+-Ag. This is supported by the absence of direct transitions between PSH and PS^+-Ag_2 (both 0→2 and 2→0), i.e. they interconvert via PS-Ag (level 1).

In addition to the levels discussed above, a level with higher conductance than level 0 (PSH) was observed occasionally after the addition of Ag^+ ion (+1.2 ± 0.4 pA, n = 3) (indicated with a red arrow in Figure 3.9a). This level could transit to and from level 0 (PSH) or level 1 (PS-Ag). Because of the paucity of occurrence, a detailed kinetic analysis of this level could not be performed. It might arise from the chelation of Ag^+ ion by the cysteine thiolate group and the amido oxygen atom in the peptide backbone or on the side chain of a nearby glutamine residue (N121, N123 or N139). A similar higher conductance level was also observed in the binding of Cu^{2+} ion to the pore-attached iminodiacetate ligand (see Chapter 4, Section 4.3.2).

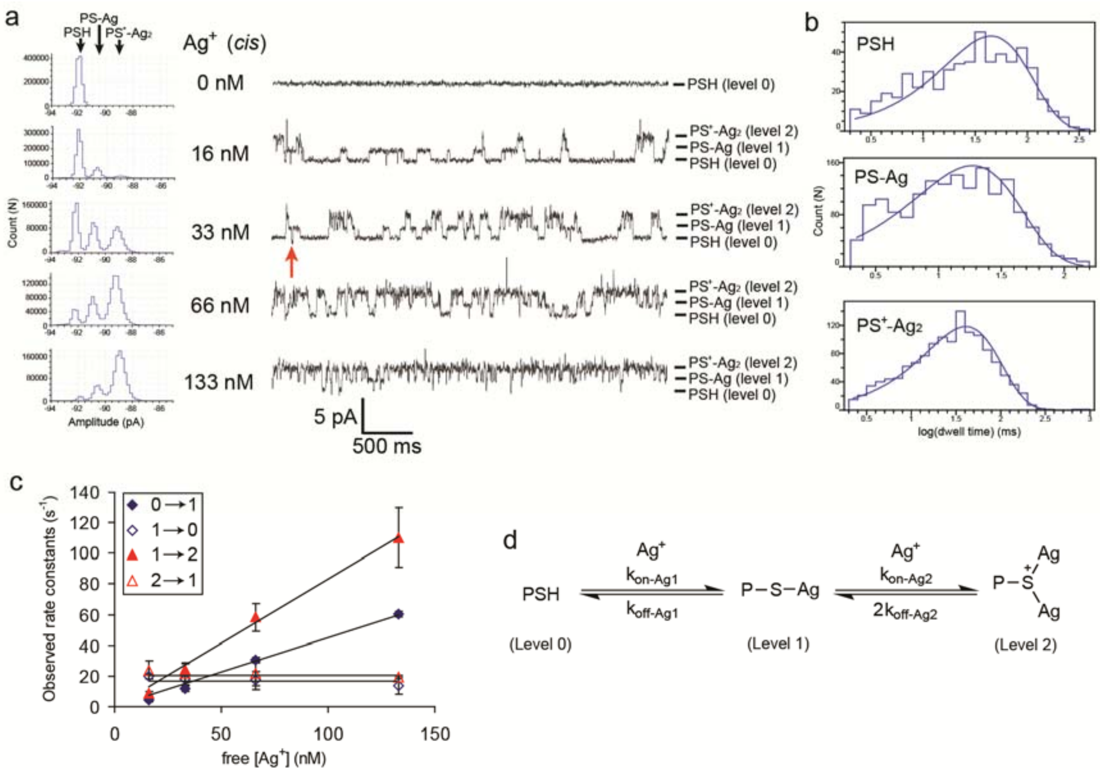

Figure 3.9. *Reversible binding of two silver(I) ions to PSH. (a) Current recording traces at different free Ag$^+$ concentrations. AgNO$_3$ was added to the cis side of (AG)$_6$(G137C-D8-AG)$_1$ (PSH). Free Ag$^+$ ion concentrations are labelled on the left hand side. The identity of each level is labelled on the right: PSH = open pore; P-S-Ag = one Ag$^+$ ion-bound; P-S$^+$-Ag$_2$ = two Ag$^+$ ions-bound. Conditions: 2 M KNO$_3$, 10 mM MOPS, 10 mM EDTA, pH 7.4 at 22 °C and –50 mV. All points amplitude histograms are shown on the left. Each histogram is obtained from a 60 s trace. Occasional events that have a higher conductance value than the PSH level is indicated by the red arrow. (b) Dwell time histograms of PSH, PS-Ag and PS$^+$-Ag$_2$ in the presence of 66 nM of free Ag$^+$ ion. Each histogram is fitted to a single-exponential function using Clampfit (Molecular Devices). (c) Plot of the observed rate constants of each transition versus free Ag$^+$ ion concentration. Ag$^+$ ion concentration inside the pore is assumed the same as that in bulk solution. Each point (mean ± s.d.) is obtained from three experiments. (d) Proposed kinetic scheme describing the sequential association of two Ag$^+$ ions to the cysteine residue. Direct transitions between PSH and PS$^+$-Ag$_2$ were not observed. The 'site' rate constant of each step is labelled next to the arrow (see legends of Table 3.3 for more details).*

Table 3.3. *Rate constants and equilibrium dissociation constants for Ag^+ binding to PSH.*

	Current blockade (ΔI) (pA)[a]	**Association rate constants ($M^{-1}s^{-1}$)**	**Dissociation rate constants (s^{-1})**	**Dissociation equilibrium constants (M)**
First Ag^+	–1.6 ± 0.3	$k_{on\text{-}Ag1}$ $(4.4 \pm 0.3) \times 10^8$	$k_{off\text{-}Ag1}$ 17 ± 1	K_{Ag1} $(4.0 \pm 0.5) \times 10^{-8}$
Second Ag^+	–3.6 ± 0.6	$k_{on\text{-}Ag2}$ $(8.3 \pm 1.3) \times 10^8$	$k_{off\text{-}Ag2}$ [b] 11 ± 3	K_{Ag2} [b] $(1.3 \pm 0.3) \times 10^{-8}$

Conditions: 2 M KNO_3, 10 mM MOPS, 10 mM EDTA, pH 7.4, at –50 mV and 22 ± 1 °C.

[a] *Relative to the open pore (PSH) level.*

[b] *These values are the 'site' rate constant and 'site' equilibrium dissociation constant,[66] i.e. they are the values for the cleavage of each Ag–S bond in PS^+Ag_2. QuB analysis gives the 'stoichiometric' rate constant for the conversion of PS^+Ag_2 to PSAg, which is the overall dissociation rate constant of the two Ag–S bonds. Since the two Ag–S bonds in PS^+Ag_2 are presumably identical, thus the 'site' rate constant $k_{off\text{-}Ag2}$ for each Ag–S bond is half of the measured 'stoichiometric' rate constant.*

The forward and reverse reaction rate constants determined from the mean residence times are summarized in Table 3.3. The associations of the first and second Ag^+ ions to the cysteine residue have bimolecular reaction rate constants of $k_{on\text{-}Ag1} = (4.4 \pm 0.3) \times 10^8\ M^{-1}s^{-1}$ and $k_{on\text{-}Ag2} = (8.3 \pm 1.3) \times 10^8\ M^{-1}s^{-1}$, respectively. The unimolecular dissociation rate constants of both Ag^+ ions are similar ($k_{off\text{-}Ag1} = 17 \pm 1\ s^{-1}$ and $k_{off\text{-}Ag2} = 11 \pm 3\ s^{-1}$). These give the equilibrium dissociation constants ($K_d = k_{off}/k_{on}$) of $K_{Ag1} = (4.0 \pm 0.5) \times 10^{-8}$ M and $K_{Ag2} = (1.3 \pm 0.3) \times 10^{-8}$ M. The overall K_d for Ag^+ binding $= K_{Ag1}K_{Ag2} = (5.3 \pm 1.4) \times 10^{-16}\ M^2$. The near-diffusion limited values of $k_{on\text{-}Ag1}$ and $k_{on\text{-}Ag2}$ agrees with the solvent accessibility of Cys-137, which is located in the β barrel and has its side chain pointing to the water-filled lumen[44] (see Section 3.1.2 and Table 3.1). The tighter binding of the second Ag^+ ion compared to that of the first one by 3-fold might due to the stabilizing argenophilic interaction (Ag···Ag) in PS^+Ag_2. Argenophilic interaction, with strength comparable to hydrogen bonding, has been proposed to stabilize silver(I)-thiol polymers in aqueous solution[34] (see Section 3.1.3).

In ensemble reaction solution, the reported K_d values for the one-to-one binding between Ag^+ ion and thiol-containing compounds that we can find in literature (β-mercaptoethanol ($pK_a = 9.4$), 2,2-bis(hydroxylmethyl)-3-mercaptopropanol ($pK_a = 9.9$) or penicillamine ($pK_a = 7.9$)) are about 10^{-11} M at pH 7.4.[65a] These are about 1000 times smaller than that of PSH. Such stronger coordination measured in bulk solution might due to the formation of silver(I)-thiolate oligomer (see next section), the presence of additional coordinating ligands, for example, in penicillamine, and/or the cysteine thiol group in PSH has higher pK_a value than those of the above compounds.

3.3.5 Silver(I)-thiolate oligomer formation

The reversible formation and breakdown of Ag^+-thiolate polymers in aqueous solution at pH 7.4 were studied with six different thiol compounds using PSH (Table 3.4). Glutathione and L-cysteine have been proposed to form linear polymers with Ag^+ ion in aqueous solutions (see Section 3.1.3). The other four structurally simpler thiol compounds were chosen to find out the necessary structural elements for Ag^+-thiolate polymer formation. In the single-channel recording experiments, $AgNO_3$ and the thiol compounds were added to the *cis* and *trans* compartments, respectively.

Formation of Ag^+-thiolate polymers

The build-up of Ag^+-thiolate polymers began from the PS-Ag level. With glutathione (GSH), stepwise events with ΔI values of about –12 pA were observed (1→2, 2→3 and 3→4 in Figure 3.10). Three such steps were seen. Interestingly, both levels 2 and 3 showed sub-levels, which were more apparent in level 2. No sub-levels were observed at level 4. None of these events were seen when the cysteine-free homoheptamer $(AG)_7$ was used, or when either Ag^+ ion or GSH was absent. With L-cysteine, thioglycolate and cysteamine, stepwise formation of polymers with ΔI of about –7, –3 and –5 pA, respectively, were observed (Figures 3.11a and b). More than five steps could be seen with each thiol. These steps also frequently led to the complete obstruction of ion flux through the pore. The higher levels reached after more steps exhibited higher peak-to-peak noise. In addition to these stepwise associations, cysteamine showed reversible and one-step full blockades of PSH as well (Figure 3.11c). The full blockades started from a level that had slightly lower conductance than PSH (~3 pA). On the other hand, β-mercaptoethanol exhibited concentration-dependent behaviour. At low concentrations (1–10 μM), no polymer

Table 3.4. *Summary of the properties of Ag^+-thiolate polymer detected with PSH.*[a]

Thiol compound	Structure	Thiol pK_a	ΔI^b (pA)	Polymer formation	Polymer breakdown
Glutathione	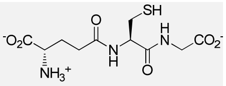	8.6[65a]	–12	Multi-step	Multi-step
L-Cysteine	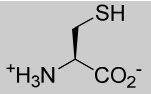	8.2[65a]	–7	Multi-step	One-step
Thioglycolate	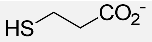	10.3[65b]	–3	Multi-step	One-step
Cysteamine	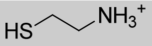	8.6[65b]	–5	Multi-step[c]	One-step
β-Mercaptoethanol	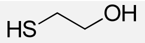	9.4[65a]	NA[d]	One-step[d]	One-step[d]
DL-Dithiothreitol (DTT)	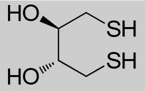	9.2, 10.1	No polymer formation[e]	No polymer formation[e]	No polymer formation[e]

[a] *In 2 M KNO_3, 10 mM MOPS, 100 μM (or 10 mM) EDTA, pH 7.4, at –50 mV.*

[b] *ΔI is the change in current when a thiol molecule attaches to the growing Ag(I)-thiolate polymer. A negative value means decrease in transmembrane ionic current.*

[c] *Stepwise oligomer formation is observed, especially at low concentrations of cysteamine, e.g. ~1–20 μM (Figure 3.11a). But most of the time, the thiol group on PSH is capped and unavailable for polymer growth. In this case, another type of pore blockade appears – reversible and one-step complete blockade (Figure 3.11c).*

[d] *NA = not applicable. At low concentrations (1–10 μM), β-mercaptoethanol does not form oligomers with Ag^+ on PSH. It sequesters Ag^+ ion from solution and no Ag^+ binding to PSH can be observed. At higher concentrations (~1 mM), however, reversible and one-step complete blocking of both PSH and $(AG)_7$ appears, which resembles the blocking caused by cysteamine in Figure 3.11c.*

[e] *DTT sequesters Ag^+ ion from solution and therefore no Ag^+ binding to PSH can be seen.*

formation on PSH was observed. At higher concentrations (1 mM), reversible and one-step full blockades similar to those observed with cysteamine (Figure 3.11c) occurred. The reversible and one-step full blockades with cysteamine and β-mercaptoethanol were also observed with the cysteine-free $(AG)_7$. DL-dithiothreitol (DTT) did not show stepwise polymer formation.

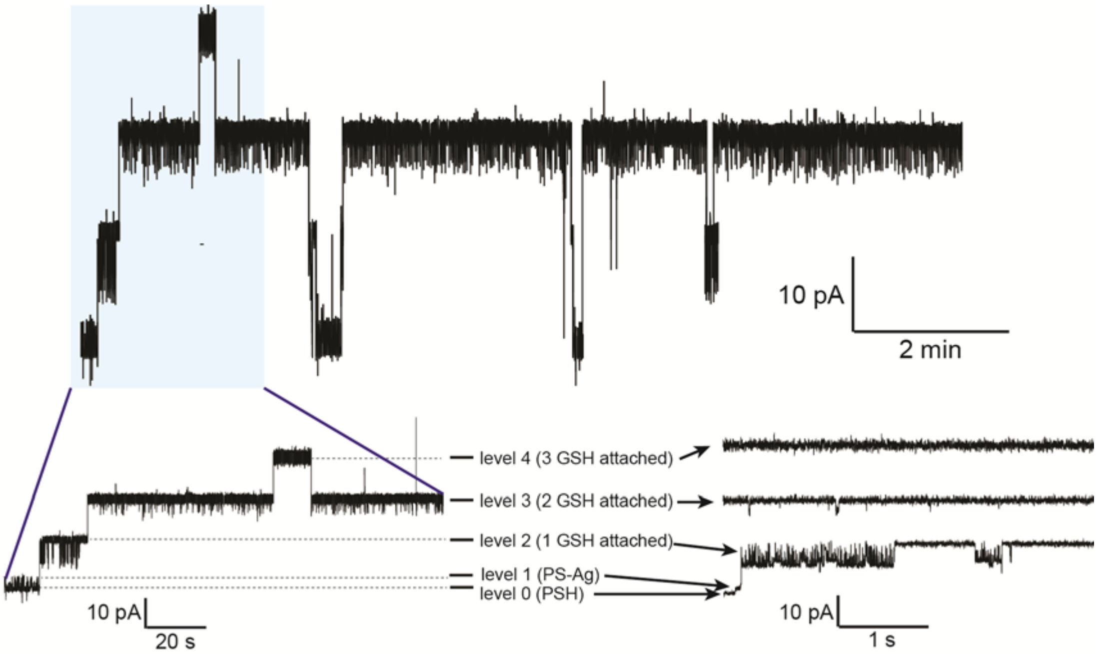

Figure 3.10. *Reversible silver(I)-glutathione (GSH) polymer formation.* $AgNO_3$ *(cis, free concentration 50 nM)/GSH (trans, 400 µM) was added to PSH at –50 mV. The current trace on top shows the stepwise polymer formation and breakdown. The polymers are very stable and can have a lifetime of 30 min. The two traces at the bottom show the expanded current recording. At the levels with one and two GSH attached, sub-levels are observed. Buffer: 2 M* KNO_3*, 10 mM MOPS, 100 µM EDTA, pH 7.4.*

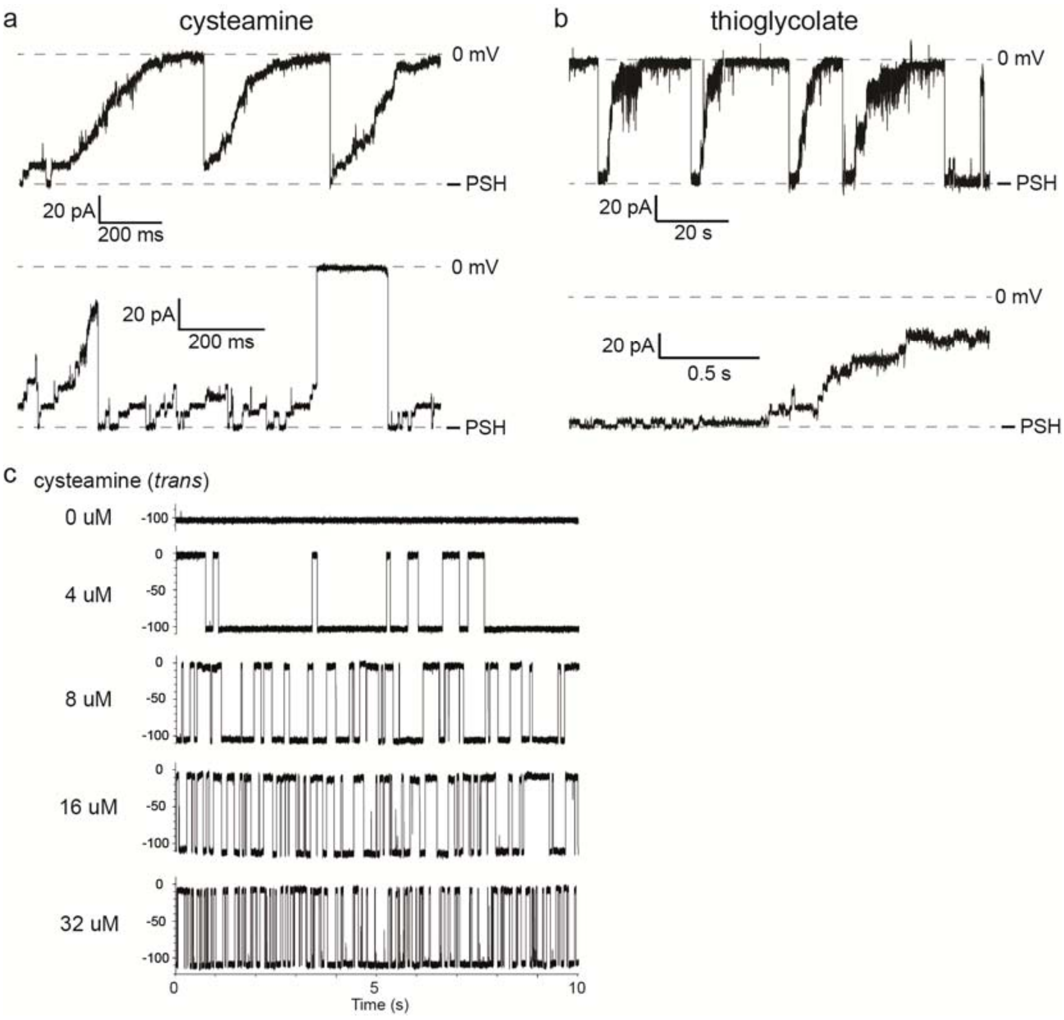

Figure 3.11. *Silver(I)-thiolate polymer formation with different thiol compounds. (a) Stepwise polymer formation with cysteamine. The two traces were collected under the same conditions. They show the stepwise build-up of different lengths of polymer that lead to different degrees of pore blockade. The polymers always break down in one step, presumably by the cleavage of the polymer chain near the pore cysteine residue. Conditions: 133 nM free Ag^+ (cis)/16 μM cysteamine (trans). (b) Stepwise polymer formation with thioglycolate. The lower trace shows a magnified region of the upper trace. As in (a), polymers of different lengths were observed. Conditions: 266 nM free Ag^+ (cis) / 1 μM thioglycolate (trans). (c) One-step complete blockade of PSH by silver(I)-cysteamine polymer. Although stepwise polymer formation in (a) was observed, silver(I)-cysteamine polymer usually causes one-step pore blockade. Current traces for the titration with cysteamine at 266 nM free Ag^+ (cis) are shown. The residence times of both open pore and blocked level show a linear dependence on the concentration of cysteamine.*

Breakdown of Ag^+-thiolate polymers

The breakdown of the Ag^+-GSH polymer was stepwise and had ΔI values (+12 pA) that were the reverse of the formation steps (Figure 3.10). In contrast, Ag^+-thiolate polymers formed with L-cysteine, thioglycolate and cysteamine underwent single-step dissociation (Figures 3.11a and b). The detachment of the polymer usually returns back to the open pore level (PSH), but sometimes a level corresponding to PSH with short Ag^+-thiolate oligomer attached was reached. The reversal of the complete blockades caused by cysteamine and β-mercaptoethanol (formed in one-step) occurred in single step as well (Figure 3.11c).

Proposed mechanism for the formation and breakdown of Ag^+-thiolate polymers

In the stepwise blocking of PSH, different thiol compounds give rise to steps of different amplitudes (Table 3.4). GSH shows the largest step (–12 pA) compared to L-cysteine (–7 pA), cysteamine (–5 pA) and thioglycolate (–3 pA), presumably due to the larger size of GSH compared to the other three thiol compounds (see the structures in Table 3.4). This also suggests that each step corresponds to the attachment of presumably one thiol molecule to the growing Ag^+-thiolate polymer. The binding of Ag^+ ion, which is expected to cause ΔI of about –1.5 to –2 pA, should occur after each thiol attachment for the growth of $(–Ag–S(R)–)_n$ polymer. However, this is invisible in our measurement. No stepwise polymer formation was observed with β-mercaptoethanol and DTT (both contain hydroxyl group(s) in addition to the thiol group(s)). However, we are not sure whether the presence of an extra Ag^+ coordinating ligand (carboxyl or amino group),[32] a more acidic thiol group ($pK_a < 9$, see Table 3.4) or an overall negatively charged thiol molecule is necessary for polymer formation.

The sub-levels observed in the silver(I)-GSH polymer (Figure 3.10) might due to the different coordination modes of GSH to Ag^+ (GSH has one amino group and two carboxyl groups). More coordinating groups on GSH might also stabilize the silver(I)-GSH polymer compared to the other silver(I)-thiolate polymers (hence the longer lifetime of silver(I)-GSH polymer). The more shielded Ag^+ centre in silver(I)-GSH polymer might also retard the cleavage of the polymer by free thiol molecules, which would lead to the one-step breakdown of polymer. Therefore, silver(I)-GSH polymer undergoes a stepwise breakdown, while other silver(I)-thiolate polymers (with L-cysteine, cysteamine and thioglycolate) undergo one-step dissociation. The higher peak-to-peak noise in levels corresponding to the longer polymers might due to the greater movement of the polymer chain inside the protein pore, which causes bigger fluctuations in the transmembrane current. The increase in transmembrane current noise with polymer length has been reported by Shin *et al.* for a disulfide-based polymer.[67]

The proposed mechanism for the stepwise formation of silver(I)-thiolate polymers is depicted in Figure 3.12. In our single-channel experiments, each major step observed during polymer growth belongs to the attachment of a thiol molecule. Then a Ag^+ ion associates with this thiol molecule (in an undetectable step). A new thiol molecule binds to this new Ag^+ centre and continues the polymer growth. In addition to the thiol group, the Ag^+ centre is coordinated by an extra ligand (carboxyl or amino), which is necessary for polymer formation.[31] The stepwise breakdown of the silver(I)-GSH polymer undergoes the reverse of these steps. One-step dissociation of silver(I)-thiolate polymers (thiolate = L-cysteine, cysteamine and thioglycolate) arises from the cleavage of S–Ag bond near the pore cysteine residue. One-step breakdown is possible in the polymers formed with the latter three thiols, presumably because free thiol molecules can attack the less highly shielded Ag^+ centers in the polymer (because of the smaller size and the fewer number of coordinating groups in these thiols compared to GSH).

The reversible one-step complete blockades in both the Ag^+/cysteamine and Ag^+/β-mercaptoethanol systems (Figure 3.11c) were observed with both PSH and the cysteine-free homoheptamer $(AG)_7$, suggesting that the cysteine thiol group in PSH is unnecessary for the blockades. With PSH, this blockade with the Ag^+/cysteamine system begins from a level that had slightly lower conductance than PSH, which possibly have the cyclic  $PS\overset{Ag}{\underset{Ag}{\rightleftharpoons}}SCH_2CH_2NH_3^+$ structure from which polymer growth cannot take place. We propose that the one-step complete blockade arises from the obstruction of the αHL pore by large silver(I)-thiolate aggregates formed in solution. The pre-formed polymer aggregates might arise from the diffusion of small amounts of thiolate and/or Ag^+ ion across the pore. Interestingly, although β-

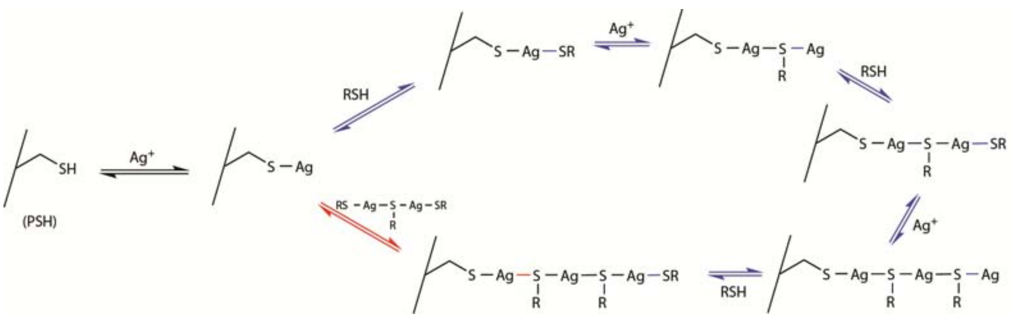

Figure 3.12. *Proposed mechanisms for the growth and breakdown of silver(I)-thiolate polymer. Alternating additions (or removals) of* Ag^+ *ion and thiol molecule (RSH) (black and blue arrows) lead to stepwise polymer growth (or breakdown). Sometimes silver(I)-thiolate polymer is preformed in solution. Its attachment (red arrow) leads to the one step blockade as seen in Figure 3.11a. One-step dissociation of the silver(I)-thiolate polymer undergoes the reverse step, which might be assisted by free thiol molecule. For simplicity, silver-thiolate oligomer containing up to three* Ag^+ *ions are drawn. Longer polymers are possible. In addition to the thiol sulfur atom, carboxyl or amino group from the thiol compound can also coordinate to silver(I).*

mercaptoethanol does not show stepwise silver(I)-thiolate polymer formation on PSH, it gives the same kind of one-step complete blockade as cysteamine when present in high concentration (~1 mM). It is uncertain why Ag^+/β-mercaptoethanol shows this behaviour.

Kinetic analysis of silver(I)-thiolate polymer formation and breakdown were not performed due to the instability of the planar lipid bilayer towards this polymer.

3.3.6 Reversible cadmium(II) ion binding

The reversible binding between Cd^{2+} ion and thiolate was studied with $Cd(NO_3)_2$ (20–160 μM, added to the *cis* side) and PSH at pH 7.4 (2 M KNO_3, 10 mM MOPS, chelex) and 22 °C. No chelating agent, for example, EDTA, was present in the buffer. PSH has a single-channel current of –100 ± 1 pA at –50 mV (n = 4). The addition of $Cd(NO_3)_2$ gave reversible blockades with an amplitude (ΔI) of –3.8 ± 0.1 pA (n = 4) relative to the unoccupied pore level (Figure 3.13a). The blockades associated with Cd^{2+} ions were not seen with $(AG)_7$, confirming a specific interaction with the cysteine residue in PSH. The frequency of the blockades with PSH increased with $Cd(NO_3)_2$ concentration. Both of these observations suggest that the new level arises from a pore-Cd^{2+} ion complex. The Cd^{2+} ion concentration inside the pore is assumed to be the same as that in bulk solution. A plot of the reciprocal of the mean inter-event dwell time (i.e. the mean dwell time for the unoccupied pore) ($1/\bar{\tau}_{PSH}$) against $Cd(NO_3)_2$ concentration was constructed and showed a linear dependence (Figure 3.13c), which agrees with a bimolecular interaction for which $1/\bar{\tau}_{PSH} = k_{on\text{-}Cd}[Cd(NO_3)_2]$. Thus only one Cd^{2+} ion is bound to the thiolate at a time and the blocked level is assigned to be the complex PS-Cd^+. Plot of the reciprocal of the mean lifetime of the complex ($1/\bar{\tau}_{P\text{-}S\text{-}Cd^+}$) versus $Cd(NO_3)_2$ concentration gives a near zero slope, which is consistent with a unimolecular dissociation mechanism in which $1/\bar{\tau}_{P\text{-}S\text{-}Cd^+} = k_{off\text{-}Cd}$. The forward and reverse reaction rate constants determined from the $\bar{\tau}$ values are $k_{on\text{-}Cd} = (5.9 \pm 0.6) \times 10^4$ M^{-1}s^{-1} and $k_{off\text{-}Cd} = 13 \pm 1$ s^{-1} (n = 4), respectively. The dissociation constant $K_{d\text{-}Cd}$ (= $k_{off\text{-}Cd}/k_{on\text{-}Cd}$) is $(2.2 \pm 0.4) \times 10^{-4}$ M (Table 3.5). The Cd^{2+} ion is usually tetrahedrally or octahedrally-coordinated,[25] so the vacant coordination sites on the pore bound Cd^{2+} ion are likely to be occupied by water

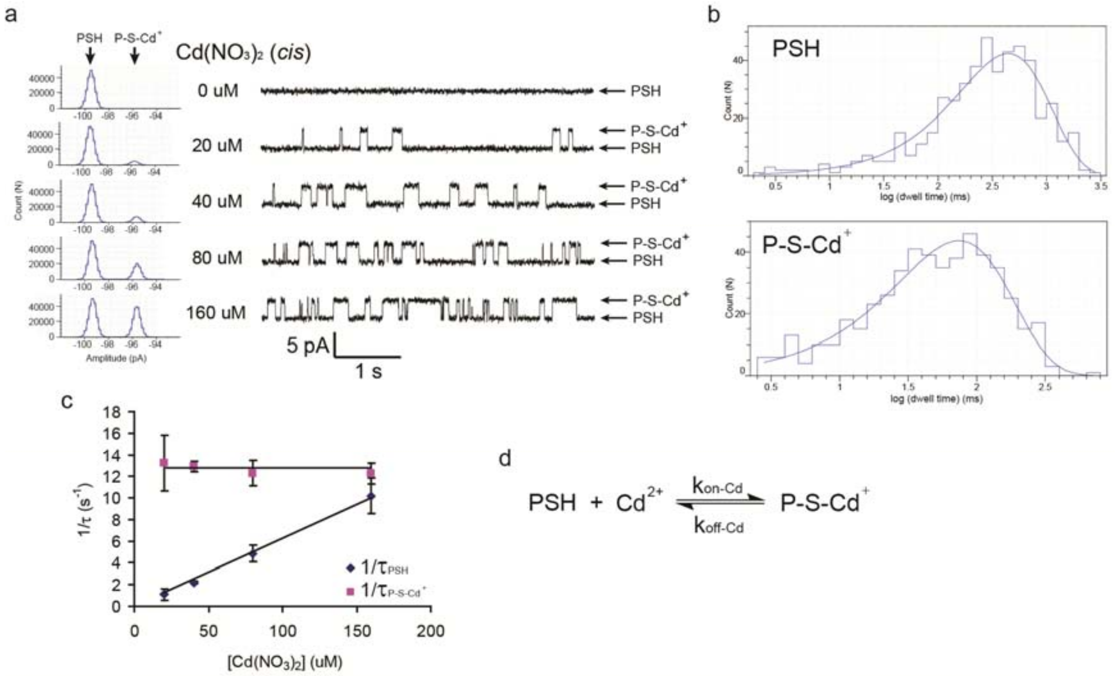

Figure 3.13. *Reversible binding of Cd^{2+} ion to PSH. (a) Stacked current recording traces of PSH at different concentrations of $Cd(NO_3)_2$ (cis). Conditions: 2 M KNO_3, 10 mM MOPS, chelex, pH 7.4, at –50 mV and 22 °C. Unoccupied pore (PSH) and cadmium(II)-bound ($P\text{-}S\text{-}Cd^+$) levels are indicated on the right hand side. All points amplitude histograms are shown on the left. The histograms are fitted to the sum of two Gaussian functions. (b) Dwell time histograms of PSH and $P\text{-}S\text{-}Cd^+$ in the presence of 40 μM $Cd(NO_3)_2$. Each histogram is fitted to a single-exponential function using Clampfit (Molecular Devices) to determine the mean dwell time $\bar{\tau}$. (c) Reciprocals of the mean dwell times of the open pore ($1/\bar{\tau}_{PSH}$) and the Cd^{2+} ion-bound ($1/\bar{\tau}_{P\text{-}S\text{-}Cd^+}$) levels versus the concentrations of $Cd(NO_3)_2$. Each data point (mean ± s.d.) is obtained from four experiments. (d) Proposed kinetic scheme describing cadmium(II) binding to PSH.*

molecules. The water exchange rate on Cd^{2+} ion is too fast to be detected ($\tau \sim 10$ ns).[25]

The introduction of an additional coordinating ligand, for example, histidine (HC mutant, i.e. $(AG)_6(L135H/G137C)_1$) or cysteine (CC mutant, i.e. $(AG)_6(L135C/G137C)_1$), at position 135 (see Chapter 1, Figure 1.8d) adjacent to the cysteine at position 137, resulted in the stronger binding of Cd^{2+} ion (Table 3.5). As in the case of PSH, a new level, appeared after the addition of $Cd(NO_3)_2$ (*cis*) (Figures 3.14a and 3.15a). Both the association and dissociation of Cd^{2+} ions are one-step processes. No singly-ligated intermediate was observed. The association of Cd^{2+} ion follows bimolecular kinetics (Figures 3.14b and 3.15b), which suggests that only one Cd^{2+} ion is bound. Binding of another Cd^{2+} ion was not observed even at higher concentration of Cd^{2+} ion (160 μM). The $K_{d\text{-}Cd}$ of the HC mutant ($(6.8 \pm 2.4) \times 10^{-6}$ M, Table 3.5) and the CC mutant ($(6.5 \pm 2.4) \times 10^{-7}$ M) are about 30 and 300 times respectively lower than that of the single cysteine mutant PSH ($(2.2 \pm 0.4) \times 10^{-4}$ M). Such stronger binding and the absence of second Cd^{2+} binding in HC and CC suggest that the two ligands in each mutant are close enough to chelate one Cd^{2+} ion. (The Cβ–Cβ distance between positions 135 and 137 is 6.3 Å. The bond lengths of Cd–S(cysteine thiolate) and Cd–N(imidazole) are ~2.5 Å[38,39,68] and ~ 2.4 Å,[38] respectively. Thus together with the C–S bond and/or the imidazole ring, ligands at positions 135 and 137 should be capable of chelating Cd^{2+}.)

The stronger binding (smaller $K_{d,Cd}$) of Cd^{2+} to HC is mainly due to the faster association ($(1.3 \pm 0.3) \times 10^6$ $M^{-1}s^{-1}$), while the even stronger binding to CC is a result of the very slow dissociation of bound Cd^{2+} ion ($(3.5 \pm 0.5) \times 10^{-2}$ s^{-1}). Quick Cd^{2+} coordination by HC might arise from the higher pK_a value of the cysteine thiol group due to the interaction with the proximal His-135 residue, and/or the fast binding by the histidine imidazole group. Sluggish dissociation from CC is presumably due to the tight intramolecular binding so that CC-Cd^{2+} complex exists mostly in the chelated form rather than the singly-liganded intermediate (Figure 3.15c). Similar argument might explain the comparable dissociation rate constants in HC (13 ± 1 s^{-1}) and PSH (9.2 ± 2.5 s^{-1}): the predominant form of the HC-Cd^{2+} complex is the singly, thiol-liganded form instead of the chelated form (Figure 3.14c). This means that the

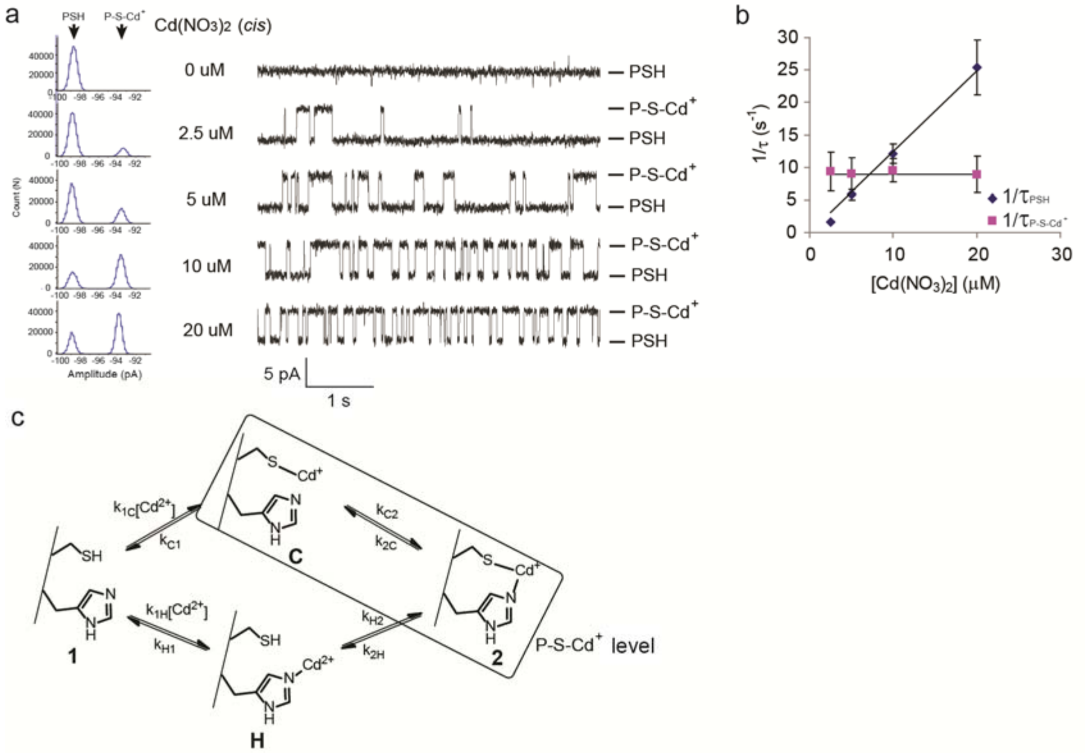

Figure 3.14. *Reversible binding of Cd^{2+} ion to the HC mutant. (a) Stacked current recording traces of the HC mutant (i.e. $(AG)_6(L135H/G137C)_1$) at different concentrations of $Cd(NO_3)_2$ (cis). Conditions were the same as in Figure 3.13a. Concentrations of $Cd(NO_3)_2$ are labelled on the left hand side. Open pore (PSH) and Cd^{2+} ion-bound (P-S-Cd^{+}) levels are indicated on the right hand side. All points amplitude histograms are shown on the left. The histograms are fitted to the sum of two Gaussian functions. (b) Reciprocals of the mean dwell times for both open pore ($1/\bar{\tau}_{PSH}$) and Cd^{2+} ion-bound ($1/\bar{\tau}_{P\text{-}S\text{-}Cd^{+}}$) levels versus the concentration of $Cd(NO_3)_2$. Each data point is the mean ± s.d. from 3 repeats. (c) Kinetic scheme showing the stepwise chelation of Cd^{2+} by the two ligands. See Section 3.6.12 for the relationship between the measured rate constants and those of the individual steps.*

histidine imidazole group is a poor second ligand in chelating Cd^{2+}. The similar association rate constants between CC ((5.3 ± 1.8) × 10^4 $M^{-1}s^{-1}$) and PSH ((5.9 ± 0.6) × 10^4 $M^{-1}s^{-1}$) might imply that their cysteine thiol groups have comparable pK_a values.

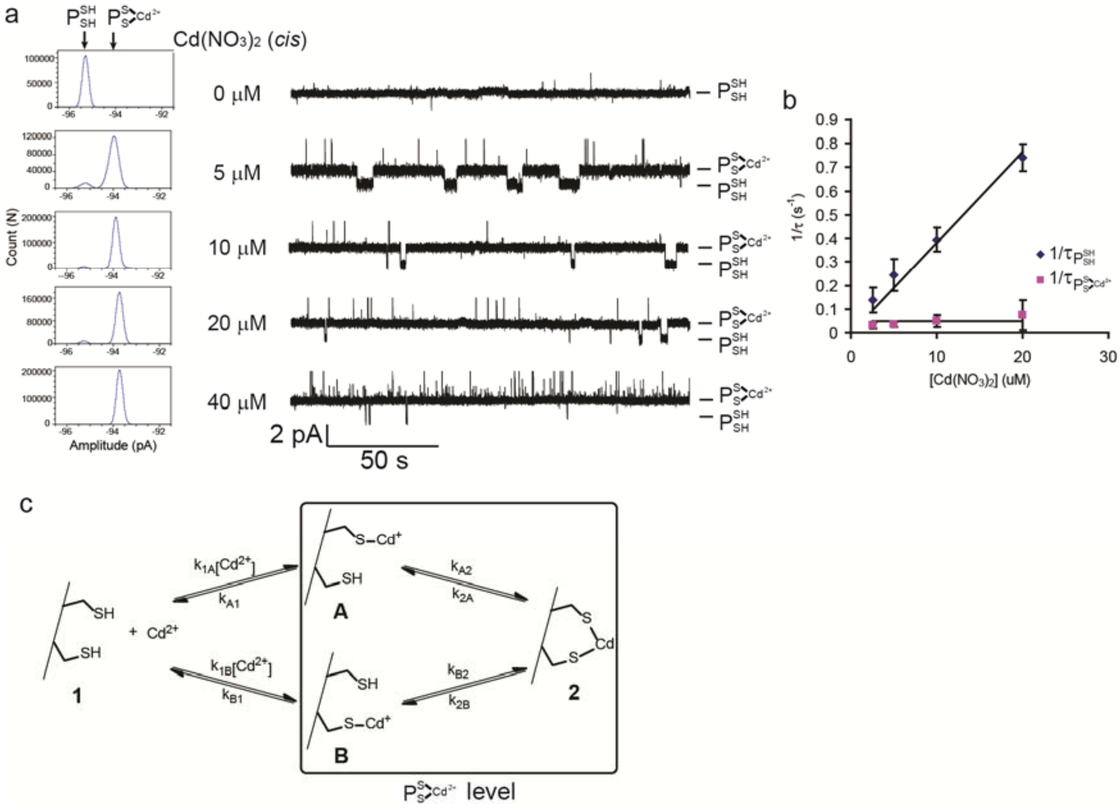

Figure 3.15. *Reversible binding of Cd^{2+} ion to the CC mutant. (a) Stacked current recording traces of the CC mutant (i.e. $(AG)_6(L135C/G137C)_1$) at different concentrations of $Cd(NO_3)_2$ (cis). Conditions were the same as in Figure 3.13a. Concentrations of $Cd(NO_3)_2$ are labelled on the left hand side. The open pore (P_{SH}^{SH}) and Cd^{2+} ion-bound ($P_{S}^{S}{>}Cd^{2+}$) levels are indicated on the right hand side. All points amplitude histograms are shown on the left. The histograms are fitted to the sum of two Gaussian functions. (b) Reciprocals of the mean dwell times for both open pore ($1/\bar{\tau}_{P_{SH}^{SH}}$) and Cd^{2+} ion-bound ($1/\bar{\tau}_{P_{S}^{S}>Cd^{2+}}$) levels versus the concentration of $Cd(NO_3)_2$. Each data point is the mean ± s.d. from 3 repeats. (c) Kinetic scheme showing the stepwise chelation of Cd^{2+} by the two cysteine thiol groups. The equilibrium between the singly-liganded intermediate and the chelated form lies to the right hand side, i.e. the chelated form. See Section 3.6.12 for the derivations of the measured rate constants into those of the individual steps.*

Table 3.5. *Kinetics constants for the binding of Cd^{2+} ion to different mutants.*

Protein	Amplitude (pA)	$k_{on\text{-}Cd}$ ($M^{-1}s^{-1}$)	$k_{off\text{-}Cd}$ (s^{-1})	$K_{d\text{-}Cd}$ (M)[a]
PSH (n = 4)	–3.8 ± 0.1	(5.9 ± 0.6) × 10^{4}	13 ± 1	(2.2 ± 0.4) × 10^{-4}
HC (n = 3)	–4.9 ± 0.6	(1.3 ± 0.3) × 10^{6} [b]	9.2 ± 2.5 [b]	(6.8 ± 2.4) × 10^{-6}
CC (n = 3)	–1.4 ± 0.2	(5.3 ± 1.8) × 10^{4} [b]	(3.5 ± 0.5) × 10^{-2} [b]	(6.5 ± 2.4) × 10^{-7}

Conditions: 2 M KNO_3, 10 mM MOPS, chelex, pH 7.4; –50 mV; $Cd(NO_3)_2$ (cis).

[a] *$K_{d\text{-}Cd}$ is the dissociation equilibrium constant, in which $K_{d,Cd} = k_{off\text{-}Cd} / k_{on\text{-}Cd}$. $K_{d,Cd}$ is calculated from the $k_{on\text{-}Cd}$ and $k_{off\text{-}Cd}$ values shown in the same row.*

[b] *These are the apparent rate constants. For example, $k_{on\text{-}Cd}$ of CC is the 'stoichiometric' association rate constant (Figure 3.15c), i.e. it is the sum of the 'site' association rate constants of the two thiol ligands (k_{01}). Another example is $k_{off\text{-}Cd}$ of CC, which is a composite rate constant that depends on the intramolecular dissociation constant (between the singly-liganded intermediate and the chelated complex) and the dissociation rate constant from the singly-liganded intermediate to the metal-free pore. $k_{off\text{-}Cd} = k_{10} / (1 + 1/2K_{d,intra})$. See Section 3.6.12 for more details.*

Derivations of the measured rate constants into the rate constants and dissociation equilibrium constants of the individual coordination steps shown in Figures 3.14c and 3.15c can be found in Section 3.6.12.

3.3.7 Reversible cadmium(II)-thiolate complex formation

Cd^{2+} ion forms tetrahedral complexes with thiolate ions in both solid and solution states (see Section 3.1.3).[25] In the study of ion channels (see Section 3.1.2), for example, Cd^{2+} ion has been reported to form a tetracysteine-coordinated complex inside a voltage-dependent K^{+} channel.[69] On the other hand, due to the propensity of the thiolate to bridge two Cd^{2+} ions, Cd^{2+}-thiolate complexes are prone to exist as clusters, as in cadmium(II)-bound metallothionein (Figure 3.1).[70]

Glutathione (GSH) is one of the most important thiol compound finds *in vivo* (1–10 mM). Apart from keeping the cytosol in a reducing environment, it is also responsible for heavy metal detoxification.[41]

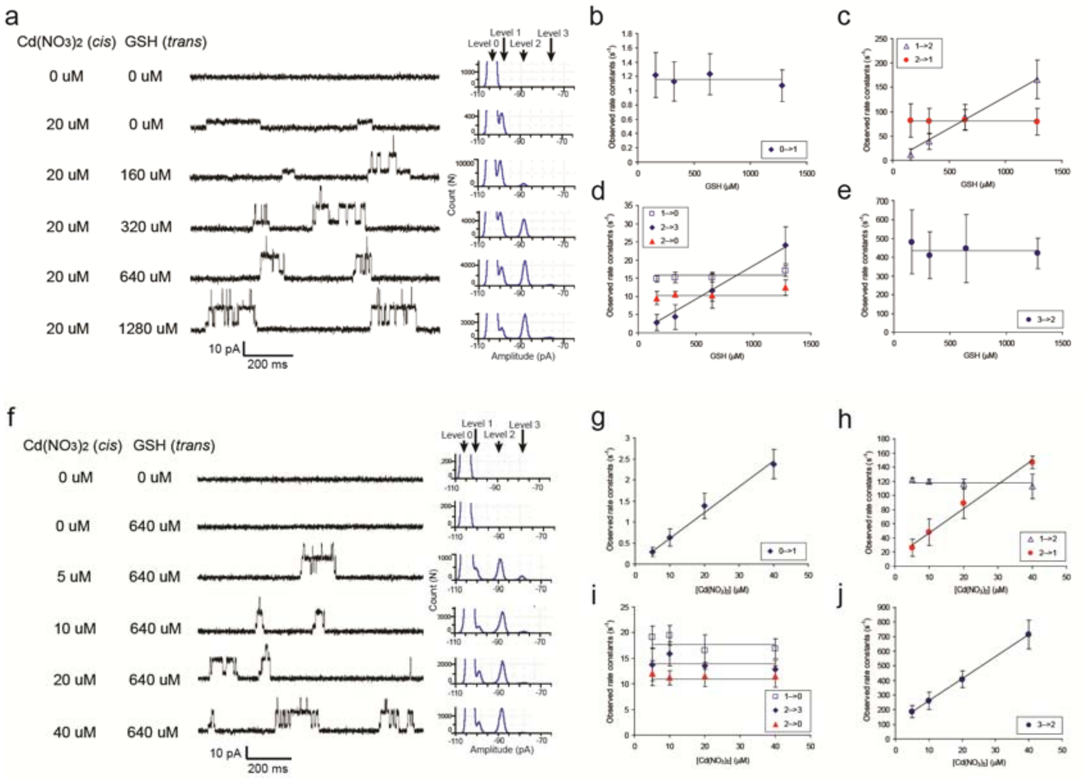

__Figure 3.16.__ Cadmium(II)-glutathione complex formation. (a,f) Stacked single-channel electrical current recording traces of PSH at various concentrations of $Cd(NO_3)_2$ *(cis) and GSH (trans). (a) Titration with GSH (160–1280 μM, trans) at fixed* $Cd(NO_3)_2$ *concentration (20 μM, cis). (f) Titration with* $Cd(NO_3)_2$ *(5–40 μM, cis) at fixed GSH concentration (640 μM, trans). Concentrations of* $Cd(NO_3)_2$ *and GSH are labelled on the left hand side of each trace. All points amplitude histograms are shown on the right hand side to show the change in the ratio of time spent at each level upon titration. Levels 0–3 are as labelled in Figure 3.17b. The peak for level 0 (unoccupied pore) is truncated to emphasize the changes among levels 1–3. (b-e) Plots of the observed rate constants calculated by QuB for each transition versus GSH concentration from the titrations shown in (a). (g-j) Plots of the observed rate constants versus* Cd^{2+} *ion concentration shown in (f). Each data point is the mean from 4 repeats. Conditions: 2 M* KNO_3*, 10 mM MOPS, chelex, pH 7.4, at –50 mV and 22 °C.*

Two sets of titration experiments were performed to decipher the reaction kinetics involved in cadmium(II)-glutathione complex formation. The first set titrates GSH (*trans*) (160–1280 μM) in the presence of a fixed concentration of $Cd(NO_3)_2$ (*cis*)

(20 μM) (Figure 3.16a). The other set titrates $Cd(NO_3)_2$ (*cis*) (5–40 μM) at a fixed concentration of GSH (*trans*) (640 μM) (Figure 3.16f). PSH was again used as the detector in 2 M KNO_3, 10 mM MOPS, chelex, pH 7.4, at –50 mV and 22 °C.

Three new levels (levels 2–4) appeared from the P-S-Cd^+ level (level 1 in Figure 3.17b, ~ –4 pA). The three steps, 1→2 (represents transition from level 1 to level 2), 2→3 and 3→4, show similar current changes of ~ –10 to –11 pA (Figure 3.17c). Transitions among these levels are reversible. Replacing GSH with GSSG does not give any of these levels (n = 3), in agreement with Delalande *et al.*[41] who found that the thiol group in GSH is necessary for Cd^{2+} binding, while the sulfur atoms in GSSG cannot bind. Both $(AG)_7$ and PSH showed no event with GSH (*trans*) alone (Figure 3.16f), while $(AG)_7$ also showed no interaction in the presence of both $Cd(NO_3)_2$ (*cis*) and GSH (*trans*). Thus, the events observed with PSH must arise from glutathione coordination to the bound Cd^{2+} in P-S-Cd^{2+}, leading to the formation of P-S-Cd^{2+}-glutathione complexes. This is supported by the kinetic analysis using the software QuB (see Section 3.6.9). Reaction rate constants and reactant concentration dependences obtained from this analysis are summarized in Table 3.6 and Figure 3.17a. Level 4 was excluded in this analysis, as it rarely occurred and not enough data could be gathered for kinetic analysis. The concentrations of Cd^{2+} ion and GSH inside the pore were assumed to be the same as that in the *cis* and *trans* compartment, respectively. Plots of the observed rate constants obtained from QuB for each transition versus $[Cd^{2+}]$ or [GSH] showed that 0→1, 2→1 and 3→2 have first-order dependences on $[Cd^{2+}]$ ($n_{0\text{-}1}/\sum\tau_0 = k_{0\text{-}1}[Cd^{2+}]$, $n_{2\text{-}1}/\sum\tau_2 = k_{2\text{-}1}[Cd^{2+}] + k_{2\text{-}1'}$ and $n_{3\text{-}2}/\sum\tau_3 = k_{3\text{-}2}[Cd^{2+}] + k_{3\text{-}2'}$) ($n_{0\text{-}1}$ represents the total number of 0→1 transitions; $\sum\tau_0$ is the sum of dwell times at level 0; $k_{0\text{-}1}$ is the second-order rate constant for 0→1; $k_{2\text{-}1'}$ is the first-order rate constant for 2→1, and so on) (Figures 3.16g,h,j). In addition, both

2→1 and 3→2 show a non-zero y-intercept ($k_{2\text{-}1'}$ and $k_{3\text{-}2'}$, respectively), indicating that they also undergo a Cd^{2+} concentration-independent pathway, i.e. a unimolecular pathway. On the other hand, 1→2 and 2→3 have a first-order dependence on [GSH] ($n_{1\text{-}2}/\sum\tau_1 = k_{1\text{-}2}$[GSH] and $n_{2\text{-}3}/\sum\tau_2 = k_{2\text{-}3}$[GSH]) (Figures 3.16c,d), i.e. the reactions are bimolecular. Both 1→0 and 2→0 have zero-order dependence on both reactants, thus both are unimolecular reactions ($n_{1\text{-}0}/\sum\tau_1 = k_{1\text{-}0}$ and $n_{2\text{-}0}/\sum\tau_2 = k_{2\text{-}0}$) (Figures 3.16d,i). Other possible transitions, such as 0→3, 3→0, 1→3, 3→1 and 0→2, are not observed (Figure 3.17a).

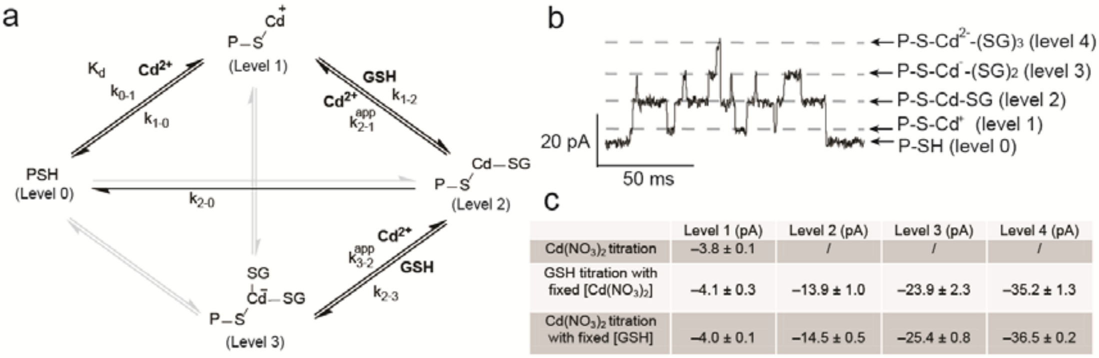

	Level 1 (pA)	Level 2 (pA)	Level 3 (pA)	Level 4 (pA)
$Cd(NO_3)_2$ titration	–3.8 ± 0.1	/	/	/
GSH titration with fixed [$Cd(NO_3)_2$]	–4.1 ± 0.3	–13.9 ± 1.0	–23.9 ± 2.3	–35.2 ± 1.3
$Cd(NO_3)_2$ titration with fixed [GSH]	–4.0 ± 0.1	–14.5 ± 0.5	–25.4 ± 0.8	–36.5 ± 0.2

Figure 3.17. *Summary of cadmium(II)-glutathione complex formation. (a) Scheme showing the transitions among the various levels. Black arrows represent transitions that are observed, while grey ones represent those that are absent.* $k_{0\text{-}1}$ *represents the rate constant for the transition from level 0 to level 1 etc.* $k^{app}_{2\text{-}1}$ *is the apparent rate constant for the transition from level 2 to level 1 etc.* $k^{app}_{2\text{-}1}$ *is equal to* $k_{2\text{-}1}[Cd^{2+}] + k_{2\text{-}1'}$. K_d *is the dissociation constant for the release of* Cd^{2+} *ion from* $P\text{-}S\text{-}Cd^{+}$. *The words,* Cd^{2+} *or GSH, shown in bold next to the arrow denote the first-order reactant dependence for that particular transition. Values of rate constants are summarized in Table 3.6. The structure shown at each level is proposed according to the results from kinetics analysis. (b) A typical cluster of events showing all five levels and the various transitions. Each level is labelled with the proposed structure. (c) Current blockades of each level relative to the unoccupied pore (PSH, assigned 0 pA). A negative value means decrease in conductance. Conditions: 2* M *KNO_3, 10* mM *MOPS, chelex, pH 7.4, at –50 mV and 22 °C.* $Cd(NO_3)_2$ *(cis)/GSH (trans).*

From the reactant concentration dependencies, we concluded that in the stepwise build-up of the Cd^{2+}-thiolate complex (0→1→2→3), a Cd^{2+} ion was first attached to PSH (0→1), followed by the addition of two GSH onto the Cd^{2+} ion in PS-Cd^{+} (1→2 and 2→3). Therefore, levels 2 and 3 are proposed to have the structures P-S-Cd-SG and P-S-Cd^{-}-$(SG)_2$, respectively (Figure 3.17a). Given the similar current change observed in 1→2, 2→3 and 3→4, it is likely that 3→4 involves the binding of the third GSH, leading to the tetra-coordinated Cd^{2+} complex, P-S-Cd^{2-}-$(SG)_3$ (level 4). In the stepwise breakdown of the complex (3→2→1→0), 1→0 is the unimolecular release of Cd^{2+} ion from P-S-Cd^{+}, as seen in the previous section in experiments with Cd^{2+} ion alone. Both 3→2 and 2→1 transitions occur through two pathways – a bimolecular one that involves the participation of a free Cd^{2+} ion, and a unimolecular dissociation of glutathione from the Cd^{2+}-thiolate complex. The free Cd^{2+} ion-dependent pathway most probably arises from the removal of the GS^{-} group as Cd^{+}-SG. Departure of Cd^{+}-SG group is also observed in the 2→0 transition.

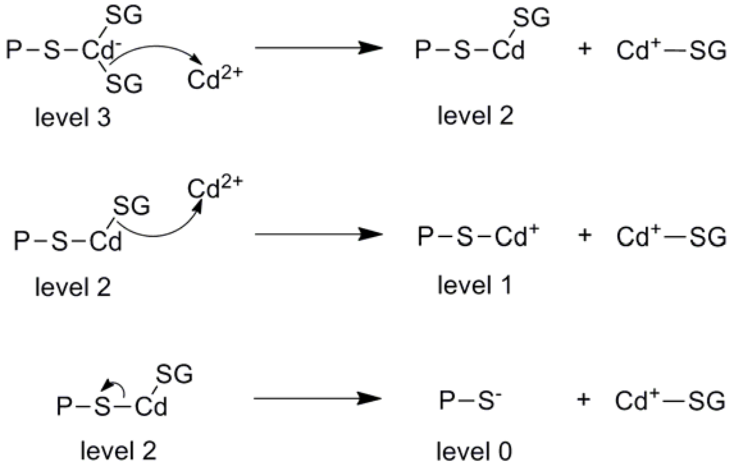

The rate constants ($k_{0\text{-}1}$, $k_{1\text{-}0}$) and the equilibrium dissociation constant ($K_{d\text{-}Cd}$) measured for Cd^{2+} ion binding here (Table 3.6) are within experimental error to those reported in Section 3.3.6. Rate constants for the binding of the first ($k_{1\text{-}2}$) and second ($k_{2\text{-}3}$) GSH molecules are $(5.3 \pm 1.3) \times 10^4$ $M^{-1}s^{-1}$ and $(1.0 \pm 0.3) \times 10^4$ $M^{-1}s^{-1}$, respectively. Dissociation of the first GSH has unimolecular ($k_{2\text{-}1'}$) and Cd^{2+}-dependent bimolecular ($k_{2\text{-}1}$) rate constants of 13 ± 4 s^{-1} and $(2.8 \pm 0.8) \times 10^6$ $M^{-1}s^{-1}$, respectively. The dissociation of the second GSH has unimolecular ($k_{3\text{-}2'}$) and Cd^{2+}-dependent bimolecular ($k_{3\text{-}2}$) rate constants of 55 ± 17 s^{-1} and $(7.0 \pm 1.0) \times 10^6$ $M^{-1}s^{-1}$. Unimolecular rate constant for the one-step cleavage of Cd^{+}-SG group from P-S-Cd-SG to give PSH ($k_{2\text{-}0}$) is 11 ± 2 s^{-1}. Note that all of the rate constants reported here are 'site' rate constants. They represent the rate constants for individual sites, that is the presence of more than one binding site or ligand has been taken into account (see legend of Table 3.6 for more details).

Table 3.6. *Summary of the reaction rate constants[a] for Cd^{2+} binding and Cd^{2+}-glutathione complex formation with PSH.*

Cd^{2+} ion association/dissociation	$k_{0\text{-}1}$ ($M^{-1}s^{-1}$)	$(6.0 \pm 1.4) \times 10^4$
	$k_{1\text{-}0}$ (s^{-1})	16 ± 3
	K_d (μM)	270 ± 50
First GSH association/dissociation	$k_{1\text{-}2}$ ($M^{-1}s^{-1}$)	$(5.3 \pm 1.3) \times 10^4$
	$k_{2\text{-}1}$ ($M^{-1}s^{-1}$)[b]	$(2.8 \pm 0.8) \times 10^6$
	$k_{2\text{-}1'}$ (s^{-1})[b]	13 ± 4
Second GSH association/dissociation	$k_{2\text{-}3}$ ($M^{-1}s^{-1}$)	$(1.0 \pm 0.3) \times 10^4$
	$k_{3\text{-}2}$ ($M^{-1}s^{-1}$)[b]	$(7.0 \pm 1.0) \times 10^6$
	$k_{3\text{-}2'}$ (s^{-1})[b]	55 ± 17
	$k_{2\text{-}0}$ (s^{-1})	11 ± 2

Conditions: 2 M KNO_3, 10 mM MOPS, chelex, pH 7.4, at –50 mV and 22 °C.

$Cd(NO_3)_2$ (cis)/GSH (trans).

[a] *These values are the 'site' rate constants.[66] For instance, Cd^{2+} in $PSCd^{+}$ has three identical binding sites for GSH. So the measured association rate constant ('stoichiometric' rate constant) for $PSCd^{+}$ to PSCd-SG conversion is three times of the association rate constant of each binding site ('site' rate constant). See Figures 3.9d–e and the legend of Table 3.3 for more details about the difference between 'site' and 'stoichiometric' rate constants.*

[b] *The cleavage of glutathione from the Cd(II)-glutathione complexes undergoes two pathways, one is unimolecular and the other is bimolecular. The unimolecular rate constant was determined from the y-intercept of the linear fitted lines of the plots in Figures 3.16h and j. The bimolecular rate constants were calculated from the slopes.*

Association of the second GSH ($k_{2\text{-}3}$) is ~5 times slower than that of the first one ($k_{1\text{-}2}$), presumably because of the higher steric hindrance and the decreased electrostatic attraction from P-S-Cd-SG (for the binding of the second GSH) compared to P-S-Cd^+ (for the binding of the first GSH). On the other hand, the Cd^{2+} ion-assisted dissociation rate constant of the second GSH ($k_{3\text{-}2}$) is 2.5 times faster than that of the first GSH ($k_{2\text{-}1}$), and the unimolecular dissociation rate constant of the second GSH ($k_{3\text{-}2'}$) is ~4 times faster than that of the first GSH ($k_{2\text{-}1'}$). As the reported rate constants are for individual sites, i.e. the number of GSH present in the complexes has been taken into account, the differences in the dissociation rate constants reflect the weakening of the Cd–SG bond strength in P-S-Cd^--$(SG)_2$ compared to that in P-S-Cd-SG.

Our proposed formation of the four-coordinate heteroleptic cadmium(II)-thiolate complex (level 4, P-S-Cd^{2-}-$(SG)_3$) agrees with the literature that cadmium(II)-thiolate complexes have a maximum coordination number of four.[2,38,39] No Cd^{2+} cluster formation on PSH via bridging GS^- ligand(s) (e.g. P-S-Cd-S(G)-Cd^+-SG) was observed. Higher complexes were not seen even when GSH was mixed with Cd^{2+} ion in the same compartment. The inability to form clusters might be because of the limited space inside the αHL pore, and the bulky nature of both the protein cysteine residue and glutathione. Indeed, in the literature, polarographic study[71] and NMR study[41] on the cadmium(II)-glutathione system have shown the formation of discrete $Cd(GS)_2$ complex in solution at physiological pH and physiological concentration of GSH (~1–10 mM). In these studies, the Cd^{2+} ion is proposed to be coordinated by two sulfur atoms, one from each glutathione. The tetrahedral coordination sphere of Cd^{2+} ion is completed by two water molecules.[41] Our rate constants for the association and dissociation of GSH also agree with the GSH exchange rate on Cd^{2+} (0.1–10 ms, measured by ^1H-^{15}N HSQC NMR at pH 7.0[41]).

In solution, the fast kinetics of metal complex formation have been studied by flow methods, relaxation spectrophotometry, nuclear magnetic resonance, pulse radiolysis and flash photolysis *etc.*[72] With the unambiguous characterization of stepwise cadmium(II)-glutathione complex formation as shown in this section, the single-molecule nanopore approach is established as a complementary technique for studying the multi-step kinetics of metal complex formation.

3.4 Discussion

3.4.1 Two silver(I) ions are bound per cysteine thiol group

Using the nanopore technique, the dynamic nature of Ag^+ ion binding to a solvent-exposed thiol group (Cys137) was examined. The isolated thiol group in the nanoreactor provided a simpler system, in which no other thiol group was present to form higher silver(I)-thiolate complexes or polymers as in bulk solution.[37] Our results (see Section 3.3.4) showed clearly that two Ag^+ ions are bound reversibly to a thiol group at pH 7.4, with the proposed structure where sulfur acts as the double bridging ligand ($Ag–S^+(P)–Ag$, Figure 3.9d). Binding of one to two Ag^+ ions per thiol group has been reported in solution, e.g. GSH binds two Ag^+ ions at pH 3.2,[36] cysteine binds 1.35–1.5 Ag^+ ions at pH 7–9.[31,37] In the solid state, a thiol sulfur atom also bridges two Ag^+ ions (see Section 3.1.3).

In the macroscopic studies of ion channels (see Section 3.1.2), e.g. the P2X purinoreceptor,[23] the Shaker K^+ channel,[17] the cyclic nucleotide-gated (CNG) channel,[28] Ag^+ ion is reported to bind irreversibly to cysteine thiol groups lining the conducting pore (Figure 3.18). The irreversible binding occurs no matter whether

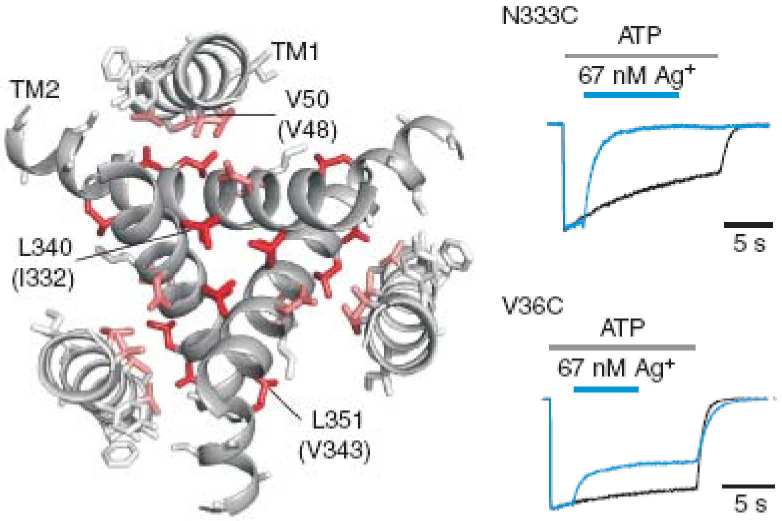

Figure 3.18. *Irreversible Ag^+ ion binding by a cysteine thiol group in the P2X purinoreceptor.*[23] *(Left) Structure of P2X (view through the channel). (Right) Asp-333 and Val-36 were separately mutated into cysteine and their Ag^+ ion sensitivities were measured. P2X requires ATP binding to open the channel. Black macroscopic current-time traces are control experiments recorded by applying ATP alone (ATP was added as indicated by the grey bars). Blue traces are recorded 2 min after the control, with both $AgNO_3$ (indicated by the blue bars) and ATP applied. The inhibitory effect of Ag^+ ion, preserved even after the removal of $AgNO_3$, demonstrating the irreversible nature of the silver-thiolate interaction inside the ion channel. The blue traces of both mutants were fitted to a single exponential function to obtain the time constant of modification (τ) for the calculation of the bimolecular modification rate constant (k) according to $k = 1/(\tau \times [Ag^+])$. Due to the trimeric nature of P2X, three cysteines were present in each mutant. Reprinted by permission from Macmillan Publishers Ltd: Nature Communications (ref. 23), copyright (2010).*

there is only one[17] or more cysteine-containing subunits[23,28] in the oligomeric ion channel. Moreover, apparent bimolecular kinetics was observed with rate constant up to 10^8 $M^{-1}s^{-1}$.[23] Our measured association rate constants (e.g. $k_{on\text{-}Ag1} = (2.2 \pm 0.2) \times 10^8$ $M^{-1}s^{-1}$, $k_{on\text{-}Ag2} = (8.3 \pm 1.3) \times 10^8$ $M^{-1}s^{-1}$ for PSH) are similar to the maximum rate constants observed in ion channel studies, consistent with the solvent-accessible nature of the thiol group of Cys137. However, opposite to the findings in ion channel works, reversible coordination of two Ag^+ is observed in our experiment. This may be because the macroscopic studies of ion channels are unable to differentiate the similar association kinetics of the two Ag^+ (only 4-fold difference in our results). Another possible reason is the first Ag^+ may block the narrow conductive pathway of ion channels completely, leading to one-step bimolecular blockade. On the other hand, most ion channels used for SCAM comprise more than one cysteine-containing subunit. Tight binding of Ag^+ by several proximal cysteine thiol groups, or by one cysteine thiol group plus ligands from other amino acid residues lining the conductive pathway may lead to the irreversible blockade of ion channels. More understanding of Ag–S chemistry is necessary to interpret the ion channel data.

3.5 Conclusions

Speed of modification of cysteine residues by thiophilic reagents is the sole data obtained from SCAM. Correct interpretation of this data, which relies on the understanding of the modification reaction, is pivotal in deciphering the molecular basis of the topology of ion channels in different conformations. In this chapter, the coordination kinetics of the two most important metal ion probes, Ag^+ and Cd^{2+}, towards cysteine thiol groups have been determined at the single-molecule level. We found that two Ag^+ ions are reversibly bound per thiol group with near diffusion limit kinetics (Section 3.3.4). On the contrary, only one Cd^{2+} ion is reversibly bound per thiol group (Section 3.3.6). The influence of neighbouring ligand (His or Cys) on the Cd^{2+} binding kinetics to a cysteine residue is also investigated. We hope our findings will enable single-molecule studies of ion channels with thiophilic metal ions, which may provide more structural information than macroscopic studies.

In addition to metal coordination, higher metal-thiolate complex formation was studied. Reversible silver(I)-thiolate polymer formation and breakdown was observed (Section 3.3.5). The stepwise built-up of cadmium(II)-glutathione complexes was clearly detected and the reaction rate constant of each step was determined unambiguously (Section 3.3.7). Notably, two pathways for the dissociation of glutathione from its cadmium(II) complexes were detected – the unimolecular dissociation and the bimolecular, free Cd^{2+}-assisted dissociation. A new cation-selective αHL mutant (AG) was designed for the above studies. In summary, these results provide detailed insights into the kinetics of metal complex formation and dissociation, which help to elucidate the ligand dissociation pathways and the coordination stoichiometry. More importantly, they demonstrate the advantage of the nanopore approach for studying multi-step reactions.

A versatile metal-ion detector based on αHL might be built by the combination of two different metal ion binding sites, such as a cysteine centre (with one or more cysteine residues) and a histidine centre[47] or an iminodiacetate ligand,[48] so that both soft and hard metal ions can be detected simultaneously. On the other hand, the bound metal ion might function as a catalytic centre (see Chapter 4), or for the detection of other biological-relevant molecules.[75]

3.6 Materials and Methods

3.6.1 Hemolytic assay

Rabbit red blood cells (rRBC) was prepared by washing rabbit blood (Harlan) with MBSA buffer (10 mM MOPS, 0.1% (w/v) bovine serum albumin, 150 mM NaCl at pH 7.4) prior to hemolytic assays. MBSA (900 µL) was added to the rabbit blood (450 µL). The solution was mixed and spun for 2 min at 100 × g and room temperature. The supernatant was removed. Another 900 μL MBSA was added and the mixture was centrifuged again. This procedure was repeated for another three times, or until the supernatant became completely clear. The rRBC were made up to 10 mL (1.0%) with MBSA and were ready for use in hemolytic assay.

To test and compare the hemolytic activity of the new AG mutant with WT αHL, a 96-well microtitre plate was used. Each initial well (column 1, lanes 1–2) was filled with 175 μL MBSA buffer, while all the other wells (column 2–12, lanes 1–2) were filled with 90 μL MBSA buffer. Then monomeric protein (5 μL, 5–25 ng) (prepared by *in vitro* transcription and translation (IVTT) (*vide infra*)) was added to each well in column 1, lanes 1–2. The mixture was mixed thoroughly with a pipette. Two-fold serial dilution of protein was carried out by transferring 90 μL of solution to each consecutive well from column 1 to column 11. The last 90 μL of solution taken from column 11 was discarded, leaving column 12 with no protein at all. 10 μL of washed rRBC was added to each well, giving a total volume of 100 μL per well. Hemolysis was monitored by following the absorbance change at 595 nm over 100 min (the first reading was taken after a 15 s interval with a 2 s mix time, the following 199 readings were taken every 30 s with a 1 s mix time) with a microplate spectrophotometer (Benchmark Plus, Bio-Rad).

For studying the denaturing effect of KNO_3 on monomeric αHL and to compare it with that of KCl, each initial well (column 1, lanes 1–2) was filled with 170 μL buffer (2.35 M KNO_3 or KCl, 150 mM NaCl, 10 mM MOPS, pH 7.4), while all the other wells (column 2–7, lanes 1) were filled with 85 μL of 150 mM NaCl, 10 mM MOPS at pH 7.4. Two-fold serial dilution of KNO_3 or KCl was carried out by transferring 85 μL of solution to each consecutive well from column 1 to column 6. The last 85 μL of solution taken out from column 6 was discarded, leaving column 7 with 0 M KNO_3 or KCl. Then 5 μL of the monomeric protein (5–25 ng, prepared by IVTT (Section 3.6.4) was added to each well in lanes 1. Finally, 10 μL of washed rRBC was added to each well to give a total volume of 100 μL per well. Hemolysis was followed as stated above.

3.6.2 Multiple site-directed mutagenesis (preparation of the αHL AG mutant)

The gene AG encodes an αHL polypeptide with four mutations, Lys8→Ala, Met113→Gly, Lys131→Gly and Lys147→Gly, and was constructed from the template pT7-WT-αHL.[76] Another gene G137C-D8-AG encodes an αHL polypeptide containing the same four mutations, with an additional Gly137→Cys mutation and a tail of eight-aspartate codons at the C terminus, was constructed from the template pT7-G137C-D8-RL3.[77] The RL3 background is a mutated version of WT. It contains silent mutations around and in the stem domain, which produce six new restriction sites.[78] It encodes the same protein sequence as WT. Both new genes, AG and G137C-D8-AG, were constructed by using multiple site-directed mutagenesis (QuikChange Lightning Multi Site-Directed Mutagenesis Kit, catalog no. 210515, Agilent Technologies) to introduce the necessary codons. For the gene AG, a polymerase chain reaction (PCR) was carried out with the following four sense primers: (K8A), 5'-GCAGATTCTGATATTAATATTGCAACCGGTACTACAGATATTGGAAGC-3', (WT_M113G), 5'-CGATTGATACAAAAGAGTATGGGAGTACTTTAACTTATGGATTCAACGG-3', (WT_K131G), 5'-TTACTGGTGATGATACAGGAGGAATTGGCGGCCTTATTGGTG-3', (WT_K147G), 5'-GTTTCGATTGGTCATACACTGGGATATGTTCAACCTGATTTCAAAAC-3'. For G137C-D8-AG, a

PCR was carried out with the following four sense primers: (K8A), 5'-GCAGATTCTGATATTAATATTGCAACCGGTACTACAGATATTGGAAGC-3', (RL3_M113G), 5'-GAATTCGATTGATACAAAAGAGTATGGGAGTACGTTAACGTACGGATTC-3', (G137C_RL3_K131G), 5'-GTTACTGGTGATGATACAGGAGGAATTGGAGGCCTTATTTGCGC-3', (RL3_K147G), 5'-GTTTCGATTGGTCATACACTTGGGTATGTTCAACCTGATTTCAAAAC-3'. The new codons are underlined. The *AflII* restriction site in pT7-G137C-D8-RL3 was removed by the K147G mutation. PCR procedure was similar to that suggested by the kit with slight modifications. In detail, each PCR (25 μL) was set up by mixing the following reagents in the order listed: 10X QuikChange Lightning Multi reaction buffer (2.5 μL), nuclease-free water (to make up the final volume of the reaction to 25 μL), double-stranded plasmid DNA template (50–100 ng), mutagenic primers (~100 ng each primer), dNTP mix (1 μL from the kit) and the QuikChange Lightning Multi enzyme blend (1 μL). The PCR reactions were carried out with following program: 94 °C for 5 min, 18 cycles of 95 °C (0.5 min), 55 °C (0.5 min), 68 °C (9 min), followed by a final extension at 68 °C for 7 min. The PCRs were cooled down to below 37 °C, followed by *Dpn I* restriction enzyme digestion (1 μL, supplied with the kit) at 37 °C for 1.5 h. Double stranded pT7 vector containing the mutant gene was generated by transforming *E. coli* XL-10 Gold ultracompetent cells with the PCR product. The DNA sequences of the genes were verified (Source BioScience).

3.6.3 Further site-directed mutagenesis (preparation of αHL HC, CC and H mutants)

The genes L135H-G137C, L135C-G137C and L135H encode αHL-AG polypeptides with mutations at positions 135 and/or 137. They were constructed from the template pT7-G137C-D8-AG (see previous section) using site-directed mutagenesis. For the gene L135H-G137C, two PCR reactions (Phusion$^{®}$ Flash PCR Master Mix, catalog no. F-548S, Finnzymes, Thermo Scientific) were carried out with the following two sets of primers: first set: mutagenic primer (sense, L135H-G137C-fw) 5'-CAGGAGGAATTGGAGGCCATA TTTGCGCAAATGTTTC-3', nonmutagenic primer (antisense, SC47) 5'-CAGAAGTGGTCCTGCAACTTTAT-3'; second set: mutagenic primer (antisense, L135H-G137C-rev) 5'-GAAACATTTGCGCAAATATGGCCTCCAATTCCTCCTG-3', nonmutagenic primer (sense, SC46) 5'-ATAAAGTTGCAGGACCACTTCTG-3'. For the gene L135C-G137C, two PCR reactions were carried out with the following two sets of primers: first set: mutagenic primer (sense, L135C-G137C-fw) 5'-GATACAGGAGGAATTGGAGGCTGTATTTGCGCAAATGTTTCGAT-3', nonmutagenic primer (antisense, SC47) 5'-CAGAAGTGGTCCTGCAACTTTAT-3'; second set: mutagenic primer (antisense, L135C-G137C-rev) 5'-ATCGAAACATTTGCGCAAATACAGCCTCCAATTCCTCCTGTATC-3', nonmutagenic primer (sense, SC46) 5'-ATAAAGTTGCAGGACCACTTCTG-3'. For the gene L135H, two PCR reactions were carried out with the following two sets of primers: first set: mutagenic primer (sense, L135H-C137G-fw) 5'-GATACAGGAGGAATTGGAGGCCATATTGGTGCAAATGTTTCGATTGGTC-3', non-mutagenic primer (antisense, SC47) 5'-CAGAAGTGGTCCTGCAACTTTAT-3'; second set: mutagenic primer (antisense, L135H-C137G-rev) 5'-GACCAATCGAAACATTTGCACCAATATGGCCTCCAATTCCTCCTGTATC-3', nonmutagenic primer (sense, SC46) 5'-ATAAAGTTGCAGGACCACTTCTG-3'. Notice that in the H gene, Cys-137 is mutated back into the αHL WT residue glycine. The new codons are underlined. The template DNA, pT7-G137C-D8-AG (100 ng/μL), was linearized with *NdeI* for the first primer set and with *HindIII* for the second set. The linearization prevents the template DNA from transforming *E. coli*, improves the PCR efficiency by removing supercoiled structure in the template DNA and also prevents concatemer formation. Each PCR (20 µL) was set up by mixing the following reagents: Phusion® Flash PCR Master Mix (10 µL, 2X), the digested template DNA (1 µL, 10 ng/µL), the two primers (1 µL each, 10 µM) and nuclease-free water (7 µL). The PCR reactions were carried out with following program: 98 °C for 30 s, 30 cycles of 98 °C (10 s), 68 °C (5 s), 72 °C (40 s), followed by a final extension at 72 °C for 60 s and then cooled down to 10 °C for storage. The two PCR products (5 µL each) for the same mutation were mixed and used to transform *E. coli* XL-10 Gold cells, which generate the pT7 vector containing the mutant gene by *in vivo* recombination. The DNA sequences of the genes were verified (Source BioScience).

3.6.4 Protein preparation

αHL heptamers were prepared as stated in Chapter 2, Section 2.6.9. The autoradiographic gel image is shown in Figure 3.19.

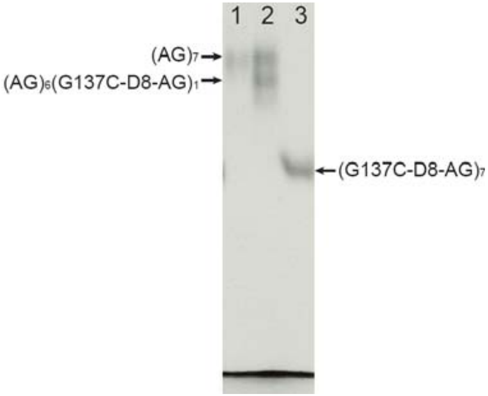

Figure 3.19. *5% SDS-PAGE gel showing the bands of αHL heptamers in the AG background. Lane 1: Heptamer made from AG monomer only. Lane 2: Heptamers formed from AG monomer and G137C-D8-AG monomer mixed in a 6:1 ratio. Lane 3: Heptamer comprising G137C-D8-AG monomer only.*

3.6.5 Planar lipid bilayer recordings

Details of experiments are as stated in Chapter 2, Section 2.6.10. Freshly thawed aliquots of protein were used each day. The Ag/AgCl electrodes were in double-layered agarose bridges: they were covered with an inner layer of 3 M KCl in 3% low-melting agarose, which was encased in an outer layer of 2 M KNO_3 in 3% low-melting agarose. Due to the denaturing effect of high concentrations of KNO_3 (≥1 M) on non-membrane-associated αHL (Section 3.3.6), αHL was inserted under asymmetrical salt conditions: 150 mM KNO_3 (*cis*)/2 M KNO_3 (*trans*) (both contained the same concentrations of buffering agent, EDTA and pH). After the insertion of a single pore, portions of the buffer in the *cis* compartment were replaced with 2.5 M KNO_3 buffer until the concentration of KNO_3 in *cis* side reached 2 M.

Stock $AgNO_3$ (1 mM) and $Cd(NO_3)_2$ (10 mM) solutions in water were prepared daily. $AgNO_3$ solution was kept in the dark. A fresh stock solution of glutathione (GSH) (100 mM) was prepared every three hours in 200 mM sodium phosphate buffer, pH 8.5. Stock GSH was kept on ice. For pK_a determination (Section 3.6.12), fresh stock solutions of tris(2-carboxylethyl)phosphine (TCEP) (100 mM) and L-selenocystine (100 mM) were prepared every three hours and kept on ice. TCEP was dissolved in water and the pH was adjusted with KOH to the same experimental pH. L-Selenocystine was dissolved in 400 mM KOH and the pH was adjusted to ~10.5. At lower pH, L-selenocystine precipitates from solution.

3.6.6 Data analysis of single-channel recordings

The current traces were filtered digitally with a 200 Hz low-pass Bessel filter in Clampfit 9.2 (Molecular Devices). Events were detected by using the single channel search feature. The mean dwell times ($\bar{\tau}$) of the current states were determined by fitting dwell-time histograms to single exponential functions. Detailed kinetic analysis was carried out using the software QuB (State University of New York at Buffalo, www.qub.buffalo.edu) (see Section 3.6.9) to determine the observed rate constants for each transition.

3.6.7 Ion selectivity

Ion selectivity (P_{K^+}/P_{Cl^-}) was determined from the reversal potentials (V_r) using the Goldman-Hodgkin-Katz (GHK) equation:[15]

$$\frac{\mathrm{P_{K^+}}}{\mathrm{P_{Cl^-}}} = \frac{[a_{\mathrm{Cl^-}}]_t - [a_{\mathrm{Cl^-}}]_c e^{V_r F/RT}}{[a_{\mathrm{K^+}}]_t e^{V_r F/RT} - [a_{\mathrm{K^+}}]_c}$$

where V_r (measured in volts) is the applied potential required to null the transmembrane ionic current, P_{K^+}/P_{Cl^-} is the permeability ratio, F is the Faraday constant (96485 Cmol^{-1}), T is the absolute temperature in Kelvin, R is the gas constant (8.314 JK^{-1}mol^{-1}), $[a_{K^+}]_c$ is the activity of K$^+$ ion in the *cis* compartment, etc.

The experiment began with symmetrical solutions (1 M KCl, 10 mM MOPS, 100 uM EDTA, pH 7.4) in both compartments at 22 ± 1 °C. Ag/AgCl electrodes in salt bridges made of agarose (3% w/v) containing high salt (3 M KCl) were used in order to minimize liquid junction potentials. The electrode DC offset was balanced under these symmetrical conditions prior to the formation of the planar lipid bilayer. After single or multiple pore insertions, 200 µL of the buffer solution in the *cis* compartment was replaced with an equal volume of 10 mM KCl, 10 mM MOPS, 100 uM EDTA, pH 7.4. Current-voltage (*I-V*) relationships (between ±100 mV) were determined. Buffer replacement and *I-V* relationships measurement were repeated to obtain a series of measurements at different salt gradients (95, 116, 143, 176, 218, 270, 334, 416, 517, 644 or 802 mM KCl (*cis*) with 1 M KCl (*trans*)). V_r was found from a second order polynomial fit of an *I-V* curve. Activities of KCl were calculated with the appropriate activity coefficients.[79]

3.6.8 Single channel conductance in KNO_3 buffer

The ionic conductivity of αHL in 2 M KNO_3 buffer was about 1.5 times lower than that in 2 M KCl buffer (Table 3.7). This is due to the lower effective concentration of KNO_3 compare to KCl. In solutions of 2 M ionic strength, the activity coefficient of KNO_3 ($\gamma = 0.33^{80}$) is ~1.7 times smaller than that of KCl ($\gamma = 0.57^{79}$). The effect of electrolyte's effective concentration on pore conductivity is further supported by single-channel experiments performed at lower electrolyte concentration. At 0.5 M electrolyte concentration, similar conductance of $(WT)_7$ were observed in buffer containing either KNO_3 ($\gamma = 0.55^{80}$) or KCl ($\gamma = 0.65^{79}$). Other possible explanations, such as the difference in the mobility of nitrate ion (7.41×10^{-4} $cm^2V^{-1}s^{-1}$) and chloride ion (7.92×10^{-4} $cm^2V^{-1}s^{-1}$ [15]) and the weak ion selectivity of the pore αHL, cannot account for the observed differences in ionic conductivity.

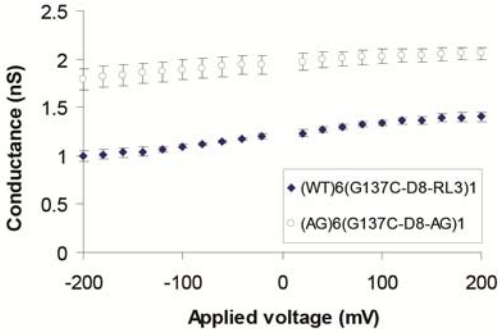

Figure 3.20. *Conductance-voltage (G-V) relationship of* $(AG)_6(G137C\text{-}D8\text{-}AG)_1$ *compared to* $(WT)_6(G137C\text{-}D8)_1$*. Buffer: 2 M* KNO_3*, 10 mM MOPS, 100 μM EDTA, pH 7.4 at 22 °C. The conductance of* $(AG)_6(G137C\text{-}D8\text{-}AG)_1$ *is about 1.6 times higher than that of* $(WT)_6(G137C\text{-}D8)_1$ *due to the enlargement of the narrow constriction by the M113G and K147G mutations.*

Table 3.7. *Conductance of WT and AG αHL in different buffers.*

			Conductance (nS)[h]		$G_{+100\,mV}/G_{-100\,mV}$	
		Activity coefficient (γ)[77,78]	WT	AG	WT	AG
2 M	KCl[a]	0.57	1.78 ± 0.01[d] (n = 5)	2.73 ± 0.01[f] (n = 5)	1.2[d] (n = 5)	1.0[f] (n = 5)
	KNO_3[b]	0.33	1.16 ± 0.01[e] (n = 5)	1.93 ± 0.10[g] (n = 5)	1.2[e] (n = 5)	1.1[g] (n = 5)
0.5 M	KCl[c]	0.65	0.35 ± 0.02[d] (n = 7)	–	–	–
	KNO_3[c]	0.55	0.35 ± 0.03[d] (n = 3)	–	–	–

[a] *with 80 mM MOPS, 100 μM EDTA, pH 7.4;* [b] *with 10 mM MOPS, 100 μM EDTA, pH 7.4;*

[c] *with 10 mM MOPS, chelex, pH 7.0;* [d] $(WT)_7$; [e] $(WT)_6(G137C\text{-}D8)_1$; [f] $(AG)_7$; [g] $(AG)_6(G137C\text{-}D8\text{-}AG)_1$.

[h] *at –50 mV and 22 °C.*

3.6.9 Analysis of stochastic single-molecule data using QuB

The analysis of simple chemical systems involving two states with distinct conductance values are straight-forward (see Chapter 1, Section 1.2.4 and the examples in Chapter 2) and can be done easily with Clampfit. When more complicated systems are involved (e.g. with more than two states), the computer program QuB (State University of New York at Buffalo, www.qub.buffalo.edu) is used for kinetic analysis. It is based on the same basic knowledge discussed in Chapter 1. For instance, at the single-molecule level, the residence time at a state is equal to the reciprocal of the sum of unimolecular rate constants of reactions leading away from it. An example for the analysis involving three reversible states is given below.

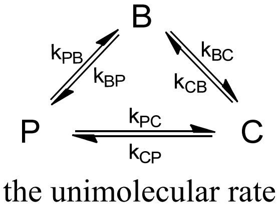

In the above model, k_{PB} is the unimolecular rate constants for the transition from state P to state B and so on. At the single-molecule level, the mean residence time ($\bar{\tau}$) at a state is equal to the reciprocal of the sum of unimolecular rate constants of reactions leading away from it.

For state P:

$\bar{\tau}_P = 1/(k_{PB} + k_{PC})$ (1)

$\bar{\tau}_P$ can be calculated by dividing the total time in state P ($\tau_{P\text{-total}}$) in the recording by the total number of transitions from it ($n_{PB} + n_{PC}$):

$\bar{\tau}_P = \tau_{P\text{-total}} / n_{PB} + n_{PC}$ (2)

where n_{PB} is the number of transitions from state P to state B in the recording and so on.

For the individual unimolecular transition from state P to state B, and from state P to state C,

$\bar{\tau}_{PB} = 1/k_{PB} = \tau_{P\text{-total}}/n_{PB}$ (3)

$\bar{\tau}_{PC} = 1/k_{PC} = \tau_{P\text{-total}}/n_{PC}$ (4)

where $\bar{\tau}_{PB}$ equals $\tau_{P\text{-total}}$ divided by the number of transitions from state P to state B and so on. Therefore

$k_{PB} = n_{PB}/\tau_{P\text{-total}}$ (5)

$k_{PC} = n_{PC}/\tau_{P\text{-total}}$ (6)

Similarly, calculations are performed for states B and C to find the other unimolecular rate constants.

QuB applies the above equations to calculate all of the unimolecular rate constants.

In bimolecular reactions, for instance, if a molecule of A is involved in the transformation from P to B, the unimolecular rate constants (k_{PB}) is related to the actual bimolecular rate constants (k'_{PB}) by

$k_{PB} = k'_{PB}[A]$ (7)

The molecularity of each transition with respect to a reactant R is determined by titration experiments with R. The concentrations of R used are usually x, 2x, 4x and

8x, where x represents the initial concentration of R. The concentration dependence of each transition is found by plotting the observed rate constants obtained from QuB against [R] (see Figures 3.9c, 3.16b-e and 3.16g-j).

For Cd^{2+}-glutathione complex formation (Section 3.3.7), the dissociations of glutathione from P-S-Cd-SG and P-S-Cd$^-$-(SG)$_2$ (2→1 and 3→2 transitions in Figure 3.17a) showed linear dependence on Cd^{2+} ion concentration, together with a non-zero intercept (Figures 3.16h,j). A bimolecular reaction alone should give a line passing through the origin (for example, Figures 3.16c,d,g). Therefore, we concluded that the dissociation of glutathione from P-S-Cd-SG and P-S-Cd$^-$-(SG)$_2$ involves two pathways, one is unimolecular and the other is bimolecular, involving free Cd^{2+} ion in solution. The plots in Figures 3.16h,j can thus be viewed as the sum of a horizontal line (at the level of the y-intercept) for the unimolecular reaction and a sloping straight line that passes through origin for the bimolecular reaction.

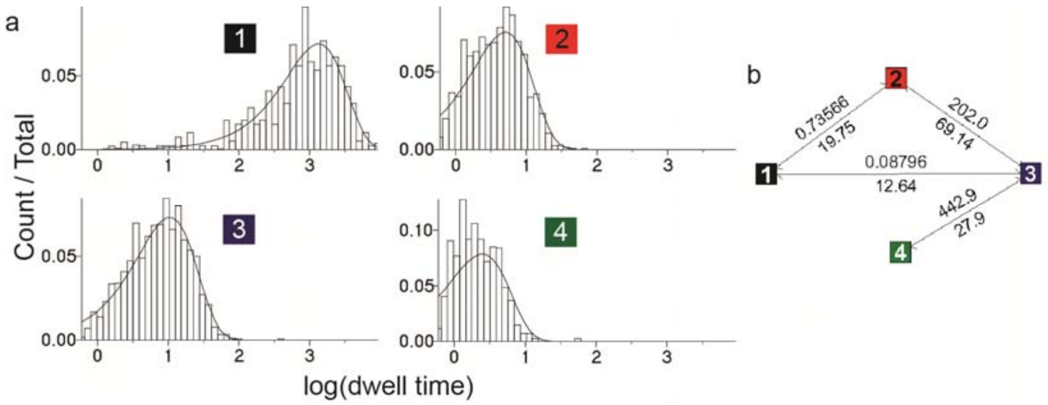

Figure 3.21. *QuB analysis of single-channel recording data. This example is obtained from a Cd^{2+}-glutathione complex formation experiment performed at 20 μM Cd(NO$_3$)$_2$ (cis)/1280 μM GSH (trans) (Section 3.3.7). (a) The dwell time histograms of levels 0–3 (see Figures 3.17a,b). In QuB, they are termed classes 1–4, respectively. (b) The observed rate constants obtained from the fittings in (a) are shown. For each transition, the observed rates obtained at different reactant concentrations were plotted against reactant concentrations to determine the rate constants summarized in Table 3.6.*

3.6.10 Proof of the presence of a single cysteine residue in PSH

The similar kinetics in the binding of the first and the second Ag^+ ions to PSH (see Section 3.3.4) might cast doubts that it might arose from the presence of two cysteine residues per pore, e.g. $(AG)_5(G137C)_2$ was used by mistake and each cysteine thiol group binds only one Ag^+ ion. Ensemble way to prove that $(AG)_6(G137C)_1$ was used can be done by densitometry. To do densitometry, the gel-purified heteroheptamer is heated to disassemble into the constituent monomers. The relative intensity of their bands on SDS-PAGE (visualized by, for example, autoradiography) shows their ratio in the heteroheptamer. A single-molecule way to distinguish the two cases ((i) two cysteine residues and each binds one Ag^+; (ii) one cysteine residue that binds two Ag^+) is by the addition of another reagent that undergoes known chemistry with the cysteine thiol group. Cd^{2+} binding to PSH are well-characterized (see Section 3.3.6). After experiment with Ag^+ ion, $Cd(NO_3)_2$ was added to the same PSH pore (Figure 3.22a). Binding of single Cd^{2+} ion was observed, together with same kinetics as that shown in Table 3.5 (Figure 3.22b). All of these findings confirm the presence of a single cysteine residue in the heteroheptamer (PSH) that was used. These also prove that each cysteine thiol group can coordinate two Ag^+ ions.

Interestingly, the two clearly distinct levels for PS-Ag and PS^+-Ag_2 with PSH (i.e. $(AG)_6(G137C\text{-}D8\text{-}AG)_1$) could not be observed with $(WT)_6(G137C\text{-}D8)_1$. In the latter protein, pore-to-pore variance in the appearance of Ag^+ ion binding events was observed. Usually only one new level appeared upon the addition of $AgNO_3$, but sometimes two unclear new levels were seen (Figure 3.23). This inconsistency in the appearance of Ag^+ ion binding events in $(WT)_6(G137C\text{-}D8)_1$ might due to the subtle

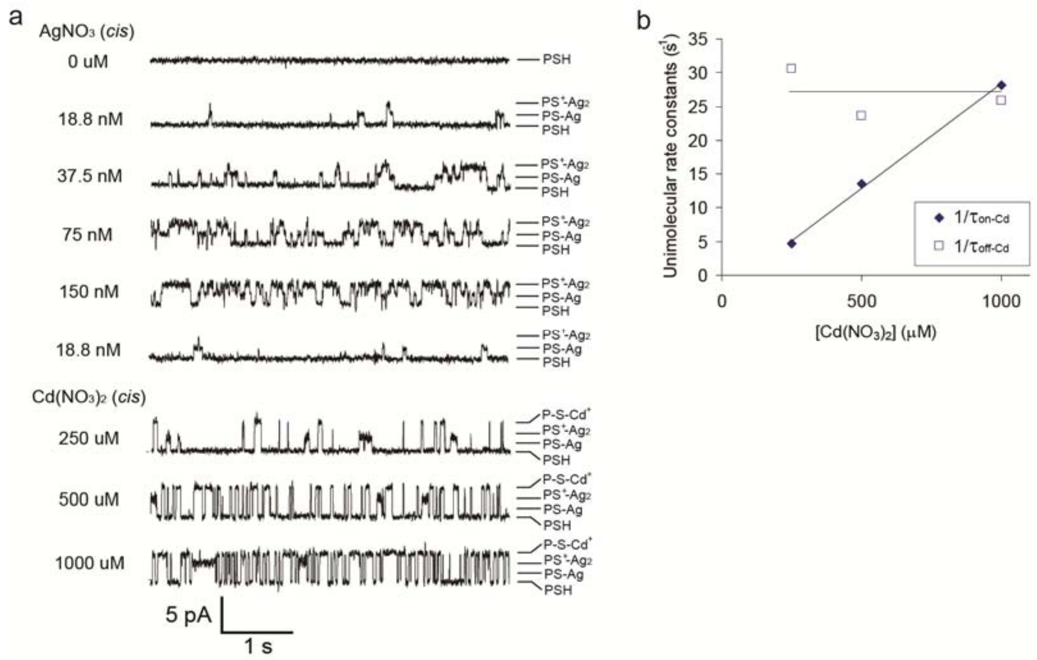

Figure 3.22. *Proof of the presence of one cysteine residue in PSH. (a) Current recording traces showing the titration of PSH with* $Cd(NO_3)_2$ *after an experiment with* $AgNO_3$*. After a titration experiment with* $AgNO_3$ *(18.8–150 nM, cis), which showed two levels for* Ag^+ *ion binding, the majority of the* $AgNO_3$ *was removed, leaving 18.8 nM residual* $AgNO_3$*. Then* $Cd(NO_3)_2$ *(250–1000 μM) was added to the cis compartment and a titration was performed. Conditions: 2 M* KNO_3*, 10 mM MOPS, 100 μM EDTA, pH 7.4, 22 °C and –50 mV. (b) Reciprocal of the mean inter-event interval at the PSH level for the binding of* Cd^{2+} *ion versus the concentration of* $Cd(NO_3)_2$*. The linear dependence shows that there is bimolecular interaction between PSH and* Cd^{2+} *ion (*$1/\bar{\tau}_{on\text{-}Cd} = n_{on\text{-}Cd}/\sum\tau_0 = k_{on\text{-}Cd}[Cd^{2+}]$*). Note that the 100 μM EDTA present in buffer chelates part of the added* Cd^{2+} *ion. Thus the linear regression of* $1/\tau_{on\text{-}Cd}$ *against the concentration of* $Cd(NO_3)_2$ *does not pass through the origin.*

difference in the conformations of individual protein, and the sensitivity of current blockade by Ag^+ ion binding to these protein conformations. Non-specific interactions between Ag^+ ions and $(WT)_6(G137C\text{-}D8)_1$ (Section 3.3.1) would not cause this variance. PSH has four mutations (Lys8→Ala, Met113→Gly, Lys131→Gly and Lys147→Gly) relative to $(WT)_6(G137C\text{-}D8)_1$. So changes in the pore environment, even not close to the site of interaction with the analyte, can help to improve the current resolution. Similar mutant-dependent observations with the αHL pore have been reported by Shin *et al.*[77,81] in the study of the pyramidal inversion at an arsenic(III) centre attached via an S–As bond to a cysteine residue. In their example, Cys137 shows detectable current change associated with the inversion, while Cys117 does not.

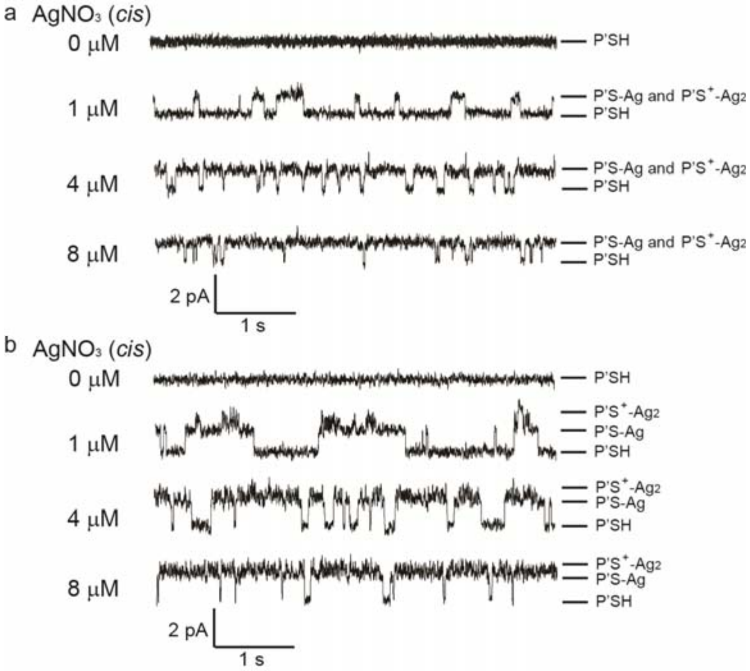

Figure 3.23. *Ag^+ ion binding to $(WT)_6(G137C\text{-}D8)_1$ (P′SH). Current traces showing the pore-to-pore variation in the appearance of Ag^+ ion binding events are depicted. The appearance can be divided into two types: (a) Only one new level after the addition of Ag^+ ion. The majority of pores showed this behaviour. (b) Two unclear new levels. The minor fraction of pores exhibited this behaviour. The total concentrations of $AgNO_3$ added (cis) are stated on the left of each current trace. The open pore level (P′SH) and the proposed Ag^+ ion bound levels (P′S-Ag and $P'S^+\text{-}Ag_2$) are labelled on the right hand side. Buffer: 2 M KNO_3, 10 mM MOPS, 100 μM EDTA, pH 7.4 and 22 °C. Applied potential: –50 mV.*

3.6.11 Complete blockade of αHL induced by Ag^+ ion

Apart from the reversible S–Ag bond formation (see Section 3.3.4), Ag^+ ion also induced complete blockade of PSH. 64% of experiments (87 out of 136) showed blockade within 10 min after the addition of a sub-micromolar amount of free Ag^+ ion (Figures 3.24a,b). The blockade was usually stepwise and the process took less than 30 s. We propose that the blockade is caused by the formation of Ag^+-thiol coordination polymers[34,35] on the protein cysteine residue with the residual thiol compounds from the protein preparation (thioglycolate, β-mercaptoethanol and DTT (at the tens nM level)). Blockade did not occur with $(AG)_7$, showing that the protein cysteine residue (i.e. the thiol group) is necessary for the occurrence of blocking. Pore blockade could be reversed by the addition of excess thiol compounds (1–10 μM, i.e. >1 equivalent relative to the total amount of $AgNO_3$ added), such as DTT, cysteamine or β-mercaptoethanol, to either the *cis* or *trans* compartment. Pore 're-opening' occurred in either one-step (Figure 3.24c) or stepwise (Figure 3.24d) mechanism, with the conductance of the pore returned to the original open pore level. Full blockade arose again if the concentration of the added thiol compound was diluted to about 100 nM level. In the presence of ~100 nM level of added thiol compounds (e.g. cysteine, thioglycolate, cysteamine), the onset of the Ag^+ ion-induced blockade took place sooner. Other metal ions, for example, Cd^{2+}, Ni^{2+}, Pb^{2+} and Hg^{2+}, do not cause complete blockade of PSH. Colloidal silver (Ag^0) formation by light-driven reduction[80] was avoided by keeping the reaction chamber in the dark during the experiment. Altogether these lead to the conclusion that the growth of Ag^+-thiolate polymer on the Cys-137 obstructs the ionic current flow. Since the Ag^+-thiolate polymer is a copolymer and its formation is a reversible process in solution,[33] the addition of an excess amount of one monomer, such as the thiol, breaks the attached large polymer into shorter polymers, which diffuse away and unblock the pore. The unblocking process appeared as single (Figure 3.24c) or multiple steps (Figure 3.24d), depending on the initial site of polymer cleavage (similar to the cases depicted in Figure 3.12).

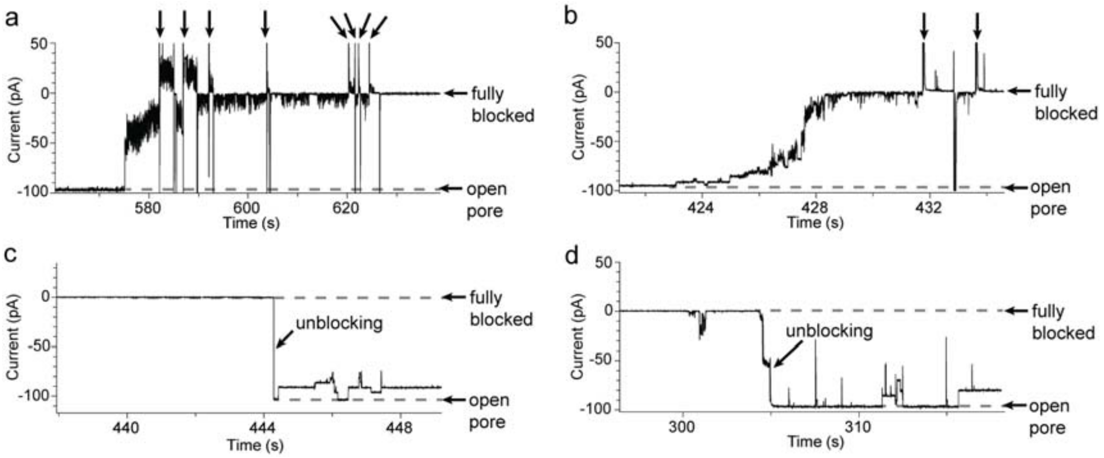

Figure 3.24. *Complete blockade of PSH induced by AgNO$_3$. (a,b) Full blockade of PSH after the addition of AgNO$_3$ (cis, sub-micromolar level of free Ag$^+$ ion). Soon after the appearance of reversible Ag$^+$ ion binding events (at –50 mV) as shown in Figure 3.9a, PSH showed a stepwise decrease in conductance, which eventually led to complete pore blockade (64% of experiments). The applied potential was changed to +50 mV as indicated by black arrows on top of the current traces. In (a), a sudden large drop in conductance was first observed, followed by a stepwise decrease in conductance. In (b), a stepwise decrease in conductance from the open pore level to the fully blocked level was seen. (c,d) 'Re-opening' of blocked PSH by the addition of thiol reagents. After the full pore blockade induced by AgNO$_3$, cysteamine was added to the cis compartment and the pore was unblocked. More than one equivalent of cysteamine relative to the total amount of AgNO$_3$ (cis) was necessary for the unblocking. Cysteamine forms oligomers with Ag$^+$ ion in solution. The oligomer sometimes adheres onto the protein cysteine residue, leading to the partial blockade seen after unblocking of channel. (c) and (d) show the one-step and stepwise unblocking, respectively.*

3.6.12 Kinetics of the individual binding steps in HC and CC mutants

The apparent rate constants reported for HC and CC mutants in Table 3.5 (Section 3.3.6) are stoichiometric rate constant ($k_{on\text{-}Cd}$ of CC) or composite rate constants ($k_{off\text{-}Cd}$ of both mutants and $k_{on\text{-}Cd}$ of HC). They can be solved into the site rate constant or the rate constants and equilibrium constants of individual steps as follow.

CC mutant

Our experimental results summarized in Table 3.5 (Section 3.3.6) shown that (1) CC and PSH have similar Cd^{2+} association rate constants and (2) the dissociation rate constant of CC is much smaller than that of PSH (370 times). Thus the binding events observed in Figure 3.15a are likely contributed by the species shown in the box in the following kinetic scheme (same as Figure 3.15c).

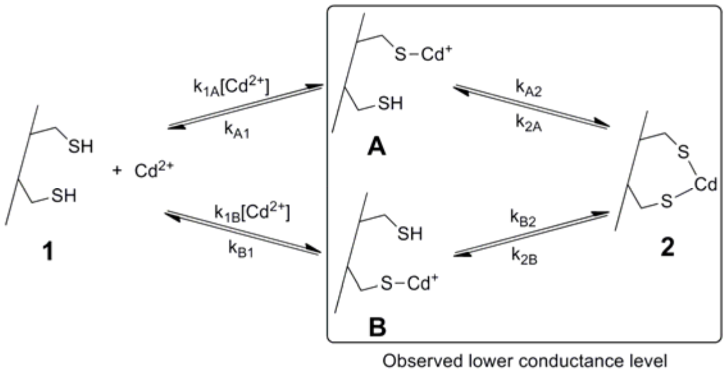

The probabilities at each of the three stages, **2**, **A** and **B**, in the box are[98,99]

$p_2 = k_{A2}k_{B2} / (k_{A2}k_{B2} + k_{2A}k_{B2} + k_{A2}k_{2B})$ …(1)

$p_A = k_{2A}k_{B2} / (k_{A2}k_{B2} + k_{2A}k_{B2} + k_{A2}k_{2B})$ …(2)

$p_B = k_{A2}k_{2B} / (k_{A2}k_{B2} + k_{2A}k_{B2} + k_{A2}k_{2B})$ …(3)

where $p_2 + p_A + p_B = 1$.

The apparent Cd^{2+} dissociation rate v_{-1} is

$$v_{-1} = k_{A1}p_A + k_{B1}p_B$$

Put in equations (2) and (3),

$$v_{-1} = (k_{A1}k_{2A}k_{B2} + k_{B1}k_{A2}k_{2B}) / (k_{A2}k_{B2} + k_{2A}k_{B2} + k_{A2}k_{2B}) = k_{off\text{-}Cd} \qquad \ldots(4)$$

where $k_{off\text{-}Cd}$ is the apparent dissociation rate constant (Table 3.5, Section 3.3.6).

Thus the mean lifetime in the box ($\bar{\tau}_2$) = $1/v_{-1}$

$$= (k_{A2}k_{B2} + k_{2A}k_{B2} + k_{A2}k_{2B}) / (k_{A1}k_{2A}k_{B2} + k_{B1}k_{2B}k_{A2}) \qquad \ldots(5)$$

Lifetime outside the box ($\bar{\tau}_1$) = $1/((k_{1A} + k_{1B})[Cd^{2+}])$ …(6)

$$= 1/(k_{on\text{-}Cd}[Cd^{2+}])$$

where $k_{on\text{-}Cd}$ is the apparent association constant (Table 3.5).

If the two cysteine thiol groups are equivalent, i.e. have the same association and dissociation rate constants of Cd^{2+}, e.g. $k_{1A} = k_{1B}$, $k_{2A} = k_{2B}$ etc, equations (5) and (6) simplify to

$$\bar{\tau}_2 = (1/k_{A1}) * (1 + k_{A2}/2k_{2A}) = 1/k_{off\text{-}Cd} \qquad \ldots(7)$$

$$\bar{\tau}_1 = 1/\ 2k_{1A}[Cd^{2+}] = 1/(k_{on\text{-}Cd}[Cd^{2+}]) \qquad \ldots(8)$$

The overall (1↔2) dissociation equilibrium constant (K_d) for the chelation of Cd^{2+} is

$$K_d = K_{d,A}K_{d,2} \qquad \ldots(9)$$

where $K_{d,A}$ (= k_{A1}/k_{1A}) and $K_{d,2}$ (= k_{2A}/k_{A2}) are the dissociation equilibrium constants of the first and second steps, respectively.

The apparent dissociation constant (Table 3.5) refers to the equilibrium between "inside" and "outside" the box (low and high conductance states):

The apparent dissociation equilibrium constant ($K_{d\text{-}Cd}$) in Table 3.5 is

$K_{d\text{-}Cd} = \bar{\tau}_1[Cd^{2+}]/\bar{\tau}_2$

Substitute equations (7) and (8) into this equation,

$K_{d\text{-}Cd} = K_{d,A}{}^{*}(1/(2+1/K_{d,2}))$

$K_{d\text{-}Cd}$ reduces to K_d if ($2k_{2A} << k_{A2}$), or $2K_{d,2}<<1$.

Using equation (8), $k_{1A} = k_{on\text{-}Cd}/2 = (2.7 \pm 0.9) \times 10^4\ M^{-1}s^{-1}$

Substitute the value $k_{on\text{-}Cd}$ of PSH (Table 3.5) as k_{A1} into equation (7),

$K_{d,2} = k_{2A}/k_{A2} = (1.3 \pm 0.2) \times 10^{-3}$

Similarly,

$K_{d,A} = k_{A1}/k_{1A} = (4.8 \pm 1.7)\ x\ 10^{-4}$ M

and the overall $K_d = (6.6 \pm 2.6) \times 10^{-7}$ M.

As ($2k_{2A} << k_{A2}$), K_d is comparable to the apparent rate constant $K_{d\text{-}Cd}$, and is over 3 orders of magnitude lower than $K_{d\text{-}Cd}$ of the single cysteine PSH pore. As the rates of the individual coordination steps show, the reduced dissociation constant in this case is due to the stability of the metal coordinated by 2 cysteines, not a higher association rate.

HC mutant

Noise analysis with the histidine-only mutant H, i.e. $(AG)_6(L135H\text{-}AG)_1$ (see Figure 3.25), shows that Cd^{2+} undergoes fast association and dissociation kinetics with the imidazole group. The residence time of Cd^{2+} on P_H is very short, hence the P_H-Cd^{2+} complex does not lead to a distinct time-resolvable current level. Therefore, the system is kinetically analysed with the singly His-liganded intermediate of HC (**H** in the scheme below) having the same conductance as the metal-free HC (**1**). The binding events observed in Figure 3.14a presumably arose from the two stages shown in the box in the following kinetic scheme (same as Figure 3.14c).

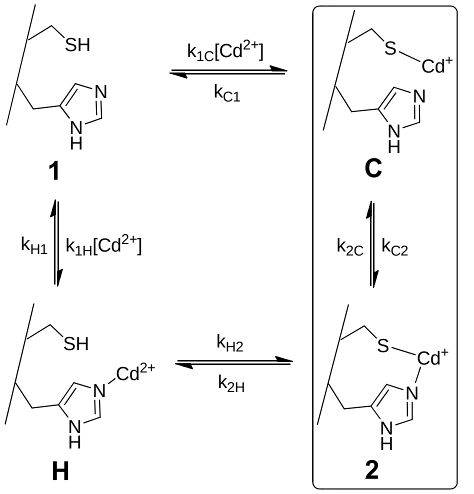

Observed lower conductance level

Our experimental results (Table 3.5, Section 3.3.6) show that (1) the association rate constant of Cd^{2+} to HC is 22-fold larger than that of PSH and (2) their dissociation rate constants are similar.

Considering the equilibrium in the box, the probabilities at **C** and **2** are

$$p_c = k_{2C} / (k_{2C} + k_{C2}) \qquad \ldots(10)$$

$$p_2 = k_{C2} / (k_{2C} + k_{C2}) \qquad \ldots(11)$$

such that $p_c + p_2 = 1$.

For moving out of the box, the dissociation rate v_{-1} is

$$v_{-1} = k_{C1}{*}p_c + k_{2H}{*}p_2$$

which substituting equations (10) and (11) results in

$$v_{-1} = (k_{C1}k_{2C} + k_{2H}k_{C2}) / (k_{2C} + k_{C2}) \qquad \ldots(12)$$

The lifetime in the box ($\bar{\tau}_2$) = $1/v_{-1}$

$$= (k_{2C} + k_{C2}) / (k_{C1}k_{2C} + k_{2H}k_{C2}) \qquad \ldots(13)$$

$$= 1/ k_{off\text{-}Cd}$$

where $k_{off\text{-}Cd}$ is the apparent dissociation rate constant (see Table 3.5, Section 3.3.6).

If $k_{2C} >> k_{C2}$ and in the extreme case that $k_{C1}k_{2C} >> k_{2H}k_{C2}$, then $\bar{\tau}_2 = 1/k_{C1}$.

If $k_{C2} >> k_{2C}$ and in the case that $k_{C1}k_{2C} << k_{2H}k_{C2}$, then $\bar{\tau}_2 = 1/k_{2H}$.

The similar dissociation rate constants of HC and PSH (Table 3.5) suggest that the first case might be possible, although k_{2H} may, by coincidence, have similar value as the dissociation rate constant ($k_{Cd,10}$) of PSH.

Considering the two species outside the box, the probabilities at **1** and **H** are

$$p_1 = k_{H1} / (k_{H1} + k_{1H}[Cd^{2+}]) \qquad \ldots(14)$$

$$p_H = k_{1H}[Cd^{2+}] / (k_{H1} + k_{1H}[Cd^{2+}]) \qquad \ldots(15)$$

such that $p_1 + p_H = 1$.

For moving into the box, the association rate v_{+1}

$$v_{+1} = k_{1C}[Cd^{2+}]*p_1 + k_{H2}*p_H$$

which substituting equations (14) and (15) results in

$$v_{+1} = (k_{1C}k_{H1} + k_{H2}k_{1H})[Cd^{2+}] / (k_{H1} + k_{1H}[Cd^{2+}]) \qquad \ldots(16)$$

The lifetime outside the box becomes

$$\bar{\tau}_1 = 1/v_{+1} = (k_{H1} + k_{1H}[Cd^{2+}]) / (k_{1C}k_{H1} + k_{H2}k_{1H})[Cd^{2+}] \qquad \ldots(17)$$

With our experimental values of $k_{H1} = (4.8 \pm 1.6) \times 10^4$ s^{-1}, $k_{1H} = (7.6 \pm 1.4) \times 10^7$ M^{-1}s^{-1} (see Figure 3.25) and the maximum $[Cd^{2+}]$ used = 20 μM, $k_{H1} > k_{1H}[Cd^{2+}]$ (31 times) and equation (17) can be simplified to

$$\bar{\tau}_1 = k_{H1} / (k_{1C}k_{H1} + k_{H2}k_{1H})[Cd^{2+}] \qquad \ldots(18)$$

which supports our observed first-order $[Cd^{2+}]$-dependence of $1/\bar{\tau}_1$ (represented by $1/\bar{\tau}_{P\text{-}S\text{-}Cd^+}$ in Figure 3.14b). So in the experimental $[Cd^{2+}]$ range of 5–20 μM, the apparent association rate constant is

$$k_{on\text{-}Cd} = (k_{1C}k_{H1} + k_{H2}k_{1H}) / k_{H1} = 1/(\bar{\tau}_1[Cd^{2+}]) \qquad \ldots(19)$$

k_{1C} and k_{C1} can, similarly to the CC pore, be assumed to correspond to $k_{on\text{-}Cd}$ and $k_{off\text{-}Cd}$ of PSH single cysteine pore respectively (Table 3.5).

From the apparent association rate $k_{on\text{-}Cd}$ of HC (Table 3.5), with the measured values for k_{1C}, k_{C1}, k_{1H} and k_{H1}, the rate k_{H2} can be derived with equation (19) to give $k_{H2} = (8 \pm 6) \times 10^2\ s^{-1}$.

In the numerator of the apparent association rate (19), the term representing initial capture by the imidazole group and subsequent chelation to the thiol dominates by over an order of magnitude the initial capture by the thiol: $k_{1C}k_{H1} \sim 3\times10^9\ M^{-1}s^{-2} << k_{1H}k_{H2} \sim 6\times10^{10}\ M^{-1}s^{-2}$. Meanwhile, the apparent dissociation rate is similar to that from the single thiol in PSH.

Both while bound and while unbound to thiol, Cd^{2+} undergoes fast association and dissociation with the imidazole group. While in both these states the reaction is shifted to the dissociation ($k_{H1}>>k_{1H}[Cd^{2+}]$, and with high likelihood $k_{2C}>>k_{C2}$), in the case of HC the 1.5 orders of magnitude reduction of the apparent dissociation equilibrium constant is due mainly to the increased association rate through histidine, and less any higher stability of the fully chelated ion.

The overall dissociation equilibrium constant (K_d) for the chelation of Cd^{2+} is

$$K_d = (k_{C1}k_{2C} + k_{H1}k_{2H}) / (k_{1C}k_{C2} + k_{1H}k_{H2}) \qquad \ldots(20)$$

The apparent dissociation equilibrium constant ($K_{d\text{-}Cd}$) in Table 3.5 refers to the equilibrium between “inside” and “outside” the box (low and high conductance states):

$$K_{d\text{-}Cd} = \bar{\tau}_1[Cd^{2+}]/\bar{\tau}_2$$

Substitute equations (13) and (17) into this equation,

$$K_{d\text{-}Cd} = (k_{H1} + k_{1H}[Cd^{2+}])(k_{C1}k_{2C} + k_{2H}k_{C2}) / (k_{1C}k_{H1} + k_{H2}k_{1H})(k_{2C} + k_{C2}) \quad \ldots(21)$$

Under our experimental conditions in which $k_{H1} > k_{1H}[Cd^{2+}]$ (see above),

$$K_{d\text{-}Cd} = k_{H1}(k_{C1}k_{2C} + k_{2H}k_{C2}) / (k_{1C}k_{H1} + k_{H2}k_{1H})(k_{2C} + k_{C2}) \quad \ldots(22)$$

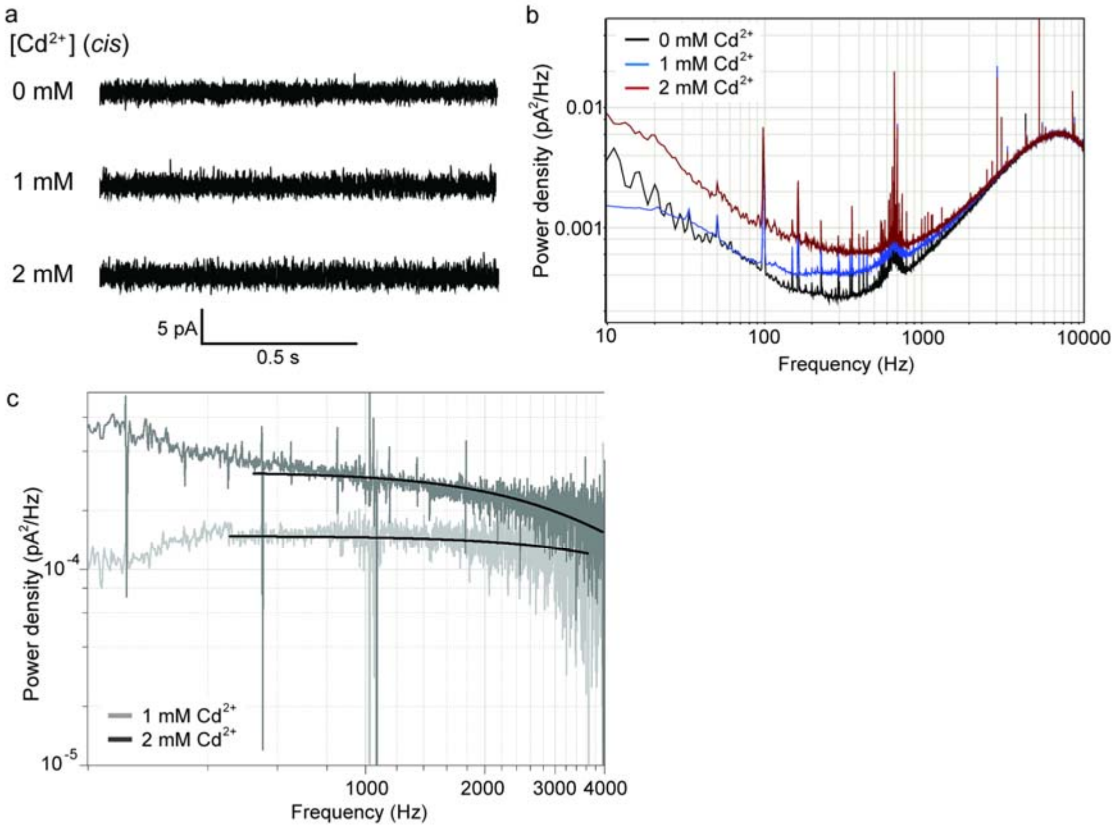

Figure 3.25. *Reversible binding of* Cd^{2+} *ion to the H mutant. (a) Stacked current recording traces of H (i.e.* $(AG)_6(L135H\text{-}AG)_1$*) at different concentrations of* $Cd(NO_3)_2$ *(cis). Experimental conditions were the same as in Figure 3.13. The traces shown were filtered with a low-pass Bessel filter at 1000 Hz. Transient binding of* Cd^{2+} *does not lead to a new discrete current level, instead it increases the noise. (b) Power spectra of the three traces shown in (a). (c) The power spectra at 1 and 2 mM of* Cd^{2+} *after the subtraction of background (without* Cd^{2+}*). They are fitted to Lorentzian distribution to determine the association and dissociation rate constants of* Cd^{2+} *binding (*$k_{on\text{-}Cd} = (7.6 \pm 1.4) \times 10^7\ M^{-1}s^{-1}$*,* $k_{off\text{-}Cd} = (4.8 \pm 1.6) \times 10^4\ s^{-1}$*,* $K_{d,H} = (6.2 \pm 0.9) \times 10^{-4}$ *M (n = 2)).* $(AG)_7$*, without the histidine mutation at position 135, shows 13 times weaker binding of* Cd^{2+}*:* $k_{on\text{-}Cd} = (1.9 \pm 0.4) \times 10^6\ M^{-1}s^{-1}$*,* $k_{off\text{-}Cd} = (1.5 \pm 0.04) \times 10^4\ s^{-1}$*,* $K_{d,H} = (8.0 \pm 1.9) \times 10^{-3}$ *M (n = 2). Thus the single His135 in the H mutant is capable of coordinating* Cd^{2+}*.*

3.6.13 Oxidation of both cysteine residues in the CC mutant

In some of the cadmium(II) binding experiments (7 in 10 experiments) with the double cysteine mutant CC (see Section 3.3.6), both cysteine thiol groups lost the Cd^{2+} binding activity simultaneously (Figure 3.26). This usually occurred within 30 min after the addition of $Cd(NO_3)_2$ (~10 μM). The single cysteine mutants (PSH and HC) do not show this behaviour. After losing the Cd^{2+} binding ability, the pore had the same conductance as that of the unoccupied pore before the lost of activity. We propose that the concurrent lost of metal binding ability of both cysteine thiol groups is due to the disulfide bond formation between Cys-135 and Cys-137. Cd^{2+} has been proposed to cause oxidative stress in neuronal cells by influencing sulfhydryl homeostasis.[95] However, no mechanistic study can be found in the literature for thiol oxidation mediated by the redox-inactive Cd^{2+}, or the closely related Zn^{2+}. Although the exact mechanism is not known, the oxidation in our system might be induced by Cd^{2+} in the presence of dissolved O_2 in the buffer solution. Intramolecular disulfide bond formation in Cys-Xaa-Cys (CXC) motif has been studied in tripeptides.[96] It is also proposed to take place at the active site CXC motif in *Bacillus subtilis* YphP disulfide isomerase.[97] Although the distance between Cys-135 and Cys-137 on the β barrel structure of αHL is too far away for disulfide bond formation (the Cβ–Cβ distance is 6.3 Å; the bond lengths of C–S = 1.8 Å and S–S = 2.1 Å), bending around Leu-136 may facilitate the oxidation. While this might distort the subunit structure, the other six subunits (without any cysteine mutations) might maintain the overall β barrel structure of αHL (see Section 1.2.1 for the structure of αHL). Further experiments and computer simulations are required to support this hypothesis.

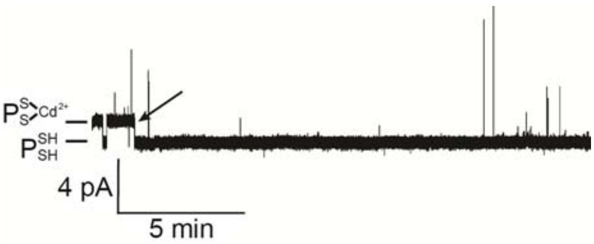

Figure 3.26. *Oxidation of the two cysteine thiol groups in the mutant CC (i.e. $(AG)_6(L135C/G137C)_1$). This current trace shows that both Cys135 and Cys137, which were capable of binding Cd^{2+} ion at the beginning of the experiment, lost their coordination ability at the time indicated by the arrow. If only one of the cysteines had become inactive towards Cd^{2+} binding, the pore would still show Cd^{2+} binding – as in the case of the single cysteine mutant PSH (Figure 3.13a). The open pore (P^{SH}_{SH}) and the Cd^{2+} ion-bound ($P^{S}_{S}{>}Cd^{2+}$) levels are labelled on the left hand side. $Cd(NO_3)_2$ (5 μM) was present in the cis compartment.*

3.6.14 Attempt to determine the cysteine thiol pK_a values

Thiol-disulfide[83–85] and selenol-diselenide[86,87] exchange reactions occur only with the deprotonated forms of thiols and selenols, i.e. thiolate and selenoate. These anions are also the active species in mixed exchange systems, such as thiol-selenylsulfide[87] and thiol-diselenide.[88] Measurement of the rate of exchange reactions as a function of pH can be applied to determine the pK_a values of protein cysteine thiol groups, where the observed rate constant at a given pH value is proportional to the extent of thiol deprotonation.

Using the single-channel recording technique, the pK_a values of the thiol groups in the PSH, HC and CC mutants of αHL (i.e. $(AG)_6(G137C)_1$, $(AG)_6(L135H/G137C)_1$ and $(AG)_6(L135C/G137C)_1$, respectively) were determined from the kinetics of the thiol-diselenide exchange reaction with L-selenocystine (added to the *trans* compartment) (Figure 3.27a). The selenylsulfide formed in the pore lumen is reduced with tris(2-carboxyethyl)phosphine (TCEP) (added to the other compartment, *cis*), to regenerate the protein cysteine thiol group[89] (Figures 3.27a,b). The same reactions of a cysteine mutant of αHL with L-selenocystine (*trans*)/TCEP (*cis*) have been investigated by Rogers *et al.*[90] The details of the chemistry involved in the thiol-diselenide exchange reaction and TCEP reduction are depicted in Figure 3.27c. The thiolate (represented by PS^-) undergoes an S_N2 reaction on the diselenide bond in L-selenocystine, forming a selenylsulfide (PS-selenocysteine) and the selenoate of L-selenocysteine. TCEP then reduces the selenylsulfide bond via two possible reaction mechanisms: (1) an S_N2 mechanism, as in the reduction of disulfide bond by TCEP. Nucleophilic attack at the electrophilic Se atom by TCEP leads to the formation of thiolate (PS^-) and R'_3P^+–selenocysteine. Hydrolysis of the latter species produces $Se{=}PR'_3$ and selenocysteine. (2) a free radical mechanism.[91] Homolytic cleavage of the selenylsulfide bond induced by TCEP leads to the formation of thiyl (PS·) and R'_3P·–selenocysteine radical. The PS· radical is converted to thiol/thiolate, which can start another cycle of thiol-diselenide exchange/TCEP reduction. R'_3P·–selenocysteine radical undergoes homolytic C–Se bond cleavage to yield $Se{=}PR'_3$ and an alanine free radical. Abstraction of a hydrogen atom by the latter species gives alanine as the deselenization product from selenocysteine. We have carried out ^1H NMR experiments of a mixture of TCEP (100 mM) and L-selenocystine (10 mM) at pD 7.0. We found the formation of selenocysteine and alanine in ~9:1 molar ratio. So both mechanisms are feasible, with the first one being the major reaction pathway. Single-molecule detection with our αHL cysteine mutants observes reactions occurring on the cysteine thiol group only, so the conversion of the R'_3P·–selenocysteine radical to alanine, for example, is not observable. Thiol, thiolate and thiyl forms of the cysteine residue on αHL are believed to have indistinguishable current conductance. Thus the

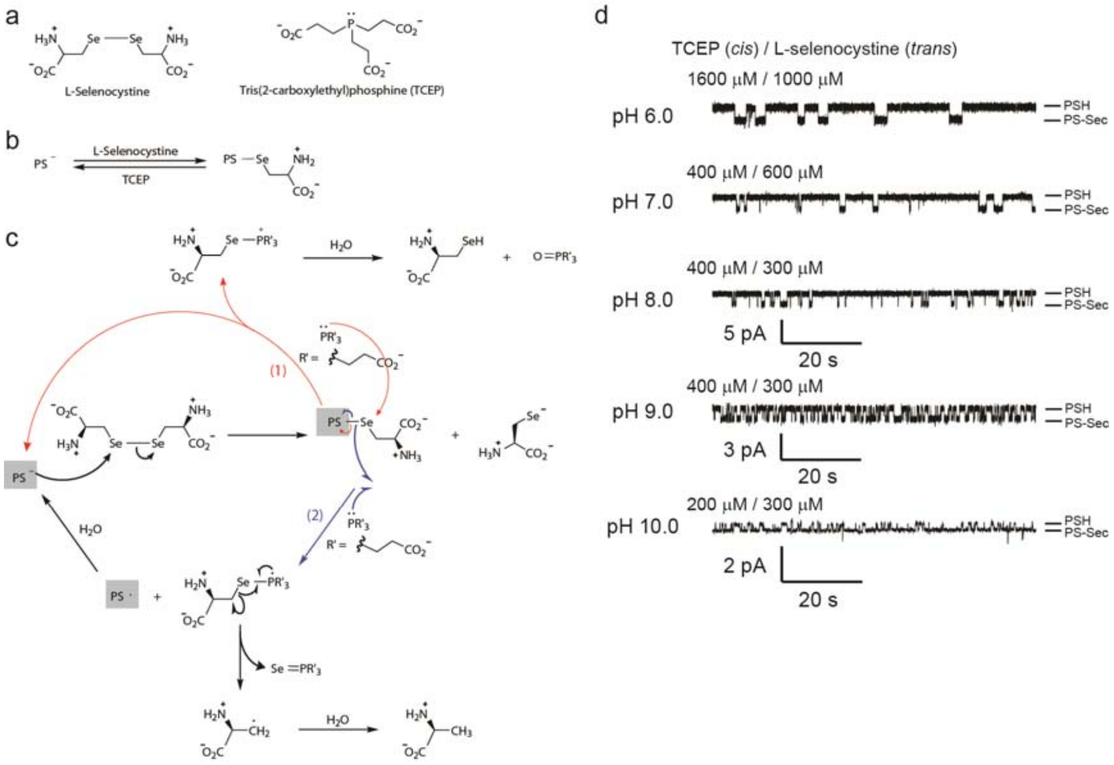

Figure 3.27. *Determination of the pK$_a$ value of a protein cysteine thiol group by the thiol-diselenide exchange reaction. (a) Structures of L-selenocystine and TCEP. (b) Overall transformation that is observed at the single-molecule level. (c) Detailed mechanisms showing the thiol-diselenide exchange reaction of protein cysteine thiolate (represented as PS$^-$) with L-selenocystine, followed by the regeneration of the thiol group by TCEP. The latter occurs by two pathways as discussed in the text. αHL pore with thiol, thiolate and thiyl forms of the cysteine residue are assumed to have indistinguishable conductance values. Thus only one current level is observed for these three species as shown in (d). (d) Current recording traces showing the pH-dependent transformations of the cysteine thiolate group (in PSH) into selenylsulfide with L-selenocystine (trans)/TCEP (cis). The concentrations of L-selenocystine (trans)/TCEP (cis) for each trace are labelled on top. Conditions: 2 M KCl, 20 mM buffering agent, 100 μM EDTA at +50 mV and 22 ± 1 °C. The buffering agent was 2-bis(2-hydroxyethyl)amino-2-(hydroxymethyl)-1,3-propanediol (Bis-Tris) (pH 6.0), 1,3-bis[tris(hydroxymethyl)methylamino]propane (Bis-Tris propane) (pH 7.0–9.0) and 3-(cyclohexylamino)-1-propanesulfonic acid (CAPS) (pH 10.0).*

current recording traces (Figure 3.27d) appear simply as two levels – the ‘PSH’ level and the PS-selenocysteine level.

At each pH (over the pH range of 6.0–10.0), a fixed concentration of TCEP was added to the *cis* side. Titration with L-selenocystine (*trans*) was performed at four different concentrations. Reversible formation of selenylsulfide (PS-selenocysteine) was monitored under an applied potential of +50 mV. The reciprocal of the mean residence time at the open pore level ($1/\bar{\tau}_{PSH}$) was plotted against the concentration of L-selenocystine (Figure 3.30). The slope of the best-fit straight line represents the bimolecular rate constant for the thiol-diselenide exchange reaction ($1/\bar{\tau}_{PSH} = k_0$[L-selenocystine]). The average rate constant (calculated from three repeat experiments) was plotted against pH (Figure 3.28). To determine the pK_a of the protein cysteine residue, the data points were fitted to the following equation (derived from Henderson-Hasselbalch equation)[92] using OriginPro 8.1 SR3 (OriginLab Corporation).

$$k_0 = \frac{k_{SH} + k_{S^-} 10^{\mathrm{pH} - \mathrm{p}K_a}}{1 + 10^{\mathrm{pH} - \mathrm{p}K_a}} \quad \ldots(8)$$

where k_o is the observed bimolecular rate constant, while k_{SH} and k_{S}- are the rate constants for thiol and thiolate, respectively.

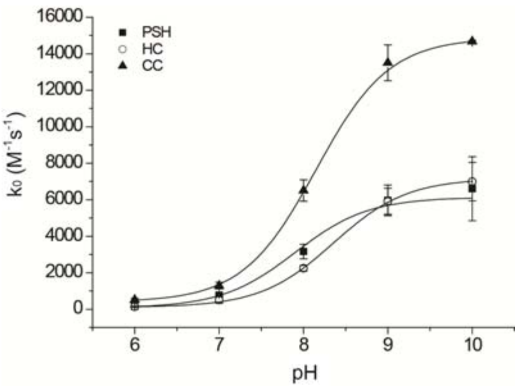

Figure 3.28. *Plot of the rate constant of the thiol-diselenide exchange reaction against pH. The data points were fitted to equation (8) to determine the pK_a value of the protein cysteine residue. The pK_a values of PSH (filled square), HC (hollow circle) and CC (filled triangle) mutants were determined to be 7.9 ± 0.1 (R^2 > 0.99), 8.4 ± 0.04 (R^2 > 0.99) and 8.2 ± 0.03 (R^2 > 0.99), respectively. The k_o value for CC is the sum of the rate constants of the two cysteine residues. The averaged pK_a value of the two cysteine thiol groups in CC is reported.[93] Each data point is the mean ± s.d. from three experiments.*

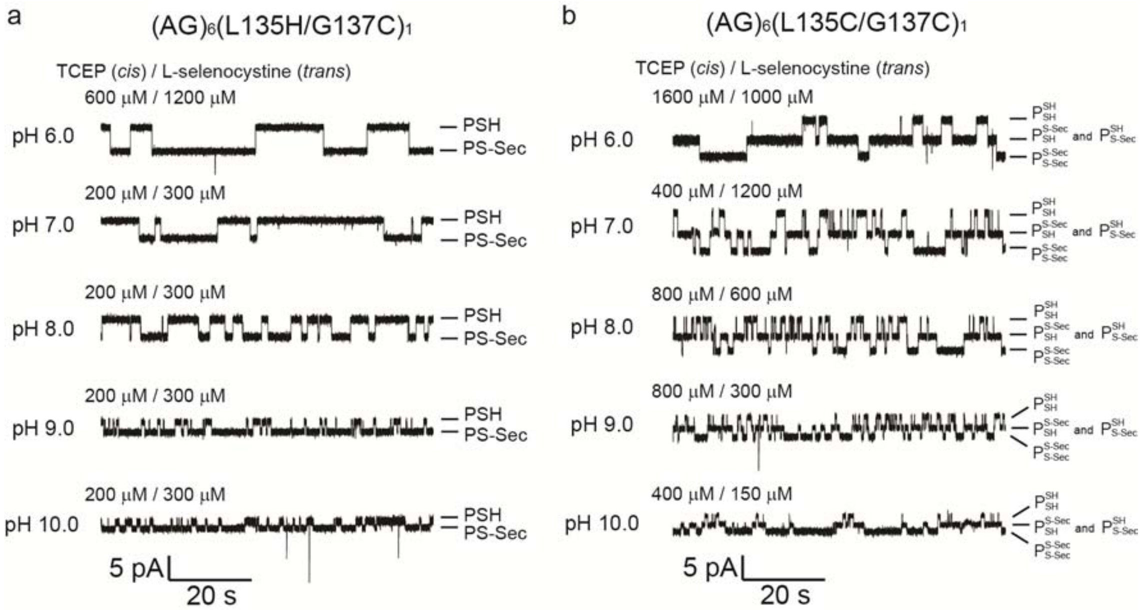

Figure 3.29. *Current recording traces showing the pH-dependent reactions of the cysteine thiolate group with* L*-selenocystine (trans)/TCEP (cis) with (a) HC mutant (i.e. $(AG)_6(L135H/G137C)_1$) and (b) CC mutant (i.e. $(AG)_6(L135C/G137C)_1$). The concentrations of* L*-selenocystine (trans)/TCEP (cis) are stated above each trace.*

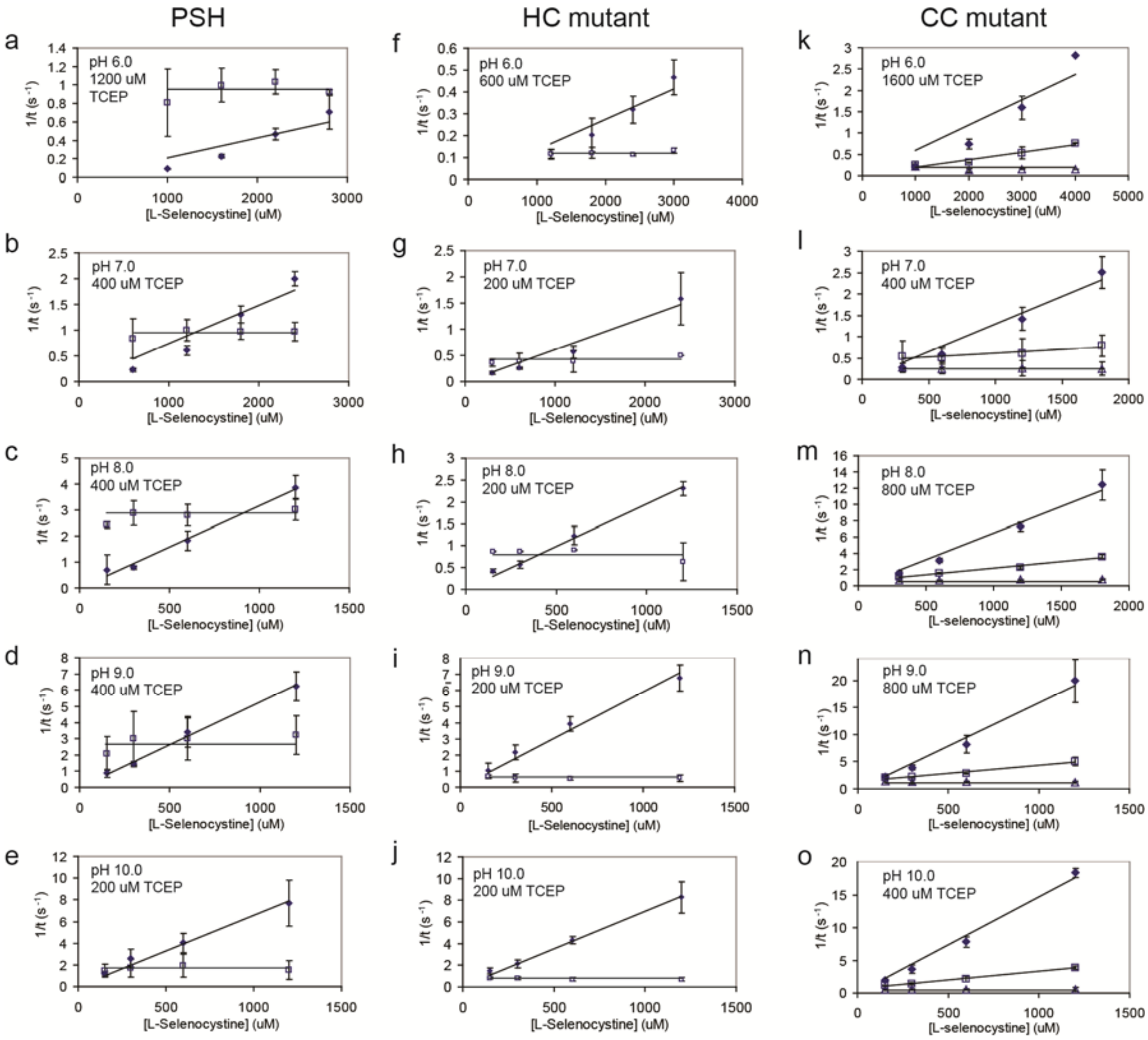

Figure 3.30. *pH-Dependence of mean residence times. Plots of the reciprocals of the mean residence times at each level against the concentration of* L*-selenocystine. The pH value and the fixed concentration of TCEP used are labelled on each graph.* L*-selenocystine and TCEP were present in the trans and the cis compartments, respectively. (a–e) PSH; (f–j) HC mutant. Closed rhombi and open squares represent* $1/\bar{\tau}_{PSH}$ *and* $1/\bar{\tau}_{PS\text{-}Sec}$*, respectively. (k–o) CC mutant. Closed rhombi, open squares and open triangles represent* $1/\bar{\tau}P^{SH}_{SH}$*,* $1/\bar{\tau}P^{SH}_{S\text{-}Sec}$ *and* $1/\bar{\tau}P^{S\text{-}Sec}_{S\text{-}Sec}$*, respectively. Each point is the mean ± s.d. from three separate experiments.*

The selenium atom is more electrophilic than sulfur.[88] Thus thiolate undergoes exchange reaction with L-selenocystine ((4.1 ± 0.4) × 10^3 $M^{-1}s^{-1}$, pH 8.0) about 30 times faster than with the disulfide compound, 5,5'-dithiobis(2-nitrobenzoic acid)

(DTNB, Ellman's reagent) ((1.3 ± 0.1) × 10^2 $\text{M}^{-1}\text{s}^{-1}$, pH 8.0).[90] The faster reaction rate of the thiolate with L-selenocystine ensures efficient data collection with low concentrations of L-selenocystine (≤3 mM). The pK_a values of the carboxyl groups and the amino groups in L-selenocystine are 2.4 and 8.9, respectively.[94] The deprotonations of the two amino groups in the studied pH range (6.0–10.0) might affect the electrophoretic translocation of L-selenocystine and also the exchange reaction with the protein thiolate. Since the deprotonation of L-selenocystine may dominate that of the cysteine thiol group on PSH, the pK_a values determined in this section is for reference purpose only. More accurate results can be obtained using a diselenide that does not show protonation/deprotonation equilibrium in the studied pH range, such as the diselenide of 3-selenolpropionic acid. The thiolate-diselenide exchange rate constant that we measured between PSH and L-selenocystine ((7.4 ± 0.4) × 10^2 $\text{M}^{-1}\text{s}^{-1}$ at pH 7.0) is slower than the literature value between cysteine and L-selenocystine ((1.0 ± 0.2) × 10^5 $\text{M}^{-1}\text{s}^{-1}$ at pH 7.0)[88] by more than two orders of magnitude. This difference might due to the steric hindrance around the cysteine residue thiol group in PSH that avoids the S_N2 attack at the Se-Se bond.

Thiol reducing agents, such as dithiothreitol (DTT), in concentrations ≥100 μM has been reported to affect the rate of the thiol-disulfide reaction in single-channel recording experiments.[89] This is presumably due to its diffusion across the pore or the lipid bilayer, leading to the depletion of the disulfide reagent present in the opposite chamber. Therefore, the negatively charged reducing agent TCEP, which has been shown by Rogers *et al.*[90] that it does not affect the thiol-diselenide reaction at concentrations as high as 3.2 mM, was employed in the measurements here.

3.7 References

1. Xu, Y.; Feng, L.; Jeffrey, P. D.; Shi, Y.; Morel, F. M. M. *Nature* **2008**, *452*, 56–62.
2. Dance, I. G. *Polyhedron* **1986**, *5*, 1037–1104.
3. Gupta, A.; Silver, S. *Nat. Biotechnol.* **1998**, *16*, 888.
4. (a) Carlson, C.; Hussain, S. M.; Schrand, A. M.; Braydich-Stolle, L. K.; Hess, K. L.; Jones, R. L.; Schlager, J. J. *J. Phys. Chem. B* **2008**, *112*, 13608–13619. (b) Holt, K. B.; Bard, A. J. *Biochemistry* **2005**, *44*, 13214–13223. (c) Lok, C.-N.; Ho, C.-M.; Chen, R.; He, Q.-Y.; Yu, W.-Y.; Sun, H.; Tam, P. K.-H.; Chiu, J.-F.; Che, C.-M. *J. Proteome Res.* **2006**, *5*, 916–924.
5. Klaassen, C. D.; Liu, J.; Choudhuri, S. *Annu. Rev. Pharmacol. Toxicol.* **1999**, *39*, 267–295.
6. Argüello, J. M. *J. Mol. Biol.* **2003**, *195*, 93–108.
7. Thévenod, F. *Toxicol. Appl. Pharmacol.* **2009**, *238*, 221–239.
8. Braun, W.; Vašák, M.; Robbins, A. H.; Stout, C. D.; Wagner, G.; Kägi, J. H. R.; Wüthrich, K. *Proc. Natl. Acad. Sci. U. S. A.* **1992**, *89*, 10124–10128.
9. Dudley, R. E.; Gammal, L. M.; Klaassen, C. D. *Toxicol. Appl. Pharmacol.* **1985**, *77*, 414–426.
10. Vašák, M.; Romero-Isart, N. in *Encyclopedia of Inorganic Chemistry, Vol. V*; King, R. B., Eds.; John Wiley & Sons, Ltd., Chichester, UK, 2005; pp 3208–3221.
11. Marambio-Jones, C.; Hoek, E. M. V. *J. Nanopart. Res.* **2010**, *12*, 1531–1551.
12. Silver, S. *FEMS Microbiol. Rev.* **2003**, *27*, 341–353.
13. Silver, S.; Phung, L. T. Silver, G. *J. Ind. Microbiol. Biotechnol.* **2006**, *33*, 627–624.
14. Carpenter, E. P.; Beis, K.; Cameron, A. D.; Iwata, S. *Curr. Opin. Struct. Biol.* **2008**, *18*, 581–586.

15. Hille, B. *Ionic channels of excitable membranes*, 2nd ed.; Sinauer Associates, Sunderland: MA, 1992.
16. Karlin, A.; Akabas, M. H. *Methods Enzymol.* **1998**, *293*, 123–136.
17. Lü, Q.; Miller, C. *Science* **1995**, *268*, 304–307.
18. Frelin, C.; Cognard, C.; Vigue, P.; Lazdunski, M. *Eur. J. Pharmacol.* **1986**, *122*, 245–250.
19. Pérez-García, M. T.; Chiamvimonvat, N.; Marban, E.; Tomaselli, G. F. *Proc. Natl. Acad. Sci. U.S.A.* **1996**, *93*, 300–304.
20. Webster, S. M.; del Camino, D.; Dekker, J. P.; Yellen, G. *Nature* **2004,** *428*, 864–868.
21. Preston, G. M.; Jung, J. S.; Guggino, W. B.; Agre, P. *J. Biol. Chem.* **1993,** *268*, 17–20.
22. del Camino, D.; Yellen, G. *Neuron* **2001**, *32*, 649–656.
23. Li, M.; Kawate, T.; Silberberg, S. D.; Swartz, K. J. *Nat. Commun.* **2010**, *1*:44.
24. Marcus, Y. *Ion properties*, Dekker, New York, 1997.
25. Lever, A. B. P. in *Comprehensive coordination chemistry. II: from biology to nanotechnology*, Vol. 1, McCleverty, J. A.; Meyer, T. J., Eds.; Amsterdam; Oxford: Elsevier, 2004, pp 538.
26. Holmgren, M.; Shin, L. S.; Yellen, G. *Neuron* **1998**, *21*, 617–621.
27. Paas, Y.; Gigor, G.; Grailhe, R.; Savatier-Duclert, N.; Dufresne, V.; Sunesen, M.; de Carvalho, L. P. Changeux, J.-P.; Attali, B. *Proc. Natl. Acad. Sci. U. S. A.* **2005**, *102*, 15877–15882.
28. Flynn, G. E.; Zagotta, W. N. *Neuron* **2001**, *30*, 689–698.
29. Shannon, R. D. *Acta Cryst.* **1976**, *A32*, 751–767.
30. Dance, I. G.; Fitzpatrick, L. J.; Rae, A. D.; Scudder, M. L. *Inorg. Chem.* **1983**, *22*,

3785–3788.

31. Andersson, L.-O. *J. Polym. Sci. Part A1* **1972**, *10*, 1963–1973.
32. Isab, A. A.; Wazeer, M. I. M. *Spectrochim. Acta, Part A* **2007**, *6*, 364–370.
33. Shen, J.-S.; Li, D.-H.; Cai, Q.-G.; Jiang, Y.-B. *J. Mater. Chem.* **2009**, *19*, 6219–6214.
34. Shen, J.-S.; Li, D.-H.; Zhang, M.-B.; Zhou, J.; Zhang, H.; Jiang, Y.-B. *Langmuir* **2011**, *27*, 481–486.
35. Nan, J.; Yan, X.-P. *Chem. Eur. J.* **2010**, *16*, 423–427.
36. Cecil, R. *Biochem. J.* **1950**, *47*, 572–584.
37. Kolthoff, I. M.; Eisenstädter, J. *Anal. Chim. Acta* **1961**, *24*, 83–90.
38. Rulisek, L.; Vondrasek, J. *J. Inorg. Biochem.* **1998**, *71*, 115–127.
39. Enescu, M.; Renault, J.; Pommeret, S.; Mialocq, J.; Pin, S. *Phys. Chem. Chem. Phys.* **2003**, *5*, 3762–3767.
40. Liau, S. Y.; Read, D. C.; Pugh, W. J.; Furr, J. R.; Russell, A. D. *Lett. Appl. Microbiol.* **1997**, *25*, 279–283.
41. Delalande, O.; Desvaux, H.; Godat, E.; Valleix, A.; Junot, C.; Labarre, J.; Boulard, Y. *FEBS J.* **2010**, *277*, 5086–5096.
42. Walker, B.; Kasianowisc, J.; Krishnasastry, M.; Bayley, H. *Protein Eng.* **1994**, *7*, 655–662.
43. Walker, B.; Braha, O.; Cheley, S.; Bayley, H. *Chem. Biol.* **1995**, *2*, 99–105.
44. Kasianowicz, J. J.; Burden, D. L.; Han, L. C.; Cheley, S.; Bayley, H. *Biophys. J.* **1999**, *76*, 837–845.
45. Song, L.; Hobaugh, M. R.; Shustak, C.; Cheley, S.; Bayley, H.; Gouaux, J. E. *Science* **1996**, *274*, 1859–1866.
46. Braha, O.; Walker, B.; Cheley, S.; Kasianowisc, J. J.; Song, L.; Gouaux, J. E.;

Bayley, H. *Chem. Biol.* **1997**, *4*, 497–505.

47. Braha, O.; Gu, L.-Q.; Zhou, L.; Lu, X.; Cheley, S.; Bayley, H. *Nat. Biotechnol.* **2000**, *18*, 1005–1007.
48. Hammerstein, A. F.; Shin, S.-H.; Bayley, H. *Angew. Chem. Int. Ed.* **2010**, *49*, 5085–5090.
49. Hammerstein, A. F. Engineering of an α-hemolyin pore. DPhil Dissertation, University of Oxford, March 2012.
50. Li, M.; Chang, T.-H.; Silberberg, S. D.; Swartz, K. J. *Nat. Neurosci.* **2008**, *11*, 883–887.
51. Gruen, L. C. *Biochim. Biophys. Acta* **1975**, *386*, 270–274.
52. Lee, V. W.-M.; Li, H.; Lau, T.-C.; Guevremont, R.; Siu, K. W. M. *J. Am. Soc. Mass. Spectrom.* **1998**, *9*, 760–766.
53. Shoeib, T.; Siu, K. W. M.; Hopkinson, A. C. *J. Phys. Chem. A* **2002**, *106*, 6121–6128.
54. Jover, J.; Bosque, R.; Sales, J. *Dalton Trans.* **2008**, 6441–6453.
55. Rabilloud, T. *Electrophoresis* **1990**, *11*, 785–794.
56. Chevallet, M.; Luche, S.; Rabilloud, T. *Nat. Protoc.* **2006**, *1*, 1852–1858.
57. Walker, B.; Bayley, H. *Protein Eng.* **1994**, *7*, 91–97.
58. Movileanu, L.; Cheley, S.; Howorka, S.; Braha, O.; Bayley, H. *J. Gen. Physiol.* **2001**, *117*, 239–251.
59. Merzlyak, P. G.; Capistrano, M.-F. P.; Valeva, A.; Kasianowicz, J. J.; Krasilnikov, O. V. *Biophys. J.* **2005**, *89*, 3059–3070.
60. Noskov, S. Y.; Im, W.; Roux, B. *Biophys. J.* **2004**, *87*, 2299–2309.
61. Hatefi, Y.; Hanstein, W. G. *Methods Enzymol.* **1973**, *31*, 770–790.
62. Baldwin, R. L. *Biophys. J.* **1996**, *71*, 2056–2063.

63. Su, C.-Y.; Chen, C.-L.; Zhang, J.-Y.; Kang, B.-S. Silver(I) Coordination Polymers in *Design and Construction of Coordination Polymers*; Hong, M.-C.; Chen, L., Eds.; Wiley: Hoboken, N. J., 2009; pp 111–144.
64. http://maxchelator.stanford.edu
65. (a) Martell, A. E.; Smith, R. M. *Critical Stability Constants*, Plenum Press: New York and London, 1974. (b) http://www.chem.wisc.edu/areas/reich/pkatable/index.htm and references therein.
66. Ferguson-Miller, S.; Koppenol, W. H. *Trends Biochem. Sci.* **1981**, *6*, R4–7.
67. Shin, S.-H.; Bayley, H. *J. Am. Chem. Soc.* **2005**, *127*, 10462–10463.
68. Mah, V.; Jalilehvand, F. *J. Biol. Inorg. Chem.* **2010**, *15*, 441–458.
69. Liu, Y.; Holmgren, M.; Jurman, M. E.; Yellen, G. *Neuron* **1997**, *19*, 175–184.
70. Willner, H.; Vašák, M; Kägi, J. H. R. *Biochemistry* **1987**, *26*, 6287–6292.
71. Cruz-Vásquez, B. H.; Díaz-Cruz, J. M.; Ariño, C.; Esteban, M; Tauler, R. *Analyst* **2002**, *127*, 401–406.
72. Kalidas, C. *Chemical kinetic methods: principles of fast reaction techniques and applications*, 2nd ed.; New Age International: New Delhi, 2005.
73. Hille, B.; Schwarz, W. *J. Gen. Physiol.* **1978**, *72*, 409–432.
74. Qu, W.; Moorhouse, A. J.; Cunningham, A. M.; Barry, P. H. *Proc. R. Soc. Lond. B* **2001**, *268*, 1395–1403.
75. (a) Boersma, A. J.; Brain, K. L.; Bayley, H. *ACS Nano* **2012**, *6*, 5304–5308. (b) Boersma, A. J.; Bayley, H. *Angew. Chem. Int. Ed.* **2012**, *51*, doi: 10.1002/anie.201205687.
76. Walker, B.; Krishnasastry, M.; Zorn, L.; Kasianowicz, J.; Bayley, H. *J. Biol. Chem.* **1992**, *267*, 10902–10909.
77. Shin, S.-H.; Steffenson, M. B.; Claridge, T. D. W.; Bayley, H. *Angew. Chem. Int.*

Ed. **2007**, *46*, 7412–7416.

78. Wolfe, A. J.; Mohammad, M. M.; Cheley, S.; Bayley, H.; Movileanu, L. *J. Am. Chem. Soc.* **2007**, *129*, 14034–14041.
79. Zemaitis, J. F.; Clark, D. M.; Rafal, M.; Scriver, N. *Handbook of aqueous electrolyte thermodynamics: theory and application*; American Institute of Chemical Engineers: New York, 1986.
80. Hamer, W. J.; Wu, Y.-C. *J. Phys. Chem. Ref. Data* **1972**, *1*, 1047–1099.
81. Shin, S.-H.; Luchian, T.; Cheley, S.; Braha, O.; Bayley, H. *Angew. Chem. Int. Ed.* **2002**, *41*, 3707–3709.
82. Greenwood, N.N., Earnshaw, A. *Chemistry of the Elements*; Permagon Press: New York, 1984; pp 1185–1187.
83. Whitesides, G. M.; Lilburn, J. E.; Szajewski, R. P. *J. Org. Chem.* **1977**, *42*, 332–338.
84. Szajewski, R. P.; Whitesides, G. M. *J. Am. Chem. Soc.* **1980**, *102*, 2011–2026.
85. Wilson, J. M.; Bayer, R. J.; Hupem D. J. *J. Am. Chem. Soc.* **1977**, *99*, 7922–7926.
86. Pleasants, J. C.; Guo, W.; Rabenstein, D. L. *J. Am. Chem. Soc.* **1989**, *111*, 6553–6558.
87. Bachrach, S. M.; Demoin, D. W.; Luk, M.; Miller Jr., J. V. *J. Phys. Chem. A* **2004**, *108*, 4040–4046.
88. Steinman, D.; Nauser, T.; Koppenol, W. H. *J. Org. Chem.* **2010**, *75*, 6696–6699.
89. Luchian, T.; Shin, S.-H.; Bayley, H. *Angew. Chem. Int. Ed.* **2003**, *42*, 3766–3771.
90. Rogers, S. E. A selenocysteine containing αHL for single molecule studies. DPhil. Dissertation, University of Oxford, March 2012.
91. Metanis, N.; Keinan, E.; Dawson, P. E. *Angew. Chem. Int. Ed.* **2010**, *49*, 7049–7053.

92. Lewin, A.; Crow, A.; Oubrie, A.; Le Brun, N. E. *J. Biol. Chem.* **2006**, *281*, 35467–35477.
93. Nelson, J. W.; Creighton, T. E. *Biochemistry* **1994**, *33*, 5974–5983.
94. Potin-Gautier, M.; Boucharat, C.; Astruc, A.; Astruc, M. *Appl. Organomet. Chem.* **1993**, *7*, 593–598.
95. Figueiredo-Pereira, M. E.; Yakushin, S.; Cohen, G. *J. Biol. Chem.* **1998**, *273*, 12703–12709.
96. Zhang, R.; Snyder, G. H. *J. Biol. Chem.* **1989**, *264*, 18472–18479.
97. Derewenda, U.; Boczek, T.; Gorres, K. L.; Yu, M.; Hung, L.-W.; Cooper, D.; Joachimiak, A.; Raines, R. T.; Derewenda, Z. S. *Biochemistry* **2009**, *48*, 8664–8671.
98. Moczydlowski, E. in *Ion channel reconstitution*. Miller, C. Eds.; Plenum: New York and London, 1986, pp 75–114.
99. Colquhoun, D.; Hawkes, A. G. in *Single-channel recording*. Sakmann, B.; Nehre, E., Eds., Springer: New York, London, 2009, pp 397–482.

Chapter 4. Copper(II)-Catalyzed Diels-Alder Reactions

4.1 Introduction

4.1.1 Artificial metalloenzymes

Metal catalysts are important in both nature and chemical synthesis; about one-third of the structurally characterized enzymes contain metal cofactors,[1] and several important industrial processes rely on metal catalysts, such as the Haber-Bosch process for ammonia production and sulfuric acid manufacture. Metalloenzymes exhibit high substrate selectivity, high enantioselectivity, large turnover number, and function in aqueous solutions.[2] On the other hand, small molecule catalysts show broad substrate scope. Further, they can be easily engineered to generate the opposite enantiomer of the product and perform chemistry which is not the case with metalloenzymes. However, small molecule catalysts usually exhibit limited turnover number.

To construct novel catalysts that combine the advantages of metalloenzymes and small molecule catalysts, a small organometallic center is incorporated onto a biomolecular host, such as a protein, RNA and DNA.[2] These hybrid catalysts are collectively called artificial metalloenzymes and they can be applied for synthesis and mechanistic studies. Three approaches have been used for the attachment, namely non-covalent, covalent and dative covalent interactions.[3] Non-covalent (also called supramolecular) anchoring usually utilizes biotin-(strept)avidin binding (Figure 4.1[4]), π-π stacking interactions between aromatic compounds and double stranded DNA (dsDNA)[5] (Figure 4.4b) or hapten-antibody binding.[6,7] Covalent assembly is by the targeted chemical modification of proteins (usually at cysteine residue) or by modification of 5' or 3' terminal amino-modified oligonucleotides (Figure 4.4c[8]). Dative attachment is through the coordination of amino acid side chain(s) from the host protein to the catalytic metal centre, such as a His/His/Asp site for Cu^{2+} ion binding[9] (Figure 4.3b).

The first example of an artificial metalloenzyme was reported in 1978 by the Whitesides group.[4] An asymmetric hydrogenation catalyst was constructed by embedding a biotin-linked achiral diphosphinerhodium(I) compound (Btn-Rh^+) into avidin (Figure 4.1). Modest enantioselectivity (44%) was obtained by chirality transfer from the protein to the product of the catalytic reaction.

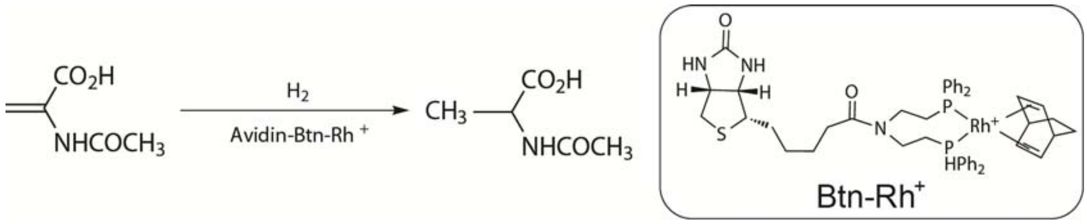

Figure 4.1. *Artificial metalloenzyme for asymmetric hydrogenation. The synthetic biotin-conjugated diphosphinerhodium(I) compound (Btn-Rh^+) was incorporated into avidin through the strong non-covalent binding of biotin to avidin. Hydrogenation of α-acetamidoacrylic acid in aqueous solution (0.1 M Na_2HPO_4, pH 7.0, and 0 °C for 48 h) with hydrogen gas (1.5 atm pressure) yields predominantly the S product (up to 44% e.e.). Adapted with permission from ref. 4. Copyright (1978) American Chemical Society.*

In the last decade, significant progress has been made in the development of a vast variety of artificial metalloenzymes that are capable of catalyzing different chemical reactions. In addition to the asymmetric hydrogenation discussed above, metal-catalyzed Diels-Alder reaction (*vide infra*),[10] Michael addition,[11] Friedel-Crafts reaction,[12] hydration of α,β-unsaturated ketones,[13] sulfoxidation,[14] epoxidation,[15,16] epoxide hydrolysis,[17] fluorination,[18] dihydroxylation,[19] olefin metathesis[20] have been reported.[2,3] The following sections will focus on Cu^{2+}-catalyzed Diels-Alder reactions.

4.1.2 Metal-catalyzed Diels-Alder reaction

The Diels-Alder reaction[21] is of synthetic importance in both pharmaceutical and industrial chemistry. This is because a salient building block, a cyclohexene carrying up to four new stereogenic centres, is formed when the diene reacts with an alkene (dienophile) in a concerted manner (Scheme 4.1). Two new carbon-carbon single bonds are formed.

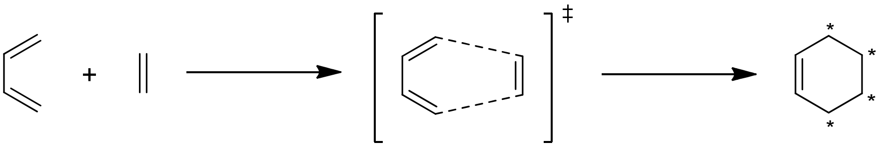

Scheme 4.1. *Diels-Alder reaction. A diene reacts with an alkene to form a cyclohexene. The four new potential stereogenic centres in the product are marked with an asterisk.*

Metal ion-catalyzed Diels-Alder reactions in aqueous solutions were first reported by Otto *et al.*[22] The reaction involves a bidentate dienophile (such as the azachalcone in Figure 4.2), which can bind to transition metal ions (e.g. Ni^{2+}, Co^{2+}, Cu^{2+} and Zn^{2+}). The metal ion acts as a Lewis acid. The coordination of a bidentate dienophile to the metal centre withdraws electron density from the conjugated alkene. This lowers the LUMO energy of the alkene and favors its interaction with the HOMO of the diene.[10,22,23] Cu^{2+} ion is the most efficient catalyst among the tested metal ions. The catalytic efficacy of copper(II) complexes formed with amino acid[24,25] or bipyridine[25] ligands have been investigated as well. In general, these copper(II) complexes show comparable or slightly weaker catalytic power (in terms of the catalytic rate constant k_{cat} (Figure 4.2)) than the free Cu^{2+} ion. These kinds of copper(II) complexes have been applied in the construction of artificial Diels-Alderases (see Section 4.1.3).

Mechanism of copper(II)-catalyzed Diels-Alder reaction

The proposed catalytic cycle for the copper(II)-catalyzed Diels-Alder reaction is portrayed in Figure 4.2. The first step is the reversible binding of the bidentate dienophile (e.g. azachalcone) to the Cu^{2+} centre with an association constant K_a. K_a depends on the primary ligands (L_n) on Cu^{2+}, and in the case of metalloenzymes, it is further affected by the microenvironment provided by the biomolecule. The second step is the Diels-Alder transformation with second-order rate constant k_{cat}. The diene (e.g. cyclopentadiene) accesses the L_n-Cu^{2+}-dienophile complex and reacts with the activated dienophile to generate the Diels-Alder product. Endo products are favoured over the exo products because of the favourable secondary orbital interactions in the transition state leading to the endo products. For an achiral L_n-Cu^{2+} complex bound to a chiral biomolecule, chirality transfer from the biomolecule can induce asymmetry to the metal complex. Thus the two faces of the square-planar L_n-Cu^{2+}-dienophile complex are not identical (see the transition state structure in Figure 4.4). Reaction with diene approaching from one face is more favourable than from the other side, leading to enantioselectivity. The last step in the catalytic cycle is the dissociation (K_d) of Diels-Alder product from the metal centre, regenerating the free binding sites on Cu^{2+} for another round of catalysis.

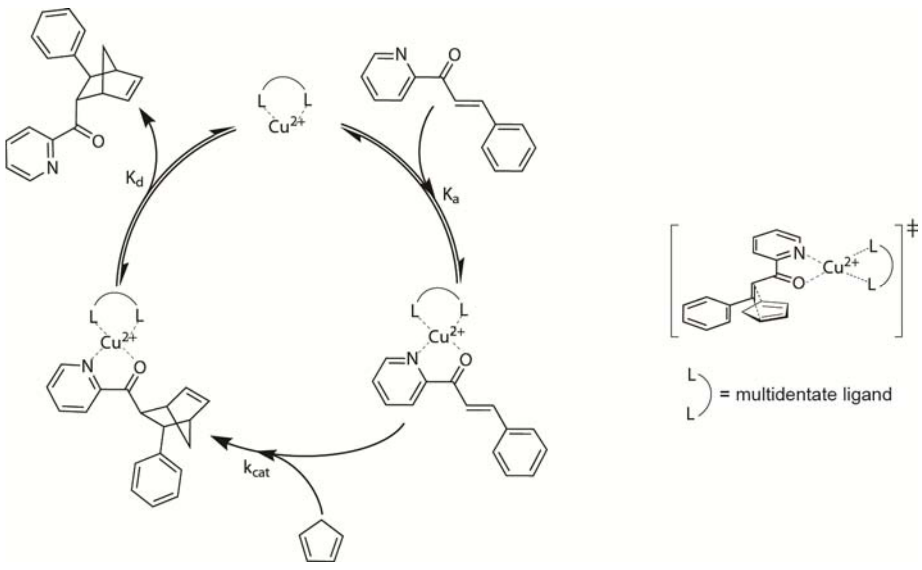

Figure 4.2. *Proposed mechanism for Cu^{2+}-catalyzed Diels-Alder reaction in aqueous solution.*[22] *Azachalcone and cyclopentadiene are used as the model reactants. The proposed transition state structure is shown on the right. Azachalcone chelates Cu^{2+} through its picolinyl group.*

4.1.3 Artificial Diels-Alderases

No natural Diels-Alderase has been unambiguously confirmed so far.[26] However, different artificial enzymes that carry out the Diels-Alder reaction in aqueous media have been constructed. They are based on protein,[9,23] peptide,[27] DNA[5] or RNA.[28] Most of these artificial Diels-Alderases utilize a metal complex, usually copper(II), to accelerate the Diels-Alder reaction (see Section 4.1.2). The metal-free alternatives, based on antibodies[6,7] or ribozymes,[28,29] catalyze Diels-Alder reactions by providing a tailor-made binding pocket that has a complementary shape to the transition state structure, thus lowering the activation energy of reaction. This section will provide a summary of the copper(II)-based artificial Diels-Alderases.

Serum albumin holding a dative covalently bound phthalocyanine-Cu^{2+} complex (Figure 4.3a) demonstrated good conversion (80%, at pH 4.0, 3 °C and 3 d) and high enantioselectivity (93%) for the model Diels-Alder reaction between cyclopentadiene and azachalcone, a Cu^{2+} binding dienophile (Figure 4.3d).[23] The protein-anchored Cu^{2+} complex is less reactive than the free complex, possibly due to the coordination of protein amino acid side chain(s) to Cu^{2+} so that the Lewis acidity and the binding affinity to the dienophile are both weakened.

A His/His/Asp Cu^{2+} binding site has been engineered on the TIM-barrel of the synthase subunit of the robust thermostable imidazole glycerol phosphate synthase from *Thermotoga maritime* (tHisF, Figure 4.3b) by site-directed mutagenesis.[9] This artificial metalloenzyme showed modest conversions (73%, at pH 7.5, 12 °C and 4 d) and enantioselectivity (46%).

A peptide-based metalloenzyme has been reported by Coquière *et al.* using the 36 amino acid long bovine pancreatic polypeptide (bPP),[27] which forms an antiparallel homodimer. A bis(pyridine) coordination site for Cu^{2+} ion was constructed by introducing a pyridine ligand to each bPP monomer at the hydrophobic dimer interface (Figure 4.3c). The pyridine ligand was incorporated as the unnatural amino acid, L-4-pyridylalanine, by solid phase peptide synthesis. Full conversion and good enantioselectivity (80%) were observed (at pH 6.5, 5 °C and 3 d).

DNA-based copper(II) Diel-Alderases[5] show superior catalytic properties compared to the protein- and peptide-based structures. A copper(II) complex is attached to the double stranded DNA (dsDNA) either by DNA intercalation[30] (Figure 4.4b) or by the covalent attachment to a 5' or 3' end[8] (Figure 4.4c). Two generations of ligands (2-aminomethylpyridine-based and 2,2'-bipyridine-based) have been utilized in the noncovalent approach (Figure 4.4a). Very high enantioselectivity (99%) and good conversion (>80%) were achieved using the second generation ligand – 4,4'-dimethyl-2,2'-pyridine (at pH 6.5, 5 °C and 3 d).[10,31] Moreover, the catalyst can be recycled without significant loss of catalytic efficiency. The dependences of reaction rate and enantioselectivity on the DNA microenvironment and the ligand have been investigated in detail by Roelfes *et al.*[30,32,33]

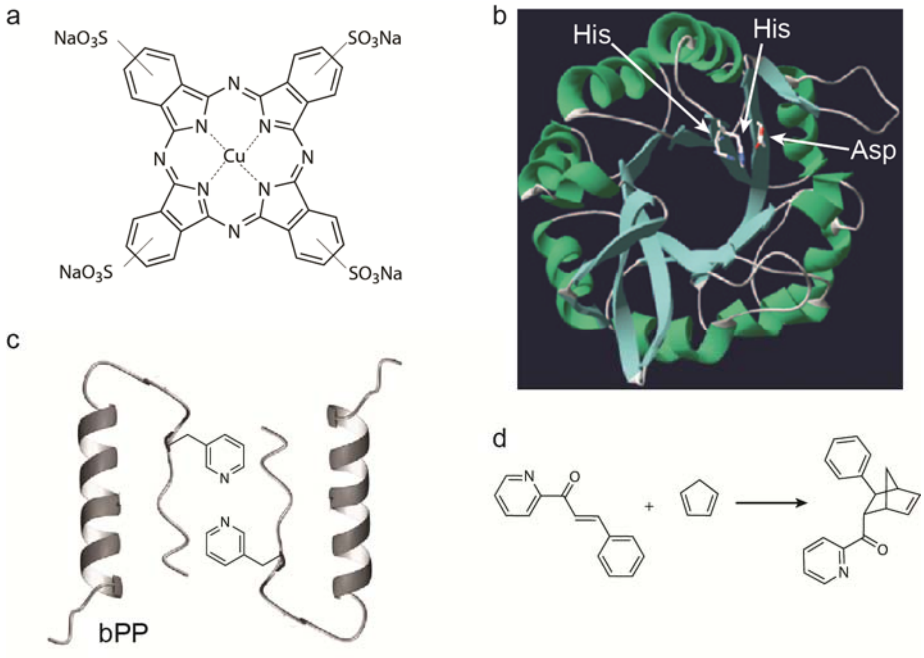

Figure 4.3. *Protein and peptide-based artificial metalloenzymes for the Diels-Alder reaction. The Lewis acid copper(II) catalytic centres in the three examples shown here are attached via dative covalent bonds. (a) Structure of the commercially available phthalocyanine-Cu^{2+} complex that was noncovalently anchored to serum albumin.*[23] *(b) A tricoordinating (His/His/Asp) Cu^{2+} binding site constructed on the TIM-barrel of the synthase subunit of the robust thermostable imidazole glycerol phosphate synthase.*[9] *Adapted with permissions from ref. 9. Copyrights (2010) by Wiley. (c) A two pyridine-based Cu^{2+} binding site formed from the homodimerization of* L*-4-pyridylalanine-containing bovine pancreatic polypeptides (bPP).*[27] *Adapted with permissions from ref. 27. Copyrights (2009) by Wiley. (d) The model Diels-Alder reaction between cyclopentadiene and azachalcone catalyzed by the metalloenzymes in (a–c). The endo isomer (shown) is the major product in (a–c).*

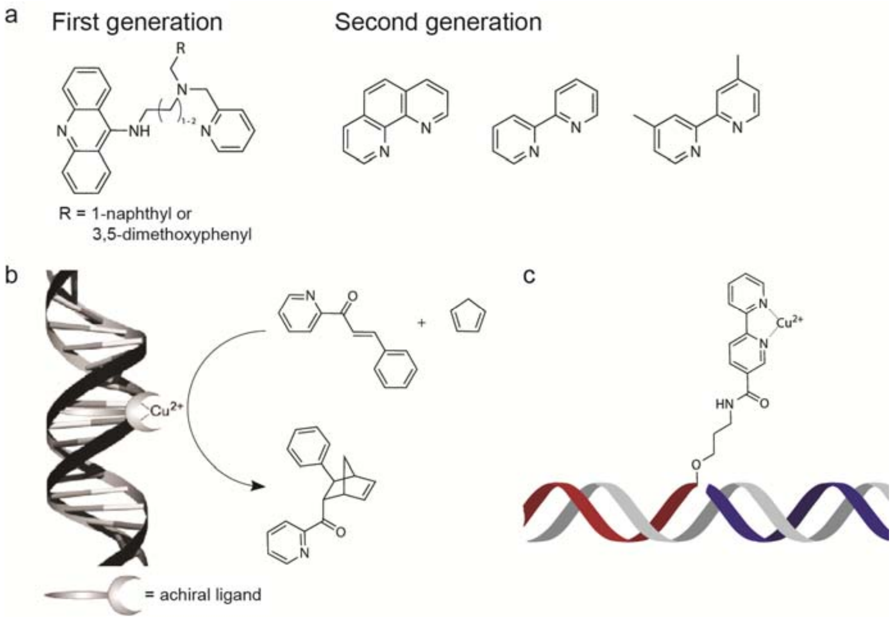

Figure 4.4. *DNA-based asymmetric catalysis for Diels-Alder reaction. (a) Examples of the first generation (2-aminomethylpyridine moiety linked to 9-aminoacridine) and the second generation (2,2'-bipyridine analogues) ligands. (b) Non-covalent incorporation of* Cu^{2+} *complex to a double stranded DNA (dsDNA). The achiral ligand is one of those shown in (a). The catalytic Diels-Alder reaction is shown. Salmon testes DNA was usually used. Adapted with permission from ref. 31. Copyrights (2007) American Chemical Society. (c) Covalently attached 2,2'-bipyridine ligand on a 5' or 3' amino-functionalized oligonucleotide (red), which was assembled with the other half DNA (blue) on a template DNA (grey) to form a dsDNA.*[8]

4.2 Objectives

So far, all of the chemical reactions studied with the single-channel recording technique are non-catalytic reactions. To extend the repertoire to catalytic reactions, a metal catalytic centre can be incorporated to αHL. Recently, our group has published the construction of metal chelating site in the β barrel of αHL via the covalent modification of cysteine residues with 2,2'-(3-(2-iodoacetamido)propylazanediyl) diacetic acid (PIDA) (see Scheme 4.2 for structure).[34] Using the same iminodiacetate-based chelator, we introduced a copper(II) centre for studying catalytic Diels-Alder reactions at the single-molecule level. Copper(II)-catalyzed Diels-Alder reaction was chosen because it is well-characterized and a range of artificial Diels-Alderases are known. The two model Diels-Alder reactions investigated are those between cyclopentadiene (**6**) and (*E*)-3-(4-nitrophenyl)-1-(2-pyridyl)-2-propene-1-one (**7**) or 5-hydroxy-1,4-naphthoquinone (**8**) (Scheme 4.3). The choices of these reactants are explained in Section 4.3.3.

4.3 Results

4.3.1 Preparation of the chelator-containing protein (P_{PIDA})

Iminodiacetate chelators have been incorporated in αHL by targeted chemical modifications of cysteine residues to study Zn^{2+} ion binding (see Chapter 3, Section 3.1.4).[34] The same synthetic procedures and protein modification steps in the published paper were followed. This section gives a brief summary about these.

The chelator molecule, 2,2'-(3-(2-iodoacetamido)propylazanediyl)diacetic acid (PIDA, **5**), consists of three parts, namely the iminodiacetate chelator, a propyl linker and an iodoacetamide alkylation site (Scheme 4.2). The iodoacetamide group acts as a handle for attaching the molecule onto the protein through an S_N2 reaction with a cysteine thiol group to form a thioether bond.

The synthetic route of PIDA is shown in Scheme 4.2 (refer to Section 4.6.2 for synthetic procedures). 3-Bromopropylamine **1** was converted to 3-azidopropylamine **2** by heating with sodium azide at 80 °C for 15 h. Dialkylation of amine in **2** with *tert*-butyl bromoacetate at room temperature yielded **3**. Staudinger reduction of the azide in **3** to the amine, followed by alkylation with *N*-iodoacetoxysuccinimide gave

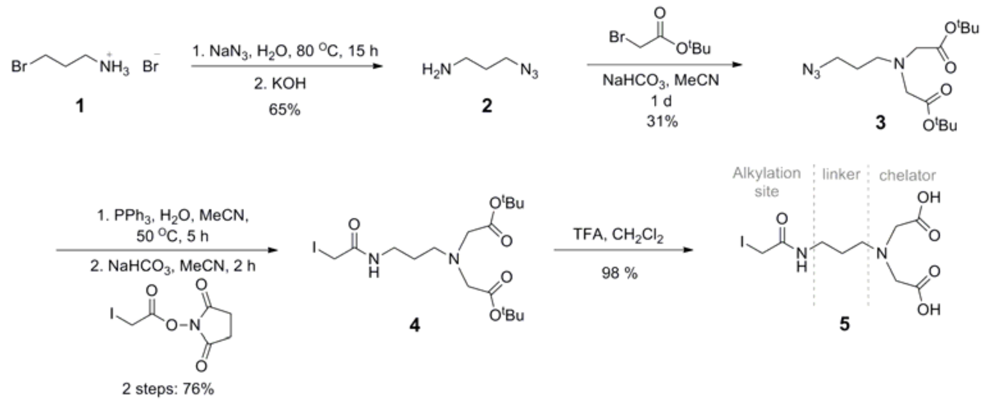

Scheme 4.2. *Synthesis of PIDA.*

the Boc-protected compound **4**. Deprotection of the Boc groups with trifluoroacetic acid formed the final product **5**.

The heteroheptameric αHL pore, (WT)$_6$(G137C-PIDA)$_1$ (abbreviated as P$_{PIDA}$), which bears only one chelator-modified subunit was prepared as follow. The cysteine-containing monomer (G137C) obtained from *in vitro* transcription and translation (IVTT) was first reacted with PIDA (1 h, r.t., pH 8.5) (see Section 4.6.3). After gel filtration to remove excess PIDA, the modified monomer, G137C-PIDA, was co-oligomerized with WT monomer in a 1:6 ratio on rabbit red blood cell membrane (rRBCm). The sample, which contained heptamers with different ratio of WT to G137C-PIDA, was purified on 5% SDS-PAGE (Figure 4.11). The band corresponding to P$_{PIDA}$ was cut out and recovered from the gel. The separation of heptamers comprising different ratios of WT to G137C-PIDA relies on the eight aspartate residues located at the C terminus of G137C subunit. Heptamers with more copies of G137C-PIDA have higher electrophoretic mobility (see Section 4.6.4).

Single-channel recording results show that ~60% of the purified proteins are modified, i.e. carry PIDA. The other 40% of proteins do not show metal ion binding activities. This is presumably due to incomplete chemical modification.

4.3.2 Binding of Cu^{2+} ion to P$_{PIDA}$

To avoid the sequestering of added Cu^{2+} ions, a chelator-free buffer solution at pH 7.0 (2 M KCl, 10 mM MOPS, treated with Chelex ion exchange resin) was employed in the following investigations. Chelator (e.g. 100 μM of EDTA) is usually present in the buffer solution for single-channel recording experiments in order to avoid the unwanted multivalent metal ion interactions with αHL and other biological reagents used, such as DNA and enzymes. To remove residual multivalent metal ions without the use of chelator, the buffer solution was (1) prepared with high purity KCl (Fluka, #05257, ≥99.9995% (metal basis)) and (2) after dissolution of KCl and MOPS, the buffer was treated with the Chelex ion exchange resin (Bio-Rad, #142-1253) by stirring at room temperature for 1 h. After the removal of resin by filtration, pH of the buffer was adjusted.

In this buffer at pH 7.0, P$_{PIDA}$ shows weak rectification ($I_{+100\ mV}/L_{-100\ mV} = 1.3$) (Figure 4.5) and carried a steady single-channel current of –74 ± 3 pA (n = 18) and +85 ± 2 pA (n = 4) at –50 and +50 mV, respectively. At +50 mV, addition of Cu^{2+} ion (as CuCl$_2$ to the *trans* side) caused reversible blockades with amplitude (ΔI) of –1.3 ± 0.2 pA (n = 5) relative to the open pore level (Figure 4.6a). These Cu^{2+} ion-related blockades were not seen with (WT)$_7$, confirming the specific interactions of Cu^{2+} ions with the iminodiacetate chelator in P$_{PIDA}$. The frequency of these blockades in P$_{PIDA}$ increased with Cu^{2+} concentration, suggesting that the new level arises from a P$_{PIDA}$-Cu^{2+} complex (abbreviated as P$_{PIDA}$-Cu^{2+}). Cu^{2+} ion concentration inside the pore is assumed to be the same as that in the bulk solution. A plot of the reciprocal of the mean inter-event interval (i.e. the mean dwell time as an open pore) ($1/\bar{\tau}_P$) against the Cu^{2+} ion concentration was shown to be linear (Figure 4.6b), which suggests bimolecular interaction for which $1/\bar{\tau}_P = k_{0\text{-}1}[Cu^{2+}]$. Thus, only one Cu^{2+} ion is bound to the chelator at a time. On the other hand, a plot of the reciprocal of the mean

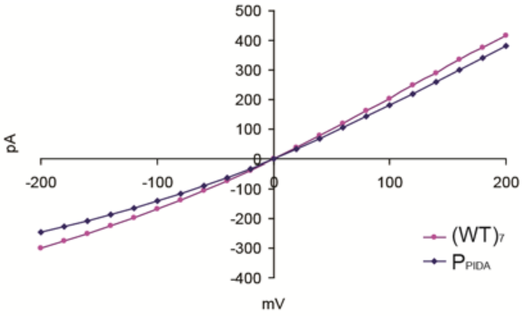

Figure 4.5. *Current-voltage (I-V) relationship of P_{PIDA}. I-V curve of $(WT)_7$ is shown for comparison. $(WT)_7$ and $(WT)_6(G137C\text{-}D8)_1$ (data not shown) have almost identical I-V relationship. Therefore the small difference in I-V relationship between P_{PIDA} and $(WT)_7$ arises from the incorporation of iminodiacetate chelator. Conditions: 2 M KCl, 10 mM MOPS, treated with Chelex, pH 7.0 and 22 °C. Voltage was applied to the trans compartment, and the cis side (where the cap domain of αHL resides) was grounded. Positive current represents the flow of cations from the trans compartment to the cis compartment.*

lifetime of the complex ($1/\bar{\tau}_{P\text{-}Cu}$) versus Cu^{2+} ion concentration gives a near zero slope, which is consistent with a unimolecular dissociation mechanism in which $1/\bar{\tau}_{P\text{-}Cu} = k_{1\text{-}0}$. The forward and reverse reaction rate constants determined from $\bar{\tau}$ values are $k_{0\text{-}1} = (12 \pm 5) \times 10^4$ $M^{-1}s^{-1}$ and $k_{1\text{-}0} = (9.1 \pm 1.1) \times 10^{-2}$ s^{-1} (n = 3), respectively. The dissociation constant K_d ($= k_{1\text{-}0}/k_{0\text{-}1}$) is 880 ± 120 nM. The structurally similar chelator, *N*-methyliminodiacetate (MIDA), has a literature K_d value of 3.3 nM at pH 7.0[41] (see Section 4.6.7). Although extra coordination possibilities by proximal amino acid residues exist on P_{PIDA}, Cu^{2+} binding to P_{PIDA} is more than 250-fold weaker than its binding to MIDA. This may due to (1) the higher pK_a value of the iminodiacetate chelator in the pore environment and/or (2) the unfavourable electrodiffusion of Cu^{2+} (added to *trans* side) through the pore at +50 mV, leading to the lower effective Cu^{2+} concentration in the lumen.

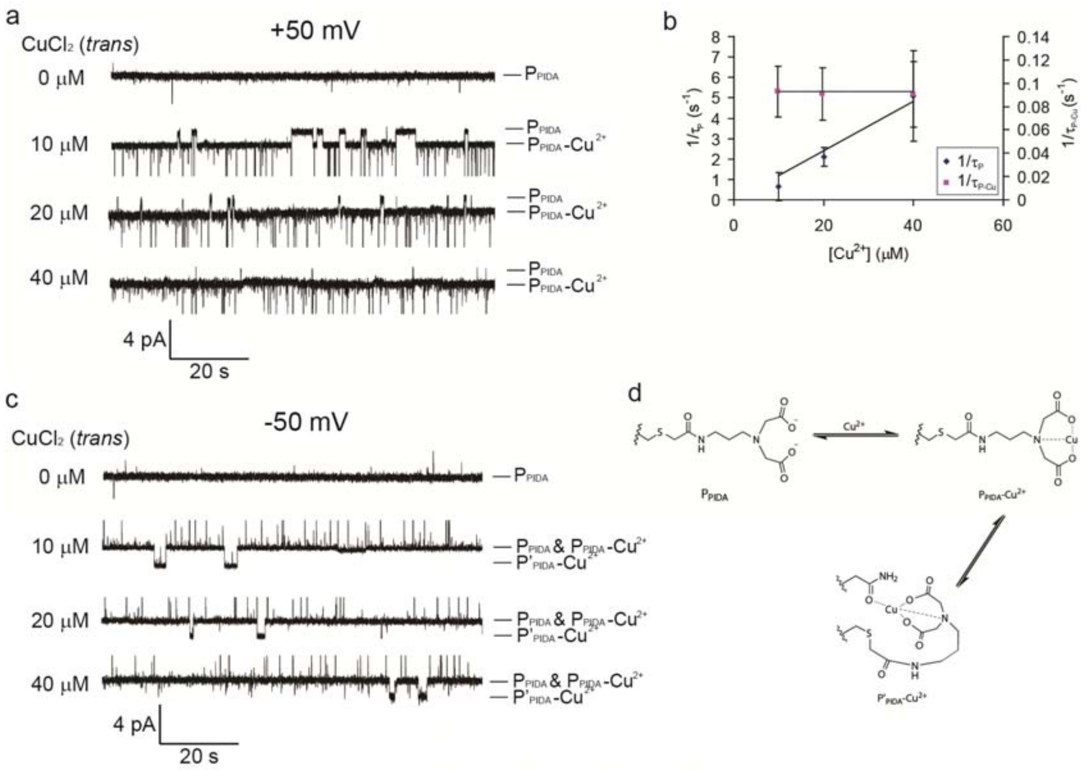

Figure 4.6. *Reversible binding of* Cu^{2+} *ions to the iminodiacetate chelator in* P_{PIDA}*. (a) Single-channel recordings at +50 mV,* Cu^{2+} *ions binding gave a distinguishable new level. Note that many short-lived events appeared on the* P_{PIDA}-Cu^{2+} *level at both +50 and –50 mV. They are attributed to the binding of* Cl^{-} *ions in buffer to the pore-bound* Cu^{2+} *ion. These events have amplitudes up to about –15 pA and are truncated in both (a) and (c) for clarity. In both (a) and (c),* Cu^{2+} *ions were added as* $CuCl_2$ *to the trans compartment. Concentrations of* $CuCl_2$ *are given on the left. Conditions: 2 M KCl, 10 mM MOPS, treated with chelex, pH 7.0 and 22 °C. (b) Reciprocals of the mean inter-event dwell times for both the* P_{PIDA} *(*$1/\overline{\tau}_P$*) and* P_{PIDA}-Cu^{2+} *(*$1/\overline{\tau}_{P\text{-}Cu}$*) levels against the concentration of* Cu^{2+} *ions at +50 mV. Each point represents mean ± s.d. from three separate experiments. (c) Single-channel recordings at –50 mV.* Cu^{2+} *ion binding (level is indicated as* P_{PIDA}-Cu^{2+}*) did not cause detectable alteration to the open pore transmembrane ionic current (*P_{PIDA}*). A new level (*P'_{PIDA}-Cu^{2+}*), which had higher conductance than the* P_{PIDA} *level, appeared after* Cu^{2+} *addition. We propose that this might arise from the coordination of chelated* Cu^{2+} *ion to the amide side chain of neighbouring asparagine residues (e.g. Asn-121, Asn-123 or Asn-139) as depicted in (d). However, further evidence is needed to prove this hypothesis. (d) Structural representations showing the binding of* Cu^{2+} *ion onto the iminodiacetate chelator and other plausible binding sites as explained in (c). Other ligands on* Cu^{2+} *ions (e.g. water molecules) are omitted for clarity. The residence time of water on* Cu^{2+} *is in ns scale*[35] *which is too short to be detected in single-channel recordings.*

At –50 mV, P_{PIDA} generated events that have no concentration dependence on Cu^{2+} (the level is denoted as $P'_{PIDA\text{-}Cu^{2+}}$ in Figure 4.6c). These events have higher conductance than the P_{PIDA} level (ΔI = +1.9 ± 0.1 pA). Addition of bidentate dienophile (see next section) showed binding events appearing from the P_{PIDA} level, suggesting that P_{PIDA}-Cu^{2+} with free binding sites on Cu^{2+} was present, and by coincidence has the same conductance as P_{PIDA}. Note that without added Cu^{2+}, the dienophile does not bind to P_{PIDA}. Dienophile binding was not seen from the P'_{PIDA}-Cu^{2+} level. As P'_{PIDA}-Cu^{2+} occurs only after the addition of Cu^{2+} and have no dependence on [Cu^{2+}], it might arise from the coordination of chelated Cu^{2+} ion to the side chain of a neighbouring amino acid residue (e.g. Asn-121, Asn-123 or Asn-139) (Figure 4.6d). A discrete P'_{PIDA}-Cu^{2+} level was not observed at +50 mV.

At both –50 and +50 mV, many short-lived events (< 1 ms, with amplitudes up to –15 pA) appeared from the P_{PIDA}-Cu^{2+} level (Figures 4.6a,b). These events were disappeared when the chloride buffer was replaced with nitrate buffer, suggesting that they arose from the binding of chloride ions onto the pore-bound Cu^{2+} centre.

4.3.3 Interactions of Diels-Alder reactants and products with the pore-bound copper(II) complex

Diels-Alder reactions between cyclopentadiene (**6**) and (*E*)-3-(4-nitrophenyl)-1-(2-pyridyl)-2-propene-1-one (**7**) or 5-hydroxy-1,4-naphthoquinone (**8**) (Scheme 4.3) were chosen as two model reactions to examine the feasibility of observing the catalytic Diels-Alder transformation on the pore-bound Cu^{2+} centre at the single-molecule level. The Diels-Alder reaction between **6** and **7** is commonly used in the literature (see Section 4.1.3), with the electron-withdrawing effect of the 4-nitro group on the phenyl ring has been shown to increase the reaction rate of azachalcone (higher k_{cat}, see Figure 4.2).[22] Reaction between **6** and **8** has been investigated[36,37] and

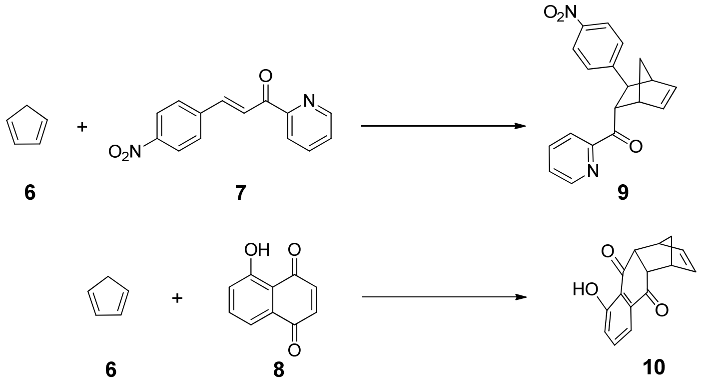

Scheme 4.3. *Two model Diels-Alder reactions for investigating the Cu^{2+}-catalyzed reaction using the nanopore approach.*

the Diels-Alder product, **10**, can bind to the P_{PIDA}-bound Cu^{2+} centre (see below).

The interaction of each reactant or product with the pore-bound Cu^{2+} centre was examined at –50 mV. Although Cu^{2+} binding to P_{PIDA} could not be observed at this voltage (see previous section), reversible binding of each of **7**, **8** and **10** were observed in the presence of Cu^{2+}. **7**, **8** and **10** gave reversible events with current blockades ΔI of –5.4 ± 0.1, –4.3 ± 0.2 and –7.7 ± 0.5 pA (n = 3), respectively (Figures 4.7c,d,f). These interactions were not observed in the absence of Cu^{2+} or when $(WT)_7$ was used, supporting that these compounds bind to the pore-bound Cu^{2+}. The difference in ΔI values between **8** and **10** (ΔΔI = 3.4 pA) is sufficient to allow the observation of Diels-Alder conversion of **8** to **10** at the single-molecule level (see next section). On the other hand, **9** showed only transient interactions to the pore-bound Cu^{2+} centre (Figure 4.7e). The different amplitudes of the observed reversible events are due to the cut-off of events with very short dwell time (<500 μs). As expected, cyclopentadiene **6** did not interact with the pore-bound Cu^{2+} centre (Figure 4.7b).

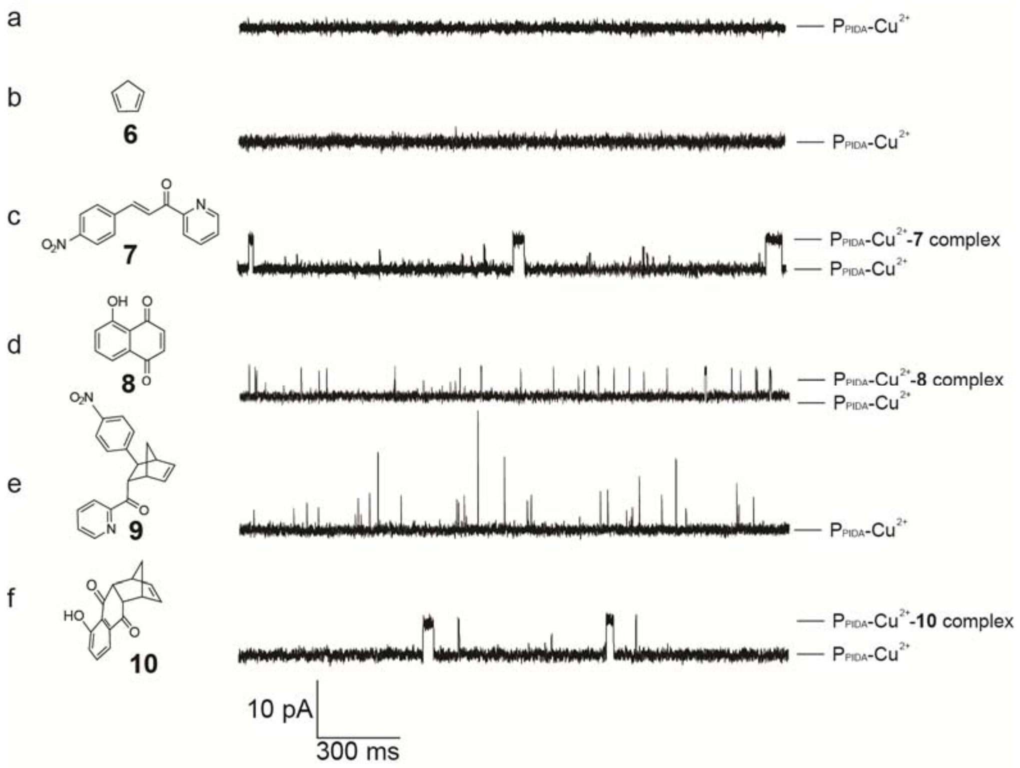

Figure 4.7. *Interactions of Diels-Alder reactants and products with P_{PIDA}-Cu^{2+}. Cu^{2+} ions were added as $CuCl_2$ (10–40 µM) to the trans compartment. (a) Cu^{2+} ion alone. (b) Cyclopentadiene (**6**) (15 mM, cis and trans). (c) (E)-3-(4-Nitrophenyl)-1-(2-pyridyl)-2-propene-1-one (**7**) (400 µM, cis). $k_{on} = 2600\ M^{-1}s^{-1}$, $k_{off} = 61\ s^{-1}$, $K_d = 23 \times 10^{-3}$ M. (d) 5-Hydroxy-1,4-naphthoquinone (**8**) (200 µM, cis). $k_{on} = 12000\ M^{-1}s^{-1}$, $k_{off} = 450\ s^{-1}$, $K_d = 39 \times 10^{-3}$ M. (e) 3-(4-Nitrophenyl)bicycle[2.2.1]-hept-5-en-2-yl)(2-pyridyl)methanone (**9**) (600 µM, cis and trans). (f) Diels-Alder product (**10**) formed from (**6**) and (**8**) (400 µM, cis). $k_{on} = 1600\ M^{-1}s^{-1}$, $k_{off} = 110\ s^{-1}$, $K_d = 97 \times 10^{-3}$ M. **9** and **10** were added as a racemic mixture that contains both endo and exo products. Conditions: 2 M KCl, 10 mM MOPS, treated with chelex, pH 7.0, at –50 mV and 22 °C.*

4.3.4 Copper(II)-catalyzed Diels-Alder reaction

In the single-channel recording chamber (see Chapter 1, Figure 1.11a), the diene (**6**) and dienophile (**7** or **8**) were added to opposite compartments[38] (*trans* and *cis* compartments, respectively) so that they would only meet inside the protein pore for catalytic reaction on the pore-bound Cu^{2+} centre. $CuCl_2$ was added to the *trans* compartment as in the two previous sections (Figure 4.8a).

Addition of Cu^{2+} (*trans*), **6** (*trans*) and **8** (*cis*) to P_{PIDA} first gave reversible events that corresponded to the binding of **8** to the pore-bound Cu^{2+} (–4.4 pA). New events that had bigger current blockade (–7.5 pA) appeared after ~5 min. The frequency of occurrence of these new events increased slowly over time. With the known Diels-Alder reaction and the current blockade, these new events were assigned to the binding of the Diels-Alder product **10**. However, the expected stepwise event for Diels-Alder conversion taking place on the pore-bound Cu^{2+} centre was rarely observed (Figure 4.8b). Only one in ~500 events at P_{PIDA}-Cu^{2+}-**8** level showed similar appearance as the expected stepwise transitions (termed 'forward' in Figure 4.8d), but the 'reverse' transitions occurred as frequently as well. Since the chosen Diels-Alder reaction is irreversible, the observations of 'reverse' events must arise from the fast substitution of **10** by **8**. The similarly frequent 'forward' events might therefore result from a similar replacement, i.e. **8** replaced by **10**, instead of a Diels-Alder reaction happening on P_{PIDA}-Cu^{2+}.

Other ways of addition of reactants and reagent to the two compartments, and experiments with another dienophile **7** were tried, but they all turned out to be unsuccessful to undergo Diels-Alder reaction on the pore-bound Cu^{2+} centre. We conclude that Cu^{2+}-catalyzed Diels-Alder transformation could not be observed at the single-molecule level with our current system.

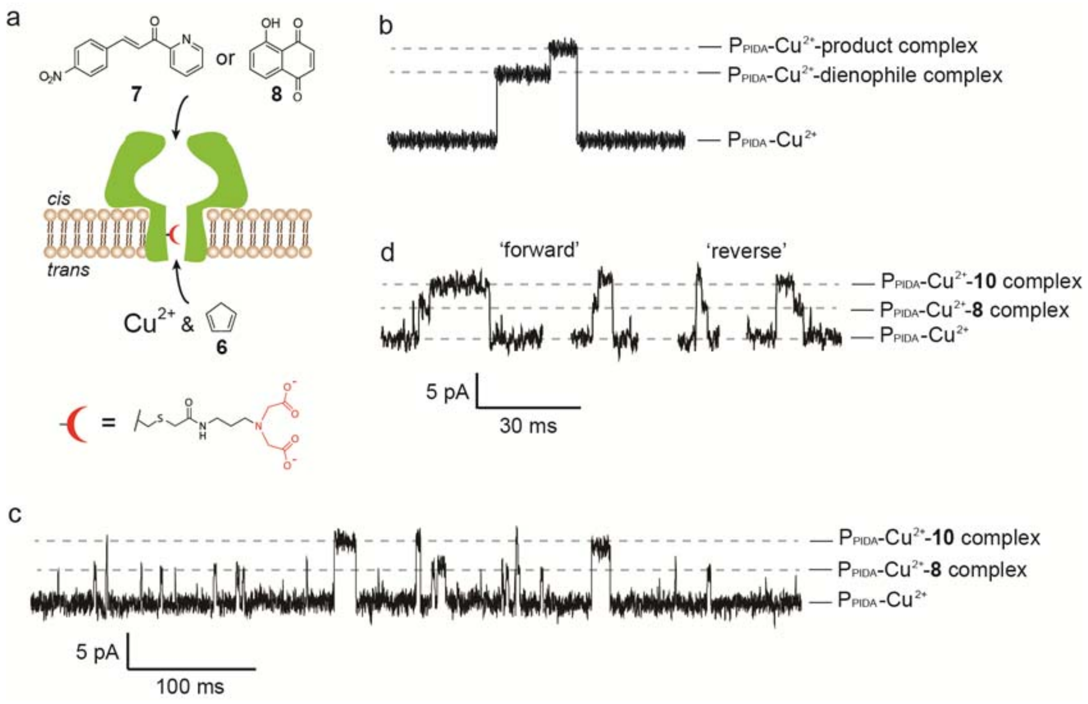

Figure 4.8. *Copper(II)-catalyzed Diels-Alder reaction inside P_{PIDA}. (a) Pictorial representation showing the sides of addition of the reactants and reagent. (b) Hypothetic current trace showing the expected appearance for the Diels-Alder conversion of* ***6*** *and* ***8*** *into* ***10*** *on the pore-bound Cu^{2+}. The three steps (association of dienophile, Diels-Alder reaction and dissociation of product) are as illustrated in the reaction mechanism shown in Figure 4.4. (c) A representative current trace obtained an hour after the addition of Cu^{2+} ion (20 µM, trans),* ***6*** *(15 mM, trans) and* ***8*** *(200 µM, cis) to P_{PIDA}. Each level is labeled on the right. (d) Selected events (termed 'forward') from the same experiment shown in (c) that resemble the idealized stepwise events depicted in (b). Events that exhibit the 'reverse' behaviour are also shown. Conditions: 2 M KCl, 10 mM MOPS, treated with chelex, pH 7.0, at –50 mV and 22 °C.*

4.4 Discussion

4.4.1 Mean waiting time for the catalytic reaction to occur – mathematical derivation

The mean waiting time $\overline{\tau}_{0,1,2\rightarrow 3}$ (Figure 4.9b) required for the Diels-Alder reaction to take place on the pore-bound Cu^{2+} can be estimated with equation (2) derived as follow.

$\overline{\tau}_{0,1,2\rightarrow 3}$ is the mean value of the sum of residence times at the open pore (P_{PIDA}, level 0) (Figure 4.9), the Cu^{2+}-bound pore (P_{PIDA}-Cu^{2+}, level 1) and the dienophile-bound ternary complex (P_{PIDA}-Cu^{2+}-dienophile, level 2) before the Diels-Alder transformation to yield the product complex (P_{PIDA}-Cu^{2+}-product, level 3) can be calculated with the following convenient equation derived by Colquhoun and Hawkes[46] according to the scheme illustrated in Figure 4.9a

$$\frac{1}{\tau_{0,1,2\rightarrow 3}} = k_{cat}[\text{diene}]\left[\frac{k_{0\text{-}1}[Cu^{2+}]\,k_{1\text{-}2}[\text{dienophile}]}{k_{2\text{-}1}k_{1\text{-}0} + k_{0\text{-}1}[Cu^{2+}]k_{2\text{-}1} + k_{0\text{-}1}[Cu^{2+}]k_{1\text{-}2}[\text{dienophile}]}\right] \quad \ldots(1)$$

where k_{cat} is the rate constant for Diels-Alder reaction (Figure 4.4) and the other k symbols represent the rate constants for the transitions depicted in Figure 4.9a. In this equation, k_{cat}[diene] is the unimolecular rate constant for the transition from level 2 to level 3 (2→3, the Diels-Alder transformation), while the fraction within the brackets is the probability at level 2 which is in equilibrium with levels 0 and 1. 1→3 transition is ignored in this equation to simplify the calculations. This is valid as the amount of Diels-Alder product is very low, at least at the beginning of experiment.

The mean waiting time $\overline{\tau}_{0,1,2\rightarrow 3}$ is

$$\tau_{0,1,2\rightarrow 3} = \frac{1}{k_{cat}[\text{diene}]}\left[\frac{K_{d\text{-}d}\,K_{d\text{-}Cu}}{[\text{dienophile}][Cu^{2+}]} + \frac{K_{d\text{-}d}}{[\text{dienophile}]} + 1\right] \quad \ldots(2)$$

where $K_{d\text{-}d} = k_{2\text{-}1}/k_{1\text{-}2}$ and $K_{d\text{-}Cu} = k_{1\text{-}0}/k_{0\text{-}1}$. $K_{d\text{-}d}$ and $K_{d\text{-}Cu}$ represent the dissociation constants of dienophile from P_{PIDA}-Cu^{2+}-dienophile and Cu^{2+} from P_{PIDA}-Cu^{2+}, respectively.

This mean waiting time $\bar{\tau}_{0,1,2\rightarrow3}$ is the sum of residence times spent at P_{PIDA}, P_{PIDA}-Cu^{2+} and P_{PIDA}-Cu^{2+}-dienophile levels between two successive Diels-Alder conversions. It should be re-emphasized that the binding of product (and hence the time spent at P_{PIDA}-Cu^{2+}-product state) is neglected to simplify the mathematical derivations. Thus the value calculated with equation (2) represents the minimum mean waiting time.

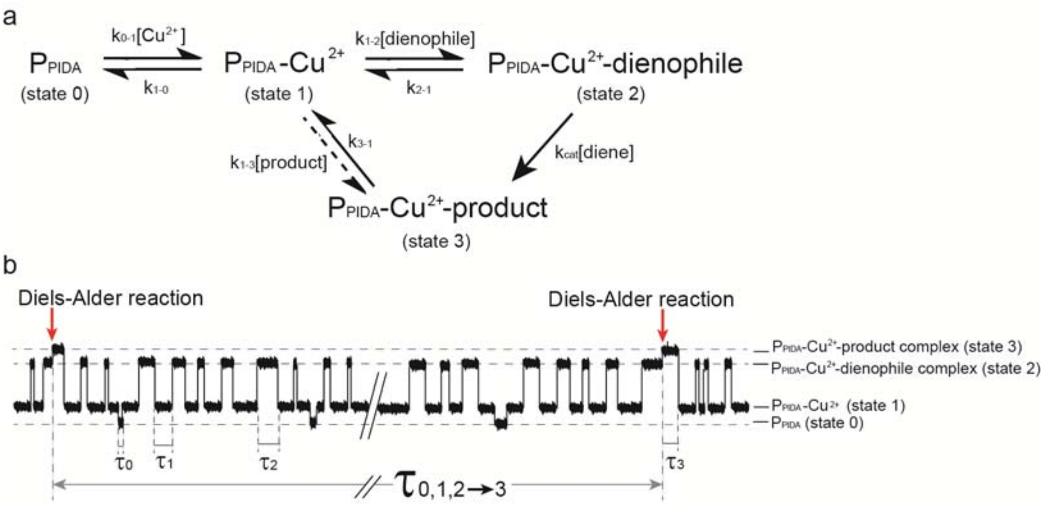

Figure 4.9. *Estimation of the mean waiting time* $\bar{\tau}_{0,1,2\rightarrow3}$. *(a) Kinetic scheme for the* Cu^{2+}*-catalyzed Diels-Alder reaction in* P_{PIDA}. *As the concentration of product is low, at least at the beginning of experiment, the binding of product to the pore-bound* Cu^{2+} *centre (i.e. 1→3 transition) is very rare and can be omitted in the mathematical derivations. (b) Hypothetical current trace showing the occurrences of catalytic Diels-Alder conversions on the pore-bound* Cu^{2+} *centre. Two Diels-Alder reactions (2→3 transitions) are indicated by red arrows. Each level is labeled on the right hand side according to the scheme in (a).* τ_0 *represents the residence time at state 0, etc.* $\bar{\tau}_{0,1,2\rightarrow3}$ *represents the mean residence time at levels 0, 1 and 2 between two successive Diels-Alder transformations on the pore-bound* Cu^{2+}.

4.4.2 Mean waiting time for the catalytic reaction to occur – theoretical calculation

Table 4.1 shows the theoretical mean waiting time ($\overline{\tau}_{0,1,2 \to 3}$) when different sets of parameters are substituted into equation (2). Entry 1 is calculated using our experimentally-determined kinetic parameters for the reaction between **6** and **8** (with k_{cat} assumed to be ~1 $\mathrm{M^{-1}s^{-1}}$ [25,32]) and the reagent concentrations that were used in our experiments. The calculated mean waiting time is 133 min. Such a long waiting time supports our conclusion in Section 4.3.4 that no Diels-Alder transformation on P_{PIDA}-bound Cu^{2+} could be observed.

Entry 2 shows if higher concentration of dienophile is used, i.e. 1 mM of the dienophile.[10,32] The calculated mean waiting time decreases by almost 5-fold (compared to entry 1) to 28 min. Increasing the concentration of Cu^{2+} by even 1000-fold (to 20 mM) does not shorten T significantly. This is presumably because of the tight binding of Cu^{2+} to the iminodiacetate chelator. Thus when [Cu^{2+}] is >10 μM, P_{PIDA} is occupied by Cu^{2+} in most of the time. 28 min is still a long waiting time for single-channel recording experiment. Moreover, the faster background reaction catalyzed by the free Cu^{2+} ions (in much larger amount and presumably more reactive that the pore-bound Cu^{2+}) and the concomitant generation of product would interfere the identification of the genuine conversion on pore-bound Cu^{2+}.

If a more reactive Cu^{2+} catalyst is incorporated (e.g. using a different chelator), the waiting time might be reduced further. For example, when a higher k_{cat} value (3.8 ± 0.8 $\mathrm{M^{-1}s^{-1}}$) is put into Entry 3 (together with the higher concentrations of both reactants as in Entry 2), the calculated waiting time is shortened to 0.88 min. This k_{cat} value, which is even larger than the k_{cat} value for reaction catalyzed by free Cu^{2+} ion, is the largest value reported in the literature. It is obtained from a DNA-based catalyst carrying a non-covalently attached 4,4'-dimethyl-2,2'-bipyridine (dmbpy) ligand.[32]

Although this k_{cat} value might represent the catalytic efficiency achievable in our nanopore if the same ligand is utilized, the microenvironment provided by DNA is drastically different from the bulk solution (and also from the αHL pore environment). So the calculated waiting time is a rough estimation only.

Cu^{2+} bound to dmbpy ligand without DNA is rather unreactive in catalyzing Diels-Alder reaction ($k_{cat} = (4.5 \pm 1.2) \times 10^{-2}$ $\text{M}^{-1}\text{s}^{-1}$ and $K_{d\text{-}d} = 2.5 \times 10^{-3}$ M; T = 86 min).[32] With 2,2'-bipyridine (bpy), larger k_{cat} value was reported and a shorter waiting time is calculated ($k_{cat} = 0.838$ $\text{M}^{-1}\text{s}^{-1}$ and $K_{d\text{-}d} = 5.6 \times 10^{-3}$ M; T = 8.8 min)[25] This waiting time is still rather long for single-channel detection.

Another type of chelators is amino acids. Stronger binding of azachalcone to L-tryptophan-Cu^{2+} (or L-tyrosine-Cu^{2+}) complex ($K_a = 3020$ M^{-1})[25] compared to free Cu^{2+} ion ($K_a = 1160$ M^{-1})[25] was reported. This is due to the favourable π-π interaction between the aromatic parts of azachalcone and the indole side chain of L-tryptophan.[25] Using this larger K_a value (hence smaller $K_{d\text{-}d}$) and the higher concentrations of both reactants as in Entry 2, the estimated mean waiting time is 1.0 min (Entry 4). This waiting time is the shortest possible one that might be achievable in the nanopore. Apart from using an L-tryptophan or L-tyrosine-based chelator, aromatic amino acid residues can be introduced near the chelation site by site-directed mutagenesis. This might enhance the association constant of the dienophile to the pore-bound Cu^{2+} complex and shorten the waiting time further. The remaining challenge is to distinguish the stepwise catalytic conversion on the pore-bound Cu^{2+} centre from the overlapping signals of reactants and products (formed by free Cu^{2+}, and also in the planar lipid bilayer[24]) (Figure 4.8d). Improved time-resolution of the current recording will be beneficial.

Table 4.1. *Theoretical mean waiting time (T) calculated with equation (14).*

Entry	**1**	**2**	**3**	**4**
[Cu^{2+}] (μM)	20	20	20	20
[dienophile] (μM)	200	1000[a]	1000[a]	1000[a]
[diene] (mM)	15	15[a]	15[a]	15[a]
$K_{d\text{-}Cu}$ (M^{-1})	880 ± 120 × 10^{-9} [b]	880 ± 120 × 10^{-9} [b]	2 × 10^{-9} [e]	7 × 10^{-9} [g]
$K_{d\text{-}d}$ (M^{-1})	39 × 10^{-3} [c]	39 × 10^{-3} [c]	2.0 × 10^{-3} [f]	3.3 × 10^{-4} [h]
$k_{3\text{-}1}$ (s^{-1})	110 [d]	110 [d]	110	110
k_{cat} ($M^{-1}s^{-1}$)	1	1	3.8 ± 0.8 [f]	1.4 [h]
T (s)	7984 (~ 133 min)	1650 (~ 28 min)	53 (~ 0.88 min)	62 (~ 1.0 min)

[a] *The typical reactant concentrations used by the Roelfes group.*[10,32]

[b] *From Section 4.3.2.*

[c] *From Section 4.3.3 for compound* ***8****.*

[d] *From Section 4.3.3 for compound* ***10****.*

[e] *Value of* Cu^{2+} *ion binding to 2,2′-bipyridine (*$K_a = 500 \times 10^6\ M^{-1}$*).*[39] *Other values in the literature are within 100-fold to this value.*[40] *Estimations of T using even 1000-fold larger (or smaller)* $K_{d\text{-}Cu}$ *do not show significant difference (<10%), this is because the term '*$K_{d\text{-}d}K_{d\text{-}Cu}/[\text{dienophile}][Cu^{2+}]$*' in equation (16) is much smaller compared to '*$K_{d\text{-}d}/[\text{dienophile}] + 1$*'.*

[f] *Values for the* Cu^{2+}*-4,4′-dimethyl-2,2′-bipyridine/st-DNA catalyst.*[32] $K_{d\text{-}d}$ *is calculated from the reported* $K_a = (5.0 \pm 1.4) \times 10^2\ M^{-1}$*. This complex has the largest* k_{cat} *reported in the literature.*

[g] *Value of* Cu^{2+} *binding onto glycine (*$pK_a = 8.15$*, i.e.* $K_a = 1.4 \times 10^8\ M^{-1}$*).*[41]

[h] *Values for* Cu^{2+}*-L-tryptophan catalyst.*[25] $K_{d\text{-}d}$ *is calculated from the reported* $K_a = 3.02 \times 10^3\ M^{-1}$*.*

4.4.3 Other problems of the catalytic system

Apart from the catalytic strength of the Cu^{2+} complex, the two Diels-Alder reactions that we have investigated might cause other problems, in particular on the turnover of the catalyst. Product inhibition arises from the binding of the product at the catalytic centre, hindering the binding of reactant and hence another reaction cycle. Products (**9** and **10**) of the two chosen reactions (Scheme 4.3) still have the same bidentate ligand as in their corresponding dienophiles. Thus product binding to the catalytic centre is possible. Our experimental results showed that the residence time of **10** on P_{PIDA}-Cu^{2+} ($\tau_{off} = 1/k_{off} = 9$ ms) is 4 times longer than that of its corresponding dienophile **8** ($\bar{\tau}_{off}$ = 2 ms), and the K_d of **10** (97 mM) is only about 3-fold larger than that of **8** (39 mM) (see Section 4.3.3, Figure 4.7). So product inhibition exists and would affect the observation of catalytic conversion with our single-molecule technique. It is worth mentioning that in the mathematically derivation in Section 4.4.1, the binding of product to the catalytic centre is ignored. This is the condition at the beginning of reaction, in which very small amount of product is generated. With product accumulation over time, another term needs to be added to equation 14 to account for product inhibition and the lengthening of the average time T for a catalytic reaction to occur.

Product of the other chosen Diels-Alder reaction, **9**, does not show detectable binding to P_{PIDA}-Cu^{2+} ($\bar{\tau}_{off}$ < 1 ms). Its corresponding dienophile **7** has longer residence time of 16 ms (see Section 4.3.3, Figure 4.7). Although **9** would not cause appreciable product inhibition, its undetectable binding makes reaction measurement impossible.

In summary, the binding property of the product to the metal catalytic centre is crucial to the success of catalysis. Weak binding avoids product inhibition. However, discernible binding to the metal centre is required for the single-molecule detection of transformation. Choices of reactants (and hence the formed product), metal complex and reaction conditions can be optimized to achieve reaction detection.

4.5 Conclusions

A metal ion binding site based on iminodiacetate was constructed inside the β barrel of αHL by genetic and chemical engineering. Bimolecular binding of Cu^{2+} ion to this chelator was characterized at pH 7.0. Although we failed to observe the copper(II)-catalyzed Diels-Alder transformation on the pore-bound copper(II) complex at the single-molecule level, theoretical calculation suggests that aromatic amino acid-based chelator might increase the opportunity for the occurrence of reaction. This metal-containing pore might also be applied as a nanosensor for monitoring reactions that involve metal-binding reactants and/or products.[42]

4.6 Materials and Methods

4.6.1 General Information

^{1}H NMR and ^{13}C NMR spectra were recorded on Bruker DPX400 (^{1}H: 400 MHz) or Bruker AV400 (^{1}H: 400 MHz; ^{13}C: 100 MHz) spectrometers. All NMR experiments were performed in $CDCl_3$ or D_2O at 22 ± 1°C unless otherwise stated. Chemical shifts are reported as parts per million (ppm) on the δ scale by using solvent residual peaks as internal standards for ^{1}H and ^{13}C NMR. Coupling constants (*J*) are reported in Hz.

Low resolution mass spectra were recorded on a Waters LCT Premier mass spectrometer using electrospray ionization (ESI). High resolution mass spectra were recorded using negative ionization mode ESI on a Bruker FT0ICR-MS Apex Qe (9.4 T) mass spectrometer. *m/z* values are reported in Daltons.

Unless otherwise stated, all reagents were purchased from commercial suppliers and used without further purification.

4.6.2 Synthetic procedures

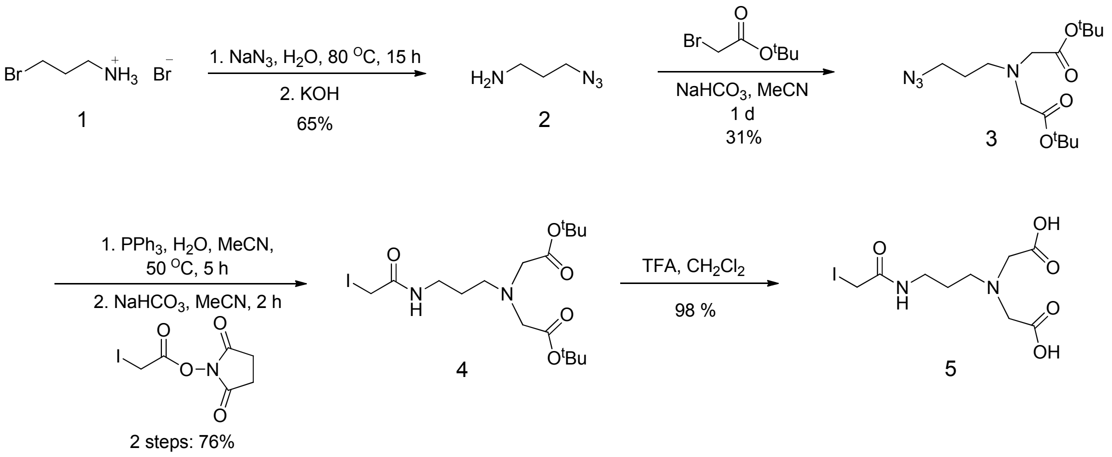

Scheme 4.4. *Synthetic scheme of the iminodiacetate chelator PIDA.*[34,43]

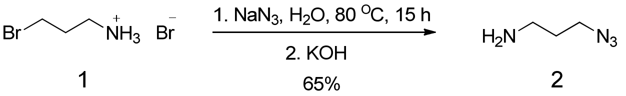

3-Azidopropyl-1-amine (2).[44] A solution of 3-bromopropylamine hydrobromide **1** (5.0 g, 22.8 mmol) and NaN_3 (4.5 g, 69.2 mmol) in H_2O (23 mL) was heated to 80 °C for 15 h. The reaction mixture was cooled down to room temperature and then cooled to 0 °C in an ice-water bath. KOH (0.5 g, 8.9 mmol) was added and the mixture was stirred until all KOH was dissolved. Target product was extracted from the aqueous solution with Et_2O (3 × 40 mL). The combined organic layer was dried with $MgSO_4$, filtered and concentrated under reduced pressure to give the product (1.5 g, 65%) as a volatile pale yellow liquid. It was used in the next step without further purification. R_f: 0.26 (MeOH); ^{1}H NMR (400 MHz, $CDCl_3$): δ 3.72 (t, J = 6.8 Hz, CH_2N_3, 2H), 2.80 (t, J = 6.8 Hz, CH_2NH_2, 2H), 1.73 (quintet, J = 6.8 Hz, $CH_2CH_2CH_2$, 2H), 1.24 (br s, NH_2, 2H).

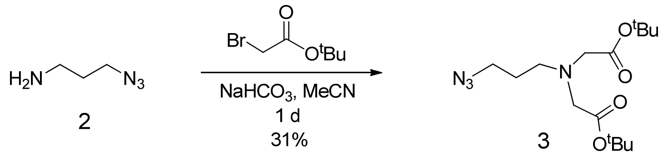

***tert*-Butyl 2,2'-(3-Azidopropylazanediyl)diacetate (3).**[34,43] A mixture of 3-azidopropan-1-amine **2** (710 mg, 7.09 mmol), *tert*-butyl bromoacetate (2.4 mL, 16.25 mmol) and $NaHCO_3$ (3.0 g, 35.5 mmol) in CH_3CN (70 mL) was stirred at room temperature under N_2 for 1 d. Solvent was evaporated and the residue was diluted with H_2O (20 mL) and extracted with Et_2O (3 × 30 mL). The combined ethereal layer was washed with brine, dried ($MgSO_4$), filtered and concentrated *in vacuo*. It was further purified by flash column chromatography (petroleum ether/Et_2O = 5/1) to afford the desired compound (728 mg, 31%) as a volatile colourless liquid. R_f: 0.25 (petroleum ether/Et_2O = 5/1); ^{1}H NMR (500 MHz, $CDCl_3$): δ 3.41 (s, NCH_2CO_2, 4H), 3.40 (t, J = 7.0 Hz, CH_2N_3, 2H), 2.79 (t, J = 7.0 Hz, CH_2CH_2N, 2H), 1.73 (quintet, J = 7.0 Hz, $CH_2CH_2CH_2$, 2H), 1.46 (s, CMe_3, 18H); ^{13}C NMR (125 MHz, $CDCl_3$): δ 170.78, 81.21, 56.21, 51.42, 49.41, 28.31, 27.65; ESI-MS (m/z): $[M+H]^+$ calcd. for $C_{15}H_{28}N_4O_4$, 329.2; found, 329.2 (73%).

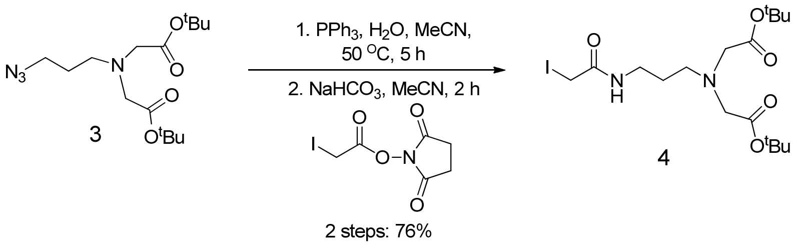

***tert*-Butyl 2,2'-(3-(2-Iodoacetamido)propylazanediyl)diacetate (4).**[34,43]

Triphenylphosphine (365 mg, 1.39 mmol) and H_2O (0.16 mL, 8.85 mmol) were added to a solution of *tert*-butyl 2,2'-(3-azidopropylazanediyl)diacetate **3** (415 mg, 1.26 mmol) in CH_3CN (8.5 mL). The solution was warmed to 50 °C for 5 h. Water was removed by adding anhydrous $MgSO_4$ to the reaction mixture followed by filtration.

N-iodoacetoxysuccinimide (343 mg, 1.21 mmol) was added to the filtrate and the coupling reaction was carried out at room temperature in the dark for 2 h. The solvent was evaporated and the residue was purified by flash column chromatography (petroleum ether/EtOAc = 3/2) to give the target compound (449 mg, 76%) as a pale yellow oil. *R_f*: 0.50 (petroleum ether/EtOAc = 1/1); ^{1}H NMR (500 MHz, $CDCl_3$): δ 8.41 (t, *J* = 5.0 Hz, CONH, 1H), 3.74 (s, CH_2I, 2H), 3.42 (q, *J* = 5.5 Hz, CH_2NH, 2H), 3.36 (s, NCH_2CO_2, 4H), 2.76 (t, *J* = 6.0 Hz, CH_2CH_2N, 2H), 1.62 (quintet, *J* = 5.5 Hz, $CH_2CH_2CH_2$, 2H), 1.47 (s, CMe_3, 18H); ^{13}C NMR (125 MHz, $CDCl_3$): δ 171.17, 168.07, 81.82, 55.89, 51.38, 38.23, 28.19, 25.36, -0.10; ESI-MS (*m/z*): $[M+H]^+$ calcd. for $C_{17}H_{31}IN_2O_5$, 471.1; found 471.1 (50%).

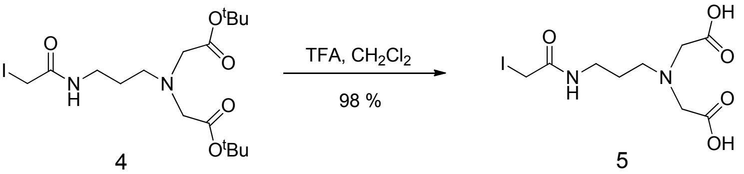

2,2'-(3-(2-Iodoacetamido)propylazanediyl)diacetic acid (5).[34,43] Trifluoroacetic acid (TFA; 223 uL, 3.26 mmol) was added to a solution of *tert*-butyl 2,2'-(3-(2-iodoacetamido)propylazanediyl)diacetate **4** (307 mg, 0.65 mmol) in CH_2Cl_2 (6.5 mL) at 0 °C. The reaction mixture was stirred at room temperature for 1 d and extra TFA (223 uL) was added at 0 °C. The mixture was stirred at room temperature for 7 h and the solvent was evaporated to afford the desired compound (229 mg, 98%) as a colourless oil. It was used for protein modification without further purification. R_f: 0.04 (EtOAc); ^{1}H NMR (500 MHz, D_2O): δ 3.92 (s, NCH_2CO_2H, 4H), 3.62 (s, CH_2I, 2H), 3.24 (2 H, m, CH_2NH), 3.19 (t, *J* = 6.5 Hz, CH_2CH_2N, 2H), 1.87 (quintet, *J* = 8.0 Hz, $CH_2CH_2CH_2$, 2H); ^{13}C NMR (125 MHz, D_2O): δ 172.54, 169.06, 55.71, 53.99, 36.46, 23.36, -2.56; ESI-MS (*m/z*): $[M–H]^-$ calcd. for $C_9H_{15}IN_2O_5$, 357.0; found: 357.0 (10%).

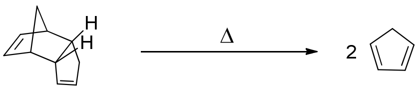

6

Cyclopentadiene (6).[45] Cyclopentadiene was distilled by cracking dicyclopentadiene over calcium hydride. The colourless distillate was stored over molecular sieves at –20 °C for up to one week.

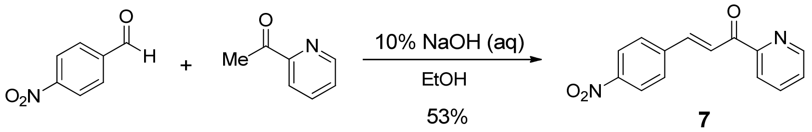

7

(*E*)-3-(4-Nitrophenyl)-1-(2-pyridyl)-2-propene-1-one (7).[22] 2-Acetylpyridine (0.3 mL, 2.70 mmol) was added dropwisely to a stirred mixture of 10% (w/v) aqueous NaOH (0.16 mL) and 4-nitrobenzaldehyde (0.4 g, 2.70 mmol) in ethanol (3.2 mL) at 0 °C over 2-3 h. Fast addition of 2-acetylpyridine will lead to the formation of a dark brown mass of unwanted side product. After stirring for an extra 2 h at 0 °C, the reaction mixture was filtered and the brownish-yellow solid collected was recrystallized from ethanol to give the pure target compound (0.68 g, 53%) as a yellow solid. *R_f*: 0.68 (petroleum ether/EtOAc = 1/1); ^{1}H NMR (500 MHz, $CDCl_3$): δ 8.69–8.88 (m, 1H), 8.35–8.57 (m, 1H), 8.22–8.35 (m, 2H), 8.15–8.22 (m, 1H), 7.77–8.07 (m, 4H), 7.46–7.62 (m, 1H); ^{13}C NMR (125 MHz, $CDCl_3$): δ 189.08, 153.73, 149.17, 148.67, 141.38, 137.33, 130.46, 129.13, 127.48, 124.94, 124.26, 123.22; ESI-MS (*m/z*): $[M+H]^+$ calcd. for $C_{14}H_{10}N_2O_3$, 255.1; found: 255.1 (100%).

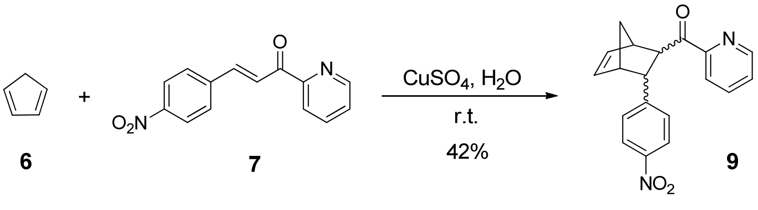

(3-(4-Nitrophenyl)bicycle[2.2.1]hept-5-en-2-yl)(2-pyridyl)methanone (9).[22]

(*E*)-3-(4-Nitrophenyl)-1-(2-pyridyl)-2-propene-1-one **7** (100 mg, 0.39 mmol) was dissolved in minimum amount of EtOH. The resultant solution was added to a stirred solution of cyclopentadiene **6** (97 uL, 1.18 mmol) and $CuSO_4 \cdot 5H_2O$ (982 mg, 3.93 mmol) in H_2O (120 mL). The resultant suspension was capped and stirred overnight at room temperature. Product was extracted from the aqueous solution with Et_2O (3 × 50 mL). The combined ethereal layer was washed with brine, dried ($MgSO_4$), filtered and concentrated under reduced pressure to give brownish-yellow oil. The oil was purified by flash column chromatography (petroleum ether/EtOAc = 10/1 gradient to 8/1) to yield the target compound (53 mg, 42%) as a pale yellow solid. R_f: 0.50 (petroleum ether/EtOAc = 3/1); ^1H NMR (500 MHz, $CDCl_3$) (both exo and endo isomers were observed, but only the chemical shifts for the major endo isomer were reported): δ 8.60–8.72 (m, ArH, 1H), 8.10–8.19 (m, ArH, 2H), 7.94–8.05 (m, ArH, 1H), 7.76–7.89 (m, ArH, 1H), 7.43–7.46 (m, ArH, 1H), 7.39–7.43 (m, ArH, 1H), 6.47 (dd, J = 3.0 and 5.5 Hz, C*H*=CH, 1H), 5.86 (dd, J = 3.0 and 5.5 Hz, CH=C*H*, 1H), 4.46 (dd, J = 3.0 and 5.0 Hz, CH, 1H), 3.54–3.66 (m, CH, 1H), 3.44–3.54 (m, CH, 1H), 3.04–3.15 (m, CH, 1H), 1.92–2.03 (m, CH_2, 1H), 1.57–1.72 (m, CH_2, 1H); ^{13}C NMR (125 MHz, $CDCl_3$): δ 200.55, 153.36, 153.17, 149.13, 139.12, 137.14, 133.56, 128.51, 127.34, 123.79, 122.46, 54.85, 49.07, 48.92, 48.35, 45.85; ESI-MS (*m/z*): $[M+H]^+$ calcd. for $C_{19}H_{16}N_2O_3$, 321.1; found: 321.1 (100%).

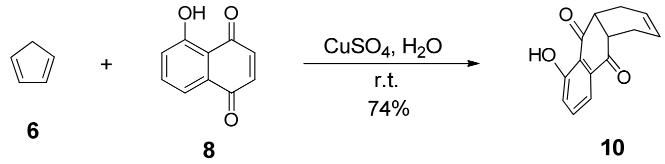

Diels-Alder product of cyclopentadiene and 5-hydroxy-1,4-naphthoquinone (10).[35] To a stirred solution of 5-hydroxynaphthoquinone **8** (100 mg, 0.56 mmol) and $CuSO_4 \cdot 5H_2O$ (13.9 mg, 0.06 mmol) in H_2O (167 mL) was added cyclopentadiene **6**

(140 uL, 1.67 mmol). The reaction mixture was capped and stirred overnight at room temperature. Product was extracted from the aqueous solution with Et_2O (3 × 50 mL). The combined ethereal layer was washed with brine, dried ($MgSO_4$), filtered and concentrated under reduced pressure to give yellow solid. It was purified with flash column chromatography (petroleum ether/EtOAc = 13/1 gradient to 10/1) to yield the target compound (102 mg, 74%) as yellow needle-shaped crystals. R_f: 0.34 (petroleum ether/EtOAc = 10/1); ^1H NMR (500 MHz, $CDCl_3$): δ 12.60 (s, OH, 1H), 7.46–7.68 (m, ArH, 2H), 7.12–7.23 (m, ArH, 1H), 5.86–6.13 (m, CH=CH, 2H), 3.57–3.77 (m, CH, 2H), 3.41–3.54 (m, CH, 1H), 3.32–3.41 (m, CH, 1H), 1.43–1.68 (m, CH_2, 2H); ^{13}C NMR (125 MHz, $CDCl_3$): δ 204.96, 197.11, 162.30 ,137.16, 135.95, 135.26, 123.69, 118.43, 50.05, 49.77, 49.50, 49.26, 49.09; ESI-MS (*m/z*): $[M–H]^-$ calcd. for $C_{15}H_{12}O_3$, 239.1; found: 239.1 (100%).

4.6.3 Targeted chemical modification

Procedure was same as reported previously by Hammerstein *et al.*[34] [^{35}S]Methionine-labeled monomeric G137C-D8 polypeptide prepared from IVTT (see previous section) was purified on a Micro Bio-Spin 6 gel filtration columns (Bio-Rad). The synthesized reagent, 2,2'-(3-(2-iodoacetamido)propylazanediyl)diacetic acid **5** (PIDA), was dissolved in water to make a 200 mM stock solution. The monomeric IVTT protein (25 μL) was reduced for 10 min in 200 mM Tris, pH 8.5 (42.5 μL), containing 1 mM DTT. The reagent (200 mM, 7.5 μL) was added to give a 20 mM final concentration. The solution was incubated at room temperature for 1 h in the dark. For control experiments, the same volume of water (7.5 μL) or methoxypoly(ethylene glycol) ortho-pyridyldisulfide (mPEG-OPSS, 5,000 Da, Creative PEGWorks) (100 mM, 7.5 μL) was added. After reaction, gel filtration was performed through Micro Bio Spin 6 columns. A portion (2 μL) of the reaction was mixed with XT sample buffer (X 2, 8 μL) and heated at 94 °C for 10 min. A 12% SDS-polyacrylamide gel (Criterion XT Bis-Tris gel, Bio-Rad) was run at 200 V for 50 min with XT MOPS running buffer (Bio-Rad). The gel was dried under vacuum and the protein bands were visualized by autoradiography (Figure 4.10). The remainder of the reaction was stored at –80 °C.

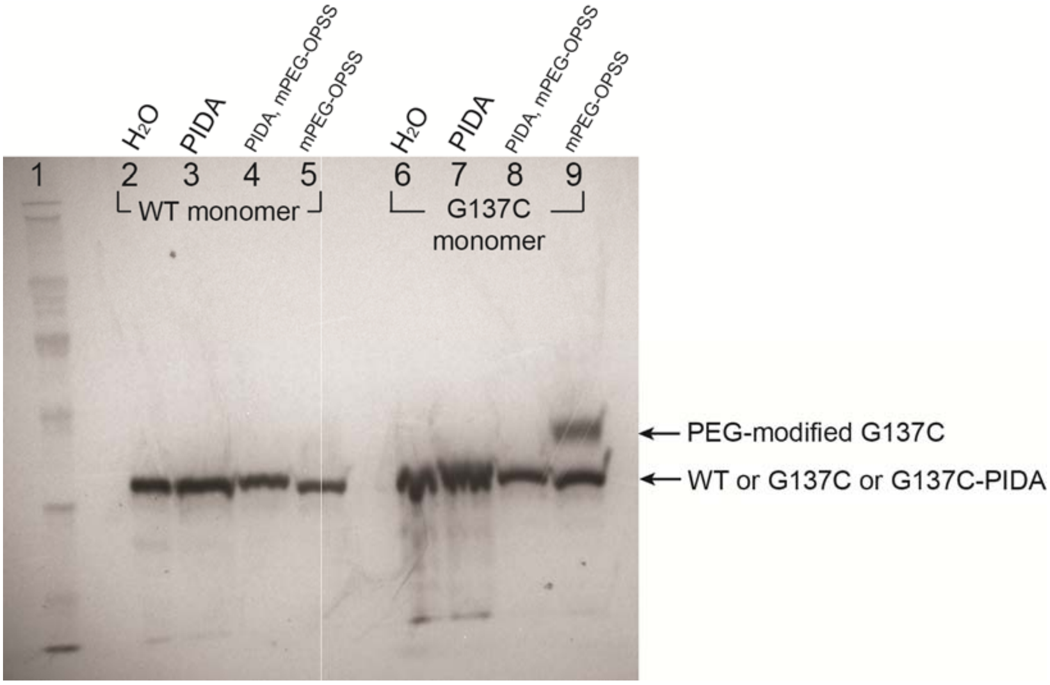

Figure 4.10. *12% SDS-PAGE gel (Criterion XT Bis-Tris gel, Bio-Rad) showing the targeted chemical modification of G137C monomer with PIDA. Lane 1: protein marker. Lanes 2–5: WT monomer. Lanes 6–9:G137C monomer. Lanes 2–9 were treated with different reagents as follow: Lanes 2,6: water. Lanes 3,7: PIDA. Lane 4,8: PIDA, follwed by mPEG-OPSS 5k. Lanes 5,9: mPEG-OPSS 5k. The identity of each band is labeled on the right hand side. Note that the cysteine modification of G137C with mPEG-OPSS was incomplete as shown by the G137C band on lane 9.*

4.6.4 Protein preparation

After the gel analysis, the chemically modified monomer (60 μL) was mixed with [^{35}S]methionine-labeled monomeric wild-type (WT) α-hemolysin prepared by

IVTT (50 μL). Oligomerization was carried out as stated in the previous section, but without any thiol reducing agent in all steps. After gel purification, the gel was dried under vacuum and exposed to photographic film for 12 h. The protein band, as visualized by autoradiography (Figure 4.11), corresponding to the heteroheptamer that contain one modified subunit was excised and rehydrated in 10 mM Tris-HCl, pH 7.5 (300 μL). The gel was crushed, filtered and aliquoted as stated in the previous section.

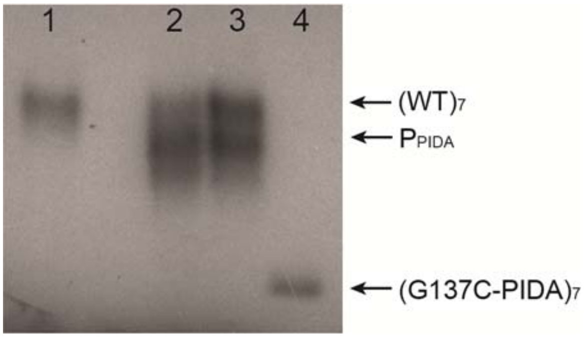

Figure 4.11. *5% SDS-PAGE gel showing the bands of different αHL heptamers. Lane 1: Heptamer made from WT monomer only. Lane 2: Heptamers formed from WT monomer and PIDA-modified G137C monomer mixed in 5:2 ratio. Lane 3: Same as in lane 2 but mixed in 6:1 ratio. Lane 4: Heptamer comprising PIDA-modified G137C monomer only. The identity of each band is labeled on the right hand side.*

4.6.5 Planar lipid bilayer recordings

Details of experiments are as stated in Chapter 2, Section 2.6.10. Stock CuNO$_3$ solution in water (10 mM) and dienophile in acetonitrile (100 mM) were prepared daily.

4.6.6 Data analysis

The current traces were filtered digitally with a 200 Hz low-pass Bessel filter in Clampfit 9.2 (Molecular Devices). Events were detected by using the single channel search feature. The mean dwell times ($\bar{\tau}$) of the current states were determined by fitting dwell-time histograms to single exponential functions.

4.6.7 Literature value of K_d between *N*-methyliminodiacetate and Cu^{2+} at pH 7.0

N-Methyliminodiacetate (MIDA) is a structural mimic of the iminodiacetate chelator in P_{PIDA}. The reported $\log_{10}$ values of the acid association constants of MIDA, $\log K_{a1}$ and $\log K_{a2}$, are 2.12 and 9.56 respectively[41] (at 25 °C and ionic strength of 0.1 M). At our experimental pH of 7.0, the major species of MIDA at equilibrium are the fully deprotonated form (represented by L) and the singly-protonated form (represented by HL) (Figure 4.12). Thus

$$[L]_{total} = [L] + [HL] \qquad \dots (15)$$

We only need to consider the following equilibrium at pH 7.0,

$$K_{a2} = [HL] / [L][H^+] \qquad \dots(16)$$

Substitute (15) into (16) gives

$$[L] / [L]_{total} = 1/ (1 + K_{a2}[H^+]) \qquad \dots (17)$$

The $\log_{10}$ value of the equilibrium binding constant of L to Cu^{2+} is 11.04[41] (Figure 4.12). No value for the binding between HL and Cu^{2+} is reported. Assume that only L coordinates Cu^{2+},

$$K_{Cu} = [L{\cdot}Cu^{2+}] / [L][Cu^{2+}] \qquad \dots (18)$$

The apparent equilibrium association constant (K^{app}_{Cu}) with respect to $[L]_{total}$ is

$$K^{app}_{Cu} = [L{\cdot}Cu^{2+}] / [L]_{total}[Cu^{2+}] \qquad \dots (19)$$

Substitute (17) and (18) into (19),

$$K^{app}_{Cu} = K_{Cu} / (1 + K_{a2}[H^+]) \qquad \dots (20)$$

With $K_{a2} = 10^{9.56}$ M^{-1} and $K_{Cu} = 10^{11.04}$ M^{-1}, at pH 7.0, K^{app}_{Cu} of MIDA is therefore 3×10^8 M^{-1}. The reciprocal, which equals the apparent dissociation equilibrium constant, is 3.3 nM.

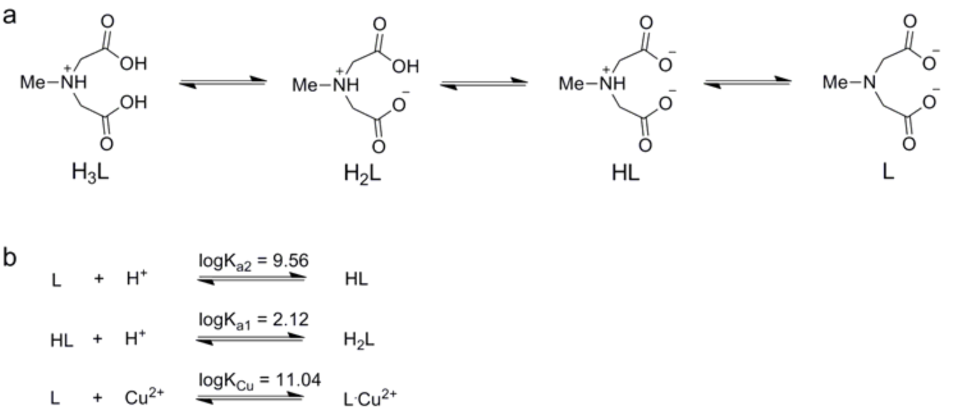

Figure 4.12. *Acid dissociation equilibria and Cu^{2+} binding equilibrium of MIDA. (a) Acid dissociation equilibria of MIDA showing its different protonation forms. (b) The reported $\log_{10}$ values of the proton or Cu^{2+} binding equilibrium constants. These values are obtained from ref. 41 and are labeled on top of the arrow of the corresponding equilibrium.*

4.7 References

1. Lu, Y. *Inorg. Chem.* **2006**, *45*, 9930–9940.
2. Ward, T. R. *Acc. Chem. Res.* **2011**, *44*, 47–57.
3. Steinreiber, J.; Ward, T. R. *Coor. Chem. Rev.* **2008**, *252*, 751–766.
4. Wilson, M. E.; Whitesides, G. M. *J. Am. Chem. Soc.* **1978**, *100*, 306–307.
5. Boersma, A. J.; Megens, R. P.; Feringa, B. L.; Roelfes, G. *Chem. Soc. Rev.* **2010**, *39*, 2083–2092.
6. Gouverneur, V.; Houk, K. N.; de Pascual-Teresa, B.; Beno, B.; Janda, K. D.; Lerner, R. A. *Science* **1993**, *262*, 204–208.
7. Romesberg, F. E.; Spiller, B.; Schultz, P. G.; Stevens, R. C. *Science* **1998**, *279*, 1929–1933.

8. Oltra, N. S.; Roelfes, G. *Chem. Commun.* **2008**, 6039–6041.
9. Podtetenieff, J.; Taglieber, A.; Bill, E.; Reijerse, E. J.; Reetz, M. T. *Angew. Chem. Int. Ed.* **2010**, *49*, 5151–5155.
10. Roelfes, G.; Boersma, a. J.; Feringa, B. L. *Chem. Commun.* **2006**, 635–637.
11. Coquière, D.; Feringa, B. L.; Roelfes, G. *Angew. Chem. Int. Ed.* **2007**, *46*, 9308–9311.
12. Boersma, A. J.; Feringa, B. L.; Roelfes, G. *Angew. Chem. Int. Ed.* **2009**, *48*, 3346–3348.
13. Boersma, A. J.; Coquière, D.; Geerdink, D.; Rosati, F.; Feringa, B. L.; Roelfes, G. *Nat. Chem.* **2010**, *2*, 991–995.
14. van de Velde, F.; Könemann, L.; van Rantwijk, F.; Sheldon, R. A. *Chem. Commun.* **1998**, 1891–1892.
15. Okrasa, K.; Kazlauskas, R. J. *Chem. Eur. J.* **2006**, *12*, 1587–1596.
16. Fernández-Gacio, A.; Codina, A.; Fastrez, J.; Riant, O.; Soumillion, P. *ChemBioChem* **2006**, *7*, 1013–1016.
17. Dijk, E. W.; Feringa, B. L.; Roelfes, G. *Tetrahedron: Asymmetry* **2008**, *19*, 2374–2377.
18. Shibata, N.; Yasui, H.; Nakamura, S.; Toru, T. *Synlett* **2007**, *7*, 1153–1157.
19. Kokubo, T.; Sugimoto, T.; Uchida, T.; Tanimoto, S.; Okano, M. *J. Chem. Soc., Chem. Commun.* **1983**, 769–770.
20. Lo, C.; Ringenberg, M. R.; Gnandt, D.; Wilson, Y.; Ward, T. R. *Chem. Commun.* **2011**, *47*, 12065–12067.
21. Fleming, I. *Pericyclic reactions*; Oxford University Press: Oxford, 1999.
22. Otto, S.; Bertoncin, F.; Engberts, J. B. F. N. *J. Am. Chem. Soc.* **1996**, *118*, 7702–7707.
23. Reetz, M. T.; Jiao, N. *Angew. Chem. Int. Ed.* **2006**, *45*, 2416–2419.

24. Otto, S.; Engberts, J. B. F. N.; Kwak, J. C. T. *J. Am. Chem. Soc.* **1998**, *120*, 9517–9525.
25. Otto, S.; Engberts, J. B. F. N. *J. Am. Chem. Soc.* **1999**, *121*, 6798–6806.
26. Kim, H. J.; Ruszczycky, M. W.; Choi, S.-H.; Liu, Y.-N.; Liu, H.-W. *Nature* **2011**, *473*, 109–112. Also the News and Views: Kelly, W. L. *Nature* **2011**, *473*, 35–36.
27. Coquière, D.; Bos, J.; Beld, J.; Roelfes, G. *Angew. Chem. Int. Ed.* **2009**, *48*, 5159–5162.
28. Seelig, B.; Keiper, S.; Stuhlmann, F.; Jäschke, A. *Angew. Chem. Int. Ed.* **2000**, *39,* 4576–4579.
29. Seelig, B.; Jäschke, A. *Chem. Biol.* **1999**, *6*, 167–176.
30. Rosati, F.; Boersma, A. J.; Klijn, J. E.; Meetsma, A.; Feringa, B. L.; Roelfes, G. *Chem. Eur. J.* **2009**, *15*, 9596–9605.
31. Boersma, A .J.; Feringa, B, L.; Roelfes, G. *Org. Lett.* **2007**, *9*, 3647–3650.
32. Boersma, A. J.; Klijn, J. E.; Feringa, B. L.; Roelfes, G. *J. Am. Chem. Soc.* **2008**, *130*, 11783–11790.
33. Roelfes, G.; Feringa, B. L. *Angew. Chem. Int. Ed.* **2005**, *44*, 3230–3232.
34. Hammerstein, A.; Shin, S.-H.; Bayley, H. *Angew. Chem. Int. Ed.* **2010**, *49*, 5085–5090.
35. Lever, A. B. P. in *Comprehensive coordination chemistry. II: from biology to nanotechnology*, Vol. 1, McCleverty, J. A.; Meyer, T. J., Eds.; Elsevier: Amsterdam and Oxford, 2004, pp 538.
36. Blokzijl, W.; Blandamer, J.; Engberts, J. B. F. N. *J. Am. Chem. Soc.* **1991**, *113*, 4241–4246.
37. Mubofu, E. B.; Engberts, J. B. F. N. *J. Phys. Org. Chem.* **2004**, *17*, 180–186.
38. Luchian, T.; Shin, S.-H.; Bayley, H. *Angew. Chem. Int. Ed.* **2003**, *42*, 3766–3771.
39. Kiel, A.; Kovacs, J.; Mokhir, A.; Krämer, R.; Herten, D.-P. *Angew. Chem. Int. Ed.*

2007, *46*, 3363–3366.

40. Martell, A. E.; Smith, R. M. *Critical Stability Constants*, Plenum Press: New York and London, 1974.
41. *Critical stability constants*; Martell A. E.; Smith, R. M.; Vol. 1; Plenum: New York; London, 1974.
42. Boersma, A. J.; Bayley, H. *Angew. Chem. Int. Ed.* **2012**, *51*, doi: 10.1002/anie.201205687.
43. Shin, S.-H. Kinetics of covalent chemistry at the single-molecule level. DPhil Dissertation, University of Oxford, Nov 2005.
44. Carboni, B.; Benalil, A.; Vaultier, M. *J. Org. Chem.* **1993**, *5*8, 3736–3741.
45. Evans, D. A.; Miller, S. J.; Lectka, T.; von Matt, P. *J. Am. Chem. Soc.* **1999**, *121*, 7559–7573.
46. Moczydlowski, E. in *Ion channel reconstitution*. Miller, C. Eds.; Plenum: New York and London, 1986, pp 75–114.

Appendix

A.1 Vector Map of pT7-WT-αHL

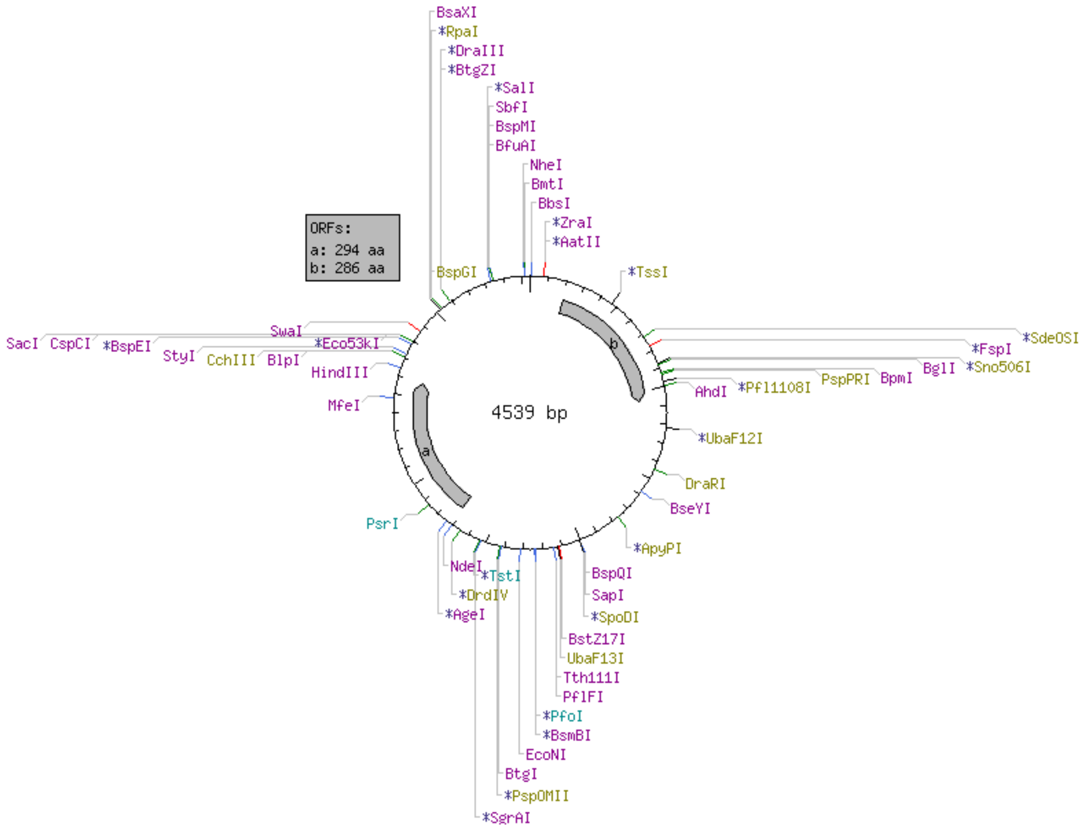

Figure A.1. Vector map of pT7-WT-αHL. The αHL gene is shown by the grey arrow labelled 'a'. The other grey arrow 'b' depicts the ampicillin resistance gene. Restriction sites are labeled. This vector map is generated using the NEBcutter provided free online from the New England BioLabs website.

A.2 DNA sequences of αHL gene in pT7 vector

The following is the DNA sequence of wild type αHL in the pT7 vector (denoted as pT7-WT-αHL). The cloning sites, *NdeI* and *HindIII*, are underlined and shown in red and purple, respectively. αHL gene is shown in blue. Stop codon of the αHL gene is shown in green.

TTCTTGAAGACGAAAGGGCCTCGTGATACGCCTATTTTTATAGGTTAATGTCATGATAATAATGGTTTCTTAGACGT
CAGGTGGCACTTTTCGGGGAAATGTGCGCGGAACCCCTATTTGTTTATTTTTCTAAATACATTCAAATATGTATCCG
CTCATGAGACAATAACCCTGATAAATGCTTCAATAATATTGAAAAAGGAAGAGTATGAGTATTCAACATTTCCGTG
TCGCCCTTATTCCCTTTTTTGCGGCATTTTGCCTTCCTGTTTTTGCTCACCCAGAAACGCTGGTGAAAGTAAAAGAT
GCTGAAGATCAGTTGGGTGCACGAGTGGGTTACATCGAACTGGATCTCAACAGCGGTAAGATCCTTGAGAGTTTTC
GCCCCGAAGAACGTTTTCCAATGATGAGCACTTTTAAAGTTCTGCTATGTGGCGCGGTATTATCCCGTGTTGACGC
CGGGCAAGAGCAACTCGGTCGCCGCATACACTATTCTCAGAATGACTTGGTTGAGTACTCACCAGTCACAGAAAA
GCATCTTACGGATGGCATGACAGTAAGAGAATTATGCAGTGCTGCCATAACCATGAGTGATAACACTGCGGCCAA
CTTACTTCTGACAACGATCGGAGGACCGAAGGAGCTAACCGCTTTTTTGCACAACATGGGGGATCATGTAACTCGC
CTTGATCGTTGGGAACCGGAGCTGAATGAAGCCATACCAAACGACGAGCGTGACACCACGATGCCTGCAGCAATG
GCAACAACGTTGCGCAAACTATTAACTGGCGAACTACTTACTCTAGCTTCCCGGCAACAATTAATAGACTGGATGG
AGGCGGATAAAGTTGCAGGACCACTTCTGCGCTCGGCCCTTCCGGCTGGCTGGTTTATTGCTGATAAATCTGGAGC
CGGTGAGCGTGGGTCTCGCGGTATCATTGCAGCACTGGGGCCAGATGGTAAGCCCTCCCGTATCGTAGTTATCTAC
ACGACGGGGAGTCAGGCAACTATGGATGAACGAAATAGACAGATCGCTGAGATAGGTGCCTCACTGATTAAGCAT
TGGTAACTGTCAGACCAAGTTTACTCATATATACTTTAGATTGATTTAAAACTTCATTTTTAATTTAAAAGGATCTA
GGTGAAGATCCTTTTTGATAATCTCATGACCAAAATCCCTTAACGTGAGTTTTCGTTCCACTGAGCGTCAGACCCCG
TAGAAAAGATCAAAGGATCTTCTTGAGATCCTTTTTTTCTGCGCGTAATCTGCTGCTTGCAAACAAAAAAACCACC
GCTACCAGCGGTGGTTTGTTTGCCGGATCAAGAGCTACCAACTCTTTTTCCGAAGGTAACTGGCTTCAGCAGAGCG
CAGATACCAAATACTGTCCTTCTAGTGTAGCCGTAGTTAGGCCACCACTTCAAGAACTCTGTAGCACCGCCTACAT
ACCTCGCTCTGCTAATCCTGTTACCAGTGGCTGCTGCCAGTGGCGATAAGTCGTGTCTTACCGGGTTGGACTCAAG
ACGATAGTTACCGGATAAGGCGCAGCGGTCGGGCTGAACGGGGGGTTCGTGCACACAGCCCAGCTTGGAGCGAAC
GACCTACACCGAACTGAGATACCTACAGCGTGAGCTATGAGAAAGCGCCACGCTTCCCGAAGGGAGAAAGGCGG
ACAGGTATCCGGTAAGCGGCAGGGTCGGAACAGGAGAGCGCACGAGGGAGCTTCCAGGGGGAAACGCCTGGTAT
CTTTATAGTCCTGTCGGGTTTCGCCACCTCTGACTTGAGCGTCGATTTTTGTGATGCTCGTCAGGGGGGCGGAGCCT
ATGGAAAAACGCCAGCAACGCGGCCTTTTTACGGTTCCTGGCCTTTTGCTGGCCTTTTGCTCACATGTTCTTTCCTG
CGTTATCCCCTGATTCTGTGGATAACCGTATTACCGCCTTTGAGTGAGCTGATACCGCTCGCCGCAGCCGAACGAC
CGAGCGCAGCGAGTCAGTGAGCGAGGAAGCGGAAGAGCGCCTGATGCGGTATTTTCTCCTTACGCATCTGTGCGG
TATTTCACACCGCATATATGGTGCACTCTCAGTACAATCTGCTCTGATGCCGCATAGTTAAGCCAGTATACACTCCG
CTATCGCTACGTGACTGGGTCATGGCTGCGCCCCGACACCCGCCAACACCCGCTGACGCGCCCTGACGGGCTTGTC
TGCTCCCGGCATCCGCTTACAGACAAGCTGTGACCGTCTCCGGGAGCTGCATGTGTCAGAGGTTTTCACCGTCATC
ACCGAAACGCGCGAGGCAGCGCTCTCCCTTATGCGACTCCTGCATTAGGAAGCAGCCCAGTAGTAGGTTGAGGCC
GTTGAGCACCGCCGCCGCAAGGAATGGTGCATGCAAGGAGATGGCGCCCAACAGTCCCCCGGCCACGGGGCCTGC
CACCATACCCACGCCGAAACAAGCGCTCATGAGCCCGAAGTGGCGAGCCCGATCTTCCCCATCGGTGATGTCGGC
GATATAGGCGCCAGCAACCGCACCTGTGGCGCCGGTGATGCCGGCCACGATGCGTCCGGCGTAGAGGATCGAGAT
CTAGCCCGCCTAATGAGCGGGCTTTTTTTTAGATCTCGATCCCGCGAAATTAATACGACTCACTATAGGGAGACCA
CAACGGTTTCCCTCTAGAAATAATTTTGTTTAACTTTAAGAAGGAGATATA**CATATGGCAGATTCTGATATTAAT**
ATTAAAACCGGTACTACAGATATTGGAAGCAATACTACAGTAAAAACAGGTGATTTAGTCACTTATGATAAA
GAAAATGGCATGCACAAAAAAGTATTTTATAGTTTTATCGATGATAAAAATCACAATAAAAAACTGCTAGTT
ATTAGAACAAAAGGTACCATTGCTGGTCAATATAGAGTTTATAGCGAAGAAGGTGCTAACAAAAGTGGTTTA
GCCTGGCCTTCAGCCTTTAAGGTACAGTTGCAACTACCTGATAATGAAGTAGCTCAAATATCTGATTACTAT
CCAAGAAATTCGATTGATACAAAAGAGTATATGAGTACTTTAACTTATGGATTCAACGGTAATGTTACTGGT

GATGATACAGGAAAAATTGGCGGCCTTATTGGTGCAAATGTTTCGATTGGTCATACACTGAAATATGTTCAA
CCTGATTTCAAAACAATTTTAGAGAGCCCAACTGATAAAAAAGTAGGCTGGAAAGTGATATTTAACAATATG
GTGAATCAAAATTGGGGACCATACGATCGAGATTCTTGGAACCCGGTATATGGCAATCAACTTTTCATGAAA
ACTAGAAATGGTTCTATGAAAGCAGCAGATAACTTCCTTGATCCTAACAAAGCAAGTTCTCTATTATCTTCA
GGGTTTTCACCAGACTTCGCTACAGTTATTACTATGGATAGAAAAGCATCCAAACAACAAACAAATATAGAT
GTAATATACGAACGAGTTCGTGATGATTACCAATTGCATTGGACTTCAACAAATTGGAAAGGTACCAATACT
AAAGATAAATGGACAGATCGTTCTTCAGAAAGATATAAAATCGATTGGGAAAAAGAAGAAATGACAAATTAA
TGTAAATTATTTGTACATGTACAAATAAATATAATTTATAACTTTAGCCGA**AAGCTT**GGATCCGGCTGCTAACAAA
GCCCGAAAGGAAGCTGAGTTGGCTGCTGCCACCGCTGAGCAATAACTAGCATAACCCCTTGGGGCCTCTAAACGG
GTCTTGAGGGGTTTTTTGCTGAAAGGAGGAACTATATCCGGATAATTCGAGCTCGGTACCCACCCCGGTTGATAAT
CAGAAAAGCCCCAAAAACAGGAAGATTGTATAAGCAAATATTTAAATTGTAAACGTTAATATTTTGTTAAAATTCG
CGTTAAATTTTTGTTAAATCAGCTCATTTTTTAACCAATAGGCCGAAATCGGCAAAATCCCTTATAAATCAAAAGA
ATAGACCGAGATAGGGTTGAGTGTTGTTCCAGTTTGGAACAAGAGTCCAGTATTAAAGAACGTGGACTCCAACGT
CAAAGGGCGAAAAACCGTCTATCAGGGCGATGGCCCACTACGTGAACCATCACCCTAATCAAGTTTTTTGGGGTC
GAGGTGCCGTAAAGCACTAAATCGGAACCCTAAAGGGATGCCCCGATTTAGAGCTTGACGGGGAAAGCCGGCGA
ACGTGGCGAGAAAGGAAGGGAAGAAAGCGAAAGGAGCGGGCGCTAGGGCGCTGGCAAGTGTAGCGGTCACGCTG
CGCGTAACCACCACACCCGCCGCGCTTAATGCGCCGCTACAGGGCGCGTGGGGATCCTCTAGAGTCGACCTGCAG
GCATGCAAGCTATCCCGCAAGAGGCCCGGCAGTACCGGCATAACCAAGCCTATGCCTACAGCATCCAGGGTGACG
GTGCCGAGGATGACGATGAGCGCATTGTTAGATTTCATACACGGTGCCTGACTGCGTTAGCAATTTAACTGTGATA
AACTACCGCATTAAAGCTAGCTTATCGATGATAAGCTGTCAAA

The αHL gene in the plasmid pT7-G137C-D8-RL3 is shown below. It is in the same pT7 vector as shown above. RL3 background is a mutagenic version of WT. It contains silent mutations around and in the stem domain for the construction of six restriction sites (underlined): *SacII*: positions 103–104; *HpaI*: positions 115–117; *BsiWI*: positions 117–119; *StuI*: positions 133–135; *AflII*: positions 146–147; *XhoI*: positions 157–158. Cys-137 is shown in red. The eight-aspartate tail is shown in blue. Stop codon is shown in green.

GCAGATTCTGATATTAATATTAAAACCGGTACTACAGATATTGGAAGCAATACTACAGTAAAAACAGGTGATTTA
GTCACTTATGATAAAGAAAATGGCATGCACAAAAAAGTATTTTATAGTTTTATCGATGATAAAAATCACAATAAA
AAACTGCTAGTTATTAGAACAAAAGGTACCATTGCTGGTCAATATAGAGTTTATAGCGAAGAAGGTGCTAACAAA
AGTGGTTTAGCCTGGCCTTCAGCCTTTAAGGTACAGTTGCAACTACCTGATAATGAAGTAGCTCAAATATCTGATT
ACTATCCGCGGAATTCGATTGATACAAAAGAGTATATGAGTACGTTAACGTACGGATTCAACGGTAATGTTACTGG
TGATGATACAGGAAAAATTGGAGGCCTTATTGCTGCAAATGTTTCGATTGGTCATACACTTAAGTATGTTCAACCT
GATTTCAAAACAATTCTCGAGAGCCCAACTGATAAAAAAGTAGGCTGGAAAGTGATATTTAACAATATGGTGAAT
CAAAATTGGGGACCATACGATCGAGATTCTTGGAACCCGGTATATGGCAATCAACTTTTCATGAAAACTAGAAAT
GGTTCTATGAAAGCAGCAGATAACTTCCTTGATCCTAACAAAGCAAGTTCTCTATTATCTTCAGGGTTTTCACCAG
ACTTCGCTACAGTTATTACTATGGATAGAAAAGCATCCAAACAACAAACAAATATAGATGTAATATACGAACGAG
TTCGTGATGATTACCAATTGCATTGGACTTCAACAAATTGGAAAGGTACCAATACTAAAGATAAATGGACAGATC
GTTCTTCAGAAAGATATAAAATCGATTGGGAAAAAGAAGAAATGACAAATGATGACGATGATGACGACGATGATT
GA

A.3 NMR spectra

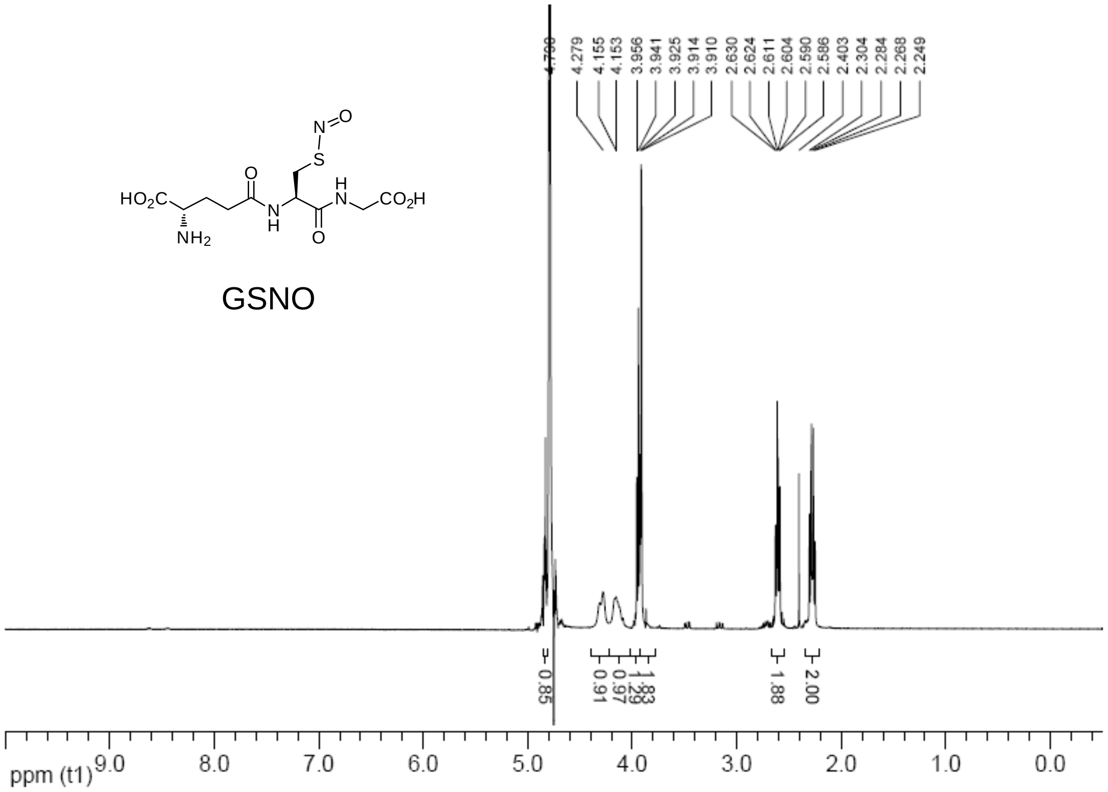
GSNO

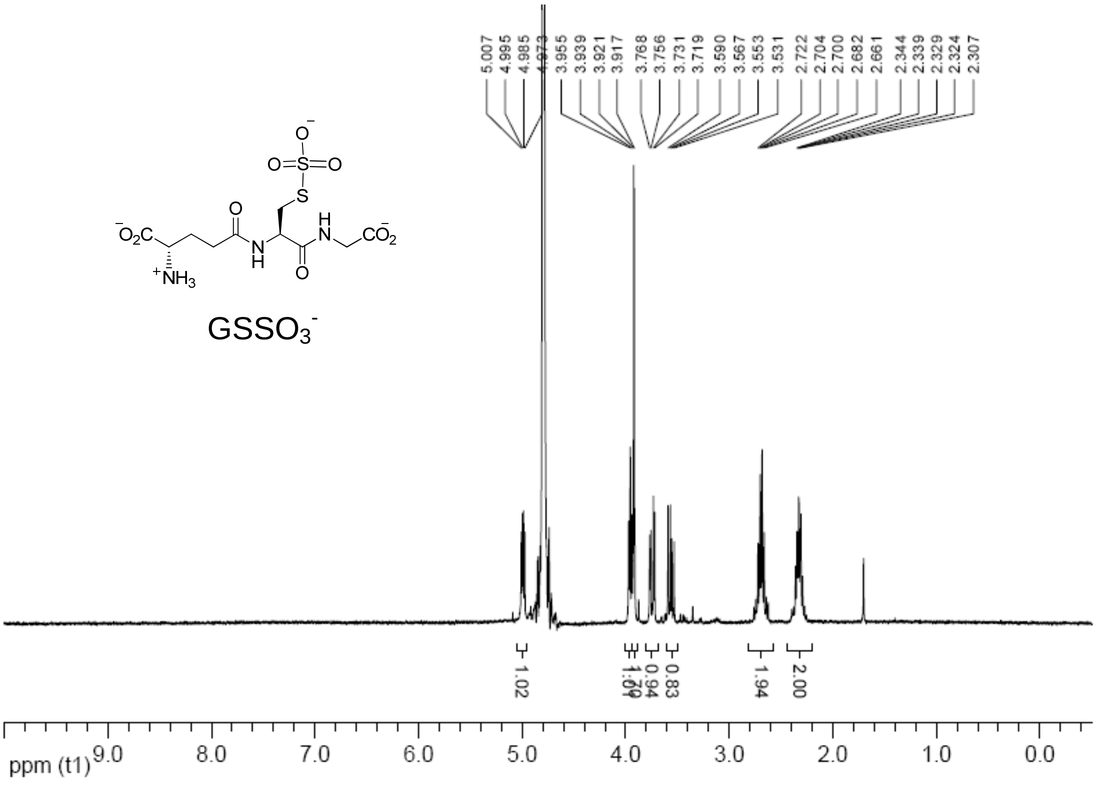
$GSSO_3^-$

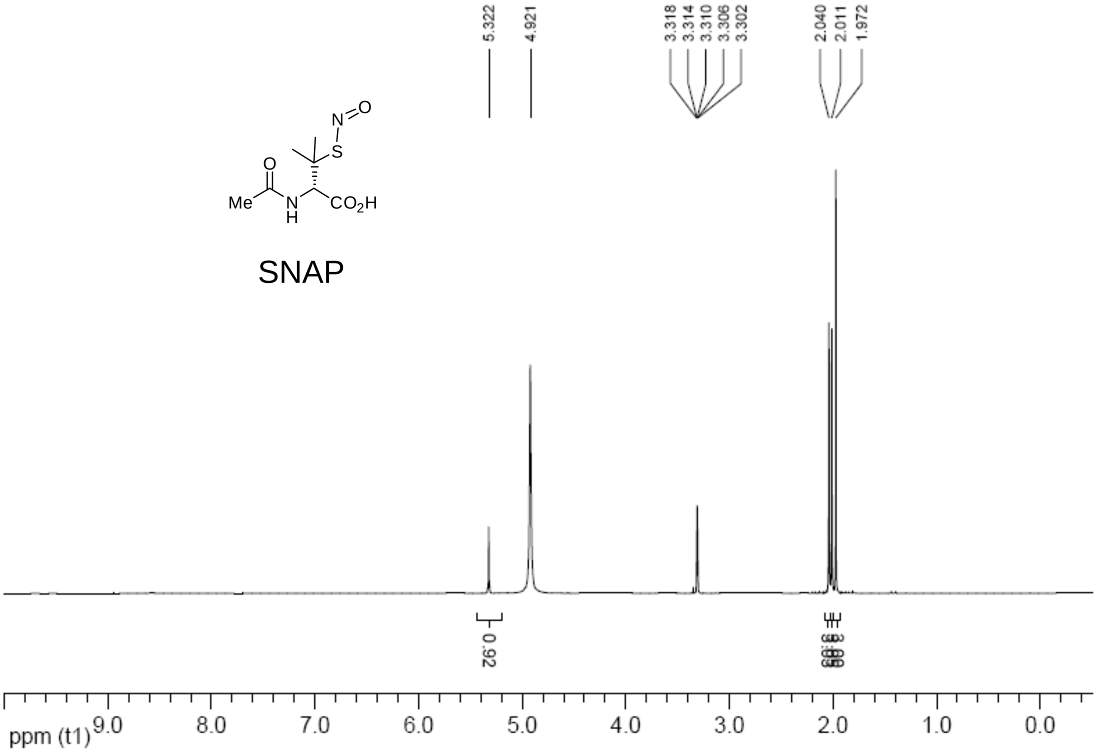
5.322
4.921
3.318
3.314
3.310
3.306
3.302
2.040
2.011
1.972
N=O
S
O
Me
N
H
CO₂H
0.92
ppm (t1)
9.0
8.0
7.0
6.0
5.0
4.0
3.0
2.0
1.0
0.0

SNAP

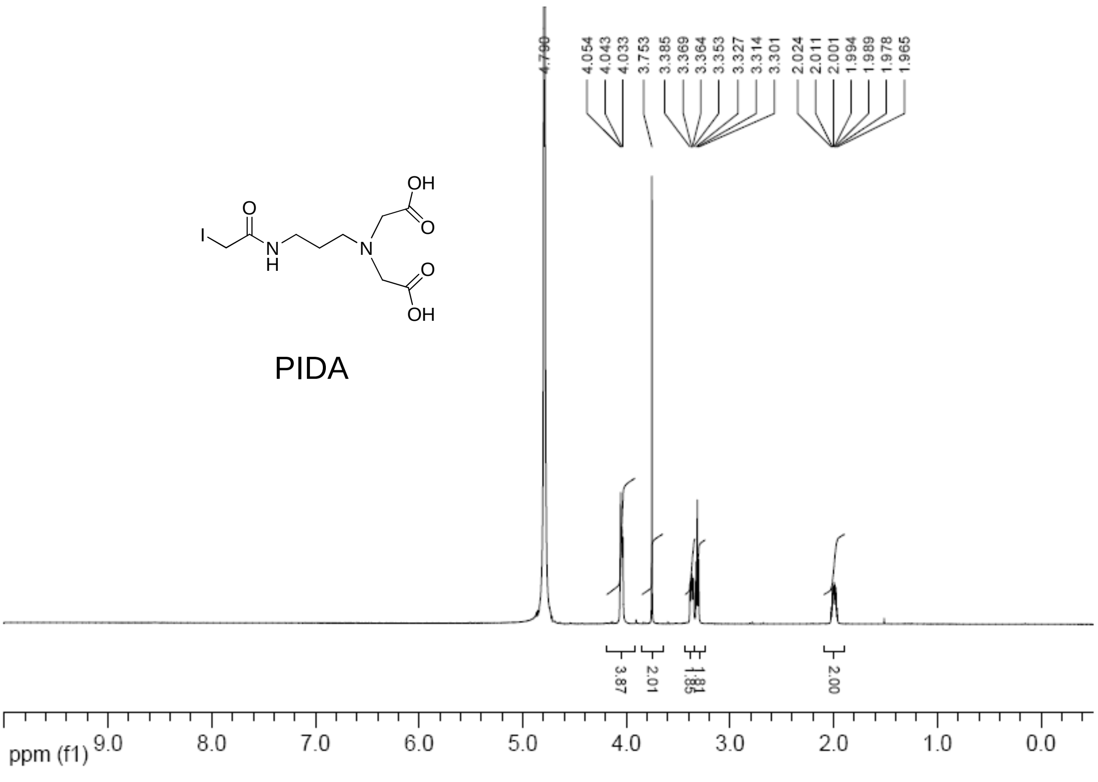
4.790
4.054
4.043
4.033
3.753
3.385
3.369
3.364
3.353
3.327
3.314
3.301
2.024
2.011
2.001
1.994
1.989
1.978
1.965
OH
O
I
O
N
H
N
O
OH
3.87
2.01
1.85
1.81
2.00
ppm (f1)
9.0
8.0
7.0
6.0
5.0
4.0
3.0
2.0
1.0
0.0

PIDA

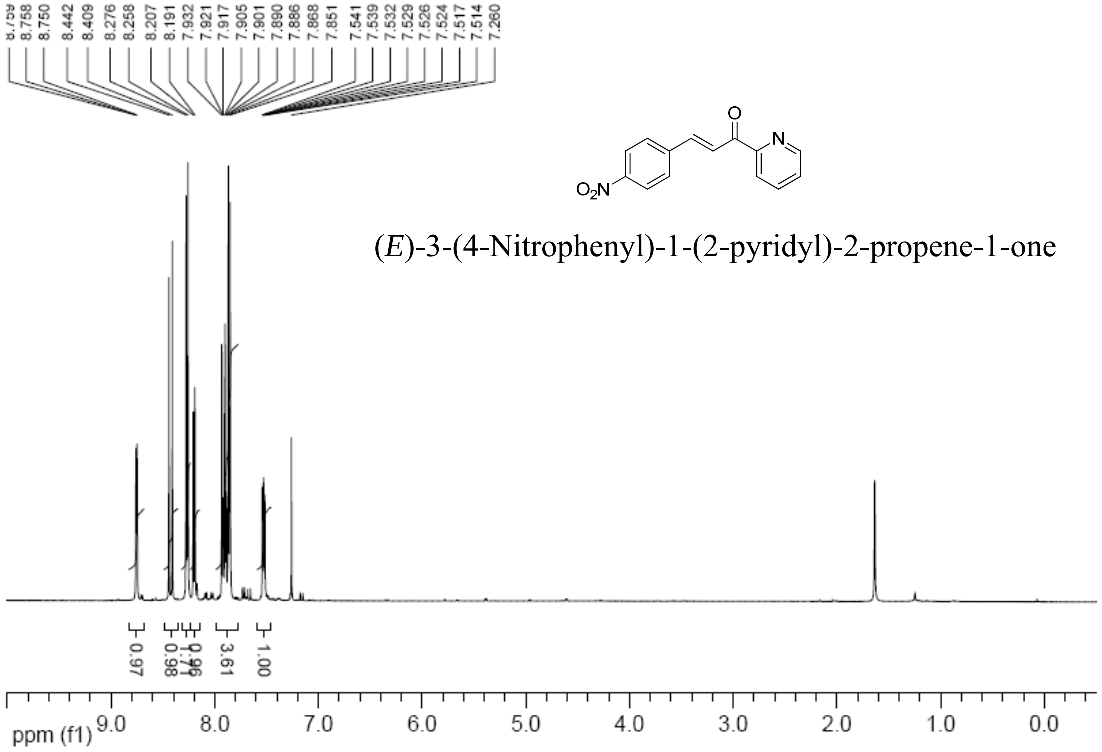

(*E*)-3-(4-Nitrophenyl)-1-(2-pyridyl)-2-propene-1-one

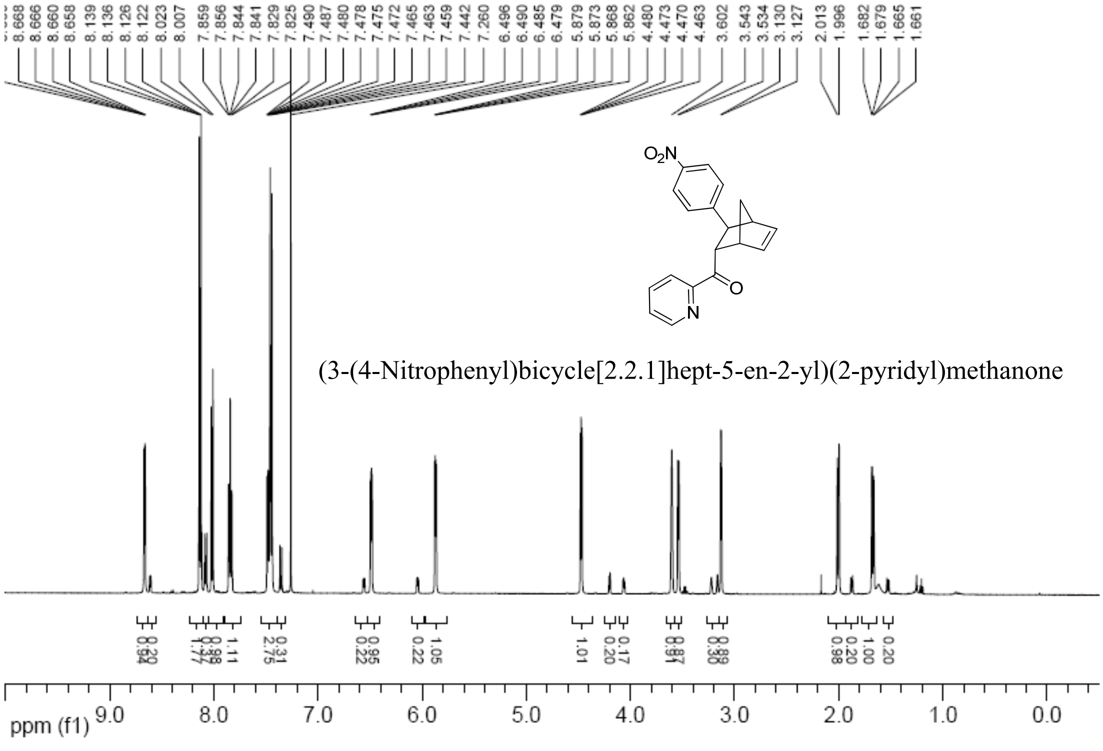

(3-(4-Nitrophenyl)bicycle[2.2.1]hept-5-en-2-yl)(2-pyridyl)methanone

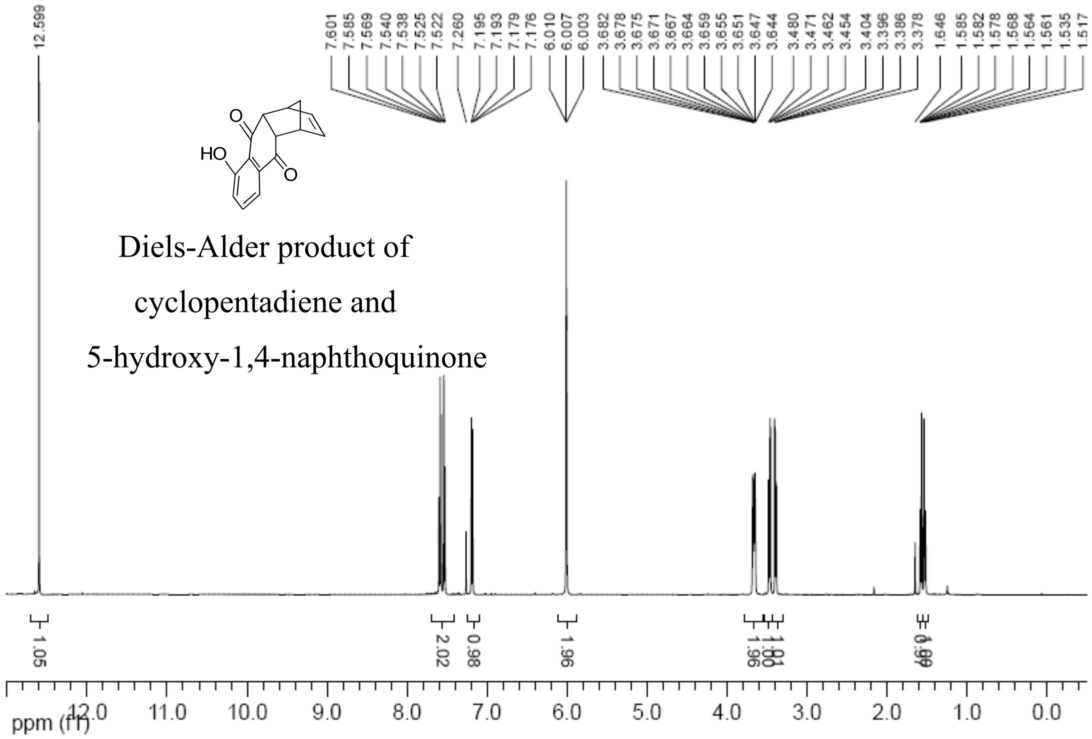

Diels-Alder product of cyclopentadiene and 5-hydroxy-1,4-naphthoquinone